Artificial Intelligence-assisted optical navigation for small body missions with application to Hera

Ph.D. Thesis

Aurelio Kaluthantrige

Aerospace Centre of Excellence
Mechanical and Aerospace Engineering
University of Strathclyde, Glasgow

August 23, 2025

This thesis is the result of the author's original research. It has been composed by the author and has not been previously submitted for examination which has led to the award of a degree.

Abstract

Planetary defence against asteroid is a booming field in the space sector. High-level of autonomy is required on board spacecraft during their proximity operations around these small bodies, both to cope with the highly uncertain non-linear dynamical environment which surrounds them, and to reduce ground operation complexity related to the significant delays in communication covering the distances involved in these missions. This thesis presents an Artificial Intelligence (AI)-assisted Image Processing (IP) algorithm to support the optical navigation of asteroid rendezvous missions during their close proximity operations. By focusing on the case scenario of the ESA's Hera mission to binary asteroid system (65803) Didymos, this work aims to tackle challenges of the current paradigm of methodologies involved in standard and intelligent IP algorithms. Firstly, by exploiting Convolutional Neural Networks, the algorithm is designed and developed to cope with scenarios involving adverse illumination conditions, irregular shape of the target body and the presence of external bodies. Secondly, the algorithm is refined and implemented in an Open Loop navigation system to assess its performances in the context of proximity operations. Finally an incremental validation test campaign is performed to assess the applicability of the developed algorithm on board asteroid rendezvous missions spacecraft. The test campaign objective is twofold: on one hand it aims to solve standard AI-related issues, i.e. bridging domain gaps to account for contingencies; on the other it aims to validate the algorithm on board spaceborne computers within the Guidance, Navigation and Control system of the spacecraft. This thesis primarily contributes by designing and implementing a structured pipeline for deploying AI-based IP algorithm in asteroid optical navigation, enabling a systematic evaluation of its suitability and performance.

Acknowledgements

I honestly do not know how to start this section. I cannot believe that only 4 years have passed. This PhD is half the work you will find reading the next 200 pages. The other half is about the experiences I made, the countries I have visited, the people I met, the cold dark winter days of Glasgow and the windy bike rides from Leiden to Noordwijk. I will try to sum up in the next few paragraphs the gratitude I express to all the people that walked with me through this immense journey. The gratitudes are following the timeline of my PhD, no ranking has been done (or maybe yes).

First and foremost, I would like to thank my supervisor, Dr. Jinglang Feng. I could spend thousands of words on the constant support she offered me, the teaching she gave me, and, of course, on some of the debates on my evergreen delay on submitting deliverables. Nevertheless, I would like to thank mostly the person behind the academic title. Jinglang, thanks for all the support during my highs, but thanks especially for all the support during my lows. I would also like to thank Prof. Massimiliano (Max) Vasile. If Jinglang taught me how to move within my work, Max taught me how to move within the global research field. I am honoured to have had both of you as my mentors during these 4 years.

Thanks to my ESA supervisor, Dr. Jesús Gil-Fernández (I know where to put the accents after 4 years of writing your full name) from ESTEC who gave me the chance to work with the Hera mission and to meet all his inspiring team, Ian Carnelli, Mark Brophy, Paolo Concari, Paolo Martino, Franco Perez, Jorge Lopez, Heli Greus and Diego Escorial. Thanks also to Andrea Pellacani from GMV, who followed me since

day one of my embarking on the GNC journey, starting from the Asteroid Impact Mission back in 2017.

Thanks to the J-men: Wail and Iosto. The nights in Glasgow would have been darker and colder if it was not for you. All the memes we generated in these 4 years will always bring me a smile: the british gold of Iosto in Dubai, the hiking Converse shoes of Wail in Isle of Arran, the "VOLAAAAAARE" in Skye and many more. I feel so lucky to have had you as colleagues!

Thanks to all the people of the Specky Office of the James Weir building: Gianluca, Marianna, Ewan, Callum, Paul, Catarina, Luis, Lewis, Yirui, Seonaid, Robert, Nathan, Abi and Fabio. Special mention to my favorite PGR Commitee fellow Michael McGurk. I hope one day you will have an infinite amount of flavoured water and Buckfast. I know that I will always have a place to stay when I go back to Glasgow to yours and Candy's. Special mention also to my partner in crime, Dr. Simão Pedro Da Graça Oliveira Marto, I think that I will never forget your full name, your birthday, and all the secrets of Fatima.

Thanks to all the people I met in Glasgow. Max, my little admirer, Phoebe, my little sister, Ana Kills, my favorite spanish, the joyful Arianna (Mille Guerre), the italian sisters FraRagone and Elenina, Juju, the little duck, my gimbros Alex and Spyros and to all the others whom I probably forgot.

Thanks to all the people I met in the Netherlands. Stefano and Lucia, who are the people with whom I have more printed mugs. La supernena Esther, my favorite spaghetti packet opener. Alex (Juju number 3), superhuman but also hawaiian shirt-dressed PhD fellow at ESTEC. Sibilla, my favorite singer and probably the person with whom I built the most in the shortest of time. My pianist Nicolas, who has a lot to learn about his german roots. The italian abbronzati Salvatore and Antonio (lasciatemi in pace vi prego). The skipper and the comedian India (CHEF CAN YOU SHOVE

THOSE EGGS RIGHT OVER HERE). The welsh climber and threatening-letters-to-Car-Rental-companies-writer Jack. And finally, to Anna, the person who understood me the most, that gave me a reason to go to ESTEC in the weekends and with whom I brightened the day of random people on the bus with Kuku.

Thanks to Mattia, I will copy paste what you wrote in the acknowledgement section of your PhD thesis, because there is no other way to express it. Pugliatti, M. (2024): *in an ideal academic world, we would be rivals due to our similar research topics. In the real world, I cherish the friendship and collaboration we have built.* I enjoyed working with you and I am pretty sure our paths will meet again, together with our future CEO Lorenzo Pasqualetto.

Thanks to the family I have in Turin, who supported me and sustained me throughout the writing of all this PhD thesis. Thanks to Benedetta Fagli-un-offerta Cattani, with whom I share the precious life in Corso Regina Margherita. To Daniele Knows-it-all Cini, who literally knows everything except from how to live. To Davide who had the patience and love to listen to all my absurd stories about love. To Rebecca, who gave me a family and a home in Turin when I needed it the most. To Marzia Francesca-Totti Trillo, who squeezes my cheeks more than my mom ever did. And finally to Giulia Krav Maga Cerfeda, who brings me a smile everyday since we met, and who probably does not know anything about Krav Maga.

Finally, to my family. The sacrifices you made to give me an education. I can never be grateful enough for everything you have done for me. Pretty sure you will not understand anything of the next 200 pages, but the next 200 pages would not exist if it was not for you.

Grazie

Aurelio Kaluthantrige
Turin, December 2024.

Contents

List of Acronyms

ACT	Average Computational Time
AE	Absolute Error
AMP	Asynchronous Multi-Processing
APE	Absolute Percent Error
AFC	Asteroid Framing Camera
AI	Artificial Intelligence
AIDA	Asteroid Impact and Deflection Assessment
ANN	Artificial Neural Network
AON	Autonomous Optical Navigation
ATB	Avionics Test Bench
AVBN	Autonomous Visual Based Navigation
CL	Closed-Loop
CNN	Convolutional Neural Network
COB	Center of Brightness
CoL	Circle of Latitude
COM	Center of Mass
COP	Close Observation Phase
CORTO	Celestial Object Rendering TOol
DART	Double Asteroid Redirection Test
DCP	Detailed Characterization Phase
DDVV	Design, Development, Validation and Verification
DKE	Dynamics, Kinematics, and Environment
DL	Deep Learning
DNN	Deep Neural Network
DRACO	Didymos Reconnaissance and Asteroid Camera for Optical navigation
ECP	Early Characterization Phase
EKF	Extended Kalman Filter
ESA	European Space Agency
EXP	Experimental Phase
FES	Functional Engineering Simulator
FOV	Field Of View
FPGA	Field Programmable Gate Array
FT	Functional Test

FUMO	Functional Model
GC	Geometrical Center
GCP	Ground Control Point
GNC	Guidance, Navigation, and Control
GT	Ground Truth
HIL	Hardware-In-The-Loop
HRNet	High Resolution Network
IP	Image Processing
JAXA	Japan Aerospace Exploration Agency
LIDAR	Light Detection And Ranging
LOS	Line Of Sight
MAE	Mean Absolute Error
MAPE	Mean Absolute Percent Error
MBA	Main Belt Asteroid
MCI	Mass, Center of gravity and Inertia
MCLS	Maximum Correlation with a Lambertian Sphere
MDE	Monocular Depth Estimation
MIL	Model-In-The-Loop
ML	Machine Learning
NASA	National Aeronautics and Space Administration
NEA	Near Earth Asteroid
NEAR	Near Earth Asteroid Rendezvous
NEO	Near Earth Object
NFOV	Narrow Field Of View
OBC	On-Board Computer
OL	Open-Loop
ONNX	Open Neural Network Exchange
OSIRIS-Rex	Origins, Spectral Interpretation, Resource Identification, Security, Regolith explorer
PALT	Planet ALTimeter
PANGU	Planet and Asteroid Natural Scene Generation Utility
PDP	Payload Deployment Phase
PIL	Processor-In-The-Loop
PSF	Point Spread Function
RO	Research Objective
RQ	Research Question
RSO	Resident Space Object
SIL	Software-In-The-Loop
SMART Nav	Small-body Autonomous Real Time Navigation
SMC	Small Monitoring Camera
SoC	System-on-a-Chip
SRP	Solar Radiation Pressure
SS	Subsolar
SSA	Space Situational Awareness
TAG	Touch-and-Go
TB/TBEqI	Target Body Equatorial Inertial

TAGSAM	Touch-and-Go Sample Acquisition Mechanism
TIRI	Thermal Infrared Imager
TM	Target Marker
UKF	Unscented Kalman Filter
UT	Unscented Transformation
UWFOV	Ultra-Wide Field Of View
WFOV	Wide Field Of View

Nomenclature

β	momentum enhancement factor
σ	standard deviation
ν	pixel size
ρ	range
AU	astronomical unit
B	byte
d	day
f	focal length
g	gram
hr	hour
m	meter
min	minute
$Megatons$	megatons
P	covariance
s	second
yr	year

Chapter 1

Introduction

Excitement lies in the exploration of the world around us

Jim Peebles

1.1 Asteroids exploration

Asteroids are small Solar system bodies that generated by accretion and one or more catastrophic events of disruption. Research on asteroids is one of the most active because of asteroids' large presence near the Earth and the possibility to trace past history of the evolution of the Solar system. Multiple missions have been launched and many others more are being planned to rendezvous with asteroids and potentially bring back samples to fathom about the solar system origins, planetesimals and to support the geological understanding of the Earth in areas of granular mechanics, landslides, earthquakes and faulting [1]. Most of the asteroids reside in a large torus called the Main Asteroid Belt (MBA) located between Mars' and Jupiter's orbits (within ~ 2 and ~ 3.3 AU) and in two groups accumulated at $\pm 60^{\circ}$ with respect to Jupiter in its orbit [2].

The inner half of the MBA is a dominant reservoir of near-Earth Asteroids (NEAs) that pose a threat to civilization considering the potential risk of impacts [3]. This hazard affects the space environment, e.g. the impact that may have catalyze the origin

of the Moon 3.5 Gyr ago, and the evolution of life, e.g. the Chicxulub impact 65 Myr ago responsible for the Cretaceous-Tertiary extinction [4]. More recently, in Siberia in 1908 the event of Tunguska occurred, with a meteroite of 30 to 60 m of diameter moving at 15 km/s entered the atmosphere and exploded at an altitude of 5 to 10 km releasing an energy between 10 to 40 *megatons* of TNT. The explosion devastated around 2150 km^2 of forest area and produced a radiant burn of flora at more than 100 km^2 [5]. On February 2013, another meteorite impact event was recorded in Russia, where the ~ 20 m Chelyabinsk meteorite struck the Ural region at 18 km/s. The object exploded in a meteor air burst with an energy of ~ 450 *kilotons* of TNT causing many injuries, especially because of the brightness of the generated light flare [6–8].

1.1.1 Space Missions for asteroid exploration

Considering the continuous hazard faced by the Earth due to the enormous amount of asteroids that may collide with its orbit, space agencies established several planetary protection programs to track, monitor and design technologies to potentially deflect asteroids' trajectory to minimize and possibly avert impact events. Due to the considerable limitations of Earth-based and space-based telescopes, studying asteroids up close is essential for planetary protection. With technological progress making this feasible, spacecraft have been deployed to either flyby or rendezvous with these bodies [3].

1.1.1.1 NEAR Shoemaker

NEAR (Near Earth Asteroid Rendezvous) Shoemaker was a NASA mission aimed at orbiting the Near Earth Asteroid Eros. Launched in the late 1990s, it experienced a missed burn and subsequent corrections before successfully rendezvousing with Eros on February 14, 2000. The spacecraft initially entered a circular 350 km orbit around the asteroid [9]. Through a series of propulsive maneuvers, this orbit was reduced to 50 km and then 35 km, allowing NEAR Shoemaker to conduct a thorough characterization of Eros. This was achieved through landmark position and ranging determination [10].

At the end of its mission, NEAR Shoemaker was landed on the surface of Eros for decommissioning. The landing was planned to maximize the spacecraft's chances of

survival, though this was not a primary design constraint and became an option during the decommissioning phase. Ultimately, NEAR was gently placed on Eros' surface, and telemetry data was collected for several days. This data helped to reconstruct the spacecraft's orientation as it rested on the asteroid [11].

1.1.1.2 Hayabusa (MUSES-C)

Hayabusa, previously known as MUSES-C, was an interplanetary mission by JAXA with the objective of delivering an asteroid sample to Earth, demonstrating key technologies for future exploration of small bodies in the Solar System. Hayabusa successfully rendezvoused with the asteroid Itokawa on September 12, 2005. Following this, the spacecraft began a three-month scheduled descent, utilizing the weak gravitational pull of the asteroid. Initially positioned 20 km from Itokawa, the spacecraft reduced its distance to 8 km by the end of September [12]. After completing the initial characterization and reconnaissance of Itokawa, Hayabusa performed two touchdown attempts. This mission marked the first successful collection and return of asteroid material, providing valuable insights into the composition and history of our solar system [13].

1.1.1.3 Dawn

The Dawn mission, led by NASA's JPL, was a pioneering interplanetary endeavour aimed at exploring two of the largest bodies in the asteroid belt, Vesta and Ceres. Launched in September 2007, Dawn was the first mission to orbit two extraterrestrial bodies using an electric propulsion system, enabling it to travel vast distances and to conduct detailed studies of these celestial objects. The spacecraft successfully rendezvoused with Vesta on July 16, 2011, revealing that the asteroid has a layered structure similar to terrestrial planets, including a basalting surface and a nickel-iron core. The mission also suggested the possibility of buried ice on Vesta, which could have influenced its surface features. After departing Vesta, Dawn arrived at Ceres on March 6, 2015 [14]. Ceres, a dwarf planet, presented a stark contrast to Vesta with its icy composition. One of the most intriguing discoveries was the presence of bright spots within the Occator Crater, later identified as carbonate salts, indicating past

water activity. Dawn's mission concluded in November 2018 after providing extensive data that has significantly advanced our understanding of these ancient bodies and the early solar system [15].

1.1.1.4 Hayabusa 2

After Hayabusa 1, JAXA Launched in December 2014 Hayabusa 2 towards the near-Earth asteroid (162173) Ryugu, arriving on June 27, 2018. The mission's objectives included surveying the asteroid, collecting samples, and returning them to Earth for detailed analysis. During its 18-month stay at Ryugu, Hayabusa 2 deployed multiple landers and rovers to gather data from both the surface and subsurface. The spacecraft successfully collected over 5 g of material, far exceeding the mission's initial target. Initial analyses of the Ryugu samples have revealed that the asteroid is carbonaceous body, rich in carbon and water-bearing minerals. This suggests that Ryugu, and similar asteroids, could be key to understanding the distribution of organic materials in the solar system. The samples showed a darker and less dense material than expected, indicating a composition that has preserved primitive solar system materials [16].

1.1.1.5 OSIRIS-REx

The OSIRIS-REx (Origins, Spectral Interpretation, Resource Identification, Security, Regolith Explorer) mission is a NASA-led project aimed at studying and returning samples from the NEA (101955) Bennu. Launched on September 8, 2016, OSIRIS-REx's primary objectives include mapping Bennu's surface, understanding its composition, and returning a sample to Earth to provide insights into the early solar system and the origins of organic compounds necessary for life. Upon arrival on December 3, 2018, OSIRIS-REx conducted a detailed survey of Bennu's surface, creating high-resolution maps and selecting a suitable site for sample collection. The mission identified the Nightingale crater as the primary sample site due to its relatively smooth terrain and minimal debris. On October 20, 2020, OSIRIS-REx successfully executed its Touch-and-Go (TAG) maneuver, briefly touching Bennu's surface to collect samples using its TAGSAM (Touch-and-Go Sample Acquisition Mechanism) arm [17]. The spacecraft

collected an estimated 60 g of material, surpassing the mission's minimum requirement. After securing the sample, OSIRIS-REx began its journey back to Earth in May 2021. The sample return capsule is scheduled to re-enter Earth's atmosphere and land in the Utah Test and Training Range on September 24, 2023. The mission successfully provided information on the processes that shaped the early solar system by analyzing the organic compounds of the target asteroid [18].

1.1.2 The Hera Mission

The previous missions had all the common scientific objective of providing in-situ measurements or returning asteroids' samples back to Earth, in order to analyze its chemical compounds and advance the understanding of the early stages of the solar system. Nevertheless space agencies devised and launched missions also to mitigate the continuous hazard represented by the asteroids. The Asteroid Impact and Deflection Assessment (AIDA) collaboration represents the first attempt at demonstrating a technique to mitigate the threat of potentially hazardous celestial objects. This international initiative, involving NASA and ESA, comprises two complementary missions: NASA's Double Asteroid Redirection Test (DART) and ESA's Hera mission. AIDA focuses on the binary asteroid system (65803) Didymos. The deflection experiment occurred on September 26, 2022, during which the DART spacecraft collided with the secondary member of the binary system at a velocity of 6.15 km/s, resulting in a change in its orbital period. Following this, the Hera spacecraft will arrive at Didymos to perform a detailed characterization of the asteroid and observe the impact results directly, ensuring precise measurements of the deflection caused by DART. The AIDA collaboration aims to generate critical new insights into the mechanical behavior and impact cratering processes of asteroids, with significant implications for planetary defense, human space exploration, and the study and utilization of near-Earth objects (NEOs). The combination of this two missions will provide data on the strength, surface properties, and internal structure of an asteroid [19].

1.1.2.1 Didymos

Binary NEA (65803) Didymos was discovered on April 11, 1996 by the Spacewatch telescope at Kitt peak. The first image of Didymos is a Delay-Doppler image obtained in November 2003 by the Goldstone Solar System Radar, as shown in Fig. 1.1 [20]. Reflectance spectroscopy from ground-based observations identifies Didymos as part of

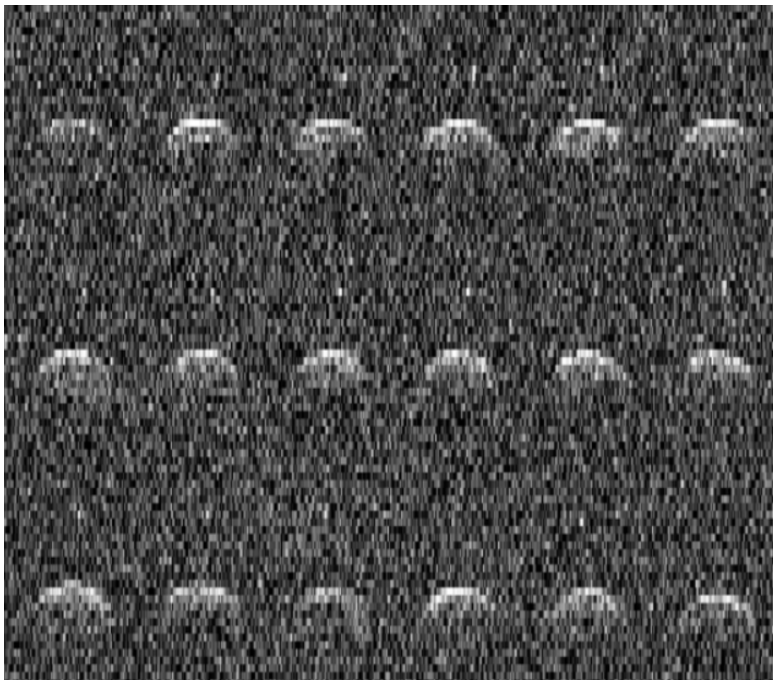

Figure 1.1: Goldstone delay-Doppler images of Didymos [20]

the "S complex" of asteroids, the most common compositional group among NEOs. This group includes the targets of previous spacecraft missions, such as (433) Eros and (25143) Itokawa, and it is associated with ordinary chondrite meteorites. Selecting an S-complex asteroid for the mitigation demonstration ensures the results will be applicable to a large fraction of the most likely potential Earth impactors [21]. The binary system consist of a primary body, Didymos, and a secondary body, Dimorphos, orbiting around the primary. The choice of a binary system over a single NEA is that an orbital deflection of the secondary with respect to the primary is easier to measure than an heliocentric one. Didymos has a top-shape appearance, resembling a spherical body with an equatorial ridge. Little was known regarding the shape of Dimorphos

prior to the impact. It was believed to be an elongated ellipsoid, as it is the case for the majority of observed near-Earth binary systems [22, 23].

1.1.2.2 DART mission and the impact

On September 26, 2022, NASA's DART mission successfully struck Dimorphos. The spacecraft collided with Dimorphos at a relative velocity of approximately 6.15 km/s, which led to an estimated reduction of about 2.7 mm/s in the along-track component of its orbital velocity (ΔV_t) in the mutual orbit. The collision, which targeted Dimorphos's leading hemisphere along its intermediate axis, shortened the mutual orbit period by roughly 33 min and decreased the semimajor axis of the orbit [24]. The effectiveness of the DART mission in deflecting Dimorphos is primarily measured by the momentum enhancement factor, β. This factor assesses the amount of momentum transferred from DART to Dimorphos as a result of the impact. According to estimates on the ΔV_t, β ranges between 2.2 and 4.9, contingent on the unknown mass of Dimorphos, with a nominal value of 3.61 $\pm$ 0.25 (1σ) assuming both Didymos and Dimorphos have equal densities of 2400 kg/m^3. The higher β value implies that the momentum transferred was significantly influenced by the ejecta generated from the impact rather than the impact itself [25]. Table 1.1 shows the parameters of the binary system Didymos prior and after the DART impact on Dimorphos, retrieved by radar observations and updated with DART measurements [26–29].

Table 1.1: Relevant physical and dynamical parameters of the Didymos system [26–29]

Parameter	**Preimpact value**	**Postimpact value**
	Binary system	
Osculating heliocentric eccentricity	$0.383294733 \pm 1.34 \cdot 10^{-10}$	Unchanged
Osculating heliocentric semi-major axis	$1.642514364 \pm 2.61 \cdot 10^{-10}$ Au	Unchanged
Osculating heliocentric inclination to the ecliptic	$3.414168803° \pm 1.62 \cdot 10^{-8}$	Unchanged
Total mass of system	$6.05 \cdot 10^{11} \pm 2.10 \cdot 10^{10}$ kg	Unchanged (assumed)
Separation distance between component centres	1.24 ± 0.014 km	1.204 ± 0.015 km
Mutual orbital period	$11.9214811 \pm 1.60 \cdot 10^{-5}$ hr	$11.3685 \pm 3.00 \cdot 10^{-5}$ hr
Mutual orbital eccentricity	< 0.03	$3.10 \cdot 10^{-2} \pm 1.70 \cdot 10^{-4}$
Mutual orbital inclination	$0°$ (assumed)	Unknown
Drift in mean anomaly	$0.15° \pm 0.14°$ yr^{-2}	Unknown
	Didymos	
Volume-equivalent diameter	730 ± 17 m	Unchanged (assumed)
Bulk density	2950 ± 300 kg/m^3	Unchanged (assumed)
Rotation period	2.260 ± 0.0001 hr	2.260 ± 0.001 hr
Extent along principal axis x $[m]$	832 ± 25 m	849 ± 5.6 m
Extent along principal axis y $[m]$	837 ± 25 m	851 ± 5.6 m
Extent along principal axis z $[m]$	786 ± 39 m	620 ± 5.6 m
	Dimorphos	
Volume-equivalent diameter	150 ± 2.5 m	Unchanged (assumed)
Bulk density	2400 ± 300 kg/m^3	Unchanged (assumed)
Rotation period	$11.921481 \pm 1.60 \cdot 10^{-5}$ hr (assumed)	Unknown
Extent along principal x-axis	208 m (assumed)	177 ± 1.2 m
Extent along principal y-axis	160 m (assumed)	174 ± 1.2 m
Extent along principal z-axis	133 m (assumed)	116 ± 1.2 m

The DART mission featured a single primary instrument, the Didymos Reconnaissance and Asteroid Camera for Optical navigation (DRACO). DRACO, a narrow-angle telescope, boasted a 208 mm aperture, a field of view spanning 0.29°, and a 2560×2160 raw pixel CMOS detector. Its design was inspired by the high-resolution imager from the New Horizons mission. Images captured by DRACO were processed by the onboard autonomous system known as Small-body Maneuvering Autonomous Real Time Navigation (SMART Nav). As part of the guidance, navigation, and control (GNC) system, SMART Nav was engineered to independently identify and differentiate between the asteroids Didymos and Dimorphos. It collaborated with other GNC sensors and actuators and navigation strategies to guide the spacecraft towards Dimorphos, approximately one hour before collision. During this time, SMART Nav had to operate alongside the spacecraft system and transmit images back to Earth in real-time prior to impact. A highly efficient data processing pipeline ensured that these images were promptly available to both the public and the mission team [30]. Fig. 1.2 shows one of the images downlinked by DART prior to the impact [31].

It can be seen from Table 1.1 that the measurements derived by DRACO yields to a substantial difference in the extent along the z-axis of the shape model of Didymos. Instead of appearing top-shaped, Didymos is more ellipsoidal, with an equatorial ridge that provide evidence that the body is a rubble pile. For Dimorphos, the measurements obtained with DRACO results in an oblate ellipsoidal shape [32].

1.1.2.3 Hera mission's objectives

The Hera mission is the European component of the AIDA collaboration. It is under development in the Space Safety Program of ESA for launch scheduled in October 2024. The mission objectives are the following:

1. Conduct the first thorough characterization of a binary NEA, including an analysis of its internal properties, to enable precise comparisons with theoretical models and an understanding of the binary NEA formation mechanism.

2. Determine the surface structure and regolith mobility on both Didymos and Dimorphos, providing initial insights into how material properties influence the

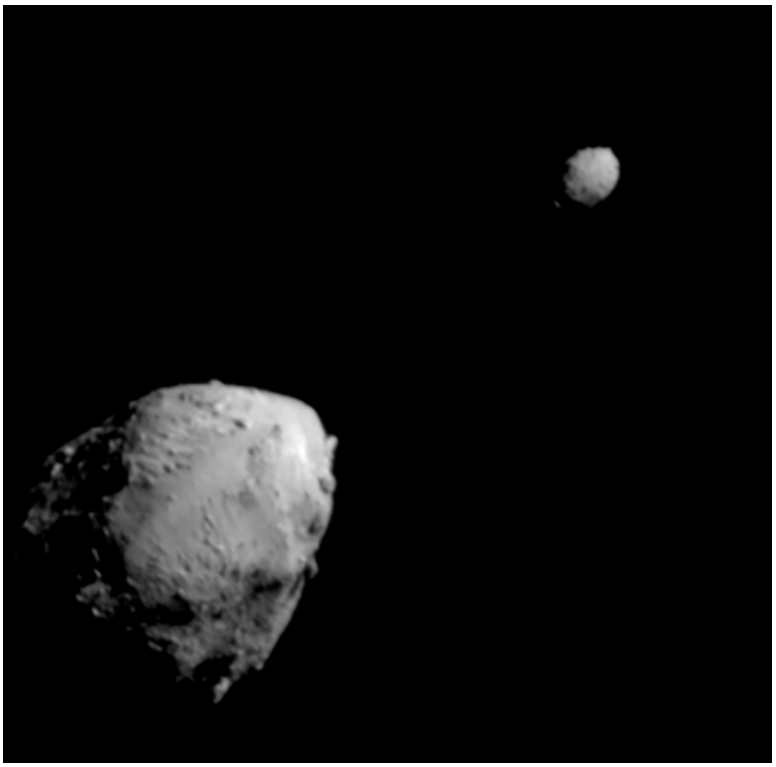

Figure 1.2: Asteroid Didymos (bottom left) and its moon, Dimorphos, about 2.5 minutes before the impact of NASA's DART spacecraft [31]

formation of asteroid satellites [33].

3. Measure the detailed surface and subsurface properties of an asteroid crater created by an impact experiment at a speed similar to typical inter-asteroid collision speeds.

4. Offer a unique opportunity to study the surface geophysics of two objects with different sizes and surface gravities, likely originating from the same material.

5. Obtain the first in-situ measurements of the properties of an asteroid, Dimorphos, which is at the threshold between gravity-dominated and strength-dominated structures.

6. Characterize a crater formed with a known energy for the first time, helping to determine whether strength or gravity is the dominant factor in crater formation on such a small asteroid [34].

7. Observe native and post-DART surface activity and particle ejection events.

8. Examine the crater formed by the DART impact to identify fresh, unweathered material on a silicate asteroid, contributing to the understanding of space-weathering processes [35].

9. Test the hypothesis that the crater produced by the Small Carry-on Impactor of Japan's Hayabusa 2 mission on asteroid (162173) Ryugu formed in the gravity regime by comparing it with the results of the DART impact on Dimorphos.

10. Investigate an asteroid, Didymos, with a spin period of 2.26 hr, which may be near the limit of structural stability [36].

1.1.2.4 Payloads

To achieve these objectives, the spacecraft is equipped with the following payloads:

- ❖ Two Asteroid Framing Cameras (AFCs);
- ❖ A microlidar (PALT);
- ❖ A spectral imager (HyperScout-H);
- ❖ A Thermal Infrared Imager (TIRI);
- ❖ Two CubeSats that will be deployed at close proximity:

  [✛] Juventas, which carries on board a low-frequency monostatic radar, a gravimeter and an accelerometer [37];

  [✛] Milani, composed of a near-infrared imager and a microthermogravimeter [38].

Fig. 1.3 shows the design of the spacecraft of the Hera mission, with all the payloads mentioned above and the Small Monitoring Cameras (SMC) [36].

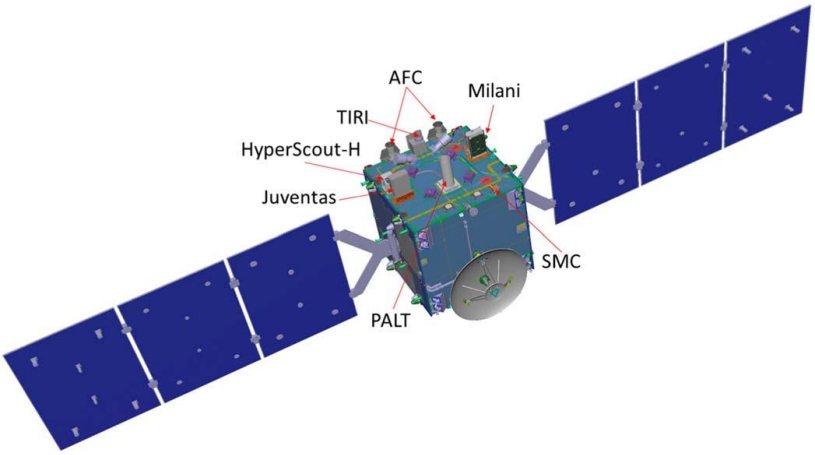

Figure 1.3: Design of the Hera spacecraft [36]

1.1.2.5 Proximity operations

After the launch in October 2024, the spacecraft will arrive to the binary system in October 2026, and it will start the proximity operations to achieve the mission objectives. A high-level overview of the mission is shown in Fig. 1.4 [39]. Table 1.2 sums up

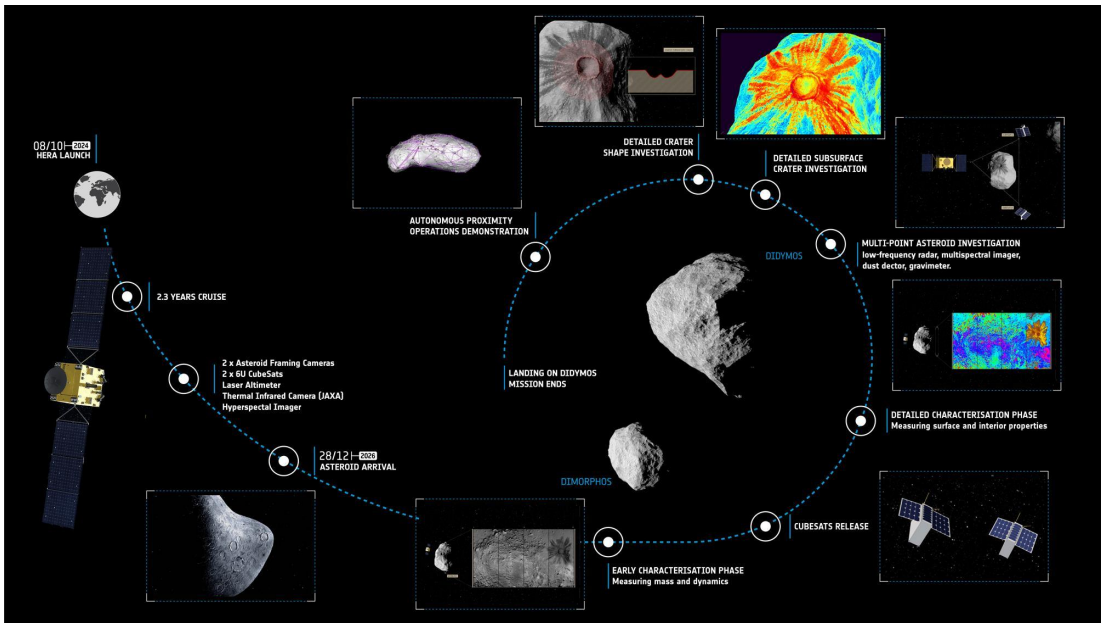

Figure 1.4: High-level overview of the Hera mission [39]

the phases of the proximity operations baselined for the mission.

Table 1.2: Proximity operation phases of the Hera mission [36, 40]

Name	**Acronym**	**Distance with the target** $[km]$	**Objectives**	**Duration**
Early Characterization Phase	ECP	$20 - 30$	Determination of global shape, mass/gravity, thermal and dynamical properties	6 weeks
Payload Deployment Phase	PDP	$20 - 30$	Release and commission of CubeSats	2 weeks
Detailed Characterization Phase	DCP	$9 - 20$	Meter-scale mapping and determination of thermal, spectral and internal properties	6 weeks
Close Observation Phase	COP	$4 - 22$	High-resolution investigations of the surface and Dimorphos' crater	6 weeks
Experimental Phase	EXP	$1 - TBD$	Very high-resolution investigations of the surface and Dimorphos' crater	6 weeks

1.2 Optical navigation

The asteroid exploration missions mentioned in the previous section were/are all equipped with autonomous, although at different level, navigation systems to cope with the uncertain dynamical environment around the target asteroid during the proximity operations. As the distance from Earth can lead to significant delays in terms of ground real-time control of the spacecraft, autonomous navigation systems represent valid alternative strategies to react rapidly to all possible contingencies. Optical navigation emerges as the preferred choice to achieve autonomy on board spacecraft, as it is shown by previous asteroid missions: combining imagers and data-processing algorithms allows the spacecraft to accurately navigate around the target and to respond rapidly in uncertain and complex environments [41]. Therefore, Autonomous Optical Navigation

(AON) systems are a key technology for asteroid exploration missions, enabling deep space navigation, relative navigation, proximity operations, terrain-relative navigation, landing and flybys. AON can be active or passive according to the type of imagers used. Passive imagers are vision-based cameras, visible or infrared, acquiring images of the mission scenario and analyzing them on board using Image Processing (IP) algorithms. Active imagers requires a light source to operate, for examples LIDARs (LIght Detection and Ranging), and interact with the environment to retrieve data [42]. The focus of this Ph.D. is on the vision-based cameras operating on visible wavelength. The main parameters that describe the properties of a vision-based camera are:

- Field Of View (FOV) that is the extent of the observable world that is seen at any given moment through the camera's lens. The FOV is typically specified in degrees and categorized as follows:

  [✢] Narrow Field of View (NFOV): The FOV is around a few degrees and the objective of these cameras is to observe in detail a small region of space or of a celestial object;

  [✢] Wide Field of View (WFOV): The FOV spans tens of degrees to capture larger areas of sky or the space;

  [✢] Ultra-Wide Field of View (UWFOV): The FOV goes up to 180 degrees and these cameras are used typically to monitor the space weather.

- Image size that is the dimensions of the image produced by the camera, expressed as the number of pixels in width by the number of pixels in height;

- Spatial resolution that is the ability of the camera to distinguish between objects that are close together;

- Focal length that is the distance between the lens and the camera sensor when the subject is in focus;

- Aperture size that defines the amount of light entering the camera;

- Exposure time that is the duration for which the camera's sensor is exposed to light;

❖ Pixel size that is the size of a single pixel on the camera's sensor.

A generic AON working with these type of sensors is shown in Fig. 1.5.

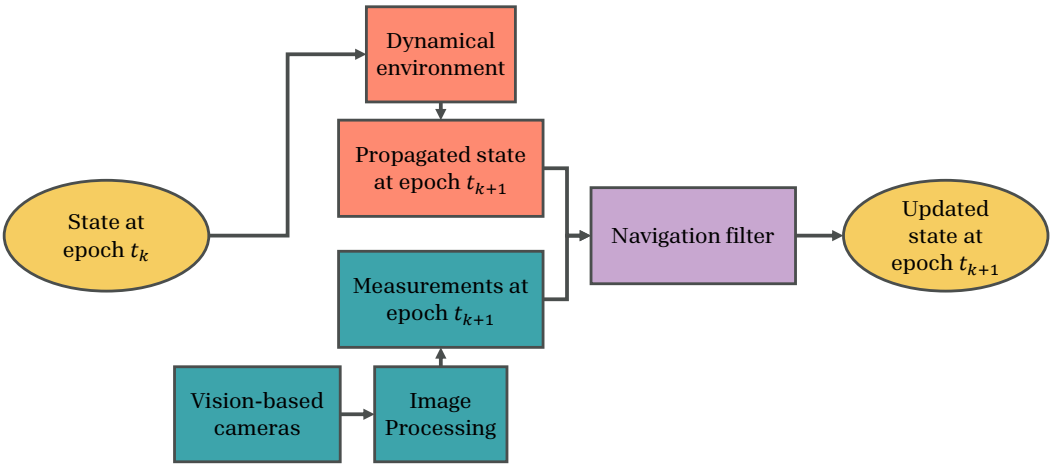

Figure 1.5: AON pipeline

The state of the spacecraft at epoch t_k refers to the estimate of its status (motion, orientation and other relevant parameters) at that specific instant. Once a set of reference systems are defined for the particular problem, the conditions often included in the state are the spacecraft's location in space, its velocity vector, its attitude and attitude rate [43]. Other additional information that the navigation of the spacecraft could benefit from are parameters describing the orbital environment, such as the gravity field, proximity to other celestial objects or the Solar Radiation Pressure (SRP). The uncertainties on the variables included in the state are represented by the covariance matrix, a statistical measure that quantifies the accuracy on the estimation of the state. Given a state x of n variables, the covariance matrix P is a $n \times n$ matrix defined with Eq. 1.1.

$$P = \mathbb{E}[(x - \hat{x})(x - \hat{x}^T)] \tag{1.1}$$

In Eq. 1.1, $\mathbb{E}$ denotes the expectation operator, x is the true state of the spacecraft and $\hat{x}$ is the estimated state. The latter and its covariance are then propagated at a new epoch t_{k+1} using the equations that best describe the dynamical environment surrounding the spacecraft and according to the adopted navigation filter [44]. At the

same epoch t_{k+1}, the IP algorithm generates from the acquired image provided by the on-board vision-based camera a set of measurements z with their own uncertainties represented by the covariance matrix R. The navigation filter combines the propagated state with the retrieved measurement together with their relative uncertainties in order to produce the best estimate of the state of the spacecraft at t_{k+1} [45]. In the following sections an in-depth description of each step of the AON pipeline is given.

1.2.1 Dynamical environment

The dynamical environment contains all the modelled forces acting on a body of mass m in the target's system. For an asteroid system, the modelled forces usually considered are the gravitational attraction of the bodies part of the system and the SRP.

1.2.1.1 Gravitational attraction

The point mass gravitational forces $\boldsymbol{f_g}$ exerted by an asteroid system made of n bodies is given by Eq. 1.2.

$$\boldsymbol{f_g} = -\sum_{i=1}^{i=n} \frac{\mu_i \hat{r}_i}{r_i^2} \tag{1.2}$$

In Eq. 1.2 μ_i and r_i denote the standard gravitational parameter and the relative position vector of each body part of the asteroid system. For an asteroid with a diameter of hundreds of meters, the standard gravitational parameter is of the order of 10^{-9} km^3/s^2 [28]. The point mass approximation is effective for modelling the gravity of spherical objects with uniform mass density such as planets [46, 47]. For small and irregularly shaped bodies such as asteroids the model of the gravitational attraction shall account the non-spherical mass distribution. This is particularly relevant for designing the trajectories around the target asteroid or to analyze the stability of these trajectories [48, 49]. Nevertheless, for the scope of this Ph.D. thesis the point mass approximation is considered sufficient.

1.2.1.2 SRP

The SRP is the force generated by the impact of the sunlight on a surface of the spacecraft. The incoming photons are absorbed and reflected according to the material properties of the surface of the spacecraft, generating a force which is quite small in magnitude. Nevertheless, around an asteroid system which exerts a weak gravitational attraction, the SRP plays a major role in the dynamics of a spacecraft. The SRP depends on the material properties, on the spacecraft shape and attitude, the distance with the Sun and with the asteroid (due to its albedo). Eq. 1.3 shows the cannonball model, the most common method to model the SRP force f_{SRP}.

$$f_{SRP} = \frac{P_{sun} A Q}{c} \tag{1.3}$$

In Eq. 1.3 P_{sun} is the SRP at a given distance from the Sun, A is the cross-sectional area of the object facing the Sun, Q is the dimensionless coefficient that accounts for the reflectivity and absorptivity of the object's surface and c is the speed of light in vacuum. For a spacecraft at distance R with respect to the Sun, the solar radiation pressure is equal to $f_{SRP} = \frac{4.54 \cdot 10^{-6}}{R^2} AQ$ [50].

1.2.2 Image Processing

IP algorithms represent the core of the AON system. The design of these algorithms depend on the mission's objectives, the target appearance, the distance with respect to the target and the properties of the on-board vision-based camera. The IP algorithm for asteroid missions usually combines different methods according to these parameters. In this section the state of the art of standard IP algorithms used specifically for AON systems is presented, going from the ones used from a range where the asteroid occupies a small portion of the FOV, to the ones used when the target body saturates the FOV and features such as boulders and/or craters are distinguishable [51]. To streamline the discussion, throughout this Ph.D. thesis the word *standard* applied to IP algorithms refers to fundamental methods, with solid mathematical formulations, accepted and validated across industries and research.

1.2.2.1 Lightcurves

A lightcurve is a measure of the variations in brightness of an object over time. Analyzing the lightcurve of an asteroid can provide measurements of its rotation period, its shape and surface properties and whether the asteroid system consists of one or more bodies. The lightcurve is also used to track the asteroid during the approach of the spacecraft [52]. Fig. 1.6 shows a lightcurve of the asteroid Didymos taken in 2003. It can be seen that the curve (panel a) can be divided into the contribution given by the rotation of Didymos (panel b) and the presence of Dimorphos (panel c) [53].

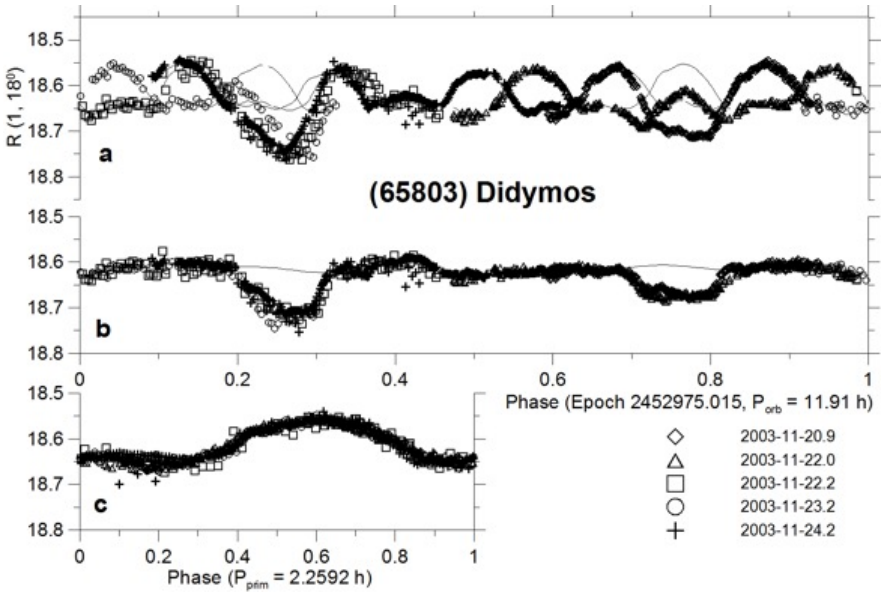

Figure 1.6: Didymos lightcurve [53]

1.2.2.2 Far centroiding

When the body is detected from the spacecraft, it appears as a point-spread function across several pixels in the focal plane, with the background showing the star field and other sources of disturbance. With the utilization of brightness-moment algorithms and Gaussian-based centroiding functions the relative position of the target asteroid can be determined [54].

1.2.2.3 Shape-based methods

When the spacecraft is near enough to the target, the latter's outline can be used for navigation. Methods such as centroiding, centroid apparent diameter, limb fitting and Maximum Correlation with a Lambertian Sphere are used for Line Of Sight (LOS) navigation, both for rendezvous, flyby and deflection, such as for the Hera and the DART missions [55–58]. These methods rely on retrieving the position in the image plane of the Center of Mass (COM) and/or the Center of Brightness (COB) of the target and tracking this point to ensure the accuracy of the camera pointing throughout the proximity operations. The simplicity of the design of shape-based methods comes at the cost of a lower applicability, since the underlying requirement is that the target's shape is almost spherical, which is not met by most of the minor bodies. Triaxial ellipsoidal shapes can be solved using non-iterative ellipse fitting horizon-based methods [59]. Attempts to solve the problem of the determination of the LOS of irregular bodies have been made by using a bidimensional figure feature database developed by the tridimensional model of the target asteroid, assumed to be reconstructed during the approach of the spacecraft [60]. Otherwise, when operating with irregularly shaped asteroids, their features can be used to trace out Circles of Latitude (CoL), which can be used to determine the spinning axis rotation [61].

1.2.2.4 Feature-based methods

When the target body occupies all the FOV, the outline of the target asteroid may not be visible in its whole, hence the methods described in the previous section are less applicable. Therefore, if the asteroids present enough visbile features such as boulders and/or craters, feature-based methods are preferred. Indeed, most of the heritage mission presented in Section 1.1.1 applied these methodologies in order to safely orbit around the target body.

During the descent phase of Hayabusa 1 to the target asteroid Itokawa from an altitude of 500 m, the navigation was based on Ground Control Point (GCPs) on the surface of the target. By tracking the GCPs positions ground control was able to determine the relative position of the spacecraft with respect to the asteroid. The

tracking scheme was based on the virtual FOV of the on-board optical camera and based on the a priori built shape model of the target asteroid. This method gives to the ground operator direct view of virtual landmark from the estimated position of the target, which were correlated to the landmark visible from the real image [62]. A similar approach was adopted by the mission Dawn around Vesta, and by OSIRIS-REx around Bennu [63, 64].

Hayabusa 2 adopted a unique landing strategy based on deployable artificial landmarks, or more simply Target Markers (TMs). Fig. 1.7 represents a schematic overview of this navigation technique. A TM is a retroreflective ball of 10 *cm* in diameter, and it was deployed near the landing site of the target asteroid Ryugu. The spacecraft had a xenon flash lamp which illuminated the TM and the reflected light was captured by the on-board camera. With a sequence of TM images, the spacecraft autonomously estimated its relative position and velocity with respect to the asteroid surface, securing a safe touchdown on the landing site [65].

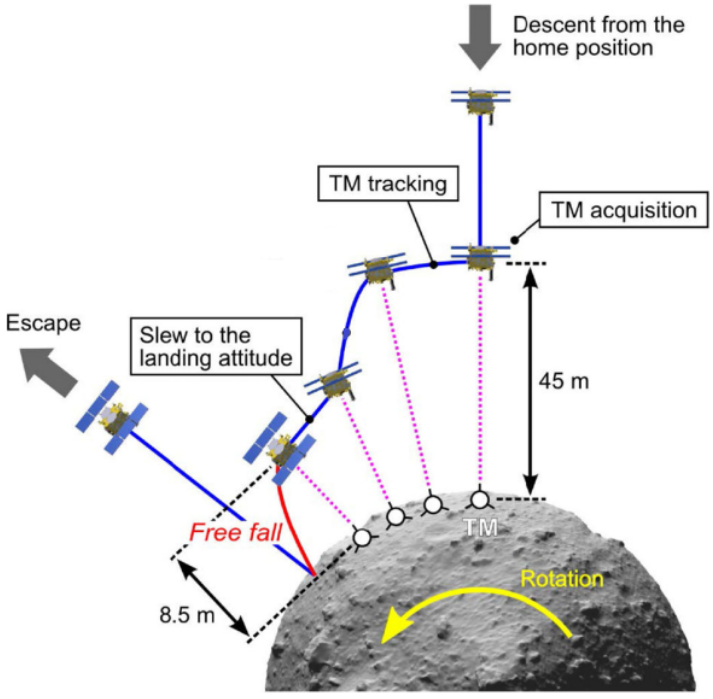

Figure 1.7: Schematic overview of the TM navigation strategy of Hayabusa 2 [65]

The feature tracking algorithm of the Hera mission is not based on a shape model

previously built. Instead, it is based on the relative position of different features in a sequence of images. By determining the displacement of the features, the algorithm is able to reconstruct its relative position to the target [58].

1.2.3 Artificial Intelligence-assisted Image Processing

The influence of Artificial Intelligence (AI) technologies on our contemporary world is increasingly significant. Initially a specialized research area in computer science and mathematics, the concept of machines achieving human-level intelligence has evolved into dependable and established industrial products. Machine Learning (ML) is a branch of AI that focuses on using data and algorithms to learn how to perform tasks without specific programming. This is achieved by applying algorithms that iteratively learn from training data generated and/or collected for the specific problem that needs to be solved.

Based on the given problem and the available data, there are three types of ML: supervised learning, unsupervised learning and reinforcement learning. *Supervised learning* requires a training dataset that encompasses both examples of inputs and outputs. The dataset is then used to calibrate the parameters of the ML model, so that it is able to predict the output when a new unseen data is given as an input. There are two types of problems that are addressed with supervised learning: regression problems, where the output has a numerical value, and classification problem, where the output is a class/category. *Unsupervised learning* has a training dataset which consists in only inputs. The goal is to find patterns and structures within the data. Typical problems that are solved with unsupervised learning are clustering, association and dimensionality reduction. *Reinforcement learning* does not require any input or output data, but a current state of the system, a goal, and a list of actions and constraints to achieve that goal by a trial and error process. Problems that can be solved with this particular ML are game playing, resource management and natural language processing [66, 67].

There are several types of ML algorithms, which depends on the task to be performed and available data. The Artificial Neural Networks (ANNs) are a type of ML inspired by biological systems and consisting of connections among artificial neurons

organized in different layers. A shallow neural network consists of the input data, one layer of neurons, usually referred to as hidden layer, and the output data. When the hidden layers are multiple, the ANN is called a Deep Neural Network (DNN). DNN allows learning complex tasks from raw input data, a process which is known as Deep Learning (DL). Several DL architectures are available, usually chosen according to the provided training dataset and the application. For computer vision, Convolutional Neural Networks (CNNs) are the most suitable DL architecture. Unlike other neural networks, CNNs leverage spatial hierarchies and local connectivity to extract meaningful patterns from image data. CNNs comprise a series of stages where specific features of the input data are learned, starting from the most basic ones (such as edges and corners) to the most detailed ones (craters, boulders) [68]. This hierarchical representation mimics the human visual cortex, which also processes visual information in a layered and localized manner. Furthermore, CNNs employ weight sharing, meaning that the same filter is applied across different spatial locations, significantly reducing the number of parameters and enhancing the model's ability to generalize [68].

CNNs have consistently demonstrated state-of-the-art performance in major computer vision benchmarks and competitions. The breakthrough model AlexNet [69], which won the ImageNet Large Scale Visual Recognition Challenge in 2012, brought global attention to the capabilities of CNNs. Since then, architectures like VGGNet [70], ResNet [71], and EfficientNet [72] have advanced the field by increasing depth, reducing parameters, and improving training stability. These architectures have been widely adopted in both academia and industry for tasks ranging from autonomous driving to medical imaging, underscoring their reliability and adaptability. Other deep learning architectures, such as RNNs, Transformers, and GANs, have specific strengths but are generally not as well-suited for vision tasks as CNNs:

- ❖ RNNs excel in sequence modeling (e.g., natural language processing, time series) but struggle with spatial data due to their sequential computation and lack of spatial inductive biases.
- ❖ Transformers, especially Vision Transformers (ViTs), have shown competitive performance in computer vision, particularly with large datasets and extensive

pretraining. However, they often require more data and computational resources than CNNs, making them less practical in many scenarios.

- ❖ GANs are powerful for image generation but are not primarily designed for discriminative vision tasks like classification or detection.

Thus, while alternative architectures offer complementary strengths, CNNs remain the most balanced and efficient choice for general-purpose computer vision applications [73]. Table 1.3 reports the most effective CNN architectures at date for the most common computer vision tasks [68, 74].

Table 1.3: Mapping of common computer vision Tasks to the most effective CNN architecture [68, 74]

Computer vision task	**Best CNN architecture**	**Remarks**
Image Classification	ResNet-50/101, EfficientNet, DenseNet	ResNet and EfficientNet provide a strong balance of accuracy and efficiency
Object Detection	Faster R-CNN, YOLOv5, RetinaNet	CNN backbones like ResNet and CSPDarknet
Semantic Segmentation	U-Net, DeepLabv3+, FCN	U-Net is favoured in biomedical imaging; DeepLabv3+ adds convolutions for detail
Instance Segmentation	Mask R-CNN	Extends Faster R-CNN to add a segmentation head
Style Transfer / Image Synthesis	VGG19, encoder-decoder CNNs	VGG used for perceptual loss; not optimal for speed but widely used for artistic tasks
Face Recognition	FaceNet, VGGFace, ArcFace	Specialized CNNs trained for face embeddings and similarity learning
Pose Estimation	OpenPose, HRNet, DeepPose	CNN backbones to regress joint positions
Super-Resolution	SRCNN, CAN	CNNs with residual and attention blocks for upscaling
Image Captioning (Vision Encoder)	ResNet-101, InceptionV3	Typically used as feature extractors before passing to an RNN or Transformer decoder

The space sector is also advancing with these developments, as numerous publications now incorporate AI-related concepts such as natural language processing, knowledge representation, automated reasoning, computer vision, and robotics. The applications of AI in this field are extensive, ranging from early spacecraft design to mission operations, guidance and control algorithms, navigation, predicting dynamics of per-

turbed motion, classifying astronomical objects, and enhancing remote sensing data, among others [75]. Related to space optical navigation, AI-assisted IP algorithms have been proposed to achieve the same purposes of the IP algorithms described in Section 1.2.2. The preference for intelligent IP algorithms over standard ones is driven by the following main reasons:

- Standard techniques use manual filters for the extraction of relevant information (centroid, light curves, etc...) from the images, while AI can automatically learn them with a higher accuracy and without explicit programming [76];
- AI is more effective at identifying unexpected phenomena in large datasets [77];
- while traditional methods require manual tweaking of their intrinsic parameters when applied to new data, AI models can be retrained or fine-tuned, enabling faster and easier adaptation to different mission scenarios [77].

Advanced lightcurve analysis with ML has been performed in order to classify Resident Space Objects (RSOs) [78, 79]. Enhanced centroiding and apparent centroid diameter techniques leveraging ML have been proposed for asteroid navigation to tackle the challenge related to their shape irregularity [80–83]. CNNs architectures have been applied to discern different morphological regions over the surface of small bodies, such as the Moon, Mars and asteroids [84–88]. CNNs have also been utilized in problems of feature extractions as the initial step of feature tracking navigation [89, 90].

1.3 Dissertation overview

1.3.1 Limitations and Challenges

As shown in the previous sections, image processing is a cornerstone for the proximity operation of asteroid exploration missions. It increases the autonomy of the spacecraft, securing safe navigation around the highly non-linear and complex dynamical environment surrounding the target body. The application of intelligent algorithms in image processing is analyzed by multiple space actors to improve the performances and increase the robustness of optical navigation systems against contingencies that

may occur during mission scenario. Moreover, it would reduce the human effort in programming a software that achieves the same objectives, thus trimming the cost of the overall mission design. In dealing with this topic, the following limitations have been identified:

1. **Synthetic vs Real images:** Standard IP algorithms go through an extensive validation and verification process supported by synthetic images generated with rendering engines that represent as accurate as possible the mission scenario. Nevertheless, when applied to real space images, standard IP algorithms tend to lack robustness and provide inaccurate estimations that can lead to the failure of the navigation system. The irregular shape of the target, the illumination conditions, generic distortions and blur, the presence of external bodies and/or disturbances, are all factors that alter the properties of the input image, and, thus, affect the accuracy of the extracted visual information. Spacecraft are usually provided with additional sensors to cope with the potential failures or inaccuracies of the implemented IP algorithm. Therefore, a stand-alone optical navigation system it has not been used yet for asteroid exploration, especially to solve for the relative position of the spacecraft.

2. **Domain gap of AI-based IP algorithms:** Domain gap in AI refers to the differences between the training domain (data used to train an AI model) and the target domain (data the model encounters during deployment). This mismatch can lead to performance degradation when the model is applied to real-world scenarios or datasets significantly different from those it was trained on. Therefore, the robustness of AI-based IP algorithms comes at the cost of a large amount of data needed for training. The training dataset has to account for all the contingencies that might occur during real mission scenario, such as a different shape of the target body or the presence of stars in the background. If the AI is trained on one domain, it may fail to generalize to new, unseen data and this leads to performance degradation.

3. **Validation for on-board application:** To meet the required level of auton-

omy during the proximity operations around a target asteroid, IP algorithms go through several tests on-ground, which are part of the Design, Development, Validation and Verification (DDVV) strategy of the mission design. The test campaign is incremental, going from Functional Tests carried with synthetic images to Hardware-In-The-Loop Tests carried with images captured by a model of the spacecraft optical camera. Nevertheless, the validation of AI-based IP algorithms is usually restricted to Functional Tests aimed to bridge domain gaps and improve the generalization capability of the model. The sequence of tests that allows the validation of the IP algorithm and its correct implementation on the On-Board Computer (OBC) of a spacecraft have not been applied extensively to AI models, mainly due to the lack of facilities and computational resources. As such, AI-based IP algorithms have been not utilized in asteroid missions yet, neither implemented on board the spacecraft as experimental payloads.

1.3.2 Research Questions & Objectives

Asteroid exploration missions can largely benefit from AI-based IP algorithms during their proximity operations with the target body. By improving upon the current limitations outlined in the previous section, the mission design paradigm could shift towards adopting stand-alone optical navigation strategies, without the necessity of increasing the redundancy of the navigation with other on-board sensors. By adopting as case scenario the Hera mission around the target binary asteroid system (65803) Didymos, this thesis aims to tackle the identified challenges. This leads to the following thesis statement:

Thesis Statement

Implementing AI-based IP algorithms within the optical navigation strategy of asteroid exploration missions, increases operational autonomy and reliability of the spacecraft during proximity phases around the target.

A set of detailed research questions and objectives is elaborated to drive the research presented in this thesis and to support the thesis statement.

Research Questions (RQ):

1. To what extent can optical navigation strategies benefit from AI-based IP algorithms?
   (a) What are the IP tasks that can be improved compared to standard approaches?
   (b) What degree of performance can be achieved adopting a stand-alone AI-based optical navigation system for positioning?
2. What are the challenges of validating AI-based IP algorithms for the implementation on a real asteroid rendezvous mission?
   (a) What are the tests needed to bridge domain gaps and optimize the generalization capabilities of AI-based IP algorithms?
   (b) What are the constraints encountered during the incremental test campaign from the SW and HW point of view?

Research objectives (RO):

1. To design and develop an AI-based IP algorithm that improves the performances of the optical navigation system of an asteroid exploration mission during its proximity operations.
2. To bridge domain gaps through Functional Tests with synthetic images representing the mission scenario in different adverse situations.
3. To validate the developed algorithm for a future utilization on board spacecraft.

1.3.3 Dissertation Structure

By considering the case study of the Hera mission's proximity operations around the target asteroid Didymos, this thesis addresses the RQs and meets the ROs with the structures defined as it follows. This chapter introduces the context, the limitations

and challenges, the research questions and objectives and the overall structure of this thesis.

Chapter 2 focuses on the design and the development of the AI-based IP algorithm. The goal is to achieve an algorithm able to estimate the outputs needed to safely navigate around the target asteroid. Furthermore, the algorithm is extended to perform other IP tasks that can increase the robustness of the navigation system. This chapter addresses RQ 1a and meets partially RO 1.

Chapter 3 delves into the application of the developed AI-based IP algorithm to the optical navigation system to achieve autonomous navigation around the asteroid. The AI-based IP algorithm is refined for this purpose, and the outputs of the AI model are interpreted to increase the robustness of the navigation system. This chapter addresses RQ 1b and it fulfills RO 1.

Chapter 4 analyzes the robustness of two AI-based IP algorithms through a series of Functional Tests with images generated synthetically. The images aim to stress test the two algorithms with conditions never seen during training, thus analyzing the generalization capability and performance limits. The two algorithms have different architectures, which allows to make assumptions in the decision-making policy of the design of an AI-based IP algorithm for an asteroid exploration mission. This chapter addressees RQ 2a and meets RO 2.

Chapter 5 discusses the validation of the developed algorithm through a series of tests embodied in DDVV strategies used for traditional IP algorithms. The tests are aimed to incrementally validate the algorithm to analyze the robustness and identify potential limits for a real mission application. This chapter addresses RQ 2b and meets RO 3.

Chapter 6 analyzes the possibility of using the developed AI-based IP algorithm to solve the continuous 6-dof pose (position and attitude) of the target asteroid. The pros and cons and the limitations of the algorithms are identified.

Finally, Chapter 7 presents the conclusions of this work and recommends future directions to continue this research. The thesis report itself is based on a collection of published/submitted journal papers.

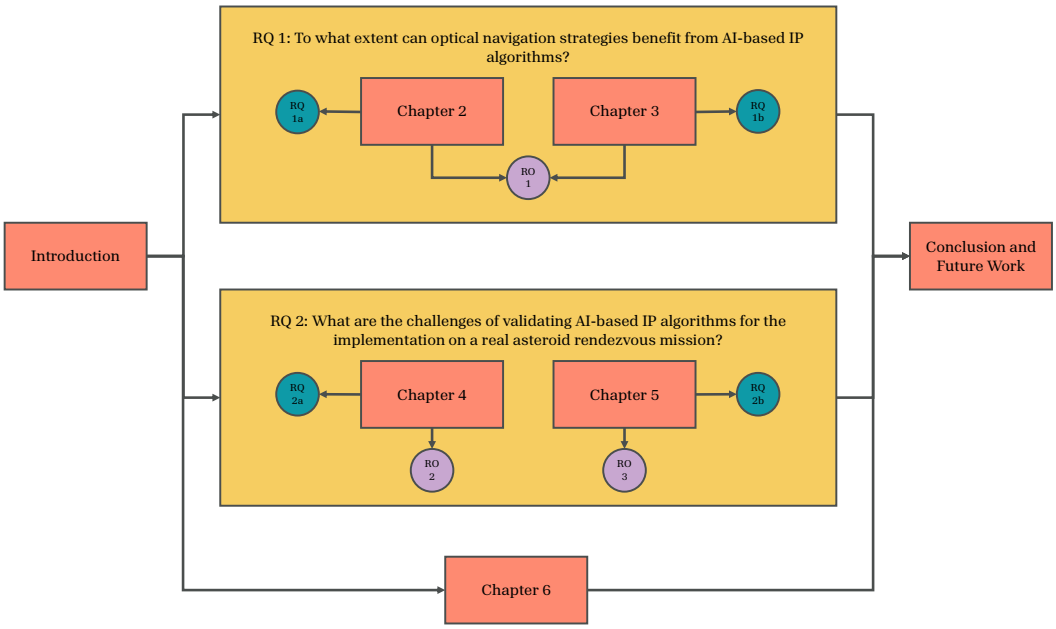

Figure 1.8: Graphical structure of the Ph.D. illustrating the relationship between chapters, RQs and ROs

The format of this thesis is based on a collection of published/submitted journal papers to facilitate readability and allow each chapter to be understood independently, without requiring reference from preceding chapters. Accordingly, a general literature review is presented in this chapter to provide the preliminary context, while each chapter includes a more focused and detailed review pertinent to its specific topic. To ensure coherence and consistency across the thesis, an inter-chapter section (named *Paper content*) is included between each chapter to provide smooth transitions and maintain a unified structure. Furthermore, in each chapter, the term paper may be used, reflecting the standalone nature of the chapters as individual publications. Each paper has been slightly revised to incorporate feedback and address comments provided by the VIVA examiners. Figure 1.8 illustrates a graphical representation of the relationships between the different chapters, RQs and ROs. It can be seen that the structure of the Ph.D. thesis is deliberately parallel: the reader begins with the Introduction, identify the research question and/or research objective they want to focus on, then proceed directly to the Chapters that address them, and finally review the Conclusions and Future Work.

Chapter 2

CNN-based Image Processing algorithm for autonomous optical navigation of Hera mission to the binary asteroid Didymos

> The more we learn about space, the more we realize it's not an empty void. It's filled with possibilities
>
> *Chris Hadfield*

Kaluthantrige A., Feng, J.[‡] and Gil-Fernández, J.[§]

Published in *Acta Astronautica*, May 2023

[‡]Associate professor, Department of Mechanical and Aerospace Engineering, University of Strathclyde

[§]Guidance, Navigation and Control Engineer, ESA ESTEC

Paper content

This chapter introduces an artificial intelligence-driven image-processing method tailored to Hera's proximity operations around Didymos/Dimorphos. It reliably estimates key navigation parameters (centroids, distance, Sun angle) even under challenging conditions, boosting the mission's navigation autonomy and robustness. Following the map and structure shown in Fig. 1.8 in Section 1.3.3, this chapter addresses RQ 1a and achieves the objective of developing an AI-based IP algorithm stated in RO 1. With this chapter, the reader will understand how intelligent image-processing algorithms, specifically those built on convolutional neural networks, significantly outperform standard, traditional IP methods in spacecraft navigation tasks.

Abstract

Hera mission is the European Space Agency's contribution to the international collaboration with NASA for the planetary defence, i.e. Asteroid Impact Deflection Assessment aiming to deflect the trajectory of its target binary asteroid system (65803) Didymos. The Early Characterization Phase and the Detailed Characterization Phase of Hera mission are two phases of the proximity operations with the objective to physically and dynamically characterize Didymos. During these phases, an Image Processing algorithm is required to estimate the position of the centroid of the primary to enable Line of Sight navigation. However, the performance of standard Image Processing algorithms is affected by the disturbances of the image, such as poor illumination conditions, the presence of external bodies and the irregular shape of the target. This research addresses this challenge by developing a robust Convolutional Neural Networks-based Image Processing algorithm to estimate the position of the centroids of Didymos and its moon Dimorphos, the pseudorange from the primary and the Sun phase angle. The training, validation and testing datasets are generated with the software Planet and Asteroid Natural scene Generation Utility using the Early Characterization Phase and the Detailed Characterization Phase trajectories as case scenario. The position in the image of the centroids of Didymos and Dimorphos is estimated using their respective position vectors. To estimate the pseudorange, the developed algorithm regresses a set of keypoints on the visible border of Didymos and evaluates its apparent radius. For the Sun phase angle, the pixel position of the subsolar point of the primary is leveraged. The High-Resolution Network is the Convolutional Neural Network architecture applied to detect keypoints with superior spatial precision. Even with the considered disturbances, the analysis shows that the proposed algorithm is able to provide an accurate estimation of the mentioned outputs for all the Early Characterization Phase trajectory and for 77.33% of the Detailed Characterization Phase trajectory, improving the robustness and autonomoy of the mission navigation.

2.1 Introduction

The Asteroid Impact Deflection Assessment (AIDA) is an international collaboration between NASA and the European Space Agency (ESA), with the primary objective of planetary defence by deflecting a binary asteroid system using kinetic impact. The NASA contribution to this mission is the Double Asteroid Redirection Test (DART), a planetary defence-driven test of a kinetic impactor launched on the 24th of November 2021 that performed the deflection in September 2022 [34]. ESA's segment of AIDA is Hera mission, whose objectives are to investigate the properties of the binary asteroid system, to observe the results of DART's impact and to provide information for asteroid impact threat mitigation, mining and science purposes [35]. Hera falls under ESA's Space Situational Awareness (SSA) initiative, which enables ESA to detect, predict and assess the risk of Near Earth Objects.

The target of this mission is the near-Earth binary asteroid (65803) Didymos. Table 2.1 illustrates relevant properties of the primary Didymos and its moon Dimorphos. In this work we refer to the pre-impact properties of the binary system, since the impact of DART has changed major parameters of Dimorphos, such as its orbit around Didymos and its physical characteristics, with potential unstable motion that can be confirmed only with the Hera's spacecraft arrival [91]. The spin axis of both bodies is orthogonal to the binary's orbital plane. Dimorphos is tidally locked with Didymos, i.e. its rotation period is equal to its revolution period around the primary [29].

Table 2.1: Didymos' system pre-impact properties [29]

Parameter	**Didymos**	**Dimorphos**
Gravitational parameter $[km^3/s^2]$	$3.5225 \cdot 10^{-8}$	$2 \cdot 10^{-10}$
Approximated diameter $[m]$	780	164
Rotation period $[hr]$	2.26	11.92
Obliquity of the binary orbit with Ecliptic plane	169.2°	169.2°

The proximity operations of Hera mission consist of different phases that depend on the mission objectives. In this work the Early Characterization Phase (ECP), 30

to 20 km distant from the target, and the Detailed Characterization Phase (DCP), 23 to 9 km distant from the target, are considered as case scenario with the objective of conducting physical and dynamical characterizations of Didymos [40].

A vision-based navigation system is designed to guarantee autonomy for the observation of the binary asteroid from short distance. This system includes an on-board camera taking images of the asteroid, an Image Processing (IP) algorithm that extracts information from these images, and a navigation filter that processes the visual data to estimate the spacecraft position, velocity and attitude with respect to the binary system. The camera used is the Asteroid Framing Camera (AFC). For the ECP and the DCP, the navigation strategy is centroid-based, meaning that the IP algorithm is designed to extract the position of the Center of Mass (COM) of the primary body, and then to estimate the Line Of Sight of the spacecraft, with the purpose of enabling autonomous attitude navigation [58].

Nevertheless, standard IP algorithms' performances are highly dependent on the intrinsic properties of the captured images. Factors such as the Signal-to-Noise ratio, illumination conditions, the presence of other bodies in the image and the irregular shape of the asteroid can affect the accuracy of the extracted visual information. Standard IP algorithms introduce correction terms that depend on the Sun phase angle (Sun-asteroid-spacecraft angle) to reduce the error caused by the illumination conditions.

Recent years have seen an increase of the implementation of Convolutional Neural Networks (CNNs) in space image processing. One of its main advantages over the standard IP algorithms is the robustness against disturbances and adverse characteristics of the images. Most of the CNNs process the input image with a network typically consisting of a series of high-to-low resolution subnetworks. This process reduces the input's resolution, which is then recovered through a low-to-high process. With this procedure, the extracted visual data have low spatial precision and accuracy that could not meet the requirement of an autonomous attitude navigation system. Therefore, this work adopts the High-Resolution Network (HRNet) architecture that has the main characteristic of maintaining a high-resolution representation through the whole net-

work while exchanging information across the parallel multiresolution subnetworks. This process leads to a keypoints regression with higher accuracy given images with high resolution [92]. The HRNet has been developed for 2D human pose estimation problems but has already found its spaceborn application to the monocular pose estimation of satellites problems, where the HRNet is used to estimate a set of landmarks from the input images of the target satellite [93, 94].

To estimate the relative position of the spacecraft, a range measurement from the asteroid is required. The on-board instrument to measure the range with Didymos is the Planet ALTimeter (PALT), a lidar experiment that determines the distance to the asteroids with an accuracy of 0.5 m operational at a distance ranging from 500 m to 14 km. Therefore, it can not be used during the ECP for range measurements, but it can be used during part of the DCP.

This work addresses the IP challenges related to the irregular shape of the asteroid, the disturbance caused by the presence of the secondary body in the images and the adverse illumination conditions. We develop an HRNet-based IP algorithm that takes as input synthetic images generated during the ECP and the DCP trajectories and outputs the elements summarized in Table 2.2, reducing and confining the errors introduced by the mentioned factors. Since it is not a direct measurement but it is derived from the images, the estimated range is a pseudorange measurement. With these measurements the navigation filter is able to estimate the relative state of the spacecraft with respect to Didymos, increasing the robustness of the navigation strategy and of the proximity operations. The estimation of the position of the centroid of the secondary body represents a unique contribution of this work. Another contribution of this work is the regression of the subsolar (SS) point on the surface of Didymos, which is leveraged with a novel methodology to estimate the Sun phase angle.

This paper is structured as follows. Section 2.2 reviews the state of the art of methodologies applied for image processing algorithms to solve the centroiding, range and phase angle problems. Section 2.3 describes more in detail the developed HRNet-based IP algorithm. Section 2.4 performs the numerical simulations and analyses the results. Finally Section 2.5 concludes this research and recommends future research

Table 2.2: Outputs of the CNN-based IP algorithm

Name	**Symbol**	**Description**
COM of Didymos	COM_{Did}	Estimated position of the centroid of Didymos $[px, px]$
COM of Dimorphos	COM_{Dim}	Estimated position of the centroid of Dimorphos $[px, px]$
Pseudorange	ρ	Pseudorange with Didymos $[km]$
Phase angle	γ	Estimated Sun Phase angle $[^\circ]$

directions.

2.2 Related methods

In this section, current IP algorithms that estimate the quantities shown in Table 2.2 are reviewed. To the authors' knowledge, the methodologies to estimate the range and the Sun phase angle from images are limited, as these parameters are usually obtained from lidars, altimeters and Sun sensors. These methodologies have been tested with the shapes of Didymos prior to the updates provided by DART mission, hence they will not work with the shape known currently.

2.2.1 Centroiding algorithms

Methods that leverage the position of the Center of Brightness (COB), the centroid of the image when each pixel is weighted by its intensity, on the image have been proposed. To locate the COB, the IP algorithm needs to perform several steps: windowing, to prevent Dimorphos to be included in the computation and detect a window that includes the primary, thresholding and binarization, to reduce the noise and locate the brightest area of the image, and finally the computation of the COB, which represents the center of the located area [55]. Gil-Fernández and Ortega-Hernando [55] applies the offset ϵ_{COB} between the COB and the COM to determine the position of the latter. The offset ϵ_{COB} depends on the Sun phase angle, the spacecraft latitude with respect to the primary Equatorial plane and the shape of the asteroid. Nevertheless, when the lighting

circumstances are inadequate this method becomes inaccurate. Pugliatti et al. [81] applies data-driven scattering laws to determine with higher accuracy the relationship between the position of the COB and the COM. Centroid Apparent Diameter, ellipse and limb fitting techniques rely on the a priori knowledge of the apparent size and shape of the asteroid. Moreover, they require that the shape of the model is regular [95, 96].

The current IP algorithm implemented by Hera for the centroiding problem resolution is the Maximum Correlation with a Lambertian Sphere (MCLS). This algorithm estimates the size of the sphere with Lambertian reflectance that maximises the normalized correlation with the binarized image of the asteroid. Hence, the bright pixels of the image play a major role in this IP technique, thus making it highly depending on the position of the Sun [58]. The dependency on the illumination conditions is minimised in this research by applying CNNs.

While Hera is focusing on identifying the COM of both bodies, DART performed the impact while aiming for the COB of Dimorphos. In the final 4 hr prior to the impact with Dimorphos, DART used the Small-body Maneuvering Autonomous Real-Time Navigation (SMART Nav) algorithm with the images captured by the on-board Didymos Reconnaissance and Asteroid Camera for Optical navigation (DRACO) to perform autonomous terminal navigation. Prior to relying fully on SMART Nav, the on-board ephemeris have been updated with the ground-processed Optical Navigation data collected by DRACO. The capability of the algorithm to be updated real-time with ground-processed data allowed to target the COB of Dimorphos with high accuracy without needing to identify the position of its COM [97, 98].

2.2.2 Pseudorange

Monocular Depth Estimation (MDE) represents the task of measuring the distance of each pixel of an input image relative to the camera by leveraging depth maps. MDE requires as input RGB images that contain a larger amount of information per pixel, and a strong knowledge of the target shape in order to match relevant feature with the corresponding depth map [99]. Nevertheless, the synthetic images used in this work are greyscale, and the precise models of Didymos and Dimorphos can only be

reconstructed during the close approach of the Hera's spacecraft [91]. Therefore, in this work we propose a method that depends only on the shape of the target, with no constrain on its surface appearance.

Methods that rely on the calculation of the apparent radius have been proposed [100]. By comparing the radius of the asteroid with the major length (δ) of the projection of the asteroid on the image plane, the range is calculated. Nevertheless, the estimated range is noisy and not accurate, as the irregular shape of the asteroid generates different values of δ. In order to meet the accuracy requirements (percent error with respect to ground truth lower than 10%) for the navigation strategy of Hera mission, in this research we develop a method of calculating multiple values of δ for each image in order to average the irregularity, which reduces the error introduced by the irregular shape of Didymos.

2.2.3 Sun Phase angle

Pugliatti et al. [81] compared different methodologies to measure the Sun phase angle obtained by analyzing a database of images of Didymos generated with the 3D computer graphics software Blender. These methods rely on the characterization of the blob of pixels representing the asteroid in the binarized image generated with Blender. The eccentricity e of this blob of pixels is found to be correlated with the phase angle. This relationship is described with the following second-order polynomial:

$$\gamma(e) = p_2 e^2 + p_1 e + p_0 \tag{2.1}$$

The coefficients p_0, p_1 and p_2 are evaluated fitting the data in the least-square sense. The estimation of the Sun phase angle is accurate for larger phase angle values. Their second method involved the application of Neural Networks and CNNs to spot relationships between different geometrical features of the blob of pixels representing the asteroid. It has been found that the CNNs outperform all the other methods with their capability of extracting spatial information from images. In this work the CNNs are used to estimate the position of the SS point that is used to estimate the Sun phase

angle.

2.3 Methodology

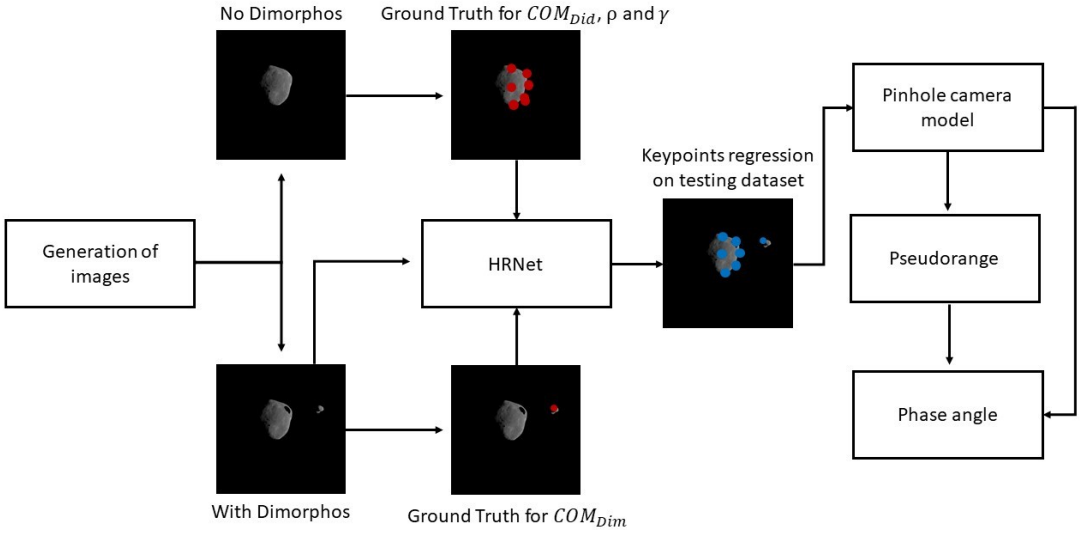

Figure 2.1: Overall pipeline of HRNet-based IP algorithm

In this section, the methodology is described in detail. Fig. 2.1 shows the main steps of the overall pipeline. With the given reference trajectories from ESA and Planet and Asteroid Natural scene Generation Utility (PANGU) software, two sets of images are generated, one without the presence of Dimorphos and one with both bodies. Both sets are processed to retrieve the Ground Truth (GT) keypoints which are used to supervise the training and validation of the HRNet. The former set is used to determine the GT position of the COM_{Did}, 24 points on the visible border of the primary and the SS point in the image. The GT keypoint COM_{Dim} is retrieved with the second set, which is also used for the training and validation of the HRNet.

The trained HRNet is then applied to estimate the position of the keypoints of the testing dataset with both bodies. Finally, the pinhole camera model is used with the regressed keypoints to estimate the pseudorange and the Sun phase angle. Details of the main steps are described in the rest of this section.

2.3.1 Reference trajectories

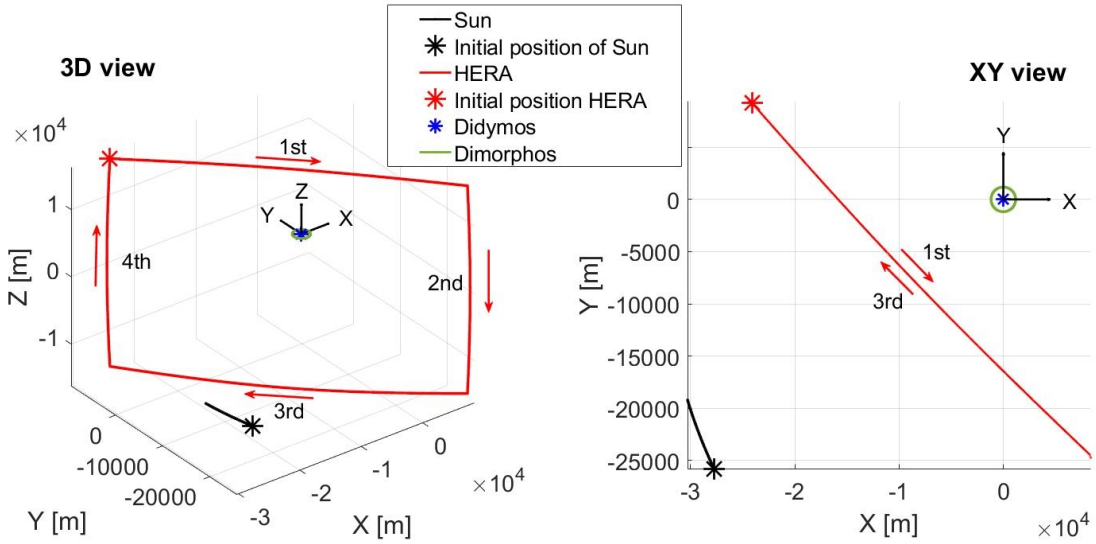

Figure 2.2: ECP trajectory

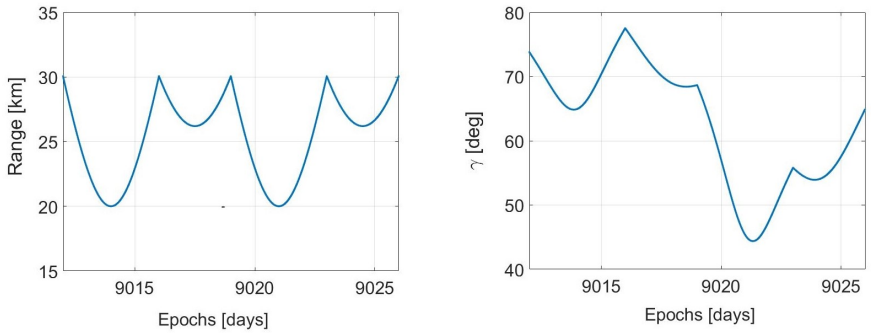

Figure 2.3: Range and phase angle of the ECP trajectory

The adopted reference frame is the Target Body Equatorial Inertial (TBEqI), which has the origin located on Didymos, the X-axis pointing towards the vernal equinox, and the XY plane coplanar to the equatorial plane of Didymos. The relative motion of the Sun around Didymos is retrograde as the binary system's orbit obliquity with respect to the ecliptic plane is larger than 90°, as shown in Table 2.1.

The ECP trajectory is provided by ESA. Fig. 2.2 illustrates the trajectory of the spacecraft, together with the position of the Sun (scaled down in the illustration) and the orbit of the secondary. The position of the Sun is calculated using the Jet Propulsion

Laboratory Small Body Database [101]. The trajectory consists of 4 hyperbolic arcs, with an initial epoch of $t_{in} = 9012\ d$ and a final epoch of $t_{fin} = 9026\ d$, calculated in the Modified Julian Date 2000. The only forces considered for each arc are the point mass gravitational attractions of both the primary and the secondary asteroids. Orbital maneuvers are performed at the joint of two arcs. The durations of the 1^{st} and 3^{rd} arcs are both 4 d while the durations of the 2^{nd} and 4^{th} arcs are both 3 d. The range from the primary varies between a minimum of 20 km and a maximum of 30 km as shown in Fig. 2.3. It can be seen from Fig. 2.2 that the ECP trajectory is located in between the Sun and Didymos, in order to provide the AFC camera with bright images of both bodies for Line of Sight navigation [40]. Fig. 2.3 shows that the phase angle γ for the ECP trajectory is lower than 90°, meaning that the spacecraft is always seeing the day side of the asteroid.

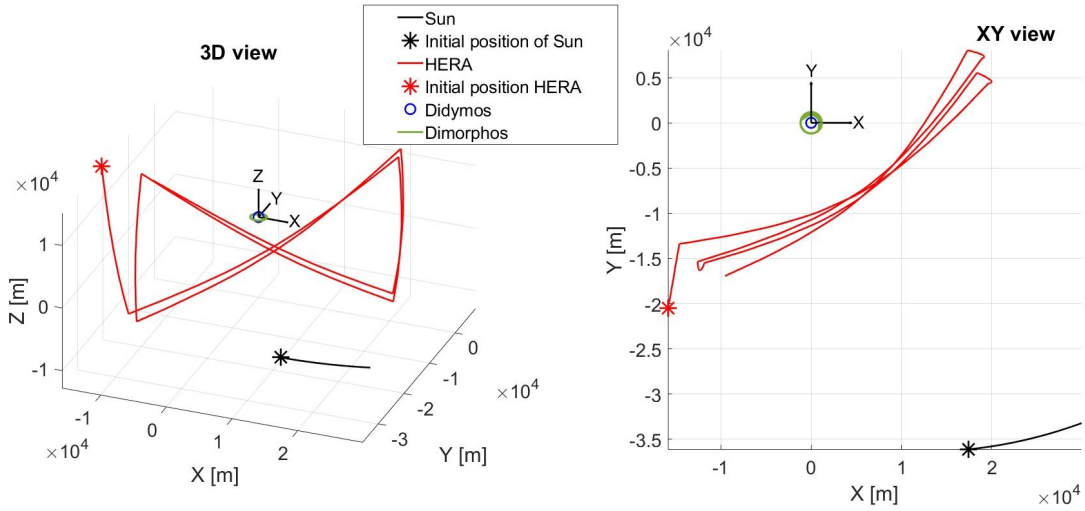

Figure 2.4: DCP trajectory

The DCP trajectory is provided by GMV Aerospace and Defence, who is in charge of the development of the Guidance, Navigation and Control system of Hera mission. Fig. 2.4 illustrates the trajectory of the spacecraft, together with the position of the Sun (scaled down in the illustration) and the orbit of the secondary. The trajectory consists of 8 hyperbolic arcs with a total duration of 28 d. The first arc is the transition between ECP and DCP, followed by repetitive trajectories with a range from the primary varying

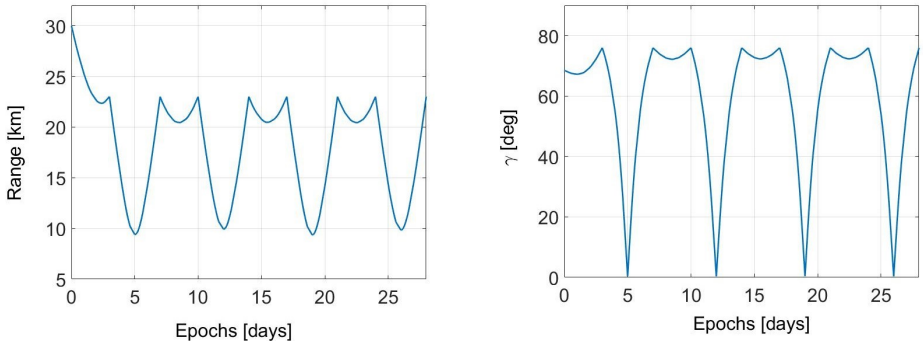

Figure 2.5: Range and phase angle of the DCP trajectory

between approximately 9 km and 23 km, as shown in Fig. 2.5. The minimum distance of 9 km is designed to ensure that the full shape of Didymos is within the Field Of View (FOV) of the AFC even in the presence of 100 m navigation error [40]. Fig. 2.5 shows that the DCP trajectory is also designed to face the camera to the binary system during the day side.

2.3.2 Image Generation

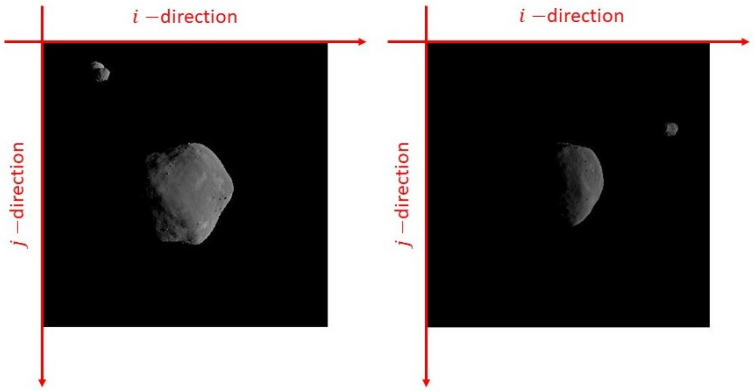

Figure 2.6: PANGU viewer with two sample images captured at different points of the ECP trajectory

The software PANGU is used to generate the database of images for this research. PANGU is a simulation tool that models planet and asteroids surfaces and provides a high-fidelity visualization of images while operating at near real-time speeds. The software has been developed by the STAR-Dundee engineering company [102]. The models of Didymos, Dimorphos and the camera are provided by GMV, and are based

on ground observations. Didymos' model is near-spherical and is a spinning top with an elevated ridge along the equator. The shape of Dimorphos is known to be near-ellipsoidal and it is approximated by scaling down the shape model of Itokawa that was the target asteroid of the Hayabusa mission. DART' s images confirmed the near-ellipsoidal shape of Dimorphos, while providing different results for Didymos, which appeared to be ellipsoidal as well, with an extent along its equatorial axes of 849 m and 851 m, larger than the 620 m extent along its rotation axis [28]. Nevertheless, in this work we refer to the pre-impact models of Didymos and Dimorphos, with final remarks in Section 2.5 about the effects that the change of shape could have on the proposed pipeline and in the results obtained.

The software generates greyscale images detected by the camera and shows them on the PANGU viewer, which is a plane with the size of the image (shown in Table 2.3) and the origin of the coordinated frame set at the top left corner. The horizontal and the vertical axes of the plane are referred as i-direction and j-direction respectively. The flight file system of PANGU is operated in order to visualize the binary asteroid system during the trajectories. Flight files are the input to PANGU and they control the viewer to generate images taken at selected epochs of the reference trajectory in the TBEqI reference system, considering the position of the Sun (range, Azimuth and Elevation) and the positions and the orientations (quaternions) of both the binary asteroid system and the AFC camera (joined with the spacecraft) [102].

For asteroid imaging, the AFC has its boresight pointing towards the primary and the vertical axis of the camera is perpendicular to the direction of the Sun with respect to the spacecraft [40]. PANGU adopts the boresight, the vertical and the horizontal axes of the camera respectively as the Z- the Y- and the X-axis of the camera reference frame [102]. Therefore, the position vector of the Sun with respect to the spacecraft lies on the XZ plane of the camera frame. As a result, the images shown in the PANGU viewer always represent the binary system illuminated from the right side. Fig. 2.6 shows two sample images generated at different epochs of the ECP trajectory, together with the i- and the j-directions of the PANGU viewer.

Table 2.3: AFC properties [103, 104]

FOV	**Focal Length:** f	**Aperture**	**Image size**	**Pixel Size:** ν
5.5°	10.6 cm	2.5 cm	1024×1024 px	14 μm

2.3.3 Ground Truth data

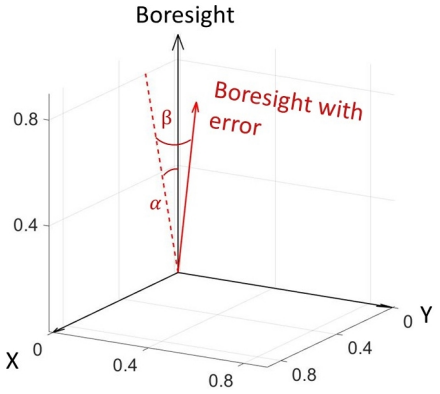

Figure 2.7: Camera pointing with error

2.3.3.1 Centroids of Didymos and Dimorphos

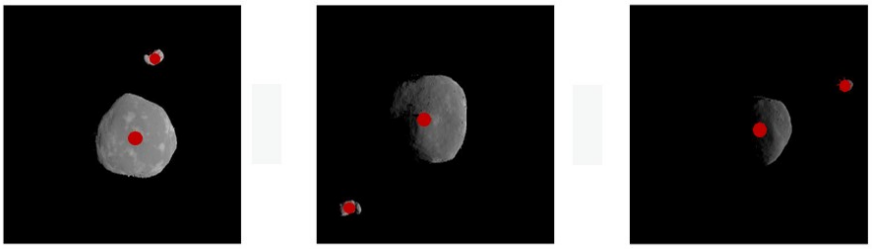

Figure 2.8: Sample images generated during the 2nd, the 3rd and 4th arc of the ECP with Ground Truth position of the centroids of Didymos and Dimorphos

When the camera is pointing perfectly towards the primary or the secondary, the latter are displayed in the middle of the PANGU viewer. With the conditions that the camera is pointing directly to either the primary or the secondary, the Geometrical Center (GC) of the selected body that is the arithmetic mean position of all the points belonging to the body, is located at the central pixel with the coordinates $(i, j) = (512, 512)$ px in the PANGU viewer. The COMs of the primary and the sec-

ondary almost coincide with their GCs because of their respectively near-spherical and ellipsoidal shapes. Since the images used in this work are all generated with PANGU, it is assumed that the GCs of Didymos and Dimorphos are their centroids.

Training the CNN algorithm with a set of images with perfect pointing conditions will result in an issue of lacking label variability. To overcome this issue, a pointing error represented by spherical coordinates and defined by two angles α and β is introduced at each epoch of the trajectory in the boresight direction of the camera reference system, as shown in Fig. 2.7. As a result, the generated images are shifted from the central position of the PANGU viewer. In order to make sure that both bodies lie within the FOV of the AFC camera, random values within an interval of $[-0.5, 0.5]^\circ$ are considered for both α and β for the ECP. With these values, the primary and secondary locations are shifted around in the PANGU viewer. By calculating the shift in pixels of the primary and the secondary from their central position, the GT pixel coordinates of COM_{Did} and COM_{Dim} are calculated for each value of α and β, as shown in Fig. 2.8. Since Dimorphos is not included in the FOV of the AFC during the DCP, its GT position is not considered during this phase. To ensure that the asteroid is fully visible in the images even at the closest approaches, the values of α and β are limited to an interval of $[-0.25, 0.25]^\circ$ for the DCP.

2.3.3.2 Pinhole camera model, pseudorange and Sun phase angle

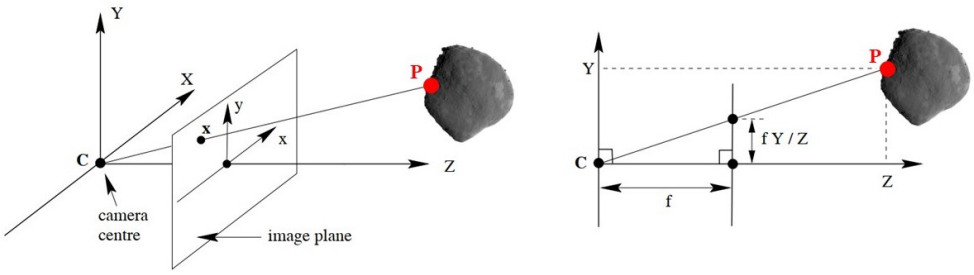

Figure 2.9: Pinhole camera model geometry [105]

The pinhole camera model is implemented in PANGU using the properties of the AFC camera, shown in Table 2.3. In the pinhole camera model, also called perspective camera model, the camera aperture is considered as a point rather than a lens.

Therefore, this model is used to achieve a first-order approximation of the relationship between the coordinates of a point in the 3D space and its projection onto the 2D image plane of the camera [106].

Fig. 2.9 shows the geometry of a pinhole camera model. In this model the center of projection **C** is the origin of the camera reference frame and the image plane is located at the focal length $f = 10.6\ cm$ (Table 2.3). It can be seen from Fig. 2.9 that a point **P** with coordinates (X, Y, Z) in space is mapped to a point with the coordinates $(\frac{fX}{Z}, \frac{fY}{Z}, Z)$ on the image plane [104]. The units conversion from meters to pixels for an object of length l on the image plane is given by $n \cdot \nu\ px$, where n is the number of pixels representing the object and ν is the pixel size (Table 2.3). Therefore, an object of length L in meters on a plane of the 3D space at distance Z from the camera and parallel to the image plane is projected onto the latter with the dimensions in pixels defined by Eq. 2.2.

$$n \cdot \nu = \frac{f \cdot L}{Z} \tag{2.2}$$

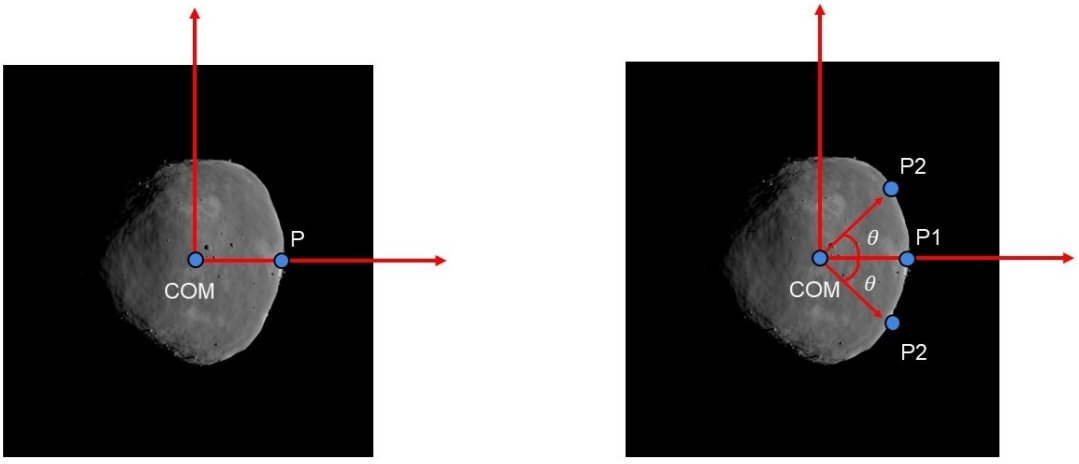

(a) Two points (b) Multiple points

Figure 2.10: Keypoints selected from the visible border of the asteroid

In order to apply the pinhole camera model to estimate the pseudorange of the spacecraft from Didymos, the shape of Didymos is approximated as a sphere of radius $R = 390\ m$ (Table 2.1). Given that on the image plane the length of the asteroid radius

has a value of n_R px, Z can be solved from Eq. 2.2, which is the distance from the center of projection $\mathbf{C}$ and the COM of Didymos, i.e. the range. Therefore, once n_R of an image captured by the camera is obtained, the pseudorange can be calculated with Eq. 2.3.

$$\rho = \frac{f \cdot R}{n_R \cdot \nu} \tag{2.3}$$

Fig. 2.10a shows how n_R is calculated for a generic synthetic image of the asteroid, which is measured by the number of pixels from COM_{Did} to the point P on the asteroid's border along the positive i-direction, considering that the asteroid is always illuminated from the right side. Dimorphos is hidden from the images as its presence in front of Didymos or near its border would disturb the evaluation of n_R.

Nevertheless, the shape of the asteroid is irregular and the accuracy of its approximation to a sphere depends on the relative attitude of the asteroid with respect to the spacecraft. To reduce the error introduced by the irregularity of the shape in the calculation of n_R, multiple points P_i on the border within the angular aperture 2θ are considered, as shown in Fig. 2.10b.

The distance n_R^i is evaluated for each point P_i and the average value $\bar{n}_R$ is calculated and used in Eq. 2.3 to calculate the pseudorange. To find the optimal value for θ and for the number of points P_i that minimize the error, the following steps are taken:

1. Given an image of the asteroid, an angular aperture 2θ with $\theta \in [0, 110]^\circ$ is considered; the maximum value of θ is determined considering that the asteroid is illuminated from the right side of the image plane, as explained in Section 2.3.2.

2. A number of points P_i at an equal angular distance from each other are taken on the asteroid's border; an upper limit of 50 points is selected considering the computational complexity (memory storage of the intrinsic parameters of the architecture and computational time) of the keypoints regression of the HRNet;

3. For each point P_i, n_R^i and the average $\bar{n}_R$ are calculated, and the pseudorange with the asteroid is evaluated with Eq. 2.3.

4. Finally, the pseudorange is compared with the GT range (i.e. the range obtained

from the reference trajectory shown in Section 2.3.1) for each image and the Mean Absolute Error (MAE) is determined with Eq. 2.4.

$$MAE = |\rho - Range| \tag{2.4}$$

Following this procedure, Fig. 2.11 is obtained with the y-axis representing the angle $\theta \in [0, 110]°$, the x-axis representing the number of points $P_i \in [1, 50]$ and the colourbar representing the MAE. It is illustrated by the red dots that the MAE has its local minima ($MAE < 350\ m$) in three different regions. The minima have a similar value of θ around 90°, and different values of number of points P_i. Hence, considering the whole illuminated side of Didymos instead of only one point on the i-direction justifies the approximation of the shape of the asteroid with a sphere and reduces the error in the pseudorange calculation.

Relying on one singular point, as in the left region of Fig. 2.11, poses a major risk of failure in the case that the HRNet is not capable of regressing that point accurately. On the other hand, the error obtained with 50 points is not low enough to justify the computational complexity implicated in the regression of such a high number of keypoints. Therefore, in this study we select 24 points P_i on the border within an angular aperture 2θ with $\theta = 87°$.

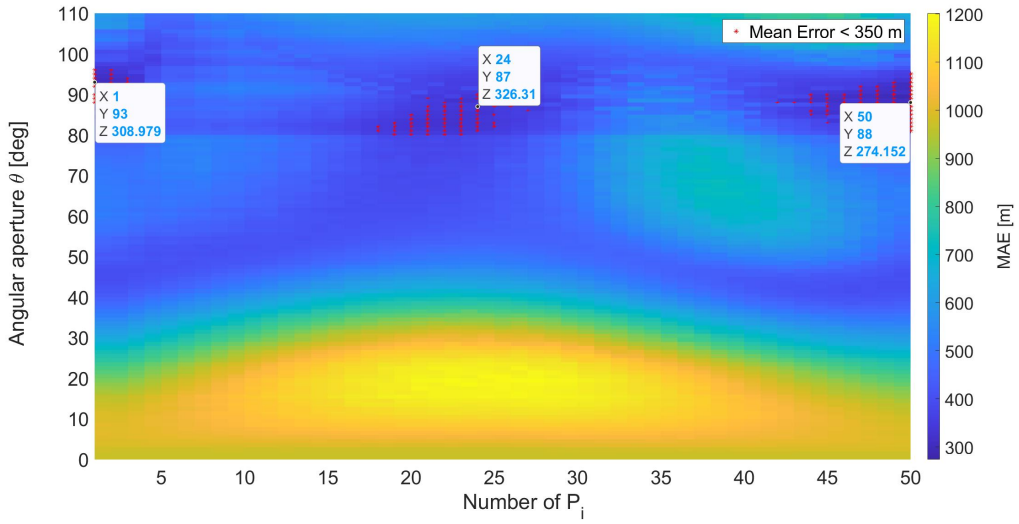

Figure 2.11: Optimization of number of keypoints for pseudorange calculation

(a) Planar view

(b) Image plane view

Figure 2.12: Illustration of subsolar point for Sun phase angle estimation

The Sun phase angle estimation relies on the SS point on Didymos, as shown in Fig. 2.12. Given an image captured by the camera, the COM and the SS projections are detected on the image plane. Dimorphos is hidden from the images as it can cause disturbance in the estimation of the position of the SS. The distance in pixels between these two points, defined here as n_P, together with the average radius of the asteroid $\bar{n}_R$, are then used to calculate the phase angle γ with Eq. 2.5, as shown in Fig. 2.12a. Eq. 2.5 applies twice the approximation of the shape of the asteroid as a sphere: one for using $\bar{n}_R$ and one for using the inverse of the sine function to calculate γ.

$$\gamma = \arcsin\left(\frac{n_p}{\bar{n}_R}\right) \tag{2.5}$$

2.3.4 HRNet

The HRNet architecture is shown in Fig. 2.13. The network maintains the high resolution representations of the input images by connecting multiple subnetworks in parallel. The first stage is a high-resolution subnetwork. New stages are formed from the gradual introduction of high-to-low subnetworks. To maintain the high-resolution representation, repeated multiscale fusions are performed using low-resolution representation of

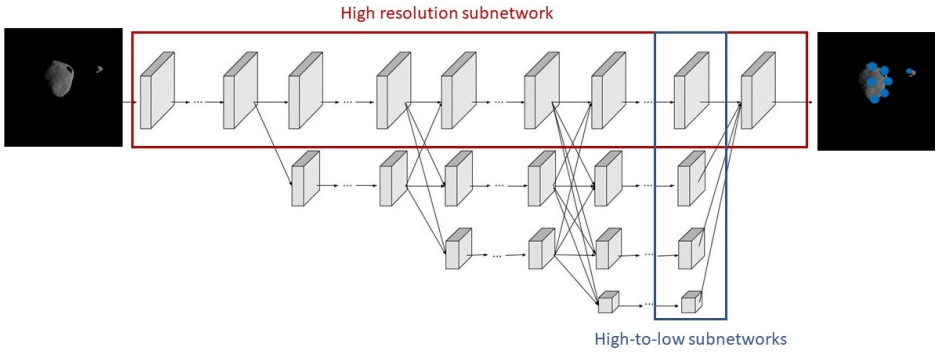

Figure 2.13: HRNet architecture

the same depth and level. The last high-resolution representation is then used for the regression of the selected visual data [92].

The keypoints to regress for each image generated during the ECP are 27 points, which are the COM_{Did} and the COM_{Dim}, 24 points on the visible border and the SS. For the DCP images the keypoints are 26, since the COM_{Dim} is not visible. Each input image of the HRNet is coupled with the corresponding keypoints that are used to supervise the training to regress the keypoints locations on the testing dataset. For this work, the CNN architecture of the pose-hrnet-w32 that was previously implemented in [107] is used, where 32 represent the widths of the high-resolution subnetwork in the last three stages. During the training, the validation dataset is used beside the training one to compute the validation losses and avoid overfitting. The Adam optimizer is used with a cosine decaying learning rate with initial value of 10^{-3} and decaying factor of 0.1. The total parameters involved in the training process are $28,536,443$. The default hyperparameters specified by [107] are adopted in this work, including those related to the network architecture, training procedure, and optimization strategy, in order to ensure consistency with the original implementation.

Dimorphos is not hidden in the images as done in Section 2.3.3.2, so that the HRNet is trained to regress the location of the keypoints despite the disturbance introduced by the presence of Dimorphos. The input database for the ECP consists of 10083 (59.91%) images for training, 1266 (7.52%) images for validation and 5031 (29.89%) images for testing, obtained by sampling the trajectory respectively every 100, 800 and 200 s and discarding the images where Dimorphos is outside of the camera frame or behind the

primary. The images generated with the DCP are 448 (2.68%) i.e. sampling every 90 min the trajectory and discarding the ones showing the border of Didymos partially outside of the FOV. The dataset of the DCP is used only for testing, in order to assess the ability of the HRNet to generalize the keypoint regression to images showing the binary system in different configurations. The network is trained for 210 epochs. The training of the network is run on the virtual machine provided by Google Colab with the NVIDIA V100 Tensor Core GPU, and it takes around 48 hr for the completion of the 210 epochs. The whole HRnet architecture together with its trained weights and biases has a total weight of 109 MB.

2.4 Results

In this section, the results of the HRNet-based IP algorithm for the estimation of the centroids of Didymos and Dimorphos, the pseudorange from the primary and the Sun phase angle are presented. Firstly, the accuracy of the HRNet on the estimation of the positions of the keypoints for the ECP is evaluated with the metric defined as follows:

$$RMSE_m = \sqrt{\frac{\sum_{n=1}^{N}(P_{mn}^{GT} - P_{mn}^{pred})^2}{N}} \tag{2.6}$$

where P_{mn} represents the m-th keypoint; the index n refers to the n-th image of the $N = 5031$ images of the ECP testing dataset; $RMSE_m$ is the Root Mean Squared Error (RMSE) between the GT position of the m-th keypoint P_{mn}^{GT} and the estimation P_{mn}^{pred} using the HRNet. The $RMSE$ value of 7.746 px obtained by the MCLS IP algorithm developed by GMV to estimate the position of the centroid of Didymos during the ECP of Hera mission is given as a reference, since their estimation meets the pointing accuracy required by the mission [58]. This result is obtained by applying the algorithm over a set of 243 images of the 1st arc of the ECP generated with PANGU by GMV.

Further, the accuracy of the developed algorithm on the estimation of the position of the centroids during the ECP is evaluated by the metric defined in Eq. 2.7, which represents the error in pixels between the position of COM_{Did} and COM_{Dim} with respect to their GT value. This metric is evaluated for both the $i-$ and the $j-$ directions

of the PANGU viewer.

$$\varepsilon_{GC} = COM^{GT} - COM^{pred} \tag{2.7}$$

The MCLS IP algorithm estimated the position of the COM of Didymos with an average error ε_{GC} of 4.83 px on the $i-$direction and 3.95 px on the $j-$direction. The accuracy of the pseudorange and the Sun phase angle during the ECP is assessed through the error between the GT values and their estimations. The distribution of the error is also analyzed for both parameters by comparing it with the Gaussian distribution that is the ideal one for navigation filters [108].

The performance of the HRNet-based IP algorithm on the estimation of the position of the centroid of Didymos, the pseudorange and Sun phase angle are also evaluated for the DCP, in order to assess the possibility and robustness of generalization to completely new images.

2.4.1 Accuracy of the keypoints regression

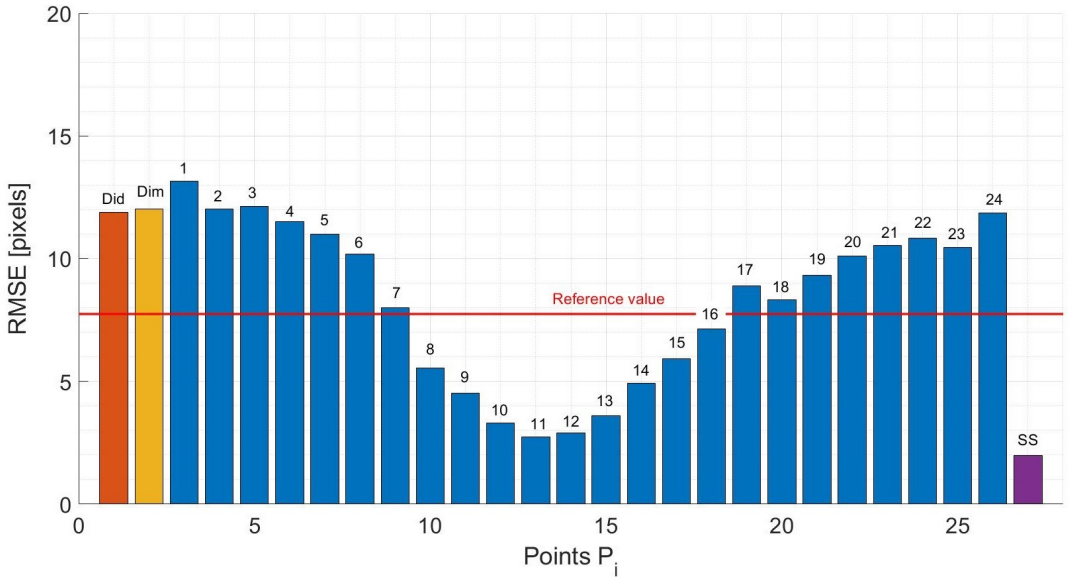

Figure 2.14: Accuracy of the keypoints regression during ECP

Fig. 2.14 is a bar chart of the $RMSE$ values obtained for the 27 keypoints regressed by the HRNet during the ECP. The first two and the last bars represent the $RMSE$ of the two COMs and of the SS position estimations respectively. The other 24 keypoints

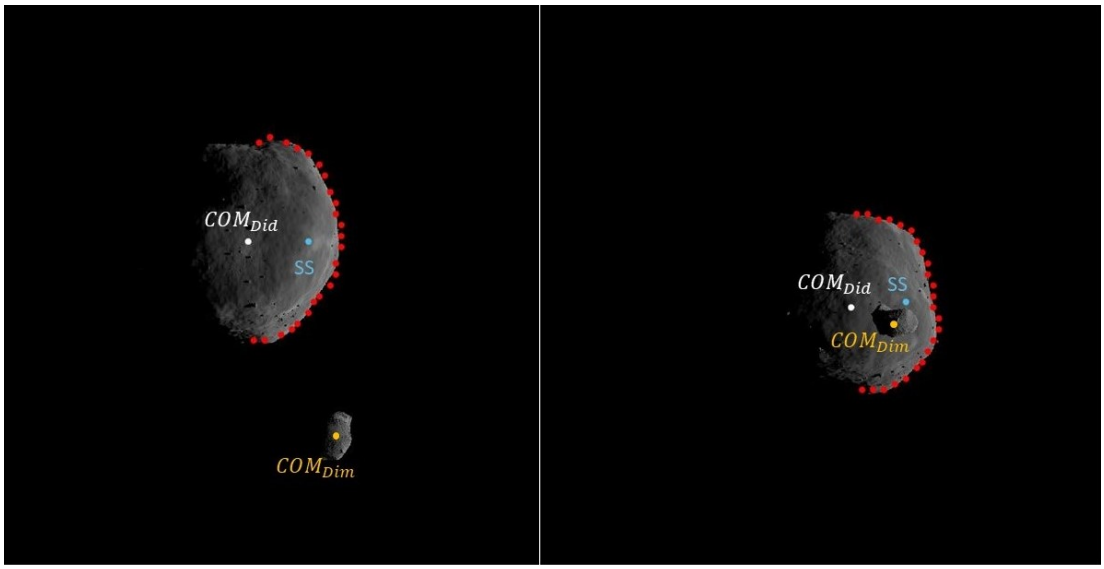

Figure 2.15: Keypoints regression results for two images of the 1st and the 3rd arc

are the ones defined in Section 2.3.3 on the border of the asteroid. It is observed that the worst performance of the HRNet is obtained for the first keypoint ($\theta = 87°$) on the border of the asteroid and the best performance for the SS point, with the $RMSE$ of 13.161 px and 1.973 px, respectively.

The difference of the estimation accuracy among the keypoints depends on the different lighting conditions and on the shape of the asteroid. Nevertheless, the values of the $RMSE$ differ from the one obtained using the MCLS IP algorithm by a maximum of around 5 px, which is negligible compared to the size of the image, reported in Table 2.3. Therefore, the HRNet is able to estimate the position of the keypoints with the same accuracy of the MCLS IP algorithm for the test scenario considered in this work, thus meeting Hera mission's pointing accuracy requirements. Fig. 2.15 illustrates two sample images generated by PANGU during the first and the third arc, together with the keypoints estimated by the HRNet.

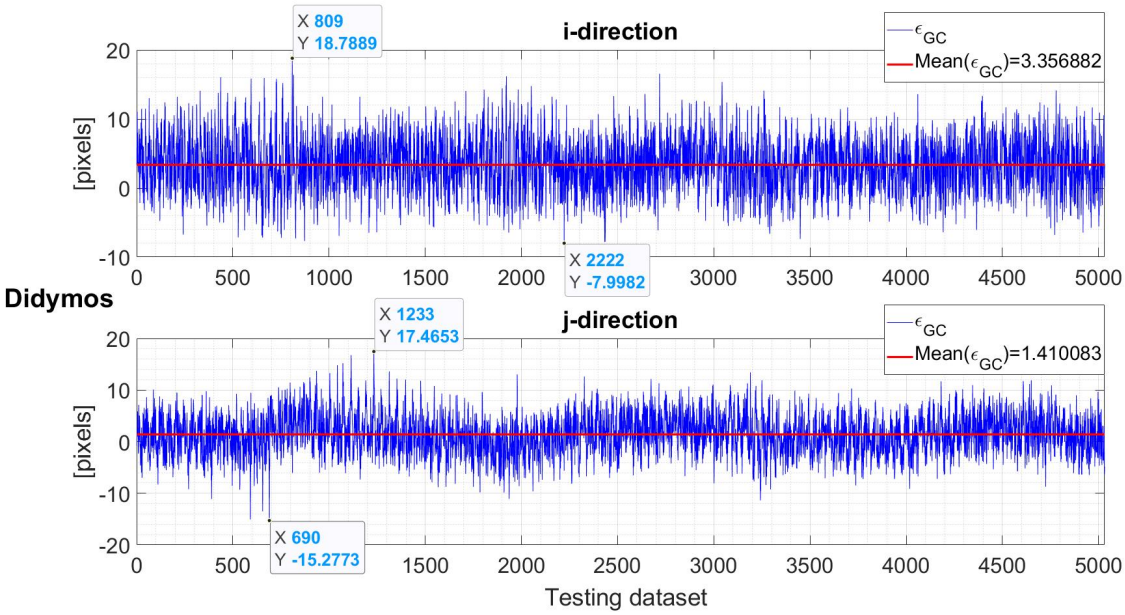

Figure 2.16: ε_{GC} for Didymos centroid during ECP

2.4.2 Estimation of COM_{Did} during ECP

2.4.2.1 Accuracy

Fig. 2.16 represents the error ε_{GC} for the centroiding of Didymos in both i and j-directions of the PANGU viewer reference frame, for the ECP testing dataset of 5031 images. It can be seen that the error oscillates around 3.35 px in the i-direction with a maximum and a minimum values of 18.78 and -7.9 px and around 1.41 px in the j-direction with a maximum and a minimum values of 17.46 and -15.27 px, respectively. The standard deviations of the error ε_{GC} are $\sigma_i = 3.74$ px and $\sigma_j = 5.65$ px which means that 68.27% of the Didymos centroiding estimation error is contained between -6.7 px and 0.78 px for the i-direction and between -5.8 px and 5.5 px for the j-direction. The reduced values of the mean and the standard deviations of ε_{GC} allow the utilization of Didymos centroiding estimations in a navigation filter. Comparing with the results on the ε_{GC} obtained by GMV, the HRNet-based IP algorithm is more accurate to solve the centroiding of Didymos.

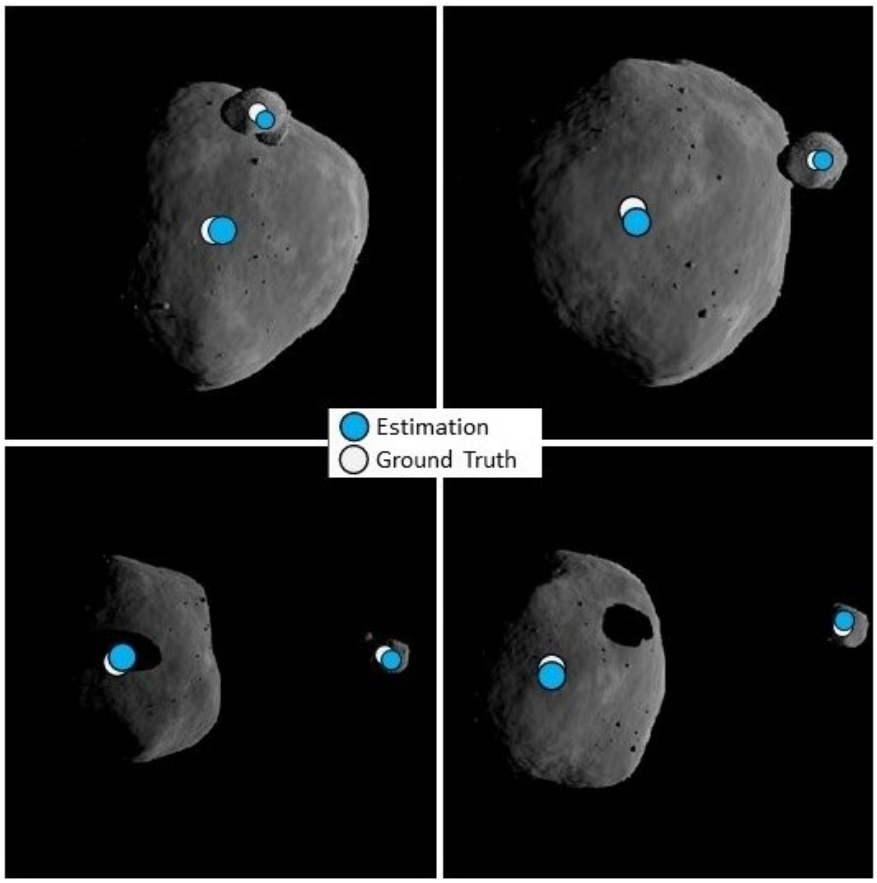

Figure 2.17: Centroiding results for images with disturbances due to the presence of Dimorphos

2.4.2.2 Illumination conditions

As mentioned in Section 2.3.2, the binary system is always illuminated from the right side in the images. Hence, the influence of the illumination can be inferred by the error on the i-direction. The systematic error of 3.35 px is negligible considering that it is lower than the peak-to-peak amplitude (26.68 px) of the error itself. Therefore, the developed centroiding algorithm is not affected by the illumination conditions of the asteroid.

2.4.2.3 Dimorphos' disturbance

The subset of images with the projection of Dimorphos on the surface of Didymos are 193 out of the 5031 of the testing dataset. The RMSE value for these images is 7.4

px. The difference of this value from the reference value is 0.346 px, which is negligible compared to the size of the image plane.

When Dimorphos is located between the Sun and Didymos, its shadow is projected on the surface of the primary. 537 out of the 5031 images of the testing dataset present this condition. For this subset, the value of the RMSE is 7.27 px, and the difference from the reference value is 0.476 px, which is negligible compared to the size of the image plane. Therefore, the proposed centroiding algorithm is robust to Dimorphos' disturbance. Fig. 2.17 shows four examples of these two disturbances analyzed in this section.

2.4.3 Estimation of COM_{Dim} during ECP

2.4.3.1 Accuracy

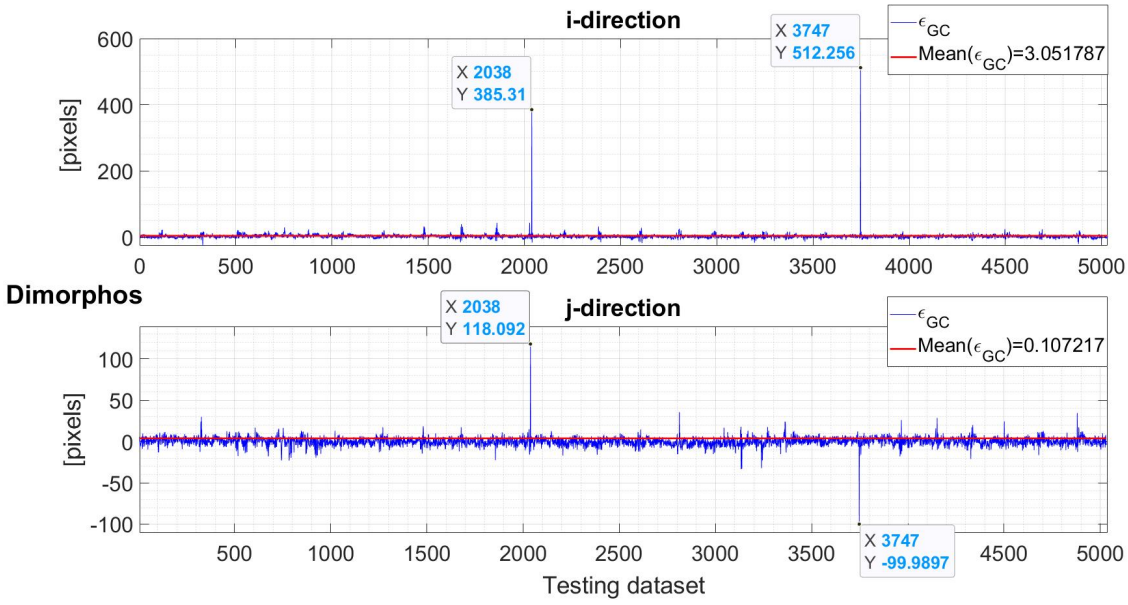

Figure 2.18: ε_{GC} for Dimorphos during ECP

Fig. 2.18 illustrates the centroiding results of Dimorphos in the i- and j-directions of the PANGU viewer for the 5031 images of the ECP testing dataset. The average value of the error is 3.05 px for the i-direction and 0.107 px for the j-direction. The standard deviations of the error ε_{GC} are $\sigma_i = 10.26$ px and $\sigma_j = 5.52$ px which means

that 68.27% of the Dimorphos centroiding estimation error is contained between -6.71 px and 13.81 px for the i-direction and between -5.1 px and 5.94 px for the j-direction. The reduced values of the mean and the standard deviations of ε_{GC} allow the utilization of Dimorphos centroiding estimations in a navigation filter.

The peaks of the error shown in Fig. 2.18 correspond to two epochs where Dimorphos is in eclipse because of the shadow of Didymos, as it will be explained in Section 2.4.3.2.

2.4.3.2 Dimorphos in eclipse

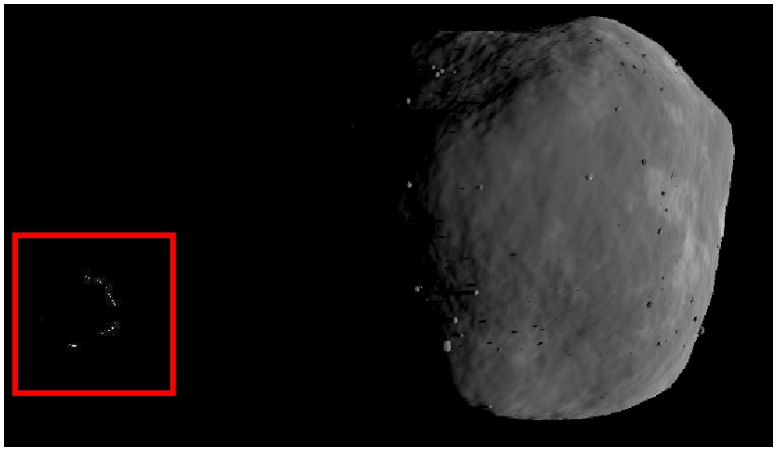

Figure 2.19: Illuminated boundary of Dimorphos when eclipse occurs

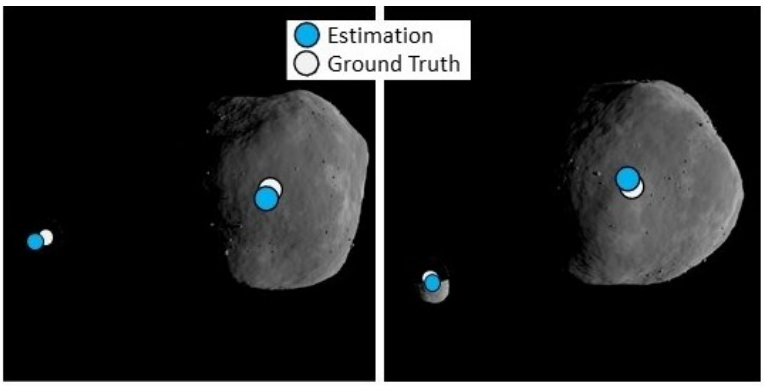

Figure 2.20: Dimorphos' centroiding results in partial and total eclipse

There are 593 images out of the ECP testing dataset that include Dimorphos in partial or total eclipse because of the primary's shadow. The centroiding algorithm is still capable of estimating the centroid as in this subset the secondary's boundary is

visible even in the worst case scenario of a total eclipse conditions, as shown in Fig. 2.19 (the boundary illumination has been enhanced in the figure for illustration purposes). The RMSE value for this subset of images is 30.24 pz. Fig. 2.20 shows the results of two images representing the partial and the total eclipse of Dimorphos.

It can be seen from Fig. 2.18 that the IP algorithm fails for image 2038 and 3747 of the ECP testing dataset, as the boundary of Dimorphos is not illuminated enough for the HRNet to determine the centroid position.

2.4.4 ECP pseudorange measurement

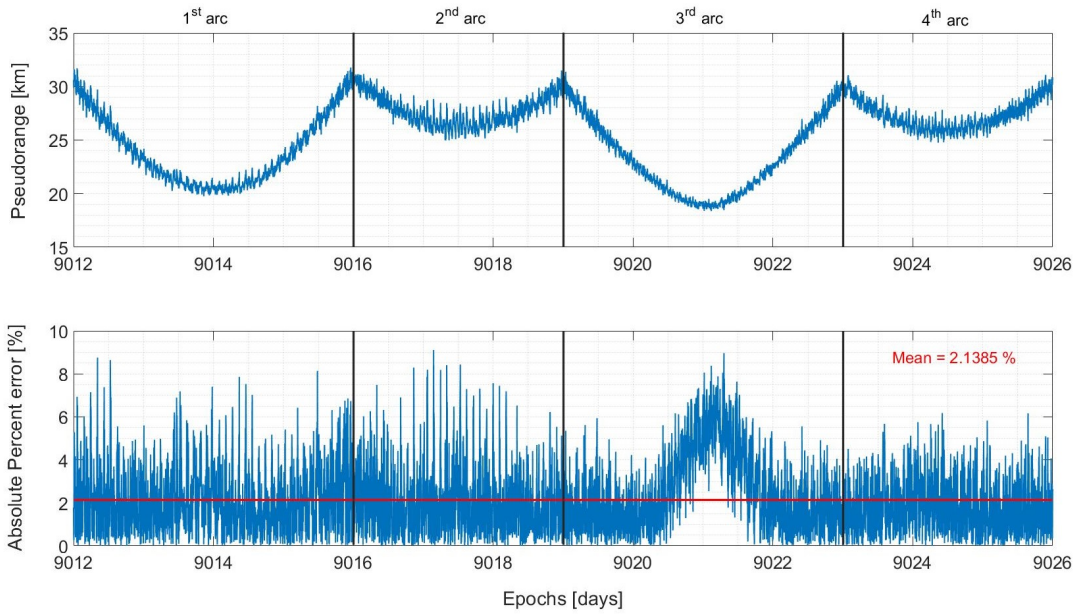

Figure 2.21: Pseudorange estimation during ECP

Fig. 2.21 shows the results obtained of the pseudorange estimation with the HRNet-based IP algorithm during ECP. The upper plot shows that the estimation is similar to the ground truth illustrated in Fig. 2.3 in Section 2.3.1. The lower plot in Fig. 2.21 shows that the absolute percentage error is smaller than 10% and oscillates around a mean value of 2.1385%. The proposed algorithm meets the Hera mission requirements which requires the absolute percentage error on the measurement of the pseudorange to be smaller than 10%. When the range reaches its local minima in the 1^{st} and 3^{rd} arcs, the absolute percentage error is higher, due to the fact that the images of the

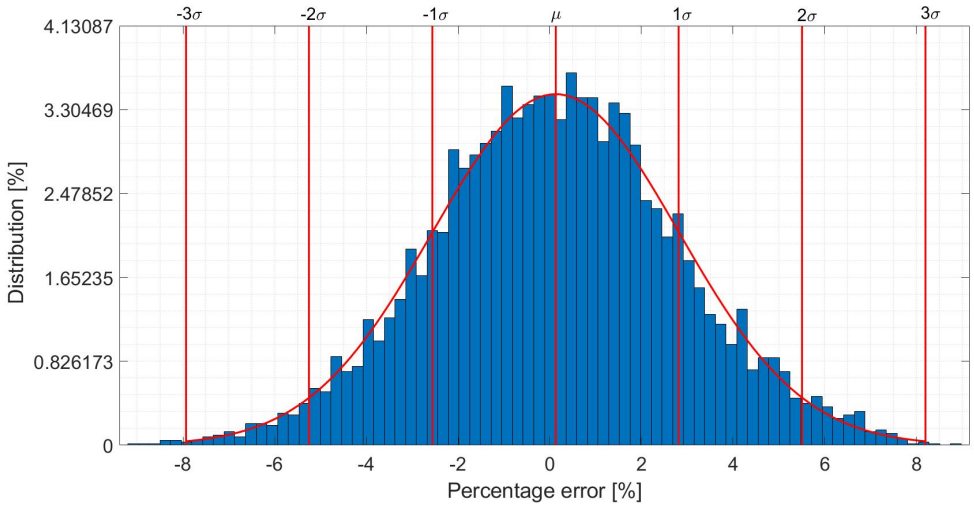

Figure 2.22: Pseudorange percentage error distribution during ECP

asteroid are appearing larger in the image plane. As a consequence, the non-spherical shape becomes more predominant and the approximation as a sphere is less accurate. In particular, the error near the local minima of the range in the third arc is larger because the phase angle is the lowest (Fig. 2.3) hence the asteroid is the brightest and its irregular shape is the most visible.

Fig. 2.22 illustrates the distribution of the percentage error of the pseudorange estimation during ECP, which is similar to a white noise with the mean value of $\mu = 0.1298\%$ near 0. The value of the error that appears the most, which is represented by the peak of the histogram, is 0.4695%. The standard deviation of the error is $\sigma = 2.6888\%$ which means that 68.27% of the pseudorange measurements have a percentage error ranging between $-2.559\%$and 2.8186% with respect to the ground truth. The distribution of the error is symmetrical ($skewness = 0.0176$) and light-tailed ($kurtosis = 3.0067$) which indicates that the percentage error distribution is similar to a Gaussian distribution. Therefore, the algorithm to estimate the pseudorange from images of Didymos can be implemented in the navigation filter of the spacecraft.

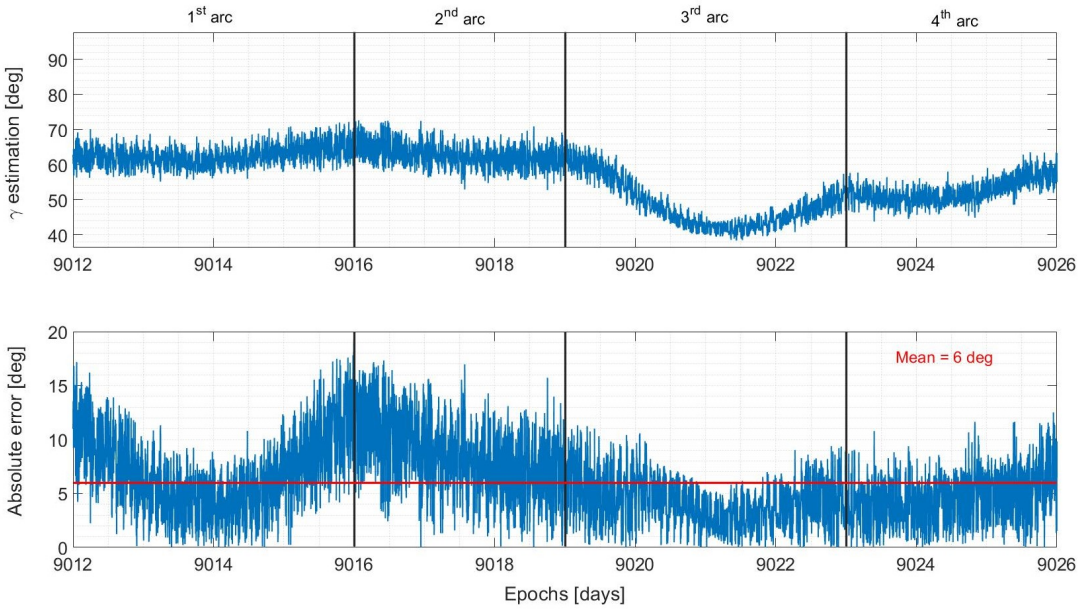

Figure 2.23: Phase angle estimation during ECP

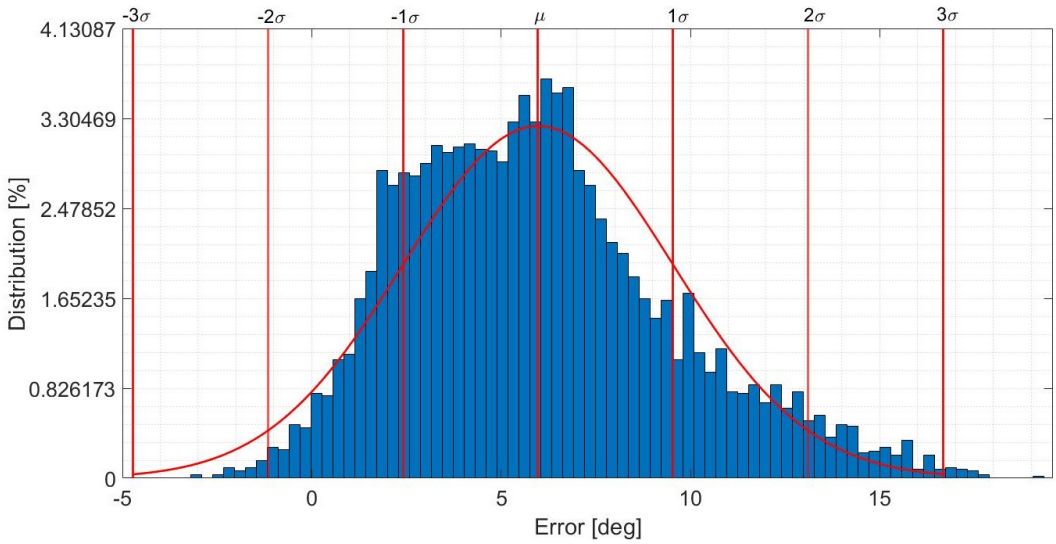

Figure 2.24: Phase angle error distribution during ECP

2.4.5 ECP Sun phase angle estimation

Fig. 2.23 shows the Sun phase angle estimation obtained by the HRNet-based IP algorithm during the ECP. The absolute error is moderate and reaches the peak value of 20°, although the SS position is estimated with a higher accuracy, as shown in Fig. 2.14.

The error is larger because the sphere approximation of the shape of the asteroid for the estimation of the phase angle is introduced twice in Eq. 2.5. Nevertheless, the mean error is small (6°) and the estimated phase angle is similar to the GT value shown in Fig. 2.3.

Fig. 2.24 illustrates the distribution of the error of the phase angle estimation during ECP. Compared with the pseudorange estimation, the white noise approximation is less accurate considering that the mean value of the error is high ($\mu = 5.976°$). The peak of the distribution is reached at 6.192° and the standard deviation is $\sigma = 3.5639°$, which means that 68.27% of the estimations have an error ranging between 9.5399°and 2.4121°. The distribution of the error is right skewed ($skewness = 0.5654$) and light-tailed ($kurtosis = 3.0946$). In conclusion, the algorithm to estimate the Sun phase angle is affected by a limited systematic error that is due to the approximation of the shape of the asteroid as a sphere. Ultimately, the Sun phase angle measurement is not ideal for a navigation filter, but it can still be implemented for redundancy.

2.4.6 Estimation of COM_{Did} during DCP

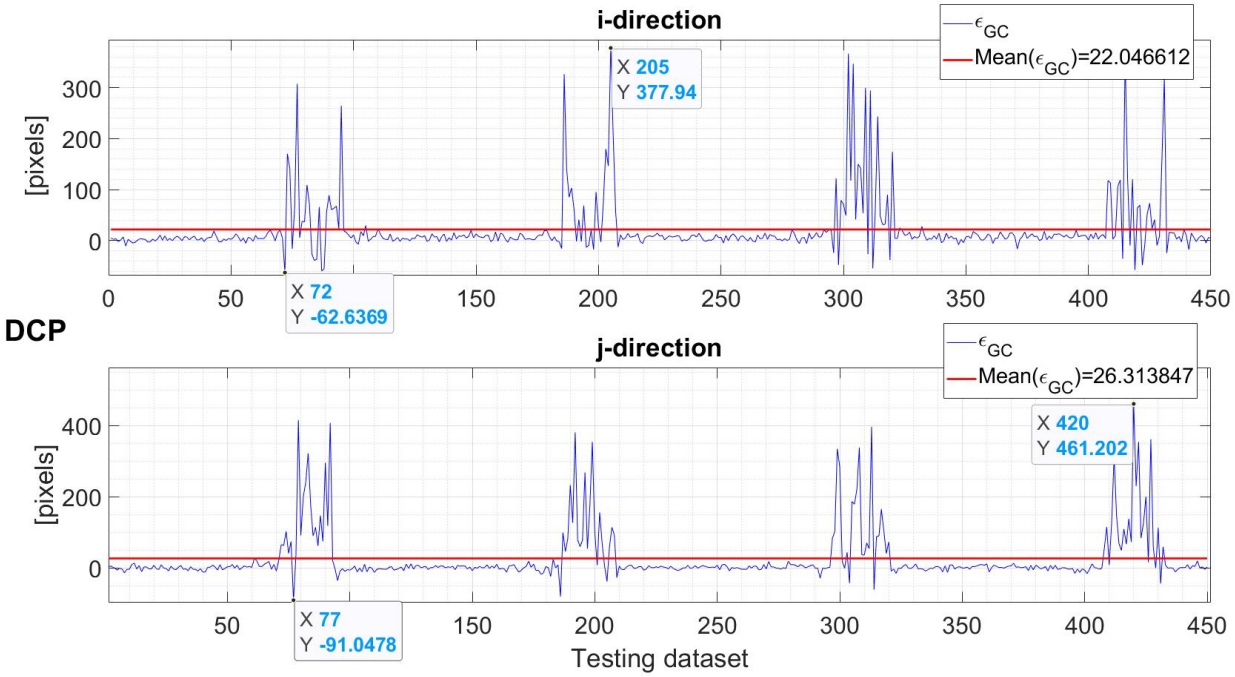

Figure 2.25: ε_{GC} for Didymos during DCP

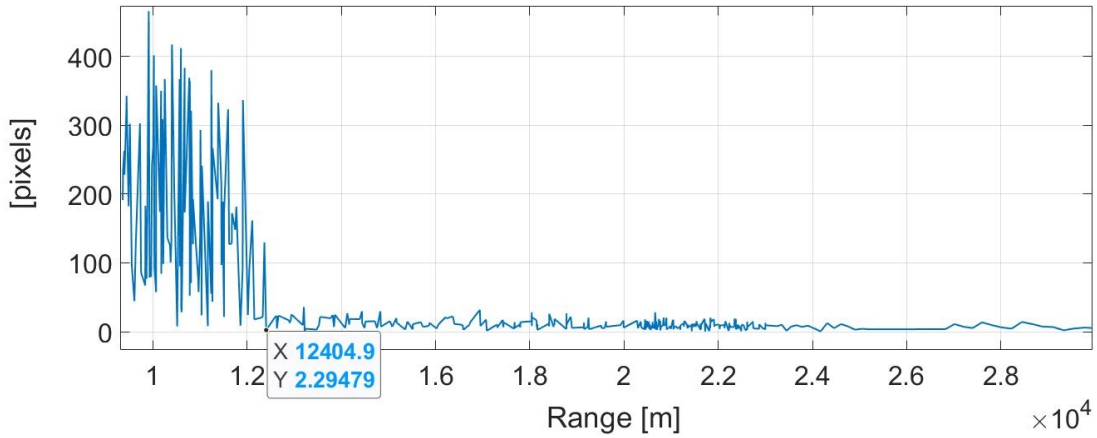

Figure 2.26: Absolute error between GT and estimated (i, j) pixel position of Didymos centroid vs range of DCP

Fig. 2.25 illustrates the centroiding results of Didymos in the i- and j-directions of the PANGU viewer for the 448 images of the testing dataset of the DCP. The average value of the error is 22.04 px for the i-direction and 26.31 px for the j-direction and the respective RMSE values are 62.03 px and 79.22 px. Since during the DCP the range from the asteroid is smaller, the apparent size of the asteroid is bigger in the images and the estimation accuracy is lower than that of the ECP. This is also illustrated by comparing Fig. 2.25 with Fig. 2.5. The epochs when the spacecraft is getting closer to Didymos coincide with the increase of the error of the estimation of the centroid.

Fig. 2.26 shows the norm of the DCP error ε_{GC} in both directions for each image with respect to the range. When the range value is larger than about 12.4 km, the asteroid is far enough for the HRNet-based IP algorithm to provide an accurate estimation of the position of the centroid. The number of images where the range of the asteroid is lower than 12.4 km is 102. Therefore, the HRNet-based IP algorithm provides accurate results for 77.33% of the DCP images. Considering that the HRNet has been trained using the ECP trajectory that has a minimum range with respect to the asteroid of 20 km, the algorithm is proved to be robust by generalizing the keypoint regression for further 7.6 km.

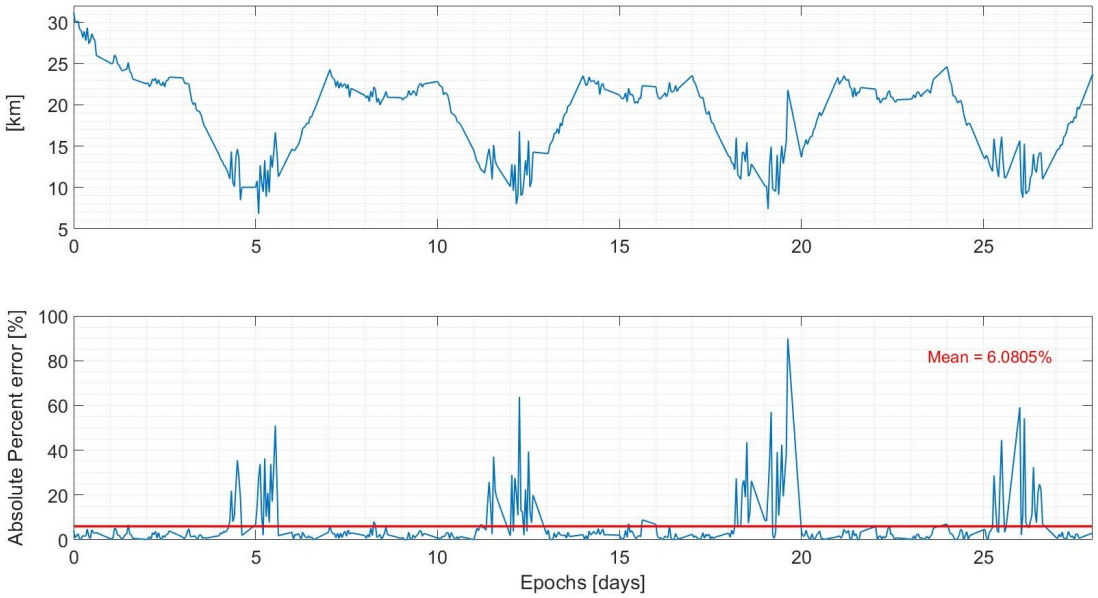

Figure 2.27: Pseudorange estimation during DCP

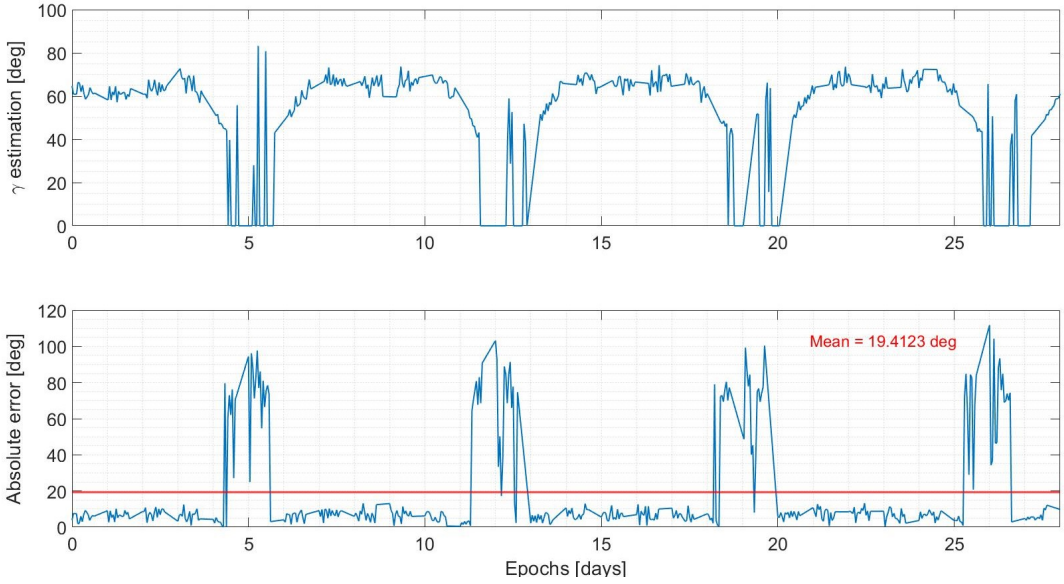

Figure 2.28: Phase angle estimation during DCP

2.4.7 DCP pseudorange and Sun phase angle estimation

Fig. 2.27 and Fig. 2.28 shows the pseudorange and the Sun phase angle estimation obtained by the HRNet-based IP algorithm during the DCP. Similarly to the error obtained with the COM_{Did}, the accuracy of the estimations is lower when the spacecraft

is closer than 12.4 km to the asteroid. When the range is higher than this value, the algorithm provides an accurate estimation of the range, as it can be seen by comparing Fig. 2.27 and Fig. 2.28 with Fig. 2.5. The errors in the pseudorange and the Sun phase angle estimations can be reduced if the HRNet-based IP algorithm results are combined with the ones of the PALT instrument, which is in operation only when the range is smaller than 14 km.

2.5 Conclusion

This paper develops a CNN-based IP algorithm addressing the problem of centroiding (Geometrical Center), range and the phase angle estimations for autonomous optical navigation around a binary asteroid system. The ECP and DCP proximity operations of Hera mission to Didymos system are studied as case scenario. The challenges tackled by the developed methodology include adverse illumination conditions of the target, irregular shape of the asteroid and the disturbances caused by the presence of the secondary.

The results show that the HRNet-based IP algorithm is able to estimate the position of the centroids of the primary, the pseudorange and the Sun phase angle with high accuracy for the ECP. In particular the centroiding method is robust to the presence of Dimorphos and its shadow projected on the surface of the primary. Besides, it exhibits no dependency on the illumination condition. If higher accuracy is required, the training database can be augmented using additional images generated from different trajectory segments around the target body. Moreover, the algorithm estimates with high accuracy the position of the centroid of the secondary body, even in partial and total eclipse conditions, which is another unique contribution of this work. The methodology to estimate the pseudorange is robust to the disturbances caused by the irregular shape of the asteroid and the presence of Dimorphos. In particular, the percentage error in the pseudorange estimation has a near-Gaussian distribution, which is ideal for navigation filters. The algorithm can also provide an accurate estimation of the position of the SS point on the surface of the asteroid during the ECP, which is used to estimate the Sun phase angle. Nevertheless, the estimation of the latter

is moderately affected by the irregular shape of the asteroid and the error does not present a Gaussian distribution.

The trained net from the ECP is able to generalize its solution to the DCP if the range is larger than a threshold value of 12.4 km, in terms of the centroid of Didymos, the pseudorange and the Sun phase angle. If higher accuracy is required for lower ranges, the training database can be augmented using additional images generated with the DCP or closer trajectories.

Nevertheless, the proposed pipeline is applied to the pre-impact models of Didymos and Dimorphos. Assuming that the same methodology is applied to images representing the actual shapes of Didymos and Dimorphos with the post impact orbital parameters, the obtained results will be different. The regression of the 27 keypoints will not be affected, as the non-spherical shapes of the target will be learned by the HRNet, as it can be seen from the regression of the COM of Dimorphos represented in this work by the irregular shape of Itokawa. Hence, the estimation of the position of the COMs from images representing the updated shapes of Didymos and Dimorphos will not be affected. On the other hand, the estimation of the range from the primary and the Sun phase angle are both based on the approximation of the shape of the primary to a sphere. Therefore, in order to apply the same pipeline, it should be taken into account the ellipsoidal shape of Didymos. Finally, notice that in this work the sole utilization of IP algorithms and the camera is considered for the requested measurements. The parallel utilization of other onboard sensors is also a viable option to refine the obtained results. It is important to address that the potential unstable motion of Dimorphos caused by the impact can cause its continuous reshaping, that might not cease at Hera's arrival [91]. In that case, a fine-tuning of the HRNet-based IP algorithm with a dataset of images taken during the first days of the ECP is necessary in order to learn the position of the COM of Dimorphos.

Our developed methodology contributes to the SSA by improving the robustness and the autonomy of the navigation strategy of the first mission ever testing asteroid deflection. Specifically, the unique contribution represented by the estimation of the SS point can be applied to any object in space. The pseudorange and Sun phase angle

estimation methodologies can be employed for any space object with a near-spherical shape, hence it can also support the tracking of space debris and other uncooperative objects.

Future work would go into the direction of other applications for the HRNet-based IP algorithm. For instance, an additional output useful for the navigation during the proximity operations is the pose estimation. Subsequently, the algorithm will be incorporated with a navigation filter to estimate the state of the spacecraft and to quantitatively evaluate the improvement of navigation performance.

Chapter 3

Convolutional Neural Network-based autonomous navigation of Hera mission around Didymos

> The path from dreams to success does exist. May you have the vision to find it, the courage to get on to it, and the perseverance to follow it
>
> *Kalpana Chawla*

Kaluthantrige A., Feng, J.[‡] and Gil-Fernández, J.[§]

Accepted for publication in *Journal of Guidance, Control and Dynamics*, July 2024

[‡]Associate professor, Department of Mechanical and Aerospace Engineering, University of Strathclyde

[§]Guidance, Navigation and Control Engineer, ESA ESTEC

Paper content

This chapter demonstrates that with the algorithm developed in Chapter 2 Hera can autonomously navigate around Didymos using purely visual data, achieving both accuracy and robustness in challenging imaging conditions. Following the map and structure shown in Fig. 1.8 in Section 1.3.3, this chapter addresses RQ 1b, completing all the answer to RQ 1, and achieves the objective of improving the performances of the optical navigation systems of asteroid mission proximity operations stated in RO 1. With this chapter, the reader will understand how to achieve spacecraft positioning around Didymos using only optical navigation, detailing the measurable performance outcomes.

Abstract

The European Space Agency (ESA)'s Hera mission requires an autonomous visual based navigation in order to safely orbit around the target binary asteroid system Didymos and its moon Dimorphos in 2027. Nevertheless, the performance of optical based navigation systems is depending on the intrinsic properties of the image, such as high Sun phase angles, the presence of other bodies and, especially, the irregular shape of the target. Therefore, to improve the navigation performance, thermal and/or range measurements from additional on-board instruments are usually needed to complement optical measurements. However, this work addresses these challenges by developing a fully visual-based autonomous navigation system using a Convolutional Neural Networks (CNN)-based Image Processing (IP) algorithm, and applying it to the Detailed Characterization Phase of the proximity operation of the mission. The images taken by the on-board camera are processed by the CNN-based IP algorithm that estimates the position of the geometrical centers of Didymos and Dimorphos, the range from Didymos and the associated covariances. The results shows that the developed algorithm can be used for a fully visual based navigation for the position of the Hera spacecraft around the target with good robustness and accuracy.

3.1 Introduction

Small celestial bodies are remnants of the ancient Solar System, holding invaluable insights into its evolutionary history. Asteroids and comets have garnered attention as prime targets for numerous space missions in the past years, such as Hayabusa 1 and 2 exploring asteroid Itokawa, Rosetta, a comet rendezvous mission targetting Comet 67P/Churyumov-Gerasimenko, and OSIRIS-REx that sampled asteroid Bennu [109–112]. The European Space Agency (ESA) contributes to small bodies exploration with Hera, a planetary defense mission under development in their Space Safety and Security Program. The Hera mission represents the European contribution to the international collaboration Asteroid Impact and Deflection Assessment (AIDA) with NASA. The main purpose of AIDA is to demonstrate the deflection of a hazardous asteroid by

means of kinetic impact. The Double Asteroid Redirection Test (DART) spacecraft is the kinetic impactor designed by NASA, which performed successfully the impact on the 26th of September 2022. The Hera mission will rendezvous in early 2027 with the target asteroid and characterize its physical and dynamical properties, including the crater made by the impactor and the momentum transfer efficiency [34, 97]. Furthermore, Hera aims to bring clarity to the currently uncertain mass measurements of the asteroid and it will delve into the possible presence of recently deposited material, which could potentially constitute reaccreted ejecta following the impact of DART.

The destination of Hera is (65803) Didymos, a binary asteroid consisting of the primary Didymos and its moon Dimorphos, objective of DART's impact. Table 3.1 shows the relevant characteristics of the binary asteroid system, provided by the Didymos Reference Model document and updated with the Design Reference Asteroid document that reports data collected with the DART mission [28,29]. Accompanying Hera on this mission are two CubeSats: Milani and Juventas. While Milani is tasked with capturing detailed imagery of the DART crater, Juventas will conduct comprehensive assessments of Dimorphos' internal structure [113].

Table 3.1: Didymos' characteristics [28, 29]

Property	**Didymos**	**Dimorphos**
Gravitational parameter $[km^3/s^2]$	$3.5 \cdot 10^{-8}$	$2 \cdot 10^{-10}$
Extent along principal axis x $[m]$	849	177
Extent along principal axis y $[m]$	851	174
Extent along principal axis z $[m]$	620	116

Following the interplanetary cruise phase, Hera will perform a series of Delta-Vs in order to reduce the relative velocity of the spacecraft with respect to the target, which marks the beginning of the proximity operations. The focus of this research is on the Early Characterization Phase (ECP) and the Detailed Characterization Phase (DCP) designed to achieve physical and dynamical characterizations of the binary asteroid [40]. Specifically, the characterization is aimed to improve the accuracy of the values shown in Table 3.1, together with other parameters related to the binary system, such as the

rotation rate of both bodies, the geometric albedo, mass properties and the gravitational field.

To ensure a high level of autonomy the spacecraft is equipped with on-board instruments to accurately determine its position relative to the asteroid system. To meet this requirement, a vision-based navigation system is implemented in the Guidance, Navigation, and Control (GNC) system of the spacecraft, which incorporates an on-board camera, image processing algorithms and a navigation filter. The HERA GNC baseline incorporates a hyperspectral/thermal camera and a laser altimeter called Planet ALTimeter (PALT). These additional instruments enhance the navigation strategy's reliability: the hyperspectral/thermal imager helps to overcome limitations caused by shadows and Sun phase angle issues, while PALT improves estimations in the radial direction, which are typically challenging for a vision-based GNC system. The camera employed in this system is the Asteroid Framing Camera (AFC) [58].

Each day during the proximity operations is divided into two operational segments: data acquisition and data transmission. Within a single operational day, one set of each is scheduled in the following sequence: 15.5 hr for acquisition and 8.5 hr for transmission. For the ECP and the DCP an autonomous attitude navigation is designed, which relies on an Image Processing (IP) algorithm that estimates the pixel-position of the Center of Mass (COM) of the main body in the images. Subsequently, the algorithm estimates the Line of Sight (LOS) of the spacecraft [58, 114]. During the ECP, the performance of the autonomous attitude navigation system is rehearsed while the spacecraft is flying at a safer distance from the target. Data gathered during the ECP is transmitted to ground within the time interval of data transmission in order to update, if necessary, the IP algorithm. Once the system is verified, the system can be used during the DCP [115].

Despite the validation process, standard IP algorithms are strongly influenced by the inherent characteristics of the taken images. Elements such as the overall noise, lighting status, the appearance of secondary or undesired objects, and the irregular shape of the target can all impact the accuracy of the optical measurements [55,116,117]. While the GNC system of the Hera mission tackles these IP challenges by relying on

the additional on-board instruments, the authors of this work addressed them with a Convolutional Neural Networks (CNN)-based IP algorithm built and presented in [80]. The algorithm is able to estimate accurately from the images captured by the AFC the position of the centroids of Didymos and Dimorphos and the range from the primary during the ECP and the DCP trajectories. The reader is referred to that work for a comprehensive understanding of the pipeline undertaken for the development of such algorithm. Nevertheless, the work is performed with the pre-impact shape models of Didymos and Dimorphos.

In this work we build upon the CNN-based IP algorithm to develop a fully autonomous visual based navigation algorithm for the DCP trajectory of the Hera mission around the target body Didymos. We leverage the previous phase of the mission, the ECP, to train the CNN-based IP algorithm with a dataset of images representing the new shape of the targets Didymos and Dimorphos. The algorithm is expanded by providing the covariance matrix associated to each measurement and a Flag that inform the filter whether the centroid of Dimorphos is visible or not, which is a unique contribution of this work. An Unscented Kalman Filter (UKF) combines the measurements obtained by the CNN-based IP algorithm with the information retrieved from the dynamical environment to provide the optimal estimate of the relative position of the spacecraft with respect to Didymos. In addition, the developed navigation algorithm relies fully on the AFC without requiring the inputs of the hyperspectral/thermal imager and PALT. Another contribution of this work is the utilization of the position of the centroid of Dimorphos for navigation.

The organization of this paper is as follows. Section 3.2 reviews the state of the art of navigation systems around smaller bodies. Section 3.3 describes more in detail the proposed IP algorithm and the navigation filter. In Section 3.4, we conduct the numerical simulations and discuss the results. Section 3.5, in conclusion, summarizes this research and suggests prospective areas for future work.

3.2 Related methods

This section gives a review on the navigation strategies adopted by previous mission that successfully approached small solar system bodies.

3.2.1 Heritage missions

3.2.1.1 Rosetta

In July 2014, the ESA interplanetary spacecraft Rosetta conducted a rendezvous with the comet 67P/Chuyumov-Gerasimenko. At 130 km of distance with respect to the target, Rosetta navigated towards the target relying on optical measurements provided by the on-board navigation camera NAVCAM. The strategy consisted in matching the newly acquired images with a database of old images for which the geometry is known, using small scale 3D high resolution maps (maplets) built around visible landmarks of the target body. The maplets consist of a height and an albedo map built on-ground with the available shape model of the target [118].

3.2.1.2 Hayabusa 1 and 2

Hayabusa 1 spacecraft performed approaching and landing on the target asteroid Itokawa in November 2005. To maintain the relative position to the asteroid during proximity operations a visual based GNC system was developed, similar with that of the Hera mission. Two wide-angle cameras, an IP algorithm estimating the position of the centroid of the target and a Light Detecting And Ranging (LIDAR) estimating the range from the target have been used.

Hayabusa 2 spacecraft approached the target asteroid Ryugu in July 2018. As its predecessor Hayabusa 1, this spacecraft is also provided with two wide-angle cameras and a LIDAR. Both spacecraft had on board a Thermal Infrared Imager and a Near-Infrared Camera Spectrometer for scientific purposes but also to increase the robustness of the navigation system as for the Hera mission [119, 120].

3.2.1.3 OSIRIS-REx

OSIRIS-REx used two wide-range cameras of the camera suite OCAMS and the touch-and-go camera system TAGCAMS for the proximity operations navigation around the target asteroid Bennu. Stereophotoclinometry was used to create digital terrain maps for landmark tracking technique, while the on-board LIDAR solves for the radial direction estimation [121].

3.2.1.4 DART

DART utilized the Small-body Maneuvering Autonomous Real-Time Navigation (SMART Nav) algorithm in conjunction with images obtained from the on-board Didymos Reconnaissance and Asteroid Camera for Optical navigation (DRACO) to carry out autonomous terminal navigation in order to target the center of brightness (COB) of Dimorphos. The on-board ephemeris was updated with optical navigation data collected by DRACO till about 4 *hr* before the impact, after which the spacecraft went fully autonomous with SMART Nav [98].

3.2.2 Summary

The navigation techniques involved in Rosetta and OSIRIS-REx have in common the usage of asteroid models to be rendered for correlation with real images acquired with the on-board cameras. Therefore, prior knowledge of the surface appearance of Didymos would be required to employ these navigation strategies. Furthermore, the more complex is the model, the more computationally expensive is to run the technique on-board. To apply DART' SMART Nav algorithm, constant direct communication with ground is necessary for the real-time updating of the ephemeris, which is not the case of Hera that alternates its attitude for data acquisition and transmission. Finally, the optical navigation solutions employed by Hayabusa 1 and 2 are similar to Hera and as such rely on multiple instruments to improve the robustness, while the purpose of this work is to provide a navigation strategy with good robustness that relies only the images captured by the on-board camera.

3.3 Methodology

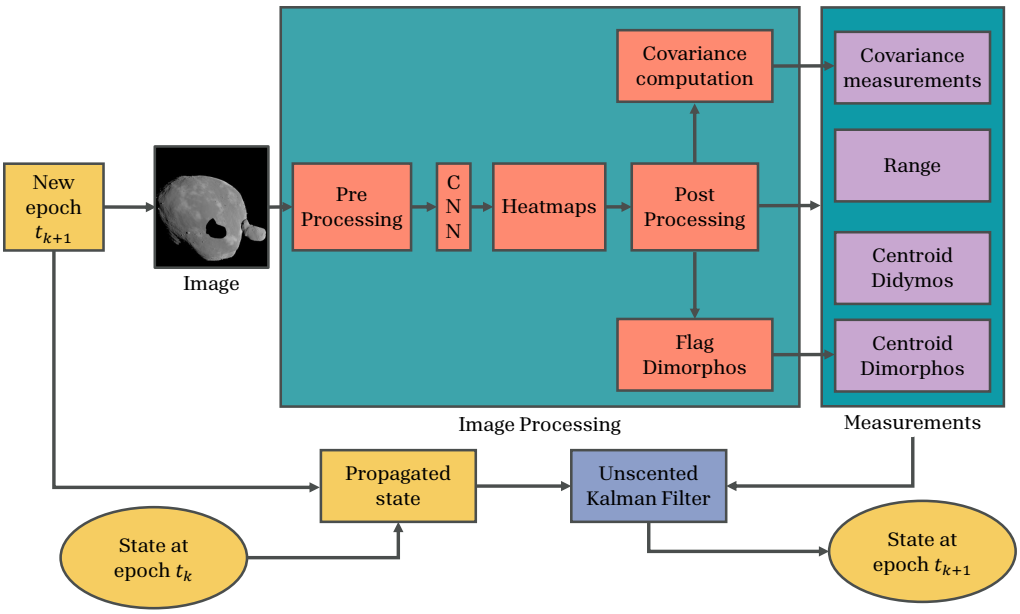

Figure 3.1: Overall visual based navigation algorithm

This section provides a detailed description of the methodology applied in this work. A terminology is briefly clarified to streamline the discussion. In this work, with centroid or Center of Mass (COM) is intended as the body's geometrical center projected on the image. While this assumption is almost valid for Didymos given its ellipsoidal shape, it is not certain if it holds true for Dimorphos consequently to the DART impact that may have modified its shape [91]. Fig. 3.1 shows the main steps of the overall pipeline. Given a reference trajectory, at epoch t_{k+1} a new image is captured by the on-board AFC. In this work, synthetic images generated with the software Planet and Asteroid Natural scene Generation Utility (PANGU) are used. The image is input to the IP block and it goes several steps detailed in Section 3.3.3 in order to provide 4 different estimations: the position of the centroid of Didymos, the range from Didymos, the centroid of Dimorphos (if available), and the associated covariance matrix for each measurement. The IP consists firstly in a Pre-Processing step where the image undergoes an initial normalization before it is handled by the CNN aimed to regress specific keypoints on the image. The CNN outputs a sequence of

heatmaps, each one associated with the regressed keypoint. The Post-Processing block analyzes the heatmaps and outputs the position of the keypoints and the intensities of the heatmaps. The latter are used to calculate the covariance matrices and to inform whether an estimate of Dimorphos' centroid position is available with a boolean variable represented by Flag Dimorphos. Finally, an UKF combines the available measurements and the propagated state to provide the best estimate for the state of the spacecraft at epoch t_{k+1}.

This work is an extension of [80], where the main focus was to build an IP algorithm supported by CNNs able to provide optical measurements for the navigation of Hera using the pre-impact shape models of Didymos and Dimorphos. In contrast, this research is focused on refining the previous algorithm with the latest shape models, and combining it with an UKF in order to solve for the state estimation of the Hera spacecraft. We use the same reference trajectories (Section 3.3.1), software to generate the database of images (Section 3.3.2), CNN architecture (Section 3.3.3.2) and centroiding and range estimation methodologies (Section 3.3.4). The subsequent part of this section contains a thorough explanation of the applied methodology.

3.3.1 Reference trajectories

The reference trajectories used in this work are represented in the Target Body Equatorial Inertial (TB) reference frame, which has the geometrical center of Didymos as origin of the axes, the X-axis pointing as the Earth-Centered Ecliptic Inertial, and the XY plane lying in the same plane as the equator of Didymos. A summary of the most relevant information of the orbit of the binary system is reported in Table 3.2 [20, 101]. The orbit of Dimorphos considered in this work is prior to the DART impact. The reference trajectories employed in this work are from the ECP and the DCP proximity operations. The former is used to train the CNN and to tune the parameters of the Post-Processing, while the latter is used as a test case scenario.

The ECP trajectory is provided by ESA while the DCP trajectory is provided by GMV Aerospace and Defence, in charge of the GNC simulator of the Hera mission. Both trajectories consist of hyperbolic arcs: the spacecraft cannot be placed into captured

Table 3.2: Selected orbital properties of Didymos system [20, 101]

Heliocentric orbit	
Semi-major axis $[AU]$	$1.642665 \pm 2.7214e-9$
Eccentricity []	$0.383264 \pm 1.3374e-10$
Inclination [°]	$3.41415 \pm 1.6188e-8$
Longitude of ascending node [°]	$72.987867 \pm 2.1852e-7$
Orbital period $[yr]$	$2.105386 \pm 5.2320e-10$
Binary orbit	
Semi-major axis $[m]$	1190 ± 30
Eccentricity []	0
Orbital period $[hr]$	11.93 ± 0.01

orbits due to the limited prior knowledge of Didymos' dynamical environment. The arcs are designed so that the AFC, whose parameters are shown in Table 3.3, is able to contain within its Field Of View (FOV) the whole shape of Didymos in a single image in order to use the centroiding algorithm [103, 104, 115].

Table 3.3: AFC properties [103, 104]

FOV	**Focal length**: f	**Aperture**	**Image size**	**Pixel size**: ν
5.5°	10.6 cm	2.5 cm	1024×1024 px	14 μm

Fig. 3.2 depicts the spacecraft's ECP trajectory along with the relative position of the Sun (reduced in size in the visual representation) and Dimorphos' orbit. The trajectory is composed of four arcs, with the initial epoch set at $t_{in} = 9012$ d and the final epoch at $t_{fin} = 9026$ d calculated in the Modified Julian Date 2000 (MJD2000). The 2^{nd} and the 4^{th} arcs are 3 d long and go respectively from Didymos' high latitudes to low latitudes and viceversa. The 1^{st} and the 3^{rd} arcs are 4 d long and cover the poles of the target. The sole gravitational forces from the point masses of both bodies and the orbital maneuvers at the joint of two arcs are taken into account. The planar view illustrated in Fig. 3.2 shows that the ECP trajectory is placed between the Sun and Didymos in order to provide the AFC with visible images of the target [40]. Fig. 3.3 shows that the distance from the primary ranges from 20 km and to 30 km.

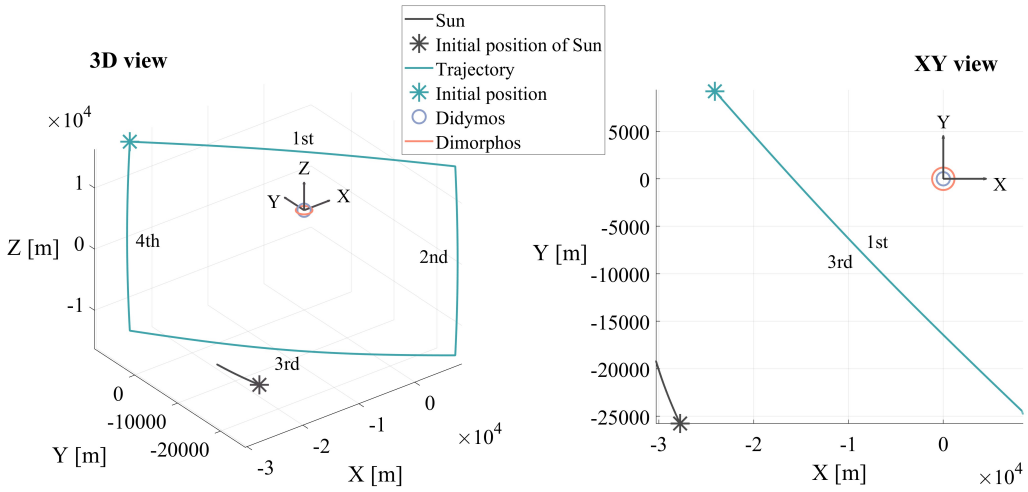

Figure 3.2: ECP trajectory

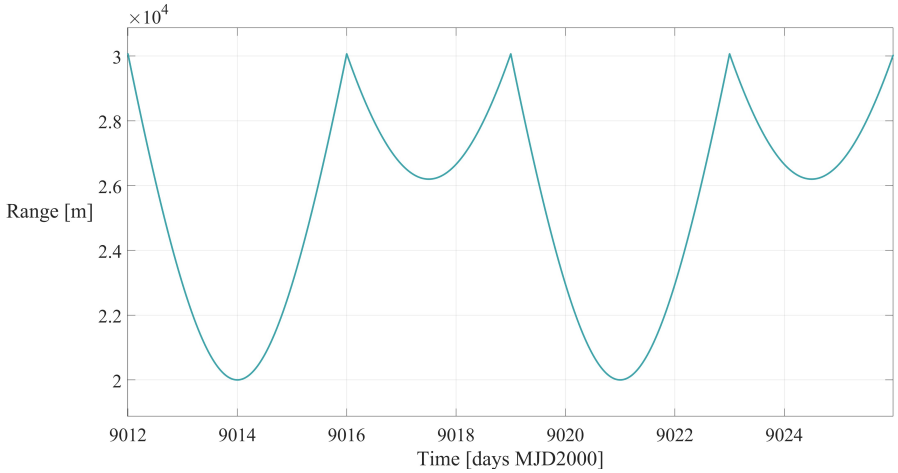

Figure 3.3: Range from Didymos during ECP trajectory

Fig. 3.4 depicts the spacecraft's DCP trajectory along with the relative position of the Sun (reduced in size in the visual representation) and Dimorphos' orbit. The trajectory is composed of eight Z-shaped arcs located between the target and the Sun's position, with a total duration of 28 d, plus 3 d of transition from the ECP. The distance from the primary ranges approximately from 9 km to 23 km, as illustrated in Fig. 3.5. The minimum distance is established to guarantee that the complete shape of Didymos remains within the FOV of the AFC, even when there is a navigation error of up to 100 m. In the actual mission, the ECP and the DCP last 4 weeks each but in this work the

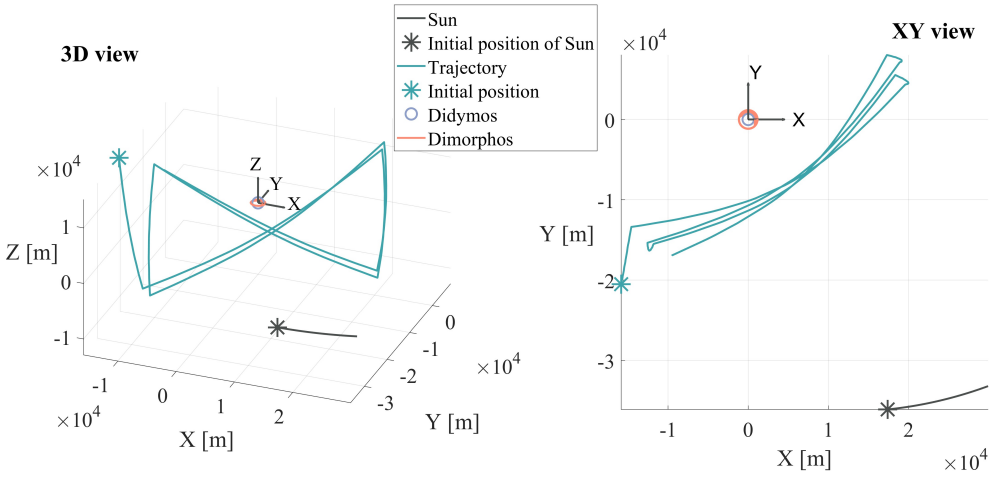

Figure 3.4: DCP trajectory

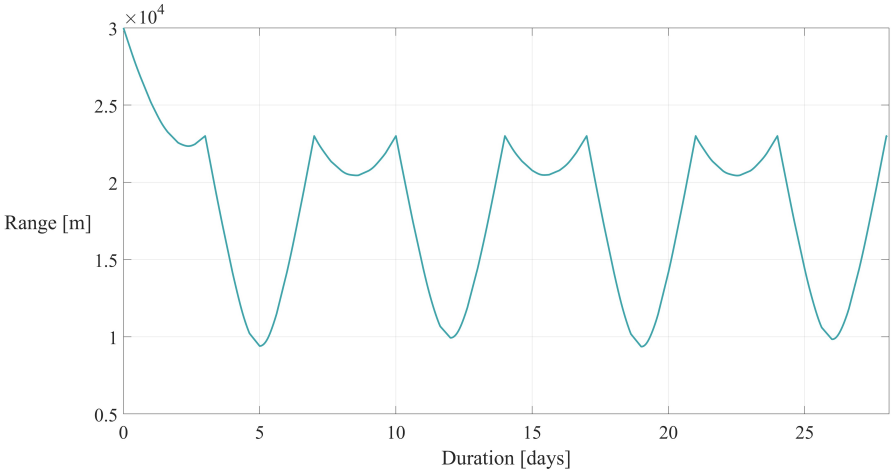

Figure 3.5: Range from Didymos during DCP trajectory

whole DCP and only half of the ECP are considered, as provided by ESA and GMV Aerospace and Defence.

3.3.2 Image Generation

The software PANGU is used to generate the database of synthetic images for this work. PANGU is a simulation tool developed by the STAR-Dundee engineering company, and it is capable of modeling planetary and asteroid surfaces and providing high-fidelity visualizations of images in near real-time [102]. The shape models of Didymos and

Dimorphos are provided by GMV and updated with the data collected with the DART mission shown in Table 3.1. Didymos' shape is ellipsoidal, with the extent along its x- and y-axes larger than the extent along its z axis, as shown in Table 3.1. Dimorphos' shape prior to DART's impact was an oblate ellipsoid, which is approximated in this work scaling down the shape model of asteroid Itokawa.

PANGU generates grayscale images as seen from the AFC with the properties shown in Table 3.3, and displays them on its viewer with its coordinate frame's origin at the top left corner and the horizontal and vertical axes referred to as i-direction and j-direction, respectively, as illustrated in the example of Fig. 3.6.

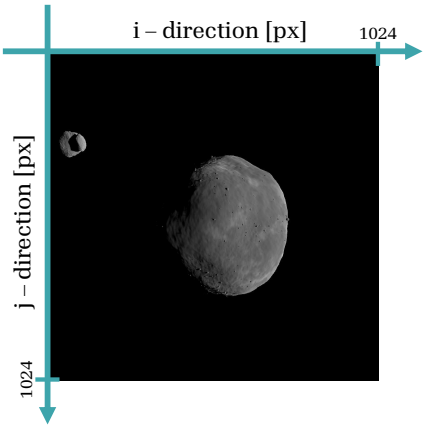

Figure 3.6: Image taken during the ECP trajectory shown on the PANGU viewer

For asteroid imaging during the ECP and DCP trajectories, the AFC's boresight is aligned with Didymos' position vector, and the camera's vertical axis is orthogonal to the spacecraft-Sun's position vector to the spacecraft [40], which results on images displayed on the viewer consistently portraying the target illuminated from the right side.

In this work, PANGU is used to generate:

- Dataset 1: $40,000$ images generated during the ECP trajectory and used for the training and validation of the CNN and to tune the parameters of the IP algorithm. Two fictitious additional arcs are considered, the first arc connecting

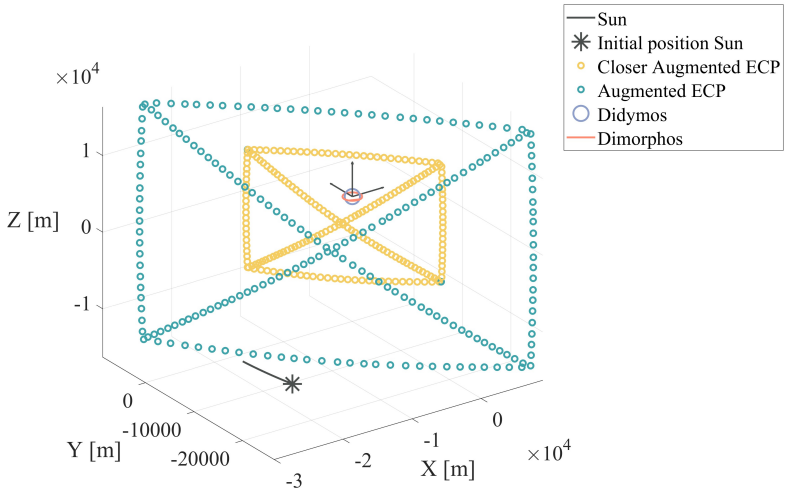

Figure 3.7: Augmented ECP trajectory

the end of the 2^{nd} arc with the beginning of the 1^{st} one, and the second one connecting the end of the 3^{rd} arc with the end of the 1^{st} one, as shown in Fig. 3.7. The augmented ECP trajectory is sampled randomly to generate a secondary trajectory closer to the target, with a minimum distance of 7 km, in order to train and validate the IP algorithm with a pool of images showing the asteroid in multiple configurations relative to the spacecraft. A pointing error of the AFC boresight direction with values spanning between $[-0.3, 0.3]^\circ$ is considered for each image to randomize the position of the projected centroid of Didymos on the image plane;

- ❖ Dataset 2: 450 images taken sampling the DCP trajectory every 3600 s and used as testing batch for the whole visual based navigation pipeline. A pointing error of the AFC boresight direction with values spanning between $[-0.5, 0.5]^\circ$ is considered for each image to randomize the position of the projected centroid of Didymos on the image plane.

The pointing error values considered in the generation of the images of Dataset 1 and Dataset 2 are chosen taking into account the only mission requirement of having the whole shape of Didymos within the FOV of the camera [40].

3.3.3 Image Processing

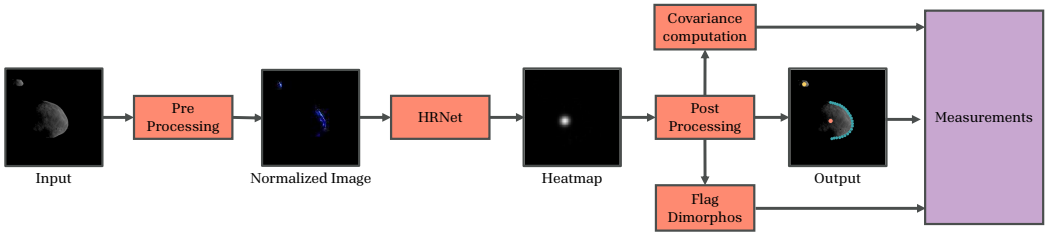

Figure 3.8: Image Processing

In this section the operations that each image undergoes with the IP algorithm are described, as represented in Fig. 3.8.

3.3.3.1 Normalization

Once an image is generated with PANGU, its size is reduced from 1024×1024 px to 256×256 px and consequently it is normalized using Eq. 3.1 to calibrate the different pixels intensities, which helps the CNN to converge faster for a given learning rate. Eq. 3.1 shows that the image is converted from grayscale to RGB as required from the specific CNN architecture chosen in this work.

$$Image = Image - Mean/std \tag{3.1}$$

where $Mean = [0.485, 0.456, 0.406]$ and $Std = [0.229, 0.224, 0.225]$. Fig. 3.8 shows the output normalized image of the Pre-Processing block (the colors of the output image are enhanced for visualization purposes).

3.3.3.2 CNN

The CNN employed in this work is the High-Resolution Network (HRNet), the state-of-the-art CNN architecture for keypoints regression, with its ability to maintain high resolution representation of the input image through the whole net [122]. The keypoints to regress for each synthetic image are 26, and they are the COM of Didymos, COM_{Did}, the COM of Dimorphos, COM_{Dim}, and 24 points on the visible limb, i.e. the right

side, segmenting Didymos from the background. The positions of the 24 points are used together with the position of the COM_{Did} to estimate the range from Didymos, as it is explained in Section 3.3.4. The reader is referred to [80] for the methodology applied to retrieve the Ground Truth (GT) positions of the 26 keypoints on the images.

In this work, we utilize the CNN architecture known as pose-hrnet-w32 [107]. Throughout the training process, the validation dataset is employed alongside the training dataset to calculate validation losses, thereby preventing overfitting. For the training and validation Dataset 1 is not used entirely, as images where Dimorphos is located outside of the image plane or behind Didymos are discarded. Whether Dimorphos is visible or not in the testing Dataset is handled by the Post-Processing block of the IP. Consequently, the training and validation datasets consist respectively of $15,156$ (93.73%) images and 520 (3.22%) images from Dataset 1, while the testing dataset consists of the whole 450 (3.05%) images from Dataset 2. The training utilizes the Adam optimizer, employing a learning rate that follows a cosine decay schedule, initialized at 10^{-3} and decaying at a rate of 0.1. The overall number of parameters engaged in the training process amounts to $28,536,410$.

The CNN model undergoes training for 210 epochs, which approximately equates to 48 hr of training time. This training is conducted on a virtual machine hosted by Google Colab, utilizing the NVIDIA V100 Tensor Core GPU. The trained model is then converted into an *ONNX* (Open Neural Network Exchange) open format and imported on Matlab. The trained HRNet with the updated weights and biases has an overall weight of 109 MB.

The outputs of the HRNet consist in a sequence of heatmaps of size 64×64 px, each one associated with the corresponding keypoint. A heatmap is a cloud of white pixels around the estimated keypoint, and it represents the estimated accuracy in regressing the position of that particular keypoint. The smaller and intense is the heatmap, the more accurate is the estimation of the position of the associated keypoint. Fig. 3.9 shows an example of the heatmap around the estimated position of the COM of Didymos.

Figure 3.9: Heatmap associated to the position of the centroid of Didymos

3.3.3.3 Post-Processing

In the Post-Processing block, the 26 heatmaps associated to each keypoint are analyzed. Specifically, the Post-Processing block has three main functions:

- ❖ To remove the white noise by thresholding each heatmap image so that the only non-black pixels are the one associated to the heatmap;
- ❖ To extract the peak intensity of the heatmap and its x and y coordinates;
- ❖ To obtain a statistical population around the heatmap's peak.

The coordinates of the points with the peak pixel intensity within the heatmap defines the estimated position of the regressed 26 keypoints. The intensity and shape of the heatmap conveys the level of confidence in accurately pinpointing the associated keypoint at that particular position. Therefore, in this work the statistical population around the regressed keypoint is used to derive the associated covariance matrix.

3.3.3.4 Flag Dimorphos

By analyzing the peak intensity of the heatmaps associated to the COM of Dimorphos and generated by the trained HRNet with the entire Dataset 1, it is derived a threshold value to determine whether Dimorphos is visible or not. Fig. 3.10 shows the mentioned peak intensities, together with their average value and the cut-off threshold value. Three main regions of peak intensities are identified:

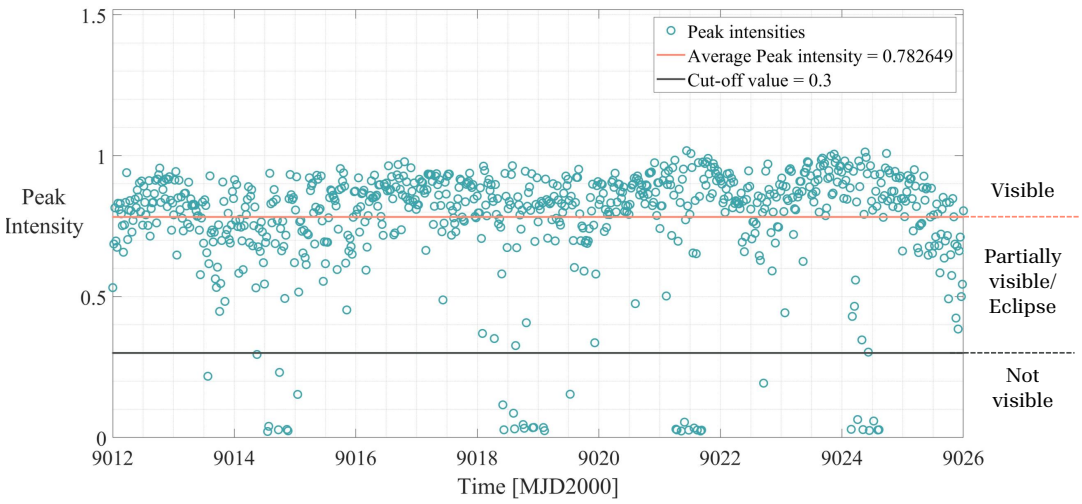

Figure 3.10: Peak intensity of the heatmaps associated to COM_{Dim} generated with Dataset 1

- ❖ 0 - 0.3: Heatmaps peak intensities associated to images where Dimorphos is hardly visible or not visible;
- ❖ 0.3 - 0.782649: Heatmaps peak intensities associated to images where Dimorphos is in eclipse or is partially visible;
- ❖ $>$ 0.782649: Heatmaps peak intensities associated to images where Dimorphos is fully visible.

Fig. 3.11 shows three sample images of each region along with the heatmaps associated with the regression of the centroids of both bodies. The output of this block is a boolean variable that is true if the peak intensity of Dimorphos' centroid heatmap is higher than 0.3, i.e. Dimorphos is at least partially visible or in eclipse.

3.3.3.5 Covariance computation

In this block of the IP algorithm, the covariance matrices associated to the error in the estimation of the position of the centroids of Didymos and Dimorphos are computed. Given the x_i- and y_i- coordinates of the $i-$th pixel belonging to the heatmap associ-

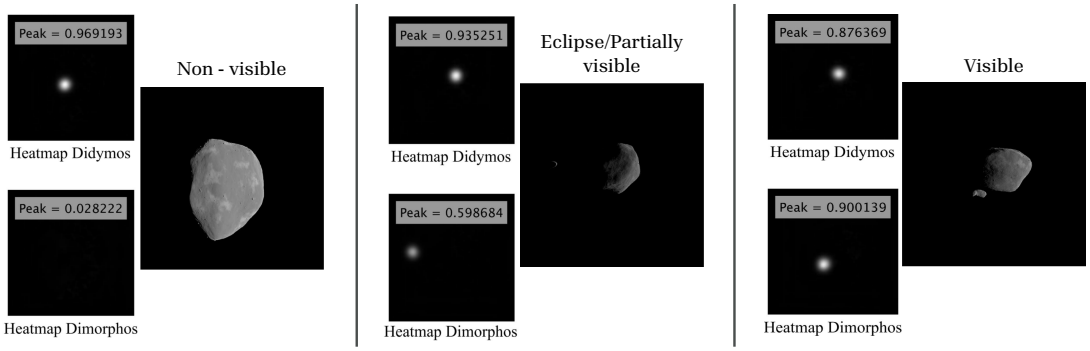

Figure 3.11: Heatmaps of COM_{Did} and COM_{Dim} associated with three sample images showing Dimorphos respectively non-visible, in eclipse and visible

ated to the regressed centroid of coordinates x_p and y_p, the covariance of the error is calculated with Eq. 3.2 and Eq. 3.3, in accordance with [93].

$$P_{COM} = \begin{pmatrix} cov(x,x) & cov(x,y) \\ cov(y,x) & cov(y,y) \end{pmatrix} \tag{3.2}$$

$$cov(x,y) = \sum_{i=1}^{n} w_i (x_i - x_p) \cdot (y_i - y_p) \tag{3.3}$$

where n is the number of pixels in each keypoint's heatmap and w_i is a weight that takes into account the intensity of the pixel belonging to the heatmap. This process aims to assign greater weight to pixels that exhibit high brightness and are situated near the peak, while assigning reduced importance to pixels with low intensity that are distant from the peak. Fig. 3.12 shows two examples of covariance matrices associated to the estimation of the centroids of both bodies. The example on the image of the right of Fig. 3.12 shows that Dimorphos' centroid estimation covariance can reach lower values than the one of Didymos due to its relative reduced size on the image. Therefore, the cloud of points associated to Dimorphos' centroid estimation is smaller. In order to account for the different size of the bodies, a tuning of the covariance is applied accordingly. The tuning consists in adjusting the parameters of the covariance matrices to weigh majorly the estimation of the centroid of Didymos with respect to the one of Dimorphos.

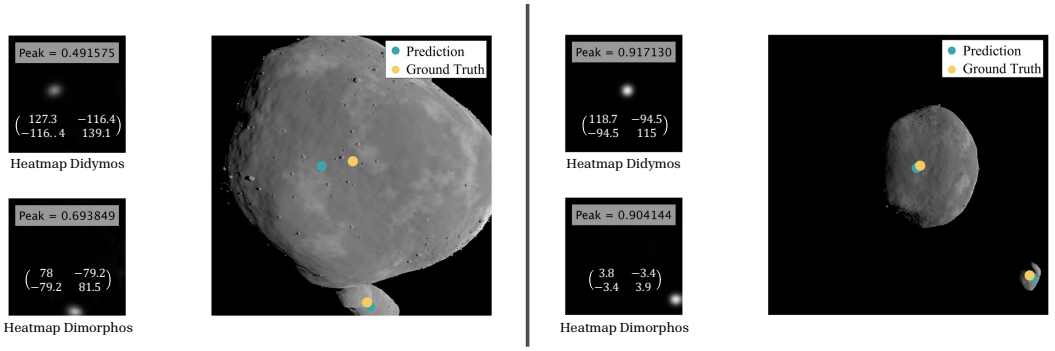

Figure 3.12: Two example of covariance matrices associated to the centroids of Didymos and Dimorphos

3.3.4 Measurements

The input measurements of the navigation filter are the estimated position of the centroids of Didymos and Dimorphos (when available) and the estimated range from Didymos. The first two are direct outputs of the IP block together with their associated covariance matrices. The range is estimated using the relative average distance in pixel (n_R) of the 24 regressed keypoints on the visible limb of Didymos with respect to its estimated COM, as explained in [80]. The 24 keypoints have an equal relative angular distance and span an angular aperture of $[-87, 87]^\circ$ with respect to the $i-$direction of the PANGU viewer. By applying the pinhole camera model using the properties of the AFC shown in Table 3.3, and by approximating the shape of Didymos as a sphere of radius $R = 773.33\ m$ (average value of the extent along the three principal axis shown in Table 3.1), the range ρ is estimated, as shown in Eq. 3.4:

$$\rho = \frac{f \cdot R}{n_R \cdot \nu} \tag{3.4}$$

where f is the focal length and ν is the pixel density, as shown in Table 3.3. The covariance of the error associated with the estimated range is obtained by applying Eq. 3.4 to Dataset 1 and by comparing it with the range's GT value. The error obtained is reported on Table 3.4 and the covariance of the error chosen in this work is $P_\rho = MAE^2$.

The Absolute Error (AE) and the Absolute Percent Error (APE) are defined as

Table 3.4: Range estimation error for Dataset 1

Mean Absolute Error (MAE) $[m]$	854.9
σ_{MAE} $[m]$	518.85
Mean Absolute Percent Error (MAPE) [%]	5.68
σ_{MAPE} [%]	4.3

follows:

$$AE = |Range_{est} - Range_{GT}|, \tag{3.5}$$

$$APE = \frac{|Range_{est} - Range_{GT}|}{Range_{GT}} \cdot 100\% \tag{3.6}$$

3.3.5 Navigation filter

To combine the measurements produced by the image processing algorithm with the dynamical environment and form an accurate estimate of the state of the spacecraft, a navigation filter is implemented. In particular, in this work the UKF is used in order to better accommodate the non-linear system of equations involved in the dynamical environment of a binary asteroid system. The relative state of the spacecraft with respect to Didymos to be estimated consist of the three coordinates of the relative position and the three coordinates of the relative velocity. The measurements are available for each image of Dataset 2, therefore every 3600 s.

The UKF is based on a non-linear uncertainty propagation technique called the Unscented Transform (UT) that captures the propagation of the statistical properties of state estimates through non-linear functions. This is done using a set of sigma points that are built with the matrix square root of the covariance matrix of the state. Assume the following n-state discrete-time non-linear system x with measurement equation

z [123]:

$$
\begin{aligned}
x_{k+1} &= f(x_k) + w_k, \\
z_k &= h(x_k) + v_k, \\
w_k &\sim (0, Q_k), \\
v_k &\sim (0, R_k)
\end{aligned}
$$

where f is a non-linear state transition function from discrete time k to $k+1$, and w and v are respectively the process and measurement noise. The individual steps of the UKF are shown in Algorithm 1. W_n^i and W_c^i are weights that determines the spread and the distribution of the sigma points around the mean state value, while c is a scaling factor based on the size of the state.

Algorithm 1 The Unscented Kalman Filter

Initialize:

$\hat{x}_0 = \mathbb{E}[x_0]$

$P_0 = \mathbb{E}[(x_0 - \hat{x}_0) \cdot (x_0 - \hat{x}_0)^T]$

for Each measurement z_k at epoch $k = 1, \ldots, t_f$ **do**

Calculate sigma points and the associated predicted measurements:

$\hat{x}^{(0)}_{k|k-1} = \hat{x}_{k|k-1}$

$\Delta x^{(i)} = (\sqrt{cP_{k|k-1}})_i$ for $i = 1, \ldots, n$

$\Delta x^{(n+i)} = -(\sqrt{cP_{k|k-1}})_i$ for $i = 1, \ldots, n$

$\hat{x}^{(i)}_{k|k-1} = \hat{x}_{k|k-1} + \Delta x^{(i)}$ for $i = 1, \ldots, 2n$

$\hat{z}^{(i)}_{k|k-1} = h(\hat{x}^{(i)}_{k|k-1})$ for $i = 1, \ldots, 2n$

Combine the predicted measurements of each sigma point to obtain the mean predicted measurement at time k:

$\hat{z}_k = \sum_{i=0}^{2n} W_n^{(i)} \hat{y}^i_{k|k-1}$

Estimate the covariance of the predicted measurement:

$P_{zz} = \sum_{i=0}^{2n} W_c^{(i)} (\hat{z}^{(i)}_{k|k-1} - \hat{z}_k) \cdot (\hat{z}^{(i)}_{k|k-1} - \hat{z}_k)^T + R_k$

Estimate the cross-covariance:

$P_{xz} = \sum_{i=0}^{2n} W_c^{(i)} (\hat{x}^{(i)}_{k|k-1} - \hat{x}_{k|k-1}) \cdot (\hat{z}^{(i)}_{k|k-1} - \hat{z}_k)^T$

Update Step:

$K_k = P_{xz} P_{zz}^{-1}$

$\hat{x}_{k|k} = \hat{x}_{k|k-1} + K(z_k - \hat{z_k})$

$P_{k|k} = P_{k|k-1} - K_k P_{zz} K_k^T$

Prediction Step:

Calculate the sigma points and propagate with function f:

$\hat{x}^{(i)}_{k|k+1} = f(\hat{x}^{(i)}_{k|k})$

Combine the predicted state for each sigma point to compute the mean predicted state at epoch $k+1$:

$\hat{x}_{k+1|k} = \sum_{i=0}^{2n} W_n^{(i)} \hat{x}^i_{k+1|k}$

Compute the covariance of the predicted state at epoch $k+1$:

$P_{k+1|k} = \sum_{i=0}^{2n} W_c^{(i)} (\hat{x}^{(i)}_{k+1|k} - \hat{x}_{k+1|k}) \cdot (\hat{x}^{(i)}_{k+1|k} - \hat{x}_{k+1|k})^T + Q_k$

end for

3.3.5.1 Dynamics and measurement equations

There are various options in terms of modelling the dynamics of the spacecraft. The main forces acting on the spacecraft are the gravitational forces from both Didymos and Dimorphos, the solar radiation pressure (SRP), and the third body gravitation of the Sun. To reduce the computational complexity, the main forces considered in this work are the gravitational attraction of the two bodies of the binary system, as shown in Eq. 3.7, where the subscripts D and d refer to Didymos and Dimorphos respectively. At the distance of the DCP, it was found that for accurate modelling the point mass model is sufficient [38]. The maneuvers to change the arcs of the DCP are not added into the dynamics, as the measurements are expected to capture these as well.

$$\boldsymbol{f} = -\frac{\mu_D \boldsymbol{r_D}}{r_D^3} - \frac{\mu_d \boldsymbol{r_d}}{r_d^3} \tag{3.7}$$

The equations of motion of the spacecraft in the TB reference frame is given as follows.

$$\ddot{\boldsymbol{r_H}} = \frac{-\mu_D \boldsymbol{r_H}}{\boldsymbol{r_H^3}} + \mu_d \left(\frac{-\boldsymbol{r_{Hd}}}{\boldsymbol{r_{Hd}^3}} - \frac{\boldsymbol{r_d}}{\boldsymbol{r_d^3}} \right) \tag{3.8}$$

where $\boldsymbol{r_H}$, $\boldsymbol{r_{Hd}}$ and $\boldsymbol{r_d}$ denote respectively the position vector of the spacecraft with respect to Didymos, the position vector of the spacecraft with respect to Dimorphos, and the position vector of Dimorphos with respect to Didymos, while μ_D and μ_d are the standard gravitational parameters of Didymos and Dimorphos.

The measurement equation correlated with the centroids' estimations is given by the pinhole camera model, which relates the three coordinates of the position x_{COM} of the COM in the TB with its two projected coordinates z_{COM} on the image plane, as shown in Eq. 3.9 [106].

$$z_{COM} = K[A|t]x_{COM} \tag{3.9}$$

where K is the calibration matrix that depends on the intrinsic properties of the AFC and A and t are respectively the rotation matrix and the translation vector from TB to the camera reference frame. The rotation matrix A at each point in time is assumed

to be given by the on-board attitude determination system.

The range measurement equation is the norm of the spacecraft position vector given in Eq. 3.10.

$$z_\rho = \sqrt{x^2 + y^2 + z^2} \tag{3.10}$$

Eq. 3.9 and Eq. 3.10 show that both measurements involve the position estimation, which means that the velocity estimation is provided just by the dynamic equation given by Eq. 3.7. It can also be seen that in the camera reference frame Eq. 3.9 affects the X and Y coordinates of the position estimation while Eq. 3.10 affects the Z coordinate.

3.4 Results

In this section, the results of the visual based navigation algorithm for the relative state estimation of Hera with respect to Didymos during the DCP trajectory are presented. The performances of the IP on estimating the position of COM_{Did} and COM_{Dim} are presented with the absolute error with respect to the GT value, using the metric defined in Eq. 3.11. This metric is applied to both $i-$ and $j-$ directions of the PANGU viewer. The analysis is conducted only for the absolute error, as the presence of potential systematic error and biases towards positive or negative values of the centroiding estimation error has already been analyzed in [80].

$$\epsilon_{COM} = |COM_{GT} - COM_{est}| \tag{3.11}$$

These results are compared with the ones shown in Table 3.5, presented in [80] and obtained applying the same CNN-based IP algorithm on 6052 images generated with PANGU during the ECP trajectory and showing the shape models of Didymos and Dimorphos prior to DART's close encounter. The results shown in Table 3.5 comply with pointing accuracy requirements of the mission [58].

Fig. 3.13 shows two sample images of Dataset 2 processed by the HRNet for the 26 keypoints regression.

The accuracy on estimating the spacecraft's range from the primary is assessed

Table 3.5: Centroiding results on old shape models of Didymos and Dimorphos [80]

Image axis	ϵ_{COM} **Didymos** $[px]$	ϵ_{COM} **Dimorphos** $[px]$
i-direction	5.35	11.05
j-direction	4.41	7.17

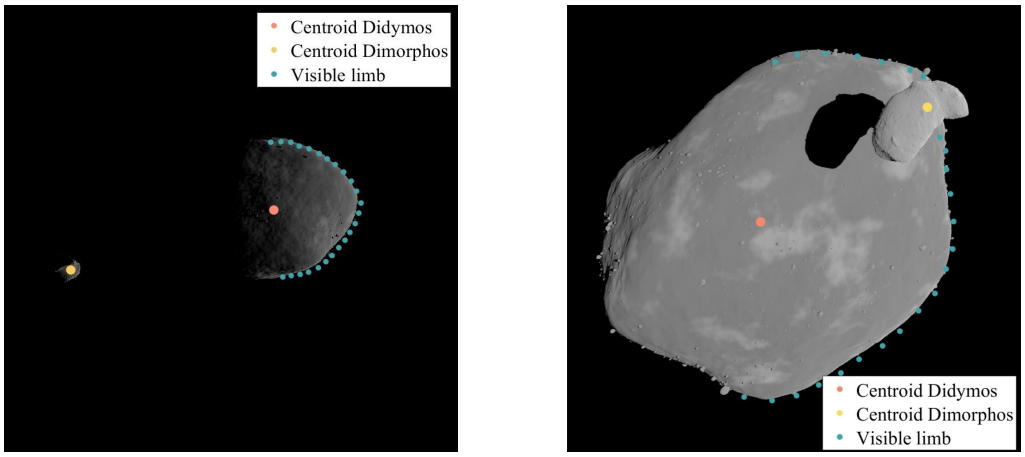

Figure 3.13: Two sample images of Dataset 2 with the estimated keypoints

through the APE with respect to the GT value. The Hera mission requires that the MAPE on the range estimation is lower than 10% along the trajectory [40]. For the ECP, the MAPE obtained by the IP algorithm developed in this work is 2.1385%, thus satisfying the mission requirements. Finally, the results of the navigation filter on the estimated state of the DCP are presented.

The trained model is run with Matlab on the NVIDIA GeForce RTX 2070 with Max Q-design GPU of the local machine. The average computational time required for processing a single image from the IP block is 2.4828 s with a standard deviation of 0.21 s. On an on-board spacecraft-like CPU processor such as the Zynq 7000 System-on-a-Chip, the average computational time is 165 s with a standard deviation of 0.15 s. On a CPU processor with higher performances such as the LEON3 on-board the Hera spacecraft, half the computational time to process a single image is expected.

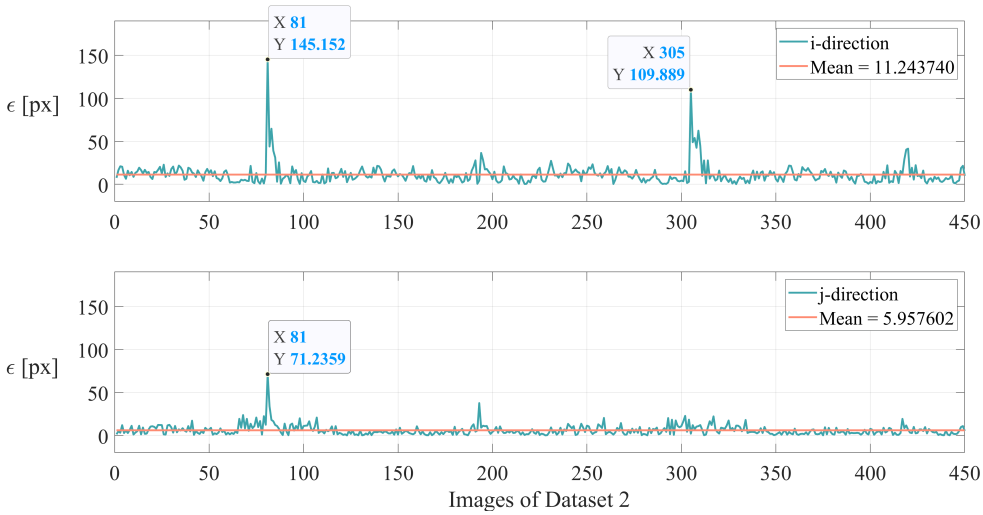

Figure 3.14: ϵ_{COM} for Didymos during DCP

3.4.1 Centroiding Didymos

Fig. 3.14 illustrates the results of the centroiding of Didymos for the DCP testing dataset of 450 images. It is possible to see that the absolute error fluctuates around 11.24 px in the $i-$direction and around 5.95 px in the $j-$direction, with a standard deviation of $\sigma_i = 11.63$ px and $\sigma_j = 6.01$ px. The error is greater in comparison to the old results shown in Table 3.5. This is due to the fact that, during the DCP, the distance from Didymos is reduced, resulting in a larger projection of Didymos on the images. This is also shown by looking at Fig. 3.14 and Fig. 3.5: the two peaks of the error on the $i-$direction and on the $j-$ direction of ϵ_{COM} correspond to two local minima of the range.

3.4.2 Flag Dimorphos

The performance of the IP block on the detection of Dimorphos in the images is assessed with the confusion matrix shown in Table 3.6. It is defined as positive class if Dimorphos is visible in the image and as negative class viceversa.

where TP, TN, FP and FN stand respectively for True Positive, True Negative, False Positive and False Negative. The confusion matrix allows to calculate the metrics to evaluate the performance of Dimorphos' recognition in the images:

Table 3.6: Confusion matrix detection Dimorphos

	Actual Positive = 276	**Actual Negative** = 174
Predicted positive = 247	$TP = 246$	$FP = 1$
Predicted negative = 203	$FN = 29$	$TN = 174$

- ❖ Accuracy (A): Overall accuracy of the algorithm;
- ❖ Precision (P): Out of all the predicted positive, what percentage is truly positive;
- ❖ Recall (R): Out of the all actual positive, what percentage is truly positive.

The results obtained are shown in Eq. 3.12, Eq. 3.13 and Eq. 3.14.

$$A = \frac{TP + TN}{TP + FP + TN + FN} = 93.3\% \tag{3.12}$$

$$P = \frac{TP}{TP + FP} = 99.6\% \tag{3.13}$$

$$R = \frac{TP}{TP + FN} = 89.4\% \tag{3.14}$$

The IP block is capable to identify the presence of Dimorphos with high accuracy and precision but with a medium-high recall. By lowering the cut-off value of the peak intensity of the heatmap generated by the HRNet in the regression of the COM of Dimorphos it is possible to minimize the FN and improve the recall. Neverthelesss, this might increase the FP that is important to minimize in order to limit the number of false measurements input to the navigation filter.

3.4.3 Centroiding Dimorphos

Fig. 3.15 illustrates the performance of the IP in estimating the position of the centroid of Dimorphos for the DCP testing subset of 247 images where Dimorphos is considered as visible by the IP. It is possible to see that the absolute error fluctuates around 17.04 px in the $i-$direction and around 7.8 px in the $j-$direction, with a standard deviation of $\sigma_i = 31.64\ px$ and $\sigma_j = 7.42\ px$. The peak of the absolute error is obtained because it represents the sole FP detected by the algorithm leading to a higher average error

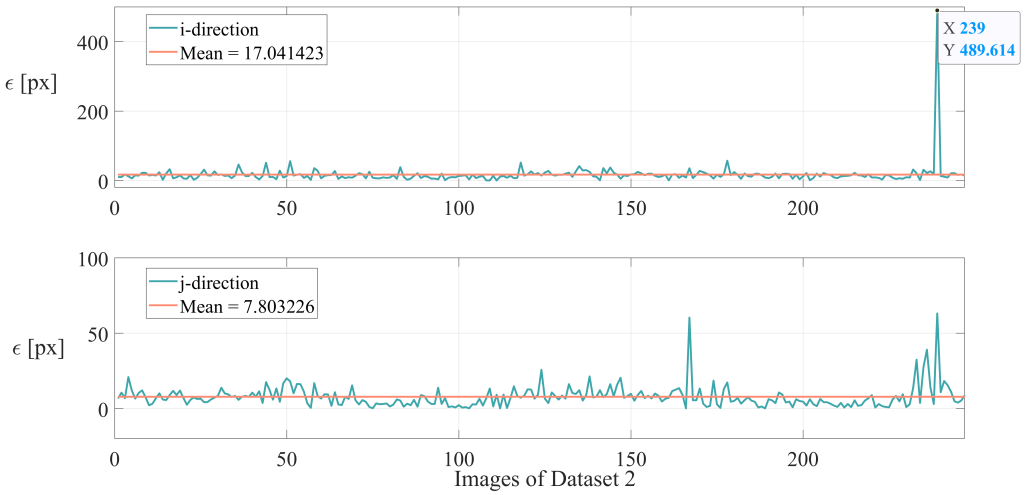

Figure 3.15: ϵ_{COM} for Dimorphos during DCP

compared to the old results shown in Table 3.5.

3.4.4 Range

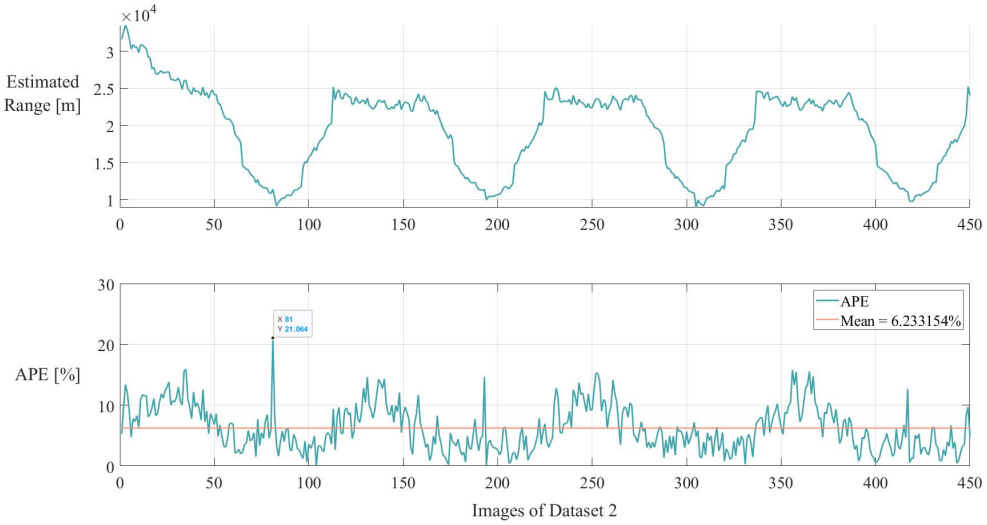

Figure 3.16: Estimated range During DCP

Fig. 3.16 shows the estimated range attained by the IP algorithm for the DCP testing dataset. The estimation is following its GT value illustrated in Fig. 3.5, with an APE that oscillates around a mean value of 6.23%. The error is higher compared to

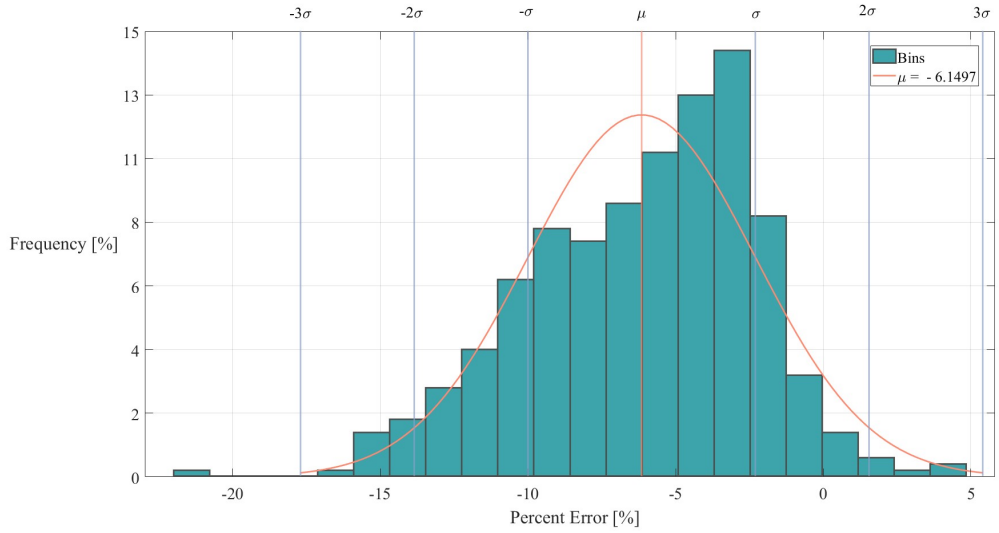

Figure 3.17: Estimated range percent error distribution during DCP

the one obtained with the ECP because of the lower range of the DCP trajectory and because of the less-spherical shape of Didymos used in this work. The APE is inversely proportional to the range, due to the fact that the projected image of Didymos is bigger for lower ranges. As a result, the ellipsoidal shape takes on a more prominent role, and the accuracy of approximating it as a sphere diminishes. In particular it can be seen that the peak of the APE is obtained for the same image where the ϵ_{COM} reached its peak (Fig. 3.14), which means that the calculated relative average distance in pixel (n_R) is inaccurate, leading to an imprecise calculation of the estimated range (Eq. 3.9). Nevertheless, the accuracy on the range estimation complies with the Hera mission requirements (APE $< 10\%$) [40].

Fig. 3.17 shows the distribution of the percent error of the estimated range obtained by the IP algorithm. The mean value is $\mu = -6.14\%$ and the standard deviation is $\sigma = 3.85\%$ which means that 68.27% of the percent error value is located between -10% and -2.29%. Ultimately, the range estimations are accurate and can be used for navigation purposes.

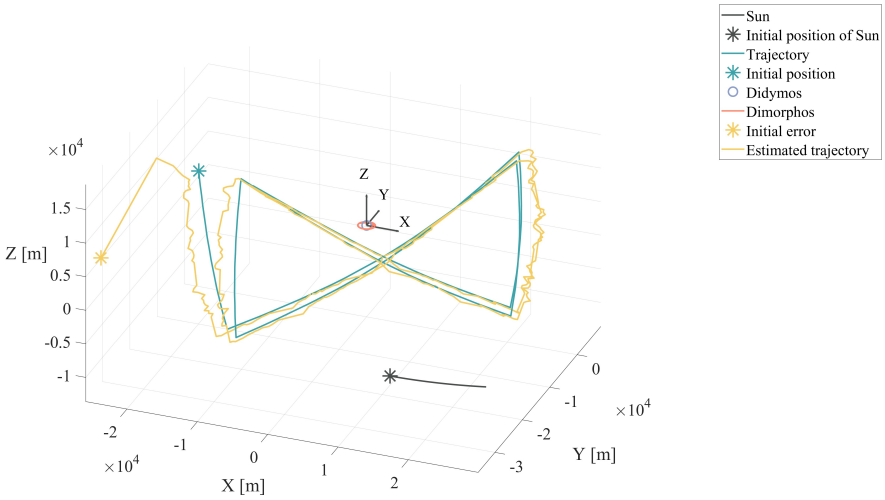

Figure 3.18: Estimated trajectory vs Real trajectory

3.4.5 Estimated State

An error of 10 km and 0.1 m/s is introduced into each coordinate of the initial estimate of the position and velocity of the spacecraft. These errors are chosen because they are relatively high compared to the ground truth state. This allows to analyze the capacity of the measurements in correcting the estimated trajectory even in the worst navigation scenario. The complete settings of the UKF parameters are given in Table 3.7. The estimated trajectory resulting from the navigation filter is shown in Fig. 3.18, and the errors in the estimated position are shown in Fig. 3.19 in the TB reference frame and in Fig. 3.20 in the camera reference frame. Since the focus of this study is to estimate the position with centroid and range measurements, and there is no velocity measurement available, the velocity estimate is not shown since it is not affected.

Fig. 3.19 shows that initial error of 10 km in the estimated position quickly decreases after incorporating the first measurement for all the three coordinates. It can be seen that the unmodelled maneuvers connecting each arc to the other does not affect the position error, which stays lower than 5 km for the whole trajectory. The appearances of local peaks are due to the fact that the attitude used in Eq. 3.9 presents some singularities given the particular relative geometry of the spacecraft/Sun/Didymos. This is shown more clearly in Fig. 3.20, where the peaks are mainly present only for

the X and Y coordinates of the position estimation in the camera frame, which are the ones affected by the attitude. Therefore, a different relative geometry of the spacecraft with respect to the target would have a large impact on the general accuracy of the navigation system. Nevertheless, the developed navigation filter trained for the ECP is still able to perform well in a new environment and to generalize its solution.

Table 3.7: Unscented Kalman Filter variables

Variable	**Symbol**	**Value**
Initial True State	x_i	$(-1.58e4\ [m],\ -2.05e04\ [m],\ 1.5e04\ [m],\ 0.0032\ [m/s],\ 0.0138\ [m/s],\ -0.1023\ [m/s])$
Initial error in position	err_p	(10, 10, 10) $[km]$
Initial error in velocity	err_v	(0.1, 0.1, 0.1) $[m/s]$
Initial covariance matrix of the state	P	$(1000^2\ [m],\ 1000^2\ [m^2],\ 1000^2\ [m^2],\ 0.1^2\ [m^2/s^2],\ 0.1^2\ [m^2/s^2],\ 0.1^2\ [m^2/s]^2)$
Covariance matrix of the process	Q	$(1000^2\ [m^2],\ 1000^2\ [m^2],\ 1000^2\ [m^2],\ 0.01^2\ [m^2/s^2],\ 0.01^2\ [m^2/s^2],\ 0.01^2\ [m^2/s^2])$
Covariance matrix of the measurements	R	Given by the IP block

3.5 Conclusion

In this work, an autonomous visual based navigation technique with a Convolutional Neural Network (CNN)-based Image Processing (IP) algorithm is developed for the Detailed Characterization Phase (DCP) proximity operation of the Hera mission around the target binary asteroid system Didymos. The selected CNN architecture for this work is the High Resolution Network (HRNet). The algorithm is trained with synthetic images generated with Planet and Asteroid Natural scene Generation Utility (PANGU) with the previous phase of the mission i.e. the Early Characterization Phase (ECP). The shape models of Didymos and Dimorphos are updated with data collected

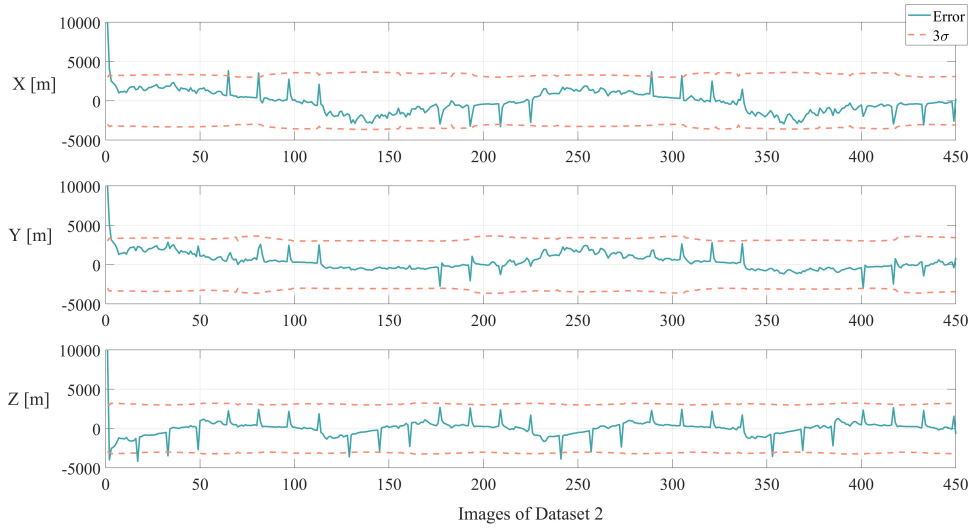

Figure 3.19: Error Estimated position for Dataset 2 in the TB reference frame

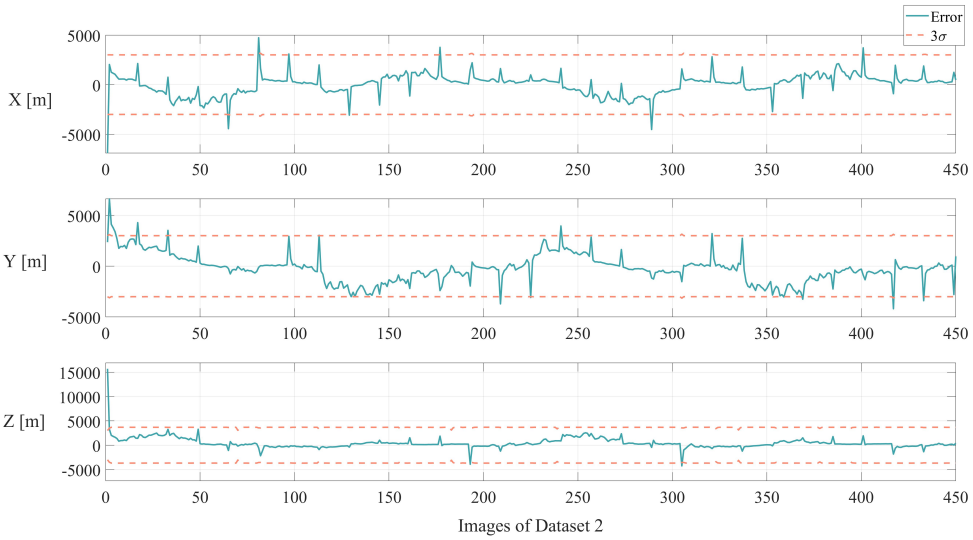

Figure 3.20: Error Estimated position for Dataset 2 in the camera reference frame

by the Double Asteroid Redirection Test (DART) mission. The algorithm estimates the position of the centroid of Didymos and Dimorphos (if available), the range from Didymos and the associated covariances. The covariance associated with the range estimation is selected using the results obtained with the training process. The covariance associated with the centroids' estimation is calculated using the heatmaps generated by the HRNet. The measurements are then combined with the dynamical environment

using a Unscented Kalman Filter (UKF) for the relative position estimation of the spacecraft.

The results shows that the IP algorithm solves the centroiding of Didymos and Dimorphos with high accuracy independently from the ellipsoidal shape. In particular the algorithm is able to identify whether Dimorphos is visible or not with high accuracy, precision and recall as shown from the confusion matrix represented in Table 3.6, which is a novelty of this work. The second main novelty is that the position of the centroid of Dimorphos is used by the UKF for the estimation of the state when available. The methodology to estimate the range is robust to the ellipsoidal shape of Didymos, with an error higher than the one obtained in [80] where the shape model of Didymos was more spherical. Nevertheless, the Absolute Percent Error (APE) is lower than 10%, meeting the Hera mission requirements. The UKF is able to estimate the state of the spacecraft accurately. The source of the largest error are from the centroid estimation, which relies on the attitude of the camera reference frame even when it is singular.

The developed pipeline in this work enhances the robustness and autonomy of the navigation strategy for the Hera mission. Specifically, this work shows that it is possible to navigate around a binary asteroid system using only optical measurements. If higher accuracy for the state estimation is required, thermal or Light Detecting And Ranging (LIDAR) measurements can be used. It is important to point out that if the actual shape of Didymos and Dimorphos is not the same one used in this work, an offline fine-tuning of the HRNet with a subset of images taken during the ECP is necessary to estimate the position of the centroids and the range from Didymos.

Chapter 4

Robustness analysis of data-driven Image Processing algorithms applied to Didymos' system

> The stars don't look bigger, but they do look brighter
>
> *Sally Ride*

Kaluthantrige A., Pugliatti, M.[‡], Feng, J.[§], Topputo, F.[¶] and Gil-Fernández, J.[||]

Published *Journal of Spacecraft and Rockets*, July 2025

[‡]PostDoc fellow, Colorado Center for Astrodynamics Research, University of Colorado Boulder

[§]Associate professor, Department of Mechanical and Aerospace Engineering, University of Strathclyde

[¶]Full professor, Department of Aerospace Science and Technology, Politecnico di Milano

[||]Guidance, Navigation and Control Engineer, ESA ESTEC

Paper content

This chapter analyzes the algorithm developed in Chapter 2 and a architecturally less complicated one, showing how two artificial intelligence-based image-processing methods perform under realistic conditions for Hera's proximity operations. It reveals that architectural complexity enhances robustness, while careful fine-tuning boosts mission-specific accuracy, outlining key trade-offs between adaptability, precision, and generalization. Following the map and structure shown in Fig. 1.8 in Section 1.3.3, this chapter addresses RQ 2a and achieves the objective of bridging gaps between the training and target domains stated in RO 2. With this chapter, the reader will understand the level of robustness of data-driven image processing algorithms can achieve under practically relevant contingency scenarios, the performance trade-offs between architectural complexity, accuracy, and adaptability and how fine-tuning shapes algorithm resilience in both specific and generalized mission contexts.

Abstract

Space proximity operations around asteroids demand precise relative navigation and high dynamic response achieved with the on-board implementation of autonomous visual based navigation systems, which comprise of image processing algorithms that extract information from images taken by on-board cameras. This work presents a series of functional tests of two data-driven image processing algorithms based on two different convolutional neural networks architectures and designed for the application to the European Space Agency's Hera mission with the target of binary asteroid system (65803) Didymos. The two data-driven methods estimate the position of the centroid of Didymos and its range from the spacecraft. Through different image datasets and comparative analyses, this work evaluates the two algorithms' performance under conditions of adverse illumination conditions, different shape of the target asteroid and different noise levels of the images, addressing questions on performance deviations, architectural discrepancies, and fine-tuning requirements upon encountering real-world scenarios. The analyses indicate that algorithms with more sophisticated and complex architectures exhibit greater robustness across various contingencies, despite being less accurate in their estimations. Furthermore, the results show that fine-tuning datasets improve the performances of the algorithms in the specific mission scenario they are generated, while reducing the performances in other circumstances.

4.1 Introduction

Space rendezvous operations require high levels of accuracy in terms of relative navigation. When the target does not actively assist in the rendezvous process, with a highly uncertain dynamical environment and with a large distance from the Earth, spacecraft are equipped with an Autonomous Visual Based Navigation (AVBN) system, which provides a precise visualization of the surrounding environment and a navigation system with a high dynamic response to the unknown settings. As such, the design, implementation and testing of an AVBN system is a crucial step in the development of a space rendezvous mission. The AVBN system is integrated with the Guidance, Navi-

gation and Control (GNC) algorithm implemented on the On-Board Computer (OBC) of the spacecraft. The end goal is to have the spacecraft able to estimate autonomously its relative position and/or attitude with respect to the target, and perform maneuvers (ground-based or calculated on board) to operate safely around the target [124–126]. An AVBN system of a space rendezvous mission usually consists of the following three main components [64, 119]:

- An optical sensor that may represent the payload of the spacecraft and that acquires images of the target body. The same sensor can be used both for scientific and navigation purposes;
- An Image Processing (IP) algorithm that analyses the acquired image and measures pre-defined quantities that gives information on the mission scenario. These may include the range from the target, the relative orientation of the spacecraft with respect to the stellar background, the position of relevant features on the target's surface, etc.;
- A navigation filter that combines the outputs of the IP algorithm with the dynamical environment and provides the best estimate of the relative state of the spacecraft with respect to the target.

In this work we focus on the IP algorithm of an AVBN system. The Design, Development, Validation and Verification (DDVV) strategy for the IP algorithm is incremental and it is based on a chain of different tests that aim to analyze the robustness of the algorithm against potential contingencies [58, 127]. The main tests that are part of a standard DDVV strategy are:

1. **Functional Tests (FT)**: the IP algorithm is tested with synthetic images generated with rendering engines that represent the mission scenario; these images include information on the target, illumination conditions considering the Sun-spacecraft-target relative geometry, relative pose of the spacecraft with respect to the target, and other additional parameters (background noise, distortions etc...). The aim of these tests is to prove that the IP algorithm can provide the

required measurements with a level of accuracy high enough for the navigation filter to estimate the spacecraft's state. Additional objectives of these tests are the robustness over external disturbances and noise/distortions of the image. For this purpose, rendering software such as the Planet and Asteroid Natural Scene Generation Utility (PANGU), SurRender, and Blender-based software such as CORTO and SISPO can be used [128–132].

2. **Model-In-The-Loop (MIL) tests**: the IP algorithm is integrated to the Functional Engineering Simulator (FES) of the GNC prototype of the spacecraft. The FES is a SW environment that includes reference models of the selected GNC solutions and algorithms defined specifically for the mission, and it allows us to test the validity of the designed GNC at a SW level. The aim of the MIL is to test the interfaces of the IP algorithm with the rest of the GNC models, and more in general that the GNC algorithm is robust to the measurements provided by the IP.

3. **Software-In-The-Loop (SIL) tests**: the GNC algorithm with the embedded IP algorithm is exported to the final programming language that will be used on the OBC of the spacecraft. The aim of the SIL tests is to verify the correctness of the SW implementation with respect to the FES and to test the interfaces with all the other on-board SW.

4. **Processor-In-The-Loop (PIL) tests**: the validated SW from the previous step is implemented on the qualified processor of the spacecraft. These tests are aimed to profile the different algorithms of the SW and to check the performances in terms of computational time and on-board memory requirements. This test allows us to tackle the issue of the HW implementation.

5. **Hardware-In-The-Loop (HIL) tests**: in these tests a representative GNC sensor/actuator is included in the loop, for an AVBN usually being the Functional Model (FUMO) of the camera designed for the mission. The aim of the HIL is to test the robustness of the embedded IP algorithm to the noise, errors and any other electro-optical effect introduced by the camera. This test is usually executed

using optical testbenches projecting the scenery on high-resolution screens or in a robotic facility using 3D-printed mock-up of the target body [133–141].

This work presents a series of FTs of two data-driven-based IP algorithms developed by the authors and presented in [81, 142]. The aim of this work is to validate the functionality and test the robustness of the developed algorithms to multiple mission scenarios and contingencies that are typical of a space rendezvous mission.

In particular, the case study of this work is the European Space Agency (ESA)'s Hera mission during the proximity operations around the target binary asteroid system (65803) Didymos, which consists in a primary body, Didymos, and a secondary body, its moon Dimorphos [36]. The mission is a planetary defense and asteroid exploration mission, key component of a broader international effort to develop asteroid deflection techniques. Hera's primary objective is to analyze the aftermath of NASA's DART (Double Asteroid Redirection Test) impact on Dimorphos, which successfully altered the moonlet's orbit in September 2022. By doing so, Hera will provide critical data on the effectiveness of the kinetic impactor technique as a method of planetary defense. The mission will also gather extensive scientific data on the Didymos system's composition, structure, and dynamics, contributing to our understanding of near-Earth asteroids. Hera was launched in October 2024 and it will arrive at the Didymos system in late 2026. It is equipped with cameras, LIDAR (Light Detection and Ranging) for topographic mapping, and a thermal infrared imager. Additionally, Hera carries two small cubesats, Milani and Juventas, which will perform specialized tasks, such as subsurface radar studies and measuring local magnetic fields. Hera also aims to demonstrate advanced autonomous navigation technologies, which are essential for future deep-space missions [36]. During the first phases of the proximity operations the navigation is an AVBN system that relies on an IP algorithm that estimates the position of the Center of Mass (COM) of the primary body from the images captured by the on-board camera. The latter's boresight is oriented towards the primary body, and the AVBN uses the IP algorithm's measurement to maintain the orientation of the spacecraft in this configuration. Periodically, the spacecraft is ground-controlled to re-orient itself towards the Earth and transmit telemetry and payload data. This re-

quires aligning the spacecraft's high-gain antenna toward Earth during communication windows. In order to estimate the relative position of the spacecraft with respect to the target, the COM measurements are combined with range measurements from the primary retrieved by the on-board LIDAR system [58, 114].

The application of data-driven methods to the IP algorithm in asteroid rendezvous missions is driven by the possibility to overcome challenges represented by adverse illumination conditions, irregular shape of the target, background noise or the presence of other bodies such as stars or moons that are usually affecting the performances of standard IP algorithms. For instance, edge detection algorithms may falsely identify cosmic rays and sensor noise captured in the image as edges. Feature matching algorithms may fail if the lightning conditions and asteroid viewing angles are different from the ones used for on-ground validation [94, 143]. Recent trends in data-driven based IP algorithms are exploring the use of Artificial Intelligence (AI), particularly deep learning, to address these challenges and bypass traditional techniques. Their utilization in space IP and navigation is becoming more and more relevant given their capability of learning complex features from the provided data [69, 75, 81, 82, 85, 144–147]. The two data-driven methods analyzed in this work are based on Convolutional Neural Networks (CNNs) with different architectures, number of parameters and with a different set of outputs.

Nevertheless, AI-based methods are not yet in general validated for critical functions of space missions. This is mainly due to the lack of complete mathematical methods to cope with the "reality gap" that separates simulated data with real data. Thus, it remains uncertain how unforeseen changes during the data acquisition process will impact the outcome of AI-based methods. For instance, input data could be blurred, suffer from under/overexposure or contain some noise sources. Therefore, it is important to assess the robustness of AI-based methods against input data alterations [148]. Most of the robustness analysis of AI techniques have been applied considering as inputs adversarial examples [148,149] and quality distorted data [150,151]. With the FTs presented in this work, we analyze the performance of the two data-driven methods applied to the IP algorithm of the Hera mission when estimating the position of the COM of Didymos

and the range from it, using images representing conditions never encountered during training. In particular, the FTs aim to provide answers to the following research questions: 1) What degree of deviations from design conditions can CNN approaches endure in terms of performance drop? 2) Are there fundamental discrepancies in terms of performance between different architectures? 3) Once Hera arrives at the Didymos system, how many images would be required to fine-tune the data-driven IP algorithms to ensure optimal performances? The first question is assessed by developing a series of challenging datasets that assess network performance with unseen conditions (with respect to training) such as high Sun phase angles (Sun-asteroid-spacecraft), different noise levels in the images, and different shape models of the target asteroid system. The second is addressed by performing the analysis with two different convolutional approaches. The third is assessed by performing a series of fine-tuning episodes with incremental dataset sizes. This emulates a possible operational scenario applicable to any data-driven method applied to a space mission, which would require a small subset of images from the real system to be fine-tuned.

While the Hera mission GNC algorithm implemented on the OBC of the spacecraft is going to use the Maximum Correlation with a Lambertian Sphere (MCLS) IP algorithm [127, 152], the FTs carried out in this work represent a fundamental validation step toward the applicability of data-driven methods in the AVBN of asteroid rendezvous missions.

This paper is structured as follows. Section 4.2 describes in detail the data-driven methods, the case study and the FTs carried in this work. Section 4.3 shows the obtained results and discusses the applicability of the developed methods to the Hera mission. Finally, Section 4.4 concludes this work.

4.2 Methodology

This section describes the methodology applied in this work to validate through FTs the data-driven methods developed by the authors. Firstly, the case study is presented, in Section 4.2.1. Then the data-driven methods are described in Section 4.2.2. The first data-driven method relies on a CNN-based architecture called High Resolution

Network (HRNet), developed in [142] and it is briefly outlined in Section 4.2.2.1. The second data-driven method relies on an architecture applied to the AVBN system of Milani, one of the CubeSats of the Hera mission [38, 153]. It is developed in [81] and it is introduced in Section 4.2.2.2 . We refer to the first data-driven method as M1 and to the second as M2. Finally, the FTs with their objectives and the datasets used are detailed in Section 4.2.4. To facilitate the discussion, we refer to Didymos as B1 and to Dimorphos as B2. The geometrical center of B1 is considered its COM for simplicity.

4.2.1 Case Study

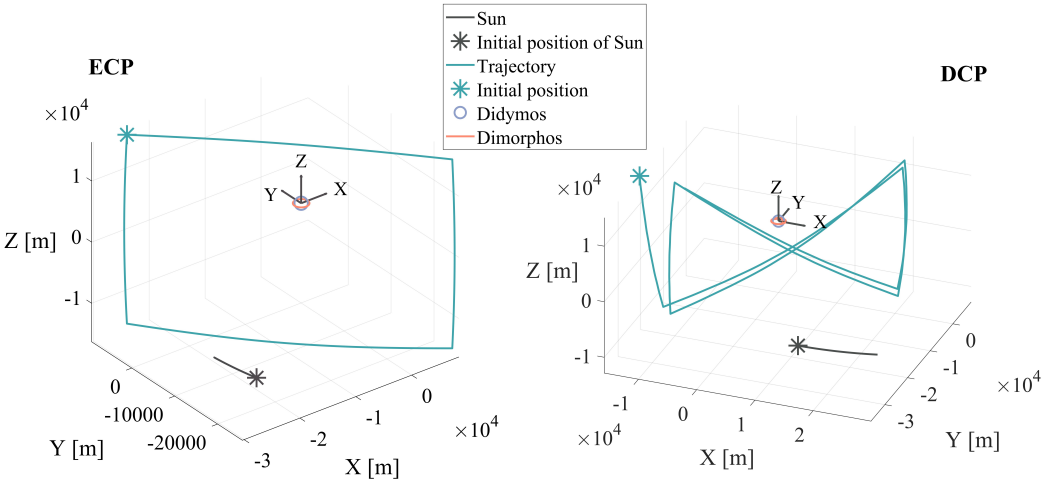

Figure 4.1: ECP and DCP trajectories

The proximity operations of the Hera mission around the target binary asteroid system Didymos represent the case study of this work. Hera serves as Europe's contribution to the Asteroid Impact and Deflection Assessment (AIDA) international collaboration with NASA. AIDA aims to demonstrate asteroid deflection using NASA's kinetic impactor Double Asteroid Redirection Test (DART) spacecraft, which achieved successfully its objective on September 26, 2022, by colliding with. Hera will rendezvous with the target asteroid in early 2027 to study its physical and dynamic properties, including the impact crater and the momentum transfer efficiency [34, 98, 153]. The current knowledge on the shapes of B1 and B2 is provided by DART's latest obser-

vations, which indicates that they are two oblate ellipsoids with the extent along the principal axes and the respective uncertainties given in Table 4.1 [28, 29]. The table shows the data retrieved by DART prior to the impact, as the shape resulted from the collision will be only resolved once the Hera spacecraft reaches the asteroid [154]. The

Table 4.1: Shapes of B1 and B2 prior to DART's impact [28, 29]

Parameter	**B1**	**B2**
Extent along principal axis x $[m]$	849 ± 5.6	177 ± 1.2
Extent along principal axis y $[m]$	851 ± 5.6	174 ± 1.2
Extent along principal axis z $[m]$	620 ± 5.6	116 ± 1.2

properties of the Hera on-board Asteroid Framing Camera (AFC) shown in Table 4.2 are used for the generation of the images [103, 104].

Table 4.2: AFC properties [103, 104]

Horizontal FOV	**Focal length**: f	**Aperture diameter**	**Image size**	**Pixel size**: ν
$5.5°$	$10.6\ cm$	$2.5\ cm$	$1024 \times 1024\ px$	$10\ \mu m$

The images of the FTs are generated with the aim to prove the robustness of the algorithm in different scenarios, including two specific phases of the proximity operations, the Early Characterization Phase (ECP) and the subsequent Detailed Characterization Phase (DCP), shown in Fig. 4.1 (courtesy of ESA). The two trajectories are represented in the Target Body reference frame (TB), which uses B1's COM as origin, the x-axis parallel to the one of the Earth-centered inertial coordinate frame and the xy-plane coplanar to the orbit of B2. As aforementioned, the navigation in these first two proximity operations require the AFC always pointing towards the centroid of the primary body. During the ECP, the navigation and the attitude profile is ground based and images of the target are captured and downlinked to Earth in order to tune the onboard IP algorithm to optimize its performances. The range of the spacecraft from

B1 varies from $\sim 20\ km$ to $\sim 30\ km$ and the Sun phase angle ranges from $\sim 45°$ to $\sim 80°$. During the DCP, the navigation is fully autonomous and it relies on the tuned IP algorithm. The range of the spacecraft from B1 varies from $\sim 9\ km$ to $\sim 20\ km$ and the Sun phase angle ranges from $\sim 0°$ to $\sim 80°$ [40, 115]. The orbit of Dimorphos prior to DART's impact is considered as the orbital changes resulting from the collision are not affecting the FTs carried out in this work.

4.2.2 Data-driven methods

4.2.2.1 M1

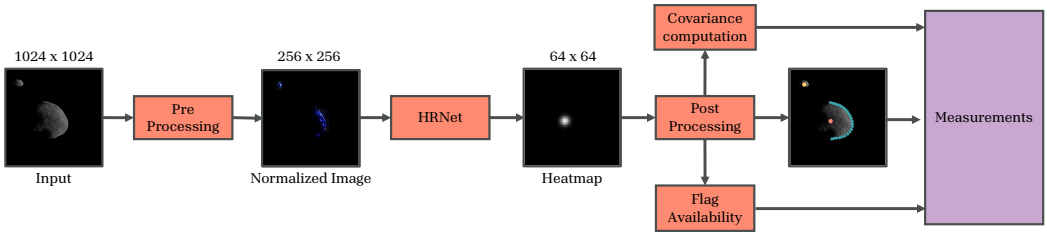

Figure 4.2: M1 data-driven method

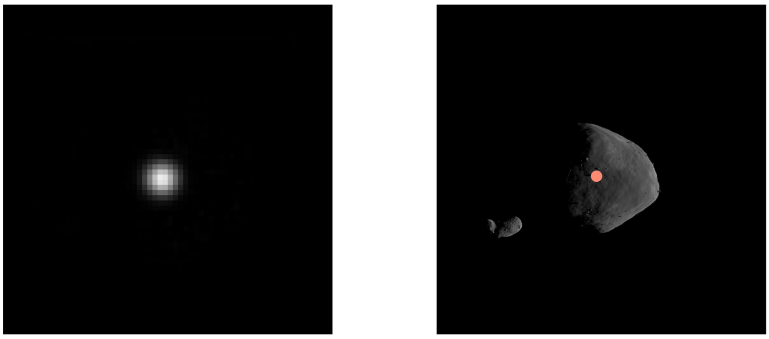

Figure 4.3: Heatmap associated to the estimation of the COM of B1

M1's pipeline is shown in Fig. 4.2 and it consists in the following blocks:

1. *Pre-Processing*: The input images are scaled down ($256 \times 256\ px$) and the magnitude of each pixel is normalized for the convergence of the HRNet;

2. *HRNet*: The HRNet block applies the HRNet to the input image in order to

regress the position of the COM of B1, the COM of B2, and 24 points on the illuminated border of B1 [107]. The output of the HRNet block is a set of 26 64×64 px heatmaps, each one associated with the regressed point [122]. The n-th heatmap manifests as a cluster of white pixels encircling the n-th predicted point, indicating the degree of accuracy in determining its position. The denser and more concentrated the heatmap, the more precise the estimation of the point's location. Refer to Fig. 4.3 for an illustration of a heatmap example, associated to the estimated position of the COM of B1.

3. *Post-Processing*: Each heatmap is denoised and analyzed to calculate the exact position of the desired point. A statistical population of pixels of the heatmap around the desired point is extracted. The 24 points on the illuminated border are used together with the COM of B1 to derive its range from the spacecraft geometrically, by approximating the shape of B1 to a sphere of diameter $D = 780$ m.

4. *Flag Availability*: If the pixels of a heatmap are less intense than a pre-defined threshold, the associated point is not given as an output and the corresponding measurement is not available.

5. *Covariance Computation*: If the pixels of the heatmap are more intense than the pre-defined threshold, the associated point is given as an output, the measurement is available and its covariance is derived by the magnitude and shape of the heatmap.

Further details about this algorithm can be found in [80, 142].

4.2.2.2 M2

M2's pipeline is shown in Fig. 4.4 while the CNN architecture is illustrated in Table 4.3 using TensorFlow 2.10 notation. The architecture's hyper-parameters are a result of a thorough search based on the use of extreme-learning machine methods and hierarchical grid search, an approach that can be found in [155].

Table 4.3: M2 Architecture, made of 3563907 parameters, all of which are trainable

Layer	**Type**	**Output Shape**	**Parameters**	**Connected to**
I	InputLayer	$B, 128, 128, 1$	0	-
C_{11}	Conv2D	$B, 128, 128, 16$	160	I
C_{12}	Conv2D	$B, 128, 128, 16$	160	I
C_{13}	Conv2D	$B, 128, 128, 16$	160	I
$CC1$	Concatenate	$B, 128, 128, 48$	0	C_{11}, C_{12}, C_{13}
$A1$	Activation	$B, 128, 128, 48$	0	$CC1$
$P1$	MaxPooling2D	$B, 64, 64, 48$	0	$A1$
C_{21}	Conv2D	$B, 64, 64, 32$	13856	$P1$
C_{22}	Conv2D	$B, 64, 64, 32$	13856	$P1$
C_{23}	Conv2D	$B, 64, 64, 32$	13856	$P1$
$CC2$	Concatenate	$B, 64, 64, 96$	0	C_{21}, C_{22}, C_{23}
$A2$	Activation	$B, 64, 64, 96$	0	$CC2$
$P2$	MaxPooling2D	$B, 32, 32, 96$	0	$A2$
C_{31}	Conv2D	$B, 32, 32, 64$	55360	$P2$
C_{32}	Conv2D	$B, 32, 32, 64$	55360	$P2$
C_{33}	Conv2D	$B, 32, 32, 64$	55360	$P2$
$CC3$	Concatenate	$B, 32, 32, 192$	0	C_{31}, C_{32}, C_{33}
$A3$	Activation	$B, 32, 32, 192$	0	$CC3$
$P3$	MaxPooling2D	$B, 16, 16, 192$	0	$A3$
C_{41}	Conv2D	$B, 16, 16, 128$	221312	$P3$
C_{42}	Conv2D	$B, 16, 16, 128$	221312	$P3$
C_{43}	Conv2D	$B, 16, 16, 128$	221312	$P3$
$CC4$	Concatenate	$B, 16, 16, 384$	0	C_{41}, C_{42}, C_{43}
$A4$	Activation	$B, 16, 16, 384$	0	$CC4$
$P4$	MaxPooling2D	$B, 8, 8, 384$	0	$A4$
C_{51}	Conv2D	$B, 8, 8, 256$	884992	$P4$
C_{52}	Conv2D	$B, 8, 8, 256$	884992	$P4$
C_{53}	Conv2D	$B, 8, 8, 256$	884992	$P4$
$CC5$	Concatenate	$B, 8, 8, 768$	0	C_{51}, C_{52}, C_{53}
$A5$	Activation	$B, 8, 8, 768$	0	$CC5$
$P5$	MaxPooling2D	$B, 4, 4, 768$	0	$A5$
$FC5$	Flatten	$B, 12288$	0	$P5$
DO	Dropout	$B, 12288$	0	$FC5$
D	Dense	$B, 3$	49156	DO

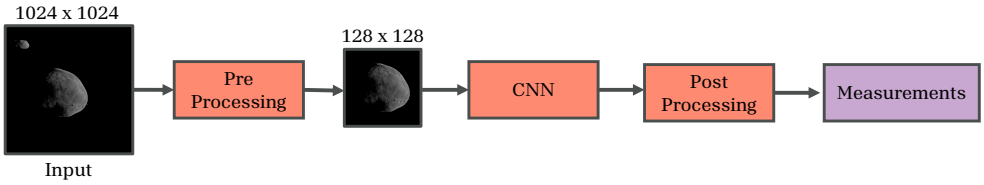

Figure 4.4: M2 data-driven method

The convolutional portion of the architecture is divided into 5 depth levels that make extensive use of dilated convolutions of 1, 2, and 3 rates (represented at each $i-th$ depth level by the C_{i1}, C_{i2}, and C_{i3} layers), concatenation, activation, and max-pooling layers. The head of the architecture is represented by a single dense output layer connected directly to the fully connected $FC5$ layer. Dropout is applied on this layer with a probability of 15%.

Differently from M1, M2 is an end-to-end architecture, since it generates an output vector consisting of B1 COM components, range from B1, and Sun phase angle. Moreover, M2 uses as input a cropped and/or resized version of the original 1024×1024 px image. Each image acquired by the camera, thus needs to be pre-processed outside the network before being considered as an input. During training, labels need to be modified accordingly to reflect the reduced input size.

While M1 uses resized 256×256 px images from the original 1024×1024 px, M2 needs a more elaborate image-label preprocessing to reduce each input to 128×128 px images. This is performed with an adaptable cropping algorithm that first produces a region of interest on the image which is one of four possible sizes (128×128 px, 256×256 px, 512×512 px, and 1024×1024 px depending on how the body appears in the image at a specific range) and then generates a resized 128×128 px image. This process also changes the values of the COM of B1 and range, which need to be adjusted both during training and testing. Further details about this algorithm can be found in [81, 155].

4.2.3 Overview of data-driven methods

Table 4.4 reports the main parameters and characteristics of the IP algorithms described in this section. It can be seen that M1 has roughly 8 times more parameters than M2,

due to its heavier and more complex architecture. This also affects the higher Average Computational Time (ACT) required by M1 to process a single image on a Zynq-7000 System-on-a-Chip (SoC) processor considered in this work as representative of a typical OBC. It can also be noted that M2 is an end-to-end data-driven method and derives the range from B1 directly with the CNN architecture, while M1 takes advantage of B1's shape and derives it geometrically.

Table 4.4: Overview of architecture of M1 and M2

Parameter	**M1**	**M2**
Number of model parameters	28.5 M	3.6 M
Weight	109 MB	13.6 MB
ACT on a Zynq-7000 SoC	165 s	9.94 s
Outputs	COM B1, COM B2, Range from B1, Associated covariances, Flag if measurement is available or not	COM B1, Range from B1, Sun phase angle
Range estimation	Derived geometrically	Estimated from network

4.2.4 FTs analysis

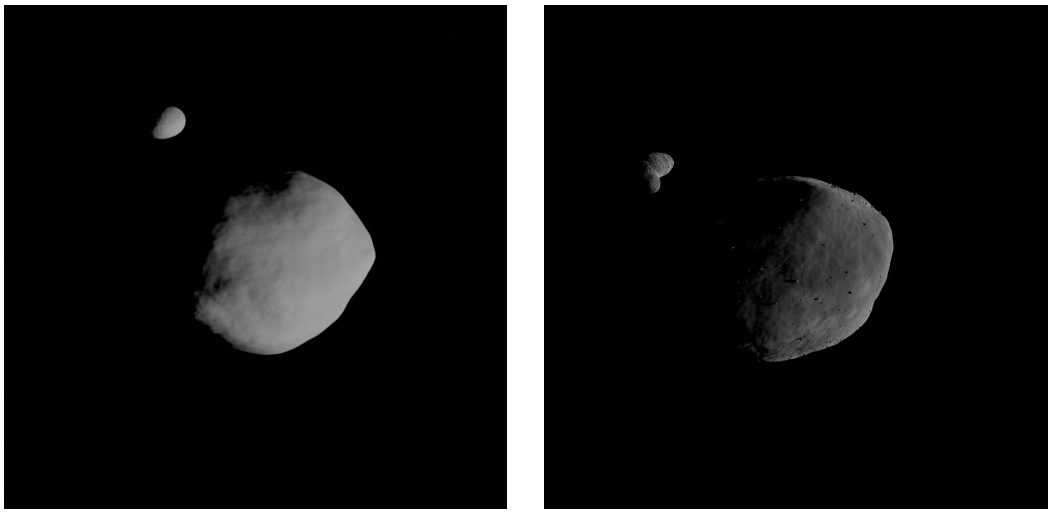

Figure 4.5: Sample image generated with CORTO (left) and PANGU (right)

The FTs run in this work are designed to test the robustness and performances of the developed IP algorithm against multiple adverse conditions that could occur during mission operations. Specifically, the objective of the FTs is to analyze the capability of the trained IP algorithm to generalize their solution when facing conditions never seen during training. In particular, the conditions analyzed in this work are of different illumination, different shape of the target body, presence/absence of B2, different Signal-to-Noise ratio, and, more in general, different images than the ones generated synthetically and used on ground. Furthermore, we analyze the applicability of the algorithm during Hera's proximity operations. Since the baseline Hera AVBN system consists of the measurements of the position of the COM of B1 given by the on-board IP MCLS algorithm and the range from B1 given by the on-board LIDAR system, only these two outputs of the developed IP algorithms are analyzed with the FTs. The next section describes in detail the different types of datasets generated in this work.

4.2.4.1 Training and Testing Datasets

In this work, several datasets are generated to train and test the data-driven methods. A summary of their main properties is represented in Table 4.5 and Table 4.6, while a representation of the distribution of the dataset in the space surrounding the Didymos system is illustrated in Fig. 4.6. Finally, samples of the images constituting the datasets are represented in Fig. 4.7 and Fig. 4.8. Table 4.7 reports the values of the length of the principal axes of the different shape models of B1 and B2 used in this work. $Shape_1$ represents the current knowledge of these shape models without uncertainties as shown in Table 4.1 [28]. The shape models of $Shape_2$ instead, considers as principal axes the ones retrieved from radar observations, prior to DART's arrival when B1's shape was thought to be more spherical [29]. $Shape_3$ represents an expanded version of $Shape_1$ in all axes. While the first three shape models are generated with the software Blender, the last one, $Shape_4$, is made with the software PANGU and it uses the same principal axes length of $Shape_1$.

The same pipeline is used to generate all the images. However, all but $DS6$ and $DS7$

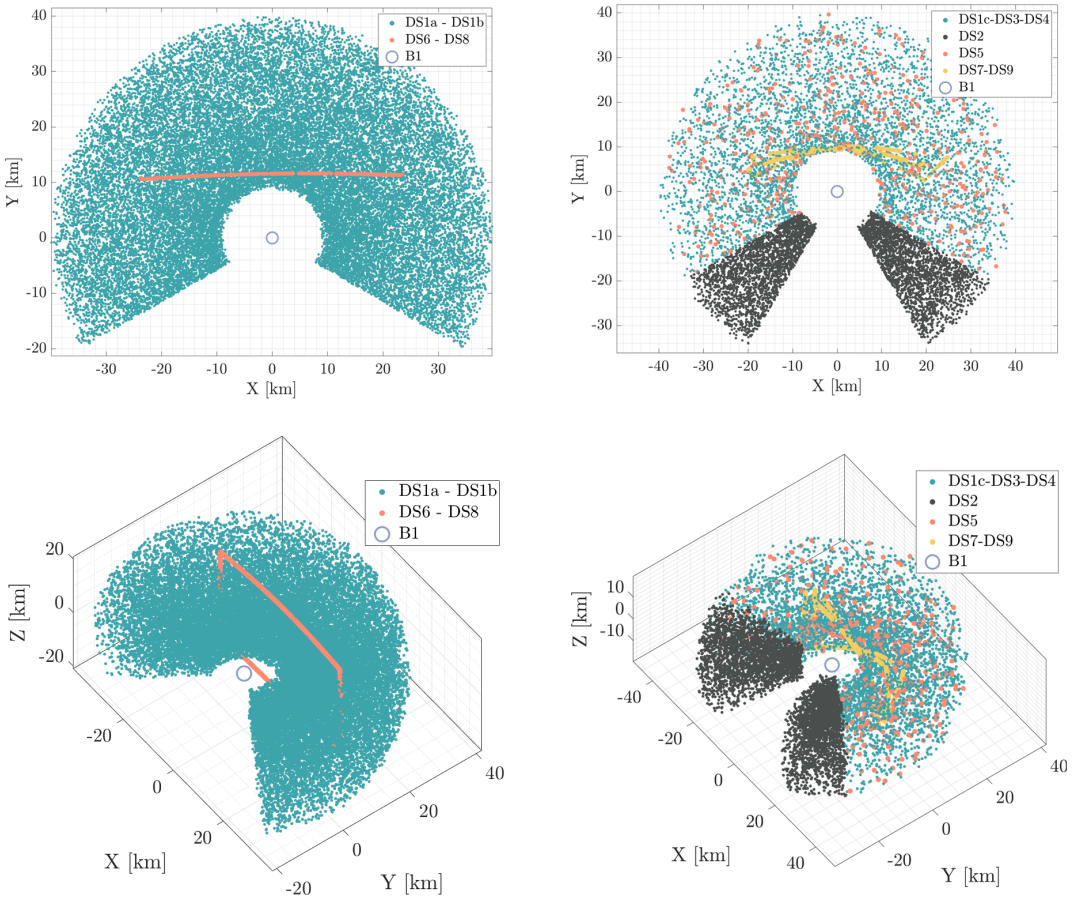

Figure 4.6: Visualization of the training (left column), and testing (right column) datasets in TB. The Sun is illuminating the asteroid system from the +Y axis. The dots and the arcs distributed around B1 represent the points where the images of the datasets are taken from

are generated in CORTO [131], while PANGU is instead used to generate $DS8$ and $DS9$. CORTO stands for Celestial Object Rendering TOol and it is an open-access [1] tool that uses Blender to generate high-fidelity, large, annotated datasets of celestial bodies. The tool represents a versatile and comprehensive solution for generating synthetic images of celestial bodies, aiding the development and validation of image processing and navigation algorithms for space missions. Fig. 4.5 shows two sample images generated with CORTO (left) and PANGU (right), using the same orbital properties of the Hera mission and with the shape models $Shape_1$ of B1 and B2. Notably, even though the

[1] https://github.com/MattiaPugliatti/corto, last accessed, 3rd of March, 2024.

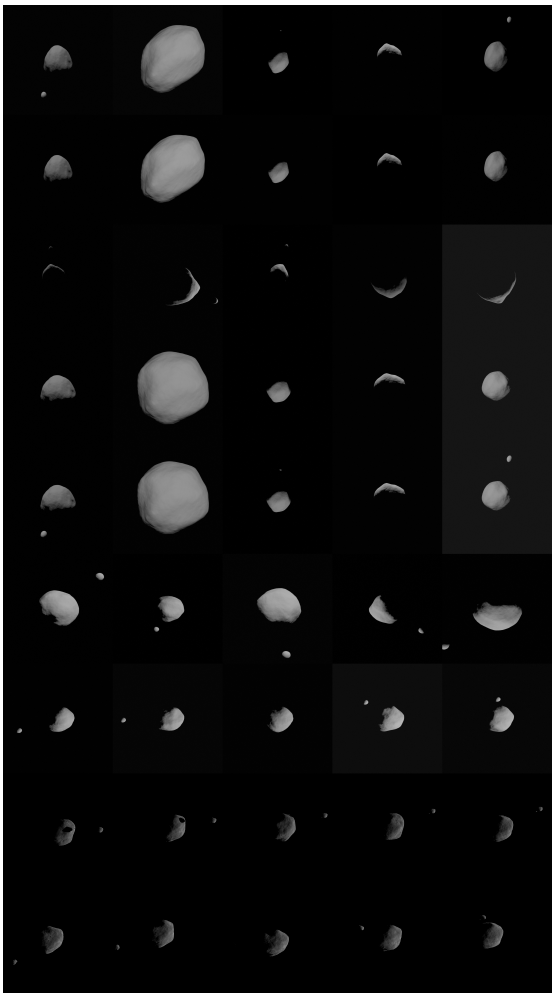

Figure 4.7: First 5 samples, from top to bottom, of $DS1_a$, $DS1_b$, $DS2$, $DS3$, $DS4$, $DS6$, $DS7$, $DS8$, and $DS9$

length of the axes of B1 and B2 are the same, since the modelling software are different the two bodies have different appearances. This can be seen especially with B2: while in CORTO the shape model of B2 is generated from an ellipsoid, adding roughness and albedo variations to simulate the surface of an asteroid, in PANGU the shape model of B2 is a scaled down version of asteroid Itokawa, the target of the Hayabusa mission [80, 81].

The training datasets are represented in Table 4.5 while the testing datasets in Table 4.6. $DS1_a$ and $DS1_b$ are used to train M2 and M1 respectively. The trained M1 and M2 are then tested with $DS1_c$, $DS2$, $DS3$, $DS4$ and $DS5$. The fine-tuning of M1

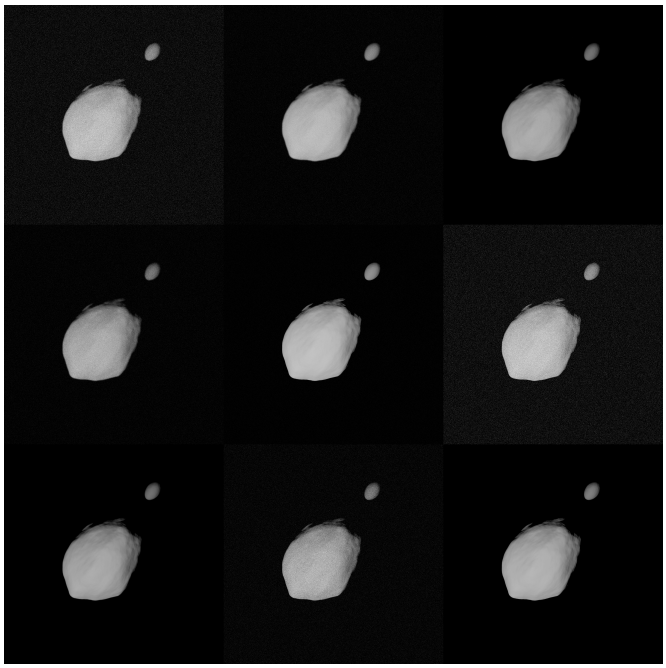

Figure 4.8: First sample of $DS5$ seen by 9 different noise subsets

Table 4.5: Summary of the properties of the training datasets

Acronym	**Number of images**	**Description**	**Shape model**	**Image generation tool**
$DS1_a$	30000	Nominal scenario	$Shape_1$	CORTO
$DS1_b$	30000	Nominal scenario, without B2	$Shape_1$	CORTO
$DS6$	8, 16, 32, 64, 128, 256, 512, 1024	ECP, new shape	$Shape_3$	CORTO
$DS8$	8, 16, 32, 64, 128, 256, 512, 1024	ECP, new shape	$Shape_4$	PANGU

and M2 is carried with $DS6$ and $DS8$ and the respective tests are done with $DS7$ and $DS9$ subsequently.

The geometric distributions of the locations where the images are generated are illustrated in Fig. 4.6. The distribution of $DS1_a$, $DS1_b$, $DS1_c$, $DS3$, $DS4$, and $DS5$

Table 4.6: Summary of the properties of the testing datasets

Acronym	**Number of images**	**Description**	**Shape model**	**Image generation tool**
$DS1_c$	5000	Nominal scenario	$Shape_1$	CORTO
$DS2$	5000	High Sun phase angles	$Shape_1$	CORTO
$DS3$	5000	Nominal scenario, new shape, without B2	$Shape_2$	CORTO
$DS4$	5000	Nominal scenario, new shape, with B2	$Shape_2$	CORTO
$DS5$	500×9	Nominal scenario, different noises	$Shape_1$	CORTO
$DS7$	450	DCP, new shape	$Shape_3$	CORTO
$DS9$	450	DCP, new shape	$Shape_4$	PANGU

Table 4.7: Axes elongation of the shape models used in this work

Shape models	$B1_x$ $[m]$	$B1_y$ $[m]$	$B1_z$ $[m]$	$B2_x$ $[m]$	$B2_y$ $[m]$	$B2_z$ $[m]$	Modelling software
$Shape_1$	849	851	620	177	174	116	Blender
$Shape_2$	821	823	786	202	159	134	Blender
$Shape_3$	861	862	626	178	175	117	Blender
$Shape_4$	849	851	620	177	174	116	PANGU

is characterized by random points between 10 km and 40 km from Didymos, with Sun phase angles ranging from 0° to 120°, and absolute values of elevation angle with respect to Didymos' equator between 0° and 30°. These conditions are referred throughout the paper as the *Nominal scenario*, i.e. the scenario used for the training dataset. The training dataset $DS1_b$ differs from $DS1_a$ simply by the absence of B2 from the images,

which is necessary to train M1. $DS3$ and $DS4$ are used to assess the IP performance with a different B1 shape model with principal axes shown in Table 4.7. While $DS3$ represents only B1 and is used to isolate the error introduced by the different shape of the target, $DS4$ represents both B1 and B2, therefore including also the dependence of the IP algorithms performances on the presence of B2.

$DS5$ represents a small subset of the first 500 points of $DS1$ in which the settings of the artificial noise are varied. For the noise model used, the reader is directed to [131]. In this work, the number of pixels considered in the horizontal motion blur (ν_{mb}), a generic isotropic blur (ν_b), a gamma correction factor (γ), mean (ν_μ) and variance (ν_σ) of Gaussian noise are sampled with random uniform distributions according to the extremal values reported in Table 4.8 (note, however, that ν_μ and ν_σ are sampled in logarithmic scale).

Table 4.8: Summary of the noise properties varied in the different subsets of $DS5$. For comparison, the first row represents the nominal values used in all other datasets

Subset	ν_{mb}	ν_b	γ	ν_μ	ν_σ	**Acronym**
Nominal values	[0.10, 2.00]	0.5	[0.9,1.1]	[1e-4,1e-1]	1e-4	-
1	[1.00, 2.00]	[1.00, 2.00]	[0.70, 1.00]	[1e-3, 1e-2]	[1e-3, 1e-2]	BgL
2	[1.00, 2.00]	[1.00, 2.00]	[0.70, 1.00]	[1e-5, 1e-3]	[1e-5, 1e-3]	Bgl
3	[1.00, 2.00]	[1.00, 2.00]	[1.00, 1.30]	[1e-5, 1e-3]	[1e-5, 1e-3]	BGl
4	[1.00, 2.00]	[1.00, 2.00]	[1.00, 1.30]	[1e-3, 1e-2]	[1e-3, 1e-2]	BGL
5	[0.20, 1.00]	[0.20, 1.00]	[0.70, 1.00]	[1e-5, 1e-3]	[1e-5, 1e-3]	bgl
6	[0.20, 1.00]	[0.20, 1.00]	[0.70, 1.00]	[1e-3, 1e-2]	[1e-3, 1e-2]	bgL
7	[0.20, 1.00]	[0.20, 1.00]	[1.00, 1.30]	[1e-5, 1e-3]	[1e-5, 1e-3]	bGl
8	[0.20, 1.00]	[0.20, 1.00]	[1.00, 1.30]	[1e-3, 1e-2]	[1e-3, 1e-2]	bGL
9	[0.20, 0.21]	[0.20, 0.21]	[0.99, 1.01]	[1e-6, 1e-5]	[1e-6, 1e-5]	bg0l

The subsets of $DS5$ from 1 to 4 are referred to as "high blur" (B) while those from 5 to 9 are considered "low blur" (b). The subsets 1, 2, 5, and 6 are referred as "low gamma" (g), the subsets 3, 4, 7, and 8 are referred as "high gamma" (G), while the subset 9 is considered "nominal gamma"(g0). Similar distinctions are also made for

"low mean and low variance" (l), such as for subsets 2, 3, 5, 7, and 9, and "high mean and high variance" (L), such as for subsets 1, 4, 6, and 8. Lastly, the distribution of $DS2$ points differs from all those described above only for one condition: the illumination conditions are adverse, with the Sun phase angles ranging from 120° to 150°.

Finally, $DS6$ and $DS8$ distributions represent points scattered uniformly across the ECP trajectory of the Hera mission. The same is done for $DS7$ and $DS9$ with the DCP. However, while $DS6$ and $DS8$ are rendered with CORTO using shape models generated with Blender, $DS7$ and $DS9$ are using shape models with the same length of the principal axes as $Shape_1$ but generated with PANGU. Both $DS6$ and $DS8$ are used in eight, separate, fine-tuning episodes in which the number of images used is doubled each time from 8 to 1024. These datasets mimic real mission scenarios in which a limited amount of images could be available to fine-tune a data-driven method. The eight different fine-tuned networks are then tested with $DS7$ and $DS9$ respectively, as they would be deployed in the next phase of the Hera mission, to assess the impact of the fine-tuning performed during the ECP.

All datasets except for $DS9$ consider a random relative attitude of the spacecraft with respect to B1 for each image, showing therefore illumination coming from any possible direction. In $DS9$ the Hera spacecraft's body reference frame is considered, having the Sun-B1 vector always lying on the horizontal axis of the image plane, thus showing the target asteroid illuminated from the right side. Furthermore, a limited pointing error is added for each image in order to shift the position of the COM of B1 from the exact center of the image.

To promote shared test benches and encourage other researchers to propose alternative methods, all datasets are available on Zenodo, while the Blender file used to render the datasets of this work is available as a dedicated scenario within the CORTO repository [2].

[2]https://zenodo.org/records/15346833, last accessed, 3rd of March, 2024.

4.3 Results

In this section, the results of the FTs of the developed data-driven methods are presented. As mentioned, the performances of the algorithms on the testing datasets are analyzed only for the estimation of the position of the COM of B1 and the range from B1. The metrics defined in Eq. 4.1 and Eq. 4.2 are used to evaluate the performances of each data-driven method for each FTs.

$$\varepsilon_{CoM} = CoM^e - CoM^t \tag{4.1}$$

$$\varepsilon_{\rho} = \rho^e - \rho^t \tag{4.2}$$

where CoM and ρ indicate the COM of B1 and the range from B1 respectively, while the superscripts t and e indicate respectively the ground truth and the estimated value. ε_{CoM} represents the error of the estimated position of the COM in the image plane (in the original 1024×1024 image size) and is calculated in px while ε_{ρ} represents the error of the estimated range and is calculated in km. Since the position of the COM of B1 on the image is defined by its (u, v) coordinates on the image plane, ε_{CoM} is a vector with coordinates (ε^u_{CoM}, ε^v_{CoM}), and its norm is ε^n_{CoM}. The (u, v) coordinates are defined in a reference frame with the origin at the top left corner of the image and the horizontal and vertical axes referred to as i and j-directions, as shown in Fig. 4.9 [142].

Lastly, $\varepsilon^{\%}_{\rho}$ is used to represent ε_{ρ} as relative percentage error with respect to the true range ρ^t, as described in Eq. 4.3.

$$\varepsilon^{\%}_{\rho} = \frac{\rho^e - \rho^t}{\rho^t} \cdot 100\% \tag{4.3}$$

In order to assess the robustness of the data-driven methods against the various noises, different shape models and adverse illumination conditions, the results of $DS2$, $DS3$, $DS5$, $DS7$ and $DS9$ are compared with the results obtained on the nominal scenario of the images of $DS1_c$. The results of $DS4$ are compared to the ones of $DS3$, to analyze the robustness of the algorithm to the presence of B2.

As mentioned in Section 4.2.2.1, the availability of the measurements of M1 depends

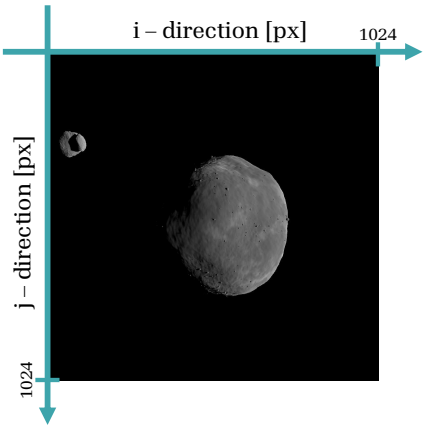

Figure 4.9: Coordinate frame of the image plane [142]

on the intensity of the heatmap generated by the HRNet from an input image. This is not the case for M2, that always converge to a solution. Therefore, it is relevant to assess the convergence of M1 for each dataset, as shown in Table 4.9, which shows for each dataset the amount of images not solved by M1. For $DS5$, the best and worst subset results are shown. For $DS7$ and $DS9$ the best and worst results obtained with the eight fine-tuned versions of M1 and M2 are shown. It can be seen that the worst

Table 4.9: Images not solved by M1 in absolute and relative terms

Dataset	**Absolute** [–]	**Rate** [%]
$DS1_c$	195	3.90
$DS2$	751	15.02
$DS3$	359	7.18
$DS4$	350	7.00
$DS5$	7-47	1.40-9.40
$DS7$	31-151	6.89-33.56
$DS9$	37-219	8.22-48.67

scenarios are given by the fine-tuning tests $DS7$ and $DS9$ for which up to 48.67% of the images are not solved by M1. In these cases, the heavier architecture of M1 seems to exhibit a higher inertia to the fine-tuning. In order for M1 to be more confident with

the provided solution and thus, exhibit intense heatmaps, M1 would require additional images for the fine-tuning.

4.3.1 From $DS1_c$ to $DS4$

Fig. 4.10, Fig. 4.11, Fig. 4.12 and Fig. 4.13 illustrate the performances of M1 and M2 on the estimation of the position of the COM of B1 and the range from B1 for the testing datasets $DS1_c$, $DS2$, $DS3$ and $DS4$, respectively. Table 4.10 reports the value of each mean μ and standard deviation σ of the metric in the curly brackets. It can be seen from the values of ε^u_{CoM} and ε^v_{CoM} that both methodologies introduce a small bias in estimating the position of the COM of B1. Independently from the shape model, noise condition, and the direction of the incoming light, M1 underestimates CoM^u, while overestimating CoM^v. On the other hand, M2 overestimates only CoM^v, but with higher values compared to M1.

Table 4.10: Performances of M1 and M2 on the estimation the position of the COM of B1 and the range from B1 for $DS1_c$, $DS2$, $DS3$ and $DS4$

Dataset	**IP**	$\mu(\sigma)\{\varepsilon^u_{CoM}\}[px]$	$\mu(\sigma)\{\varepsilon^v_{CoM}\}[px]$	$\mu(\sigma)\{\varepsilon^n_{CoM}\}[px]$	$\mu(\sigma)\{\varepsilon_\rho\}[km]$	$\mu(\sigma)\{\lvert\varepsilon_\rho\rvert\}[km]$
$DS1_c$	M1	-7.24 (-5.75)	7.82 (8.72)	12.73 (7.79)	-2.77 (1.73)	2.77 (1.72)
$DS1_c$	M2	1.80 (0.44)	9.69 (9.57)	10.67 (8.66)	-0.05 (1.10)	0.79 (0.77)
$DS2$	M1	-7.12 (-7.55)	20.31 (21.39)	25.99 (17.38)	-4.91 (4.29)	4.93 (4.27)
$DS2$	M2	1.98 (2.05)	38.18 (40.06)	44.07 (33.60)	-2.45 (3.38)	2.89 (3.01)
$DS3$	M1	-7.47 (-6.14)	17.02 (17.07)	20.56 (15.86)	1.22 (1.37)	1.41 (1.18)
$DS3$	M2	1.97 (0.48)	20.35 (19.30)	21.07 (18.62)	2.82 (1.51)	2.83 (1.50)
$DS4$	M1	-7.49 (-6.16)	17.18 (17.11)	20.57 (16.08)	1.19 (1.37)	1.39 (1.17)
$DS4$	M2	2.15 (0.62)	19.80 (18.98)	20.70 (18.14)	2.79 (1.51)	2.80 (1.50)

4.3.1.1 $DS1_c$: Nominal scenario

It can be seen from the top left plot of Fig. 4.10 that the error made by M1 on estimating the range from B1 is biased towards negative values ($\mu\{\varepsilon_\rho\} = -2.77\ km$), while the error made by M2 is distributed around 0 ($\mu\{\varepsilon_\rho\} = -0.05\ km$). Moreover, the error of the estimates made by M2 is less dispersed than those of M1, with a standard deviation respectively of $\sigma\{\varepsilon_\rho\} = 1.73\ km$ and $\sigma\{\varepsilon_\rho\} = 1.10\ km$.

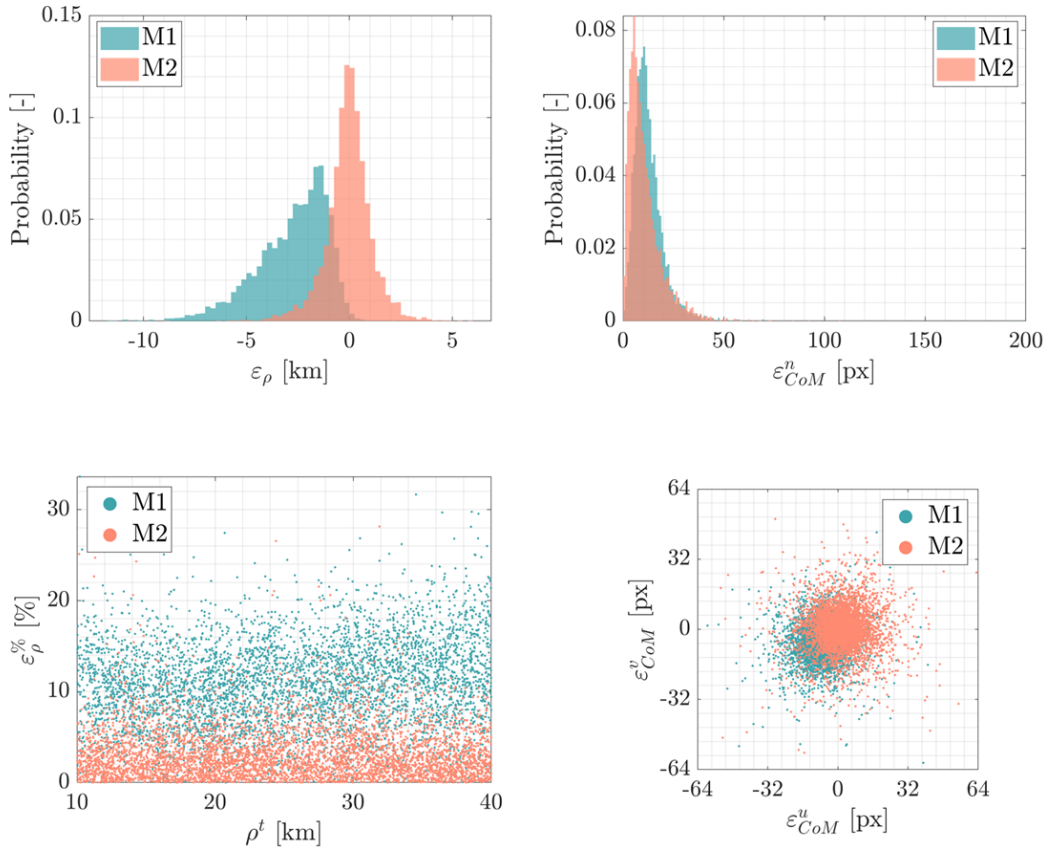

Figure 4.10: Range (left column) and centroiding (right column) error results of M1 and M2 for $DS1_c$

The worse performance of M1 on ε_ρ is due to the inaccurate approximation of the shape of B1 to a sphere to derive geometrically the range. This is also visible in the bottom left plot of Fig. 4.10, where the percent error of ε_ρ is plotted against the ground truth value of the range, showing that the error made by M1 is higher and spread more widely. Nevertheless, the bottom left plot also highlights that the range estimate of both algorithms does not exhibit any relevant trend with respect to the true range.

The top right plot of Fig. 4.10 shows the distribution of ε^n_{CoM} for M1 and M2. It can be seen that the performances are very similar, with the mean value of ε^n_{CoM} obtained by M1 slightly higher ($\mu\{\varepsilon^n_{CoM}\} = 12.73\ px$ for M1, and $\mu\{\varepsilon^n_{CoM}\} = 10.67\ px$ for M2), with a standard deviation of $\sigma\{\varepsilon^n_{CoM}\} = 7.79\ px$ and $\sigma\{\varepsilon^n_{CoM}\} = 8.66\ px$ respectively. This is also visible in the bottom right plot of Fig. 4.10, where the distribution of ε_{CoM} is plotted with its (u, v) coordinates in a neighborhood of $64 \times 64\ px$ around the ideal

results of $\varepsilon_{CoM} = (0, 0)$.

In conclusion, in the nominal scenario where the testing dataset is similar to the training one, M2 is more accurate and precise than M1 in estimating both range and COM coordinates.

4.3.1.2 DS2: high Sun phase angles

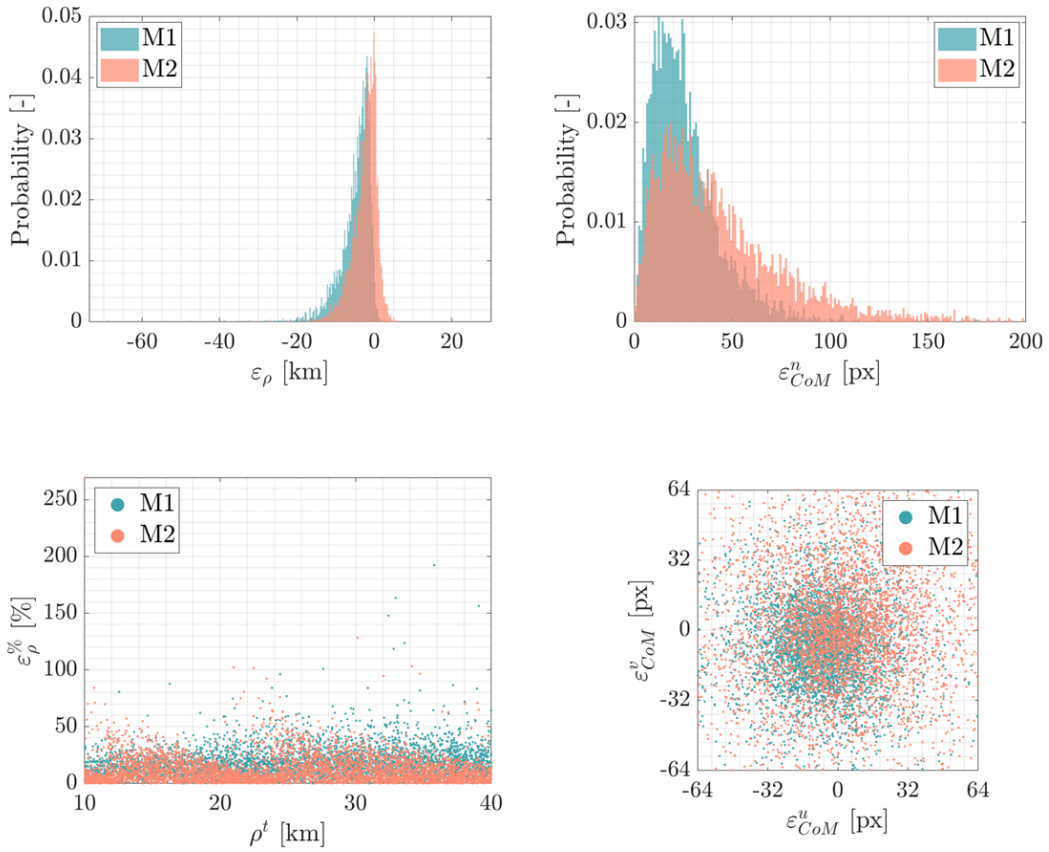

Figure 4.11: Range (left column) and centroiding (right column) error results of M1 and M2 for $DS2$

It can be seen from Table 4.10 and from Fig. 4.11 that the adverse illumination conditions represented by the high Sun phase angles of $DS2$ affect the performances of M1 and M2, shown by the higher values of $\mu\{\varepsilon_\rho\}$ and $\mu\{\varepsilon^n_{CoM}\}$. As in $DS1_c$, the error distribution on the range estimation is biased towards negative values for M1 ($\mu\{\varepsilon_\rho\} = -4.91\ km$, $\sigma\{\varepsilon_\rho\} = 4.29\ km$) with respect to M2 ($\mu\{\varepsilon_\rho\} = -2.45\ km$, $\sigma\{\varepsilon_\rho\} = 3.38\ km$). For the estimation of the position of the COM of B1, M1 performs

better than M2, with a $\mu\{\varepsilon^n_{CoM}\} = 25.99\ px$ for M1 and $\mu\{\varepsilon^n_{CoM}\} = 44.07\ px$ for M2, and with a standard deviation of $\sigma\{\varepsilon^n_{CoM}\} = 17.38\ px$ and $\sigma\{\varepsilon^n_{CoM}\} = 33.60\ px$ respectively. The worse performances of the two methods with respect to the nominal scenario can be seen from the bottom left and the bottom right plots of Fig. 4.11, which show that ε_ρ and ε^n_{CoM} are less precise compared to the nominal scenario.

To conclude, in the scenario in which higher phase angles are considered, both methods suffer a considerable drop in performance compared to the results in $DS1_c$. However, M1 seems to suffer a smaller drop compared to M2, indicating a higher degree of robustness. As it is possible to see from the sample in Fig. 4.7, the illumination conditions of $DS2$ generate relatively small illuminated limbs of the target body. From the results presented in this section, it appears that the visible edge of the body in such challenging illumination conditions works better with the geometrical derivation strategy performed with the HRNet in M1 than with the end-to-end approach of M2. This is particularly visible looking at the performance on the range, which greatly degrade for M2, while they only mildly degrade for M1 with respect to the ones obtained with $DS1_c$. However, it is also noted that M1 does not converge for a higher number of cases ($\sim$4 times higher than in $DS1_c$, see Table 4.9).

4.3.1.3 DS3: Nominal scenario, new shape of B1, without B2

It can be seen from Table 4.10 and from Fig. 4.12 that the different shape of B1 affect slightly the performances of M1 and M2. Contrarily to the results obtained in $DS1_c$ and $DS2$, the error distribution on the range estimation is now biased towards positive values for M1 ($\mu\{\varepsilon_\rho\} = 1.22\ km$, $\sigma\{\varepsilon_\rho\} = 1.37\ km$), with a higher accuracy than M2 ($\mu\{\varepsilon_\rho\} = 2.82\ km$, $\sigma\{\varepsilon_\rho\} = 1.51\ km$). Considering that in this dataset the shape of B1 is more spherical, the geometrical derivation of the range from its shape improves the performances of M1, while reducing the ones of M2. For the estimation of the position of the COM of B1, M1 performs slightly better than M2, with a $\mu\{\varepsilon^n_{CoM}\} = 20.56\ px$ for M1 and $\mu\{\varepsilon^n_{CoM}\} = 21.07\ px$ for M2 and with a standard deviation of $\sigma\{\varepsilon^n_{CoM}\} = 15.86\ px$ and $\sigma\{\varepsilon^n_{CoM}\} = 18.62\ px$ respectively. The better performances of M1 in the range estimation can be seen from the bottom left and bottom right plots of Fig. 4.12, which

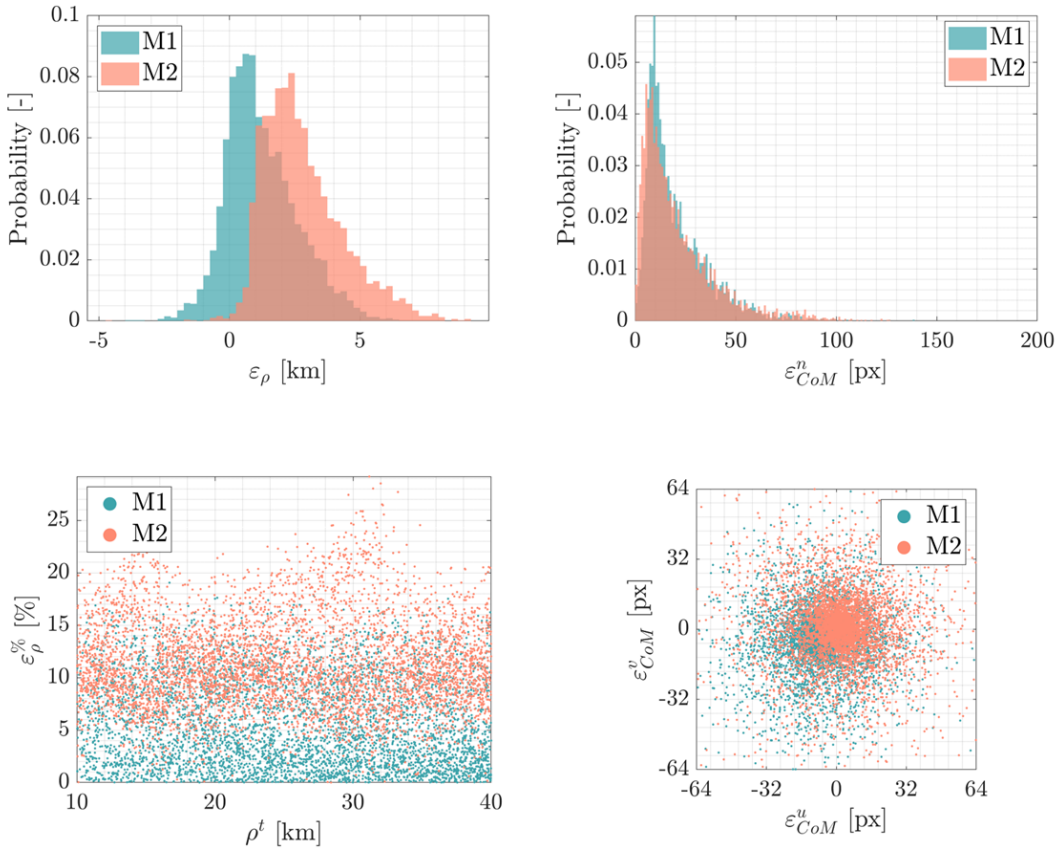

Figure 4.12: Range (left column) and centroiding (right column) error results of M1 and M2 for $DS3$

show that ε_ρ and ε^n_{CoM} have values closer to 0 with respect to M2.

To conclude, the different shape of B1 tested in $DS3$ seems to have a less drastic effect than unforeseen illumination conditions tested in $DS2$ as both M1 and M2 performance are closer to those in $DS1_c$. The different shape models seem to favor both the accuracy and precision of the range estimate of M1 compared to M2. This is attributed to the more spherical shape of B1 in this dataset, which performs better in the apparent diameter formulation used by M1 compared to the end-to-end approach used in M2. Centroiding performance on the other hand are basically very similar between M1 and M2.

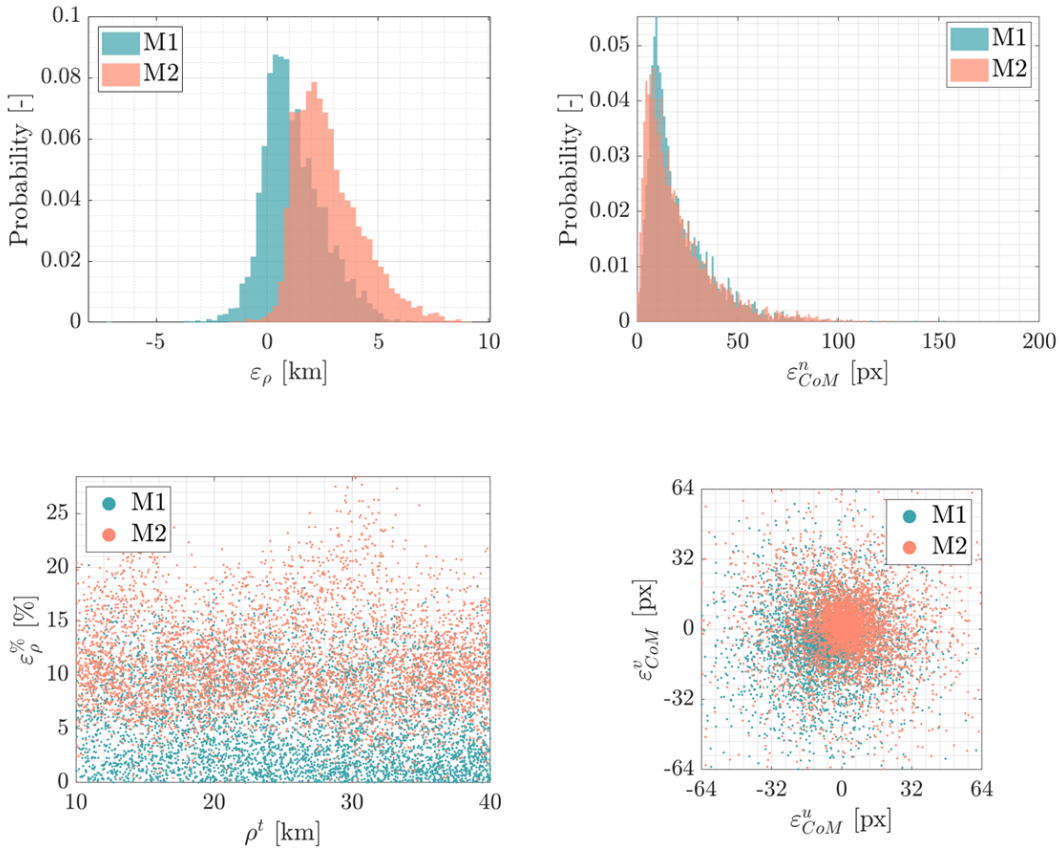

Figure 4.13: Range (left column) and centroiding (right column) error results of M1 and M2 for $DS4$

4.3.1.4 DS4: Nominal scenario, new shape of B1, with B2

It can be seen from Table 4.10 and from Fig. 4.13 that the presence of B2 does not affect the results, as they remain quite similar to the ones obtained for $DS3$. The error distribution on the range estimation is biased towards positive values for M1 ($\mu\{\varepsilon_\rho\} = 1.19\ km$, $\sigma\{\varepsilon_\rho\} = 1.37\ km$), with a higher accuracy with respect to M2 ($\mu\{\varepsilon_\rho\} = 2.79\ km$, $\sigma\{\varepsilon_\rho\} = 1.51\ km$). For the estimation of the position of the COM of B1, M1 performs slightly better than M2, with a $\mu\{\varepsilon^n_{CoM}\} = 20.57\ px$ for M1 and $\mu\{\varepsilon^n_{CoM}\} = 20.70\ px$ for M2 and with a standard deviation of $\sigma\{\varepsilon^n_{CoM}\} = 16.08\ px$ and $\sigma\{\varepsilon^n_{CoM}\} = 18.14\ px$ respectively.

To conclude, both M1 and M2 are essentially unaffected by the presence of B2 in the images, as negligible differences are observed with respect to $DS3$ of the mean values

of ε_ρ and ε^n_{CoM} are negligible. This confirms also the results shown in [80], where the influence of B2's presence on M1 is analyzed thoroughly.

4.3.2 $DS5$: Nominal scenario, different noises

Table 4.11: Performances of M1 and M2 on the estimation the position of the COM of B1 and the range from B1 for the different conditions of blur, gamma and mean and variance of the images of $DS5$

Dataset	**IP**	$\mu(\sigma)\{\varepsilon^n_{CoM}\}[px]$	$\mu(\sigma)\{\lvert\varepsilon_\rho\rvert\}[km]$
BgL	M1	15.37 (11.38)	3.19 (2.17)
BgL	M2	15.52 (9.60)	1.96 (1.85)
Bgl	M1	13.98 (9.13)	3.12 (1.91)
Bgl	M2	12.59 (8.52)	1.02 (1.08)
BGl	M1	13.64 (8.67)	3.08 (2.09)
BGl	M2	13.38 (10.26)	1.20 (1.29)
BGL	M1	14.11 (9.29)	3.42 (2.43)
BGL	M2	16.12 (11.78)	1.27 (1.26)
bgl	M1	13.06 (8.69)	2.78 (1.64)
bgl	M2	11.34 (7.94)	0.91 (0.96)
bgL	M1	14.33 (10.25)	2.76 (1.84)
bgL	M2	13.71 (8.90)	1.86 (1.75)
bGl	M1	12.76 (8.03)	2.71 (1.84)
bGl	M2	11.28 (9.43)	0.87 (0.88)
bGL	M1	13.47 (8.54)	3.01 (2.06)
bGL	M2	13.87 (10.95)	1.12 (1.10)
bg0l	M1	12.19 (6.98)	2.56 (1.59)
bg0l	M2	10.86 (8.18)	0.83 (0.86)

Table 4.11 reports in a synthetic form the values of the mean and standard deviation of ε_ρ and ε^n_{CoM} for the images of $DS5$. Since the interest is to quantify the error introduced by the different noises, the absolute value of ε_ρ is analyzed, differently from the previous cases. The values of the mean are also represented in Fig. 4.14 for a simpler visualization.

It can be seen that in the overwhelming majority of the cases, both M1 and M2 performance suffer degradation when extra noise is added to the images. Both data-

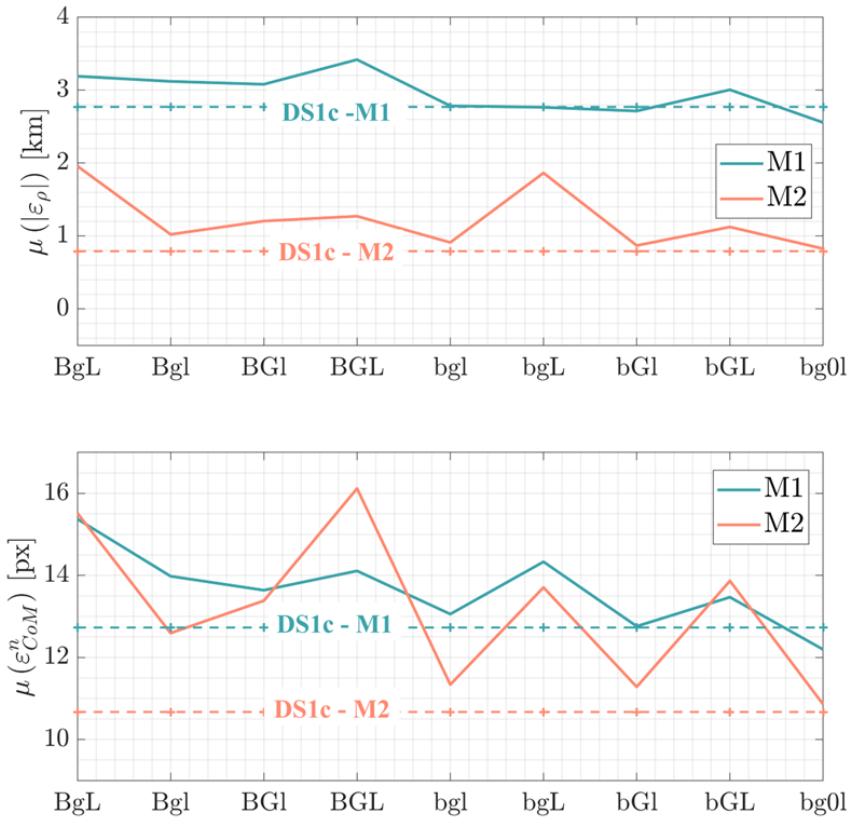

Figure 4.14: Range (top) and centroiding (bottom) error results of M1 and M2 for $DS5$

driven methods' performances worsen with the conditions of high blur, for both the estimations of the centroid of B1 and the range from it. The highest values of the means of $|\varepsilon_\rho|$ of M1 and M2 are 3.42 km (BGL) and 1.96 km (BgL) respectively, with a standard deviation of 2.43 km and 1.85 km respectively. The worst performance on the centroiding estimation are given with conditions of BgL for M1, with a mean value of ε^n_{CoM} of 15.37 px and a standard deviation of 11.38 px, and with conditions of BGL for M2, with a mean value of ε^n_{CoM} of 16.12 px and a standard deviation of 11.78 px.

Fig. 4.14 shows also the values of $|\varepsilon_\rho|$ and ε^n_{CoM} obtained with the nominal scenario of $DS1_c$, as a reference to assess the robustness of the two algorithms with respect to the noises introduced with $DS5$. The performance of M1, when extra noise is added to the images, is consistent with that in $DS1_c$ while M2 seems more susceptible.

Finally, it is interesting to note that higher blur is negatively affecting both net-

works. Higher blur levels could challenge the convolutional kernels obtained during training, spreading the input image content across larger image patches. This result could inspire future data-driven IP designers to include a higher blur level in the training dataset in those cases in which robustness to noise is more demanding.

4.3.3 $DS7$ and $DS9$: DCP, new shape

Fig. 4.15 and Fig. 4.16 show the results on $|\varepsilon_\rho|$ and ε^n_{CoM} on the testing datasets $DS7$ and $DS9$ obtained by fine-tuning M1 and M2 using an incremental batch of images (8, 16, 32, 64, 128, 256, 512 and 1024) from the ECP phase represented in $DS6$ and $DS8$. The results obtained with M1 and M2 prior to the fine-tuning are also shown, represented by a batch size of 0 images. The pair $DS6 - DS7$ is expected to stress the difference in shape while the pair $DS8 - DS9$ stresses a greater shape difference, exacerbated in this setup also by the different rendering software used to generate the datasets (i.e. PANGU instead of CORTO). The aim of this analysis is to find the amount of images taken during the ECP that minimizes the estimation errors during the DCP, i.e. the number of images that tunes the two models' parameters to adapt their solution to a target different from the one seen during training. This scenario is especially relevant for small body missions, since the property of the target body are rarely precisely known before arrival.

Ideally, using a higher amount of images of the ECP for fine-tuning is expected to improve performances, as the data-driven models would have more information about the real target, minimizing possible discrepancies due to different modeling of the body's shape. However, as illustrated in this section, this scenario is more challenging than anticipated.

Considering the $DS6 - DS7$ case, observing the trends reported in Fig. 4.15, the number of images used for the fine-tuning of M1 and M2 is not improving performances on $DS7$ apart from the range estimate in M1. Lastly, it is also noted that both M1 and M2 have robust performances prior to fine-tuning, even in the case when different artificial environments are used (CORTO and PANGU) to generate training images. In particular, it can be seen from Fig. 4.16 that M1 performs better than M2, despite

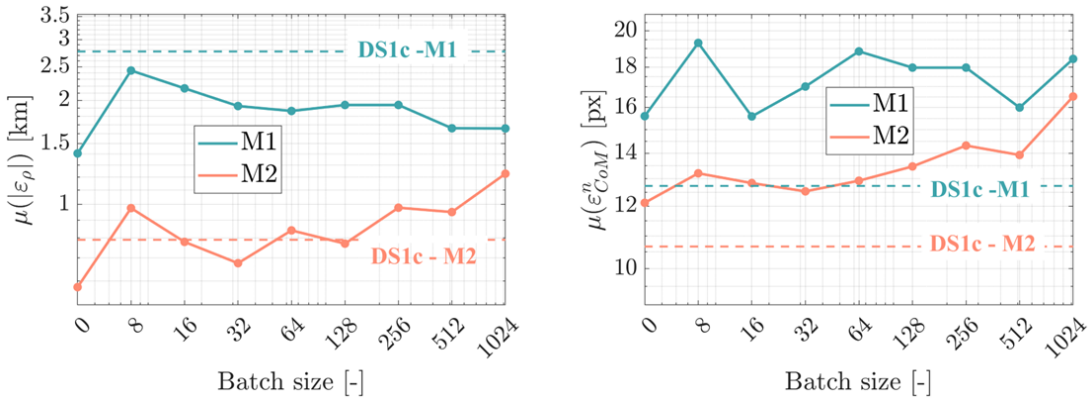

Figure 4.15: Range (left) and centroiding (right) error results of M1 and M2 for $DS7$

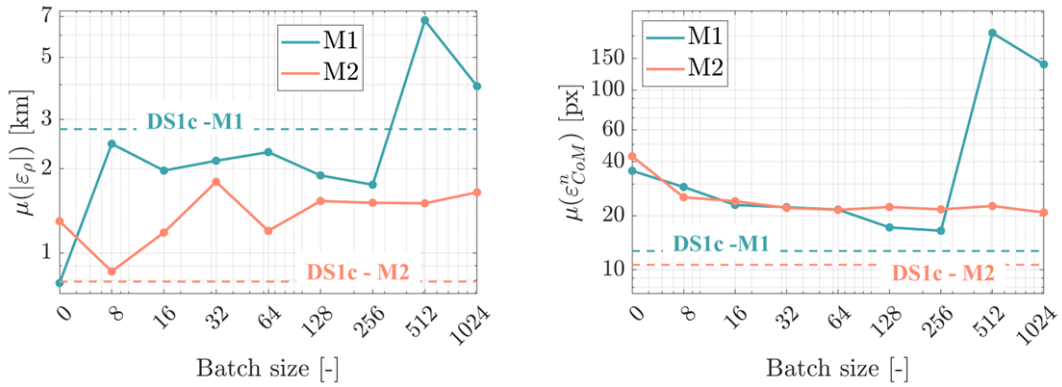

Figure 4.16: Range (left) and centroiding (right) error results of M1 and M2 for $DS9$

its worse performance with the other testing datasets generated using the same image generation tool of the training. However, it is also noted that M1 suffers in this dataset from the highest drop in convergence rates compared to all other scenarios presented in this work, as illustrated from the rates in Table 4.9.

A key conclusion is drawn from these results. Firstly, apart from specific cases (M1's range in DS7 and M2's centroid in DS9) in the majority of the cases considered, training episodes from the ECP dataset are drastically degrading both M1 and M2 performance for a robust application on the DCP datasets. A possible explanation of this phenomenon is given by the fact that both $DS1_a$ and $DS1_b$ used for the initial training are generated with a distance from the target that varies from 10 km to 40 km. The images from ECP that are used for fine-tuning represent a new target shape at a distance between 20 km and 30 km. Lastly, the testing dataset shows the new

target shape at a range between 9 km and 20 km. These different range intervals may explain why the $DS1$ dataset is more representative of the entire mission conditions than those encountered in ECP. Therefore, a possible explanation for the trend observed is that both data-driven methods are performing better when not fine-tuned, as their parameters were already optimized for ranges including the ones shown with $DS7$ and $DS9$. Effectively, both methods are challenged by the new training datasets of $DS6$ and $DS8$ to learn two contradicting information: learn about the new shape, and do that in a limited range interval. Even in an ideal training instance, in which a network would have specialized on the new shape but in a limited range interval, poor generalization performance would have been observed in a different geometric regime. This poses an interesting challenge in terms of fine-tuning data-driven methods for small-body applications. Fine-tuning episodes should be carefully designed to introduce the desired effect in the final networks.

4.4 Conclusion

This paper analyzes the robustness of two data-driven based IP algorithms designed to address the issue of centroiding (geometrical center) and range estimation of a binary asteroid system. The study examines the Hera mission's target proximity operations around the Didymos system as a case scenario. The data-driven methods are based on two different CNN approaches: M1, a heavier method based on the HRNet architecture and the point regression strategy, and M2, a custom-built end-to-end architecture made of subsequent dilated convolutional layers.

The test campaign includes FTs with images generated with CORTO and PANGU, representing conditions different from the ones seen during training. In particular, the two data-driven methods are stress-tested with images showing the target asteroid system in conditions of high Sun phase angles, different noise levels, and different shape models of the target. Considering overall performances, the results show that neither method is affected by the presence of the secondary, that M2 is slightly more accurate and precise in the estimation of the centroid and range, but also shows greater sensitivity to noises compared to the more robust M1.

Lastly, a potential operational scenario applicable to any data-driven method is also analyzed, considering a series of fine-tuning sessions simulating different batches of images downlinked to ground from the ECP phase of the Hera mission. This analysis turned out more complex and counterintuitive than expected, highlighting the challenges in fine-tuning these algorithms on specific characteristics of the target body. Indeed, both methods performed better in the DCP phase when fine-tuning was not applied, suggesting that both networks' training is affected more by different ranges than different shape models of the target asteroid. A possible explanation is that given the reference trajectories and the asteroid's rotation, both data-driven methods are trained considering images showing different orientations of the target with respect to the spacecraft. Therefore, the two methodologies are already trained with images showing a target with different shapes, since Didymos' irregular shape is shown differently in each image. On the other hand, the range depends on the apparent size of the asteroid in the images, which is unique at different range intervals.

To conclude, this work demonstrates that different data-driven approaches possess subtle differences that a coherent validation campaign can highlight. This ultimately represents an important tool for a mission designer to make informed decisions on their use. Considering overall performance, robustness, computational time, and fine-tuning inertia, one network was not clearly better than another, both exhibiting different sets of strengths and weaknesses that resonate for the better or for the worse in different untested conditions. M1 is less sensitive to new untested conditions due to its larger capacity (with $\sim$8 times more parameters than M2), showing greater robustness. This comes at a cost of high inertia to fine-tuning, slower computational time, and some highly variable convergence rates due to unclear heatmaps. M2 is a more efficient network, exhibiting greater accuracy and precision, shorter computational times, more agile fine-tuning, and always convergent to a solution. This comes at the cost of an increased sensitivity to untested conditions.

Finally, the analysis illustrated in this work would have not been possible without a shared testbench serving as a common baseline. This also motivates the decision of the authors to make both datasets and results publicly available to encourage other

researchers to propose different approaches. Future works could be focused specifically on the fine-tuning campaign of the ECP, including data-augmentation and image-manipulations as pre-processing steps of the ECP dataset. Furthermore, a hybrid training strategy and different architectures could be investigated.

Chapter 5

Incremental validation test campaign of a CNN-based Image Processing algorithm for autonomous visual based navigation applied to the Hera mission

A true adventure begins when
imagination collides with reality

Karel Capek

Kaluthantrige A., Feng, J.[‡], Di Domenico, G.[§] and Gil-Fernández, J.[¶]

Submitted to *Journal of Advances in Space Research*, August 2025

[‡]Associate professor, Department of Mechanical and Aerospace Engineering, University of Strathclyde

[§]PhD Student, Department of Aerospace Science and Technology, Politecnico di Milano

[¶]Guidance, Navigation and Control Engineer, ESA ESTEC

Paper content

This chapter presents a concise overview of the incremental validation campaign for the algorithm built in Chapter 2. The chapter demonstrates that the artificial intelligence-based image-processing algorithm is capable of providing robust and accurate optical navigation for Hera across mission-relevant proximity phases, with successful deployment on representative hardware, while highlighting implementation challenges like calibration sensitivity and memory constraints. Following the map and structure shown in Fig. 1.8 in Section 1.3.3, this chapter addresses RQ 2b, completing all the answer to RQ 2, and achieves the objective of validating the developed algorithm for a future utilization on board spacecraft stated in RO 3. With this chapter, the reader will understand how to structure a multi-stage validation campaign and what are the core factors to monitor when implementing intelligent-image processing algorithms on board a spacecraft.

Abstract

This paper presents the incremental validation test campaign of a Convolutional Neural Network-based Image Processing algorithm with application to the proximity operations of the European Space Agency's Hera mission around the target binary asteroid system (65803) Didymos. The algorithm estimates the position of the Center of Mass of both the primary and the secondary (if visible), the range from the primary, and the associated covariance matrices using the synthetic images generated with the SW Planet and Asteroid Natural Scene Generation Utility. The first step of this incremental validation process is an Open-Loop and Closed-Loop Model-In-The-Loop test, which uses the Functional Engineering Simulator of the Guidance, Navigation and Control system of the Hera mission. The second step is a bare-metal Open-Loop test run on the processing system of a Zynq 7000 System-on-a-Chip, considered in this work as the representative of a typical spacecraft On-Board Computer. The third and final step is an Open-Loop Hardware-In-The-Loop test, which includes the Hera mission's camera functional model and it is run at the GMV Optical Laboratory. The test case scenarios are the Early Characterization Phase, the Detailed Characterization Phase and the Close Observation Phase of the proximity operations of the Hera mission, when the vision-based navigation system is based on the centroid of Didymos. Therefore, the incremental validation test campaign presented in this work considers only the position of the Center of Mass of the primary estimated by the developed Image Processing algorithm. The results show that the algorithm is able to perform accurately its estimations across the multiple tests, with a slight dependency on the calibration of the camera. Nevertheless, the results show that prior to the implementation on a spacecraft On-Board computer the algorithm requires a dedicated memory optimization process.

5.1 Introduction

Vision-based navigation systems are a core module for small bodies rendezvous space missions. The European Space Agency (ESA)'s Rosetta, the Jaxa's Hayabusa 1 and 2 and NASA's OSIRIS-REx all used a vision-based navigation system, usually coupled

with a LIDAR (Light Detection and Ranging) and/or other sensors in order to provide a robust navigation algorithm and perform safely mission operations around the respective target body [64, 65, 118, 119]. Due to large communication delays, the unknown dynamical environment and to facilitate the rendezvous operations, autonomous navigation is preferred over ground-based [156]. To meet the required level of autonomy per operation scenario and to probe the algorithm's boundaries and its sensitivity to external disturbances and noise, vision-based navigation systems go through several validation tests on ground. The two main testbeds used to validate vision-based navigation systems are virtual and physical realities. The first one consists in stimulating the vision-based navigation system with images representing the mission scenario. To this end, rendering engines such as Planet and Asteroid Natural Scene Generation Utility (PANGU) used from ESA and SurRender used by Airbus are able to generate synthetic high-fidelity images of the target according to its shape, the spacecraft's relative trajectory and attitude and the Sun's position [102, 157]. The second testbed is a Hardware-In-The-Loop (HIL), which relies on the inclusion of one or more hardware manufactured for the specific mission, and performed in dedicated facilities that emulate space-representative conditions [133–141, 158].

This work presents the incremental validation of a Convolutional Neural Network (CNN)-based Image Processing (IP) algorithm applied to the vision-based navigation system of the Hera mission around the target binary asteroid system (65803) Didymos. The Hera mission is the European contribution to a joint collaboration born between NASA and ESA [34]. The aim is to send a group of spacecraft to Didymos, with the following three main goals:

- To explore the viability of a planetary defense strategy involving a kinetic impactor.
- To enhance our understanding of small celestial bodies within the solar system.
- To advance the technology required for future asteroid missions.

NASA launched the Double Asteroid Redirection Test (DART) mission in November 2021, and its primary task to execute a kinetic impact on the secondary body of the

Didymos system, Dimorphos, was accomplished in September 2022. The Hera mission is scheduled to reach the asteroid approximately five years after the impact [35]. Hera's mission objectives include a detailed investigation of the effects caused by DART's kinetic impact and the execution of additional scientific observations. As a component of the Hera mission, two CubeSats will be deployed from the main spacecraft upon arrival. These CubeSats will orbit the Didymos system closely, enabling comprehensive scientific observations. Juventas, one of these CubeSats, is designed to land on the surface of Dimorphos. During Juventas' descent, on-board cameras will acquire images of Dimorphos' surface, potentially including the impact site of DART [36, 37].

Hera will initiate the proximity operations after completing the interplanetary cruise and decreasing its velocity with respect to the target with the execution of multiple Delta-V maneuvers. This study primarily centers on the Early Characterization Phase (ECP), the Detailed Characterization Phase (DCP), and the Close Observation Phase (COP), intended to conduct thorough physical and dynamical assessments of the binary asteroid and to fully characterize the impact crater [40]. Autonomous vision-based navigation is designed for these phases based on line-of-sight and range measurements from Didymos in order to estimate the relative position of the spacecraft. The navigation system includes the on-board Asteroid Framing Camera (AFC) taking images of the asteroid, an IP algorithm that extracts information from these images, and a navigation filter that combines the visual data with the dynamical environment to estimate the relative state of the spacecraft with respect to the target [127]. The IP algorithm implemented in Hera is the Maximum Correlation with a Lambertian Sphere (MCLS) developed by GMV[1], an international space technology company in charge of the Guidance, Navigation and Control (GNC) system of the Hera mission, and designed to extract from the acquired images the position of the Center of Mass (COM) of Didymos every 48 s [58]. The goal of the autonomous visual based GNC system during the first three proximity operations is to maintain the position of the centroid of Didymos in the center of the camera frame. Therefore, the estimated position of the centroid from the IP algorithm is used to correct the error in the orientation of

[1] `https://www.gmv.com/en/sectors/space`, last accessed: 18 September 2023

the boresight of the camera of the spacecraft and achieve this goal. Throughout the ECP, the autonomous visual based navigation system's functionality is tested as the spacecraft orbits at a more secure distance from the target. Tuned parameters are then transmitted from ground to improve its performance with the robustness ensured from ground validation. Following this commissioning process, the autonomous visual based navigation system is used during the DCP and the COP to safely orbit around the target and perform the required mission operations [40].

The CNN-based IP algorithm of this work is developed and presented by the authors in [80, 142]. During the ECP, the DCP and the COP trajectories, the algorithm, using images acquired by the AFC accurately determines the centroids' positions for Didymos and Dimorphos (if accessible) along with the distance from Didymos and the covariance matrix associated to each measurement. For an in-depth understanding of the algorithm's development pipeline, readers are directed to [80,142]. Recent advancements in artificial intelligence (AI) for computer vision have shown the effectiveness of deep-learning convolutional architectures in IP tasks [82, 159, 160]. These methods are increasingly significant for space-related applications, particularly in the areas of IP, visual navigation, and control. The primary benefit of these techniques in the context of visual navigation around asteroids lies in their ability to overcome challenges usually faced by standard IP algorithms such as presence of other bodies (stars or asteroid's moons) in the image, the irregular shape of the target, low Sun phase angles, presence of hot pixels or other noises/distortions in the images. Nevertheless, this benefit comes at the cost of a large amount of data needed for training. If the target is unknown, then the utilization of an AI technique relies on an online training performed during mission operations, which requires high computational power not available on the state-of-the-art On-Board Computers (OBC) processors. Furthermore, most of the AI techniques for computer vision lack explainability, i.e. their internal processes are not easily interpretable by humans. Therefore, the verification and validation of AI-based techniques is challenging and it is essential to test them, as the one developed in this work and based on CNNs, with every mission scenario to validate their functionality across multiple contingencies that might occur during mission operations [69, 75, 145, 147, 161].

The incremental validation of the developed algorithm presented in this work consists of:

- three Model-In-The-Loop (MIL) tests run during the ECP and the DCP trajectories using the GPU of the local machine; the MIL tests use the model-based environment of the GNC system of the Hera mission developed by GMV.
- two On-processor tests run on a Zynq 7000 System-on-a-Chip (SoC)[2].
- three HIL tests with the Hera's spacecraft Functional Model (FUMO) of the AFC; the HIL tests are run in the GMV Optical Laboratory.

The MIL tests are aimed to analyze the performance and the robustness of the algorithm when integrated with the whole software-based GNC system. The On-processor tests assess the performances of the algorithm on a computing system representative of a typical spacecraft OBC processor. With the HIL tests it is possible to analyze the robustness of the algorithm to the electro-optical effects introduced by a spaceborn camera. Since during the ECP, the DCP and the COP the navigation is centroid-based, the tests are aimed to validate the developed algorithm only for this measurement. By performing these tests, this work adopts the Design, Development, Validation and Verification (DDVV) strategy by GMV applied to their GNC models and algorithms [152]. The CNN-based IP algorithm is treated as a standard IP algorithm, with the usual challenges that the latter face during this validation strategy.

To the authors' knowledge, this is the first attempt to validate an AI-based IP algorithm through the DDVV strategy for space visual navigation systems. Although previous work has been done [135, 162–164] in the field, it mostly examined performing single tests or the validation of the whole AI-based navigation system. The integration in a model-based environment of a GNC system and subsequent incremental validation test campaign of a single AI-based algorithm is a unique contribution of this work.

The main objectives of this work are: to bridge the gap between the stand-alone application of CNNs in space IP and the integrated-application in a whole GNC system;

[2] `https://www.xilinx.com/products/silicon-devices/soc/zynq-7000.html`, last accessed: 25 September 2023

to analyze the performance of the developed algorithm when the images of the target differ from the ones used for training. Specifically, the performances of the developed algorithm are analyzed in conditions of different orbital geometry, a slightly different shape of the target and considering images acquired with a space qualified hardware with all the noises and distortion introduced.

While Hera on-board GNC system is going to use the MCLS algorithm, the CNN-based IP algorithm presented in this paper may become an alternative for future asteroid missions. Moreover, the testing and validation of the CNN-based IP took benefit of realistic and very detailed Hera vision-based simulation and validation environments made available by GMV and ESA and used primarily for the Hera MCLS-based IP.

This paper is structured as follows. Section 5.2 describes more in detail the proposed IP algorithm and its validation process. Section 5.3 performs the numerical simulations and analyzes the results. Finally Section 5.4 concludes this research and recommends future research directions.

5.2 Methodology

This section provides a detailed description of the methodology applied in this work to validate the developed CNN-based IP algorithm applied to the Hera mission. With centroid or COM we refer to the geometrical center of the target body projected on the image. The developed algorithm presented in [80, 142] is briefly introduced in Section 5.2.3. While [80,142] focused on the ECP and the DCP trajectories, in this work we include also the COP (Section 5.2.1). The same software to generate synthetic images of Didymos and Dimorphos is used (Section 5.2.2). The details of the methodology of this work are presented in the next part of this section.

5.2.1 Reference trajectories

The three reference trajectories used in this work are the ECP, the DCP and the COP of the Hera mission. The ECP is the first of the proximity operations, when the spacecraft is orbiting around the target at a safer distance while conducting a

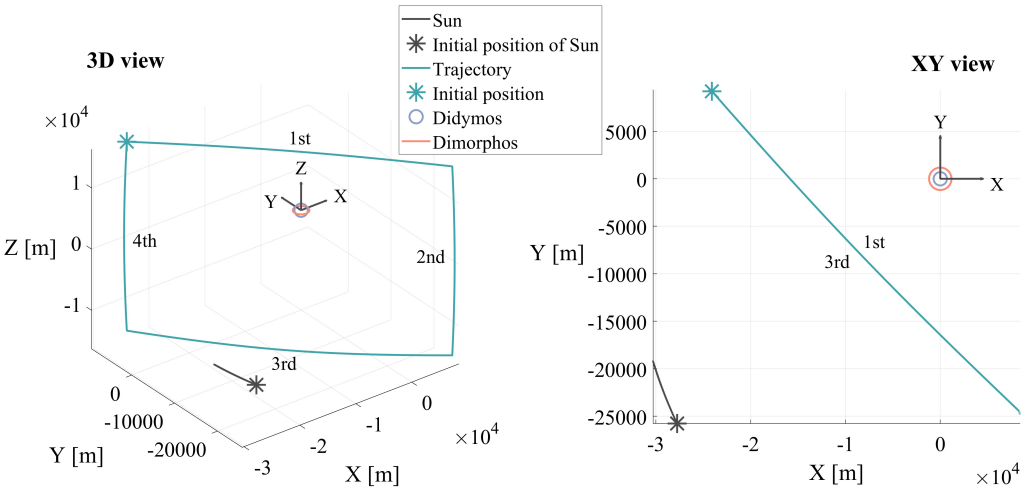

Figure 5.1: ECP trajectory [142]

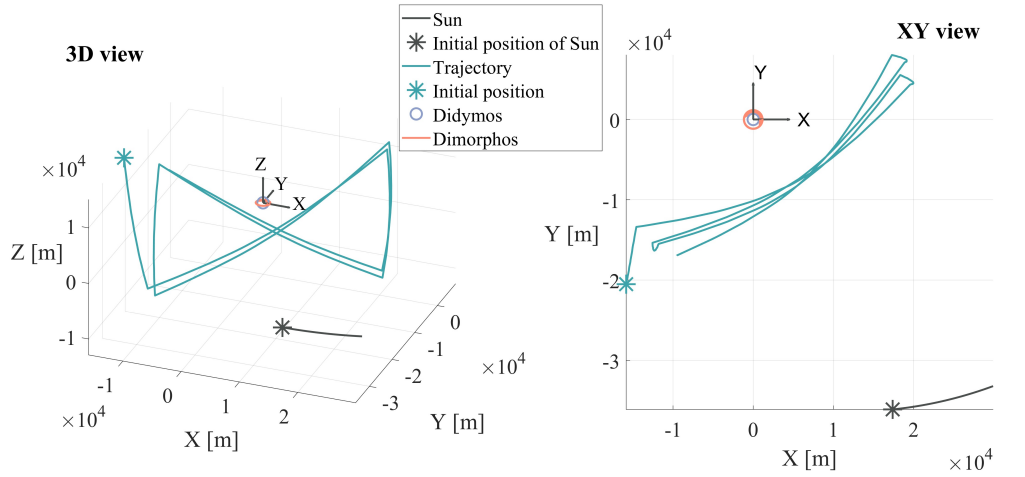

Figure 5.2: DCP trajectory [142]

preliminary physical and dynamical characterization of the asteroid [36]. Fig. 5.1, Fig. 5.2 and Fig. 5.3 illustrate respectively the ECP, DCP and COP trajectories in the Target Body Equatorial Inertial (TB) reference frame, which has the origin centered on the geometrical center of Didymos, the fundamental plane coplanar with the equatorial plane of Didymos and the X-axis of the Earth-centered Ecliptic Inertial reference frame. The ephemeris of the target are reported in Table 5.1 [20, 101]. In this work the orbit of Dimorphos around Didymos prior to the impact is used. These three proximity

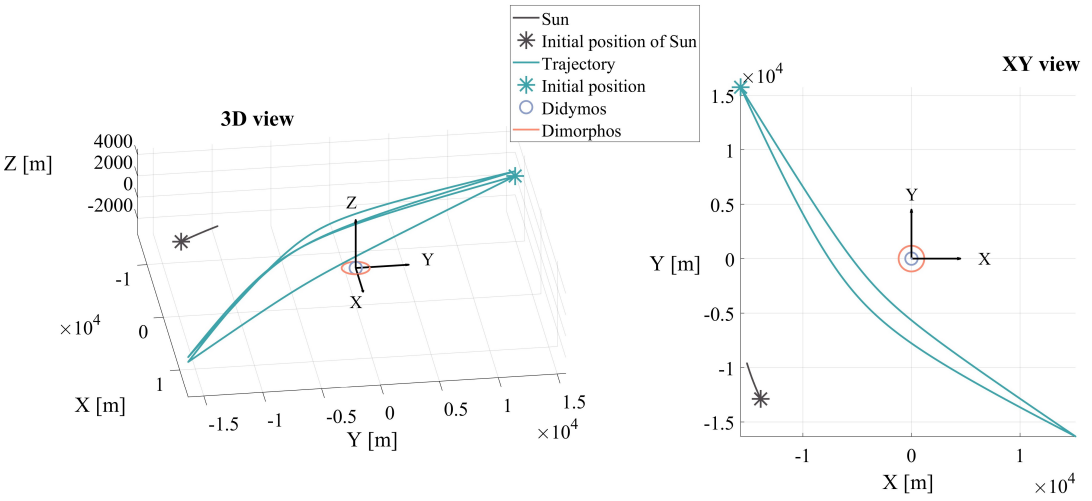

Figure 5.3: COP trajectory

Table 5.1: Orbital properties of Didymos system prior to DART's impact [20, 101]

Heliocentric orbit	
Semi-major axis $[au]$	$1.642665 \pm 2.7214e-9$
Eccentricity []	$0.383264 \pm 1.3374e-10$
Inclination [°]	$3.41415 \pm 1.6188e-8$
Longitude of ascending node [°]	$72.987867 \pm 2.1852e-7$
Orbital period $[yr]$	$2.105386 \pm 5.2320e-10$
Binary orbit	
Semi-major axis $[m]$	1190 ± 30
Eccentricity []	0
Orbital period $[hr]$	11.93 ± 0.01

operations trajectories shown in these plots are provided by ESA. Both trajectories are made by patching several hyperbolic arcs in order to be able to escape the gravitational attraction of Didymos for the safety of operations. The distance with the target and the position of the arcs with respect to the Sun take into account two main drivers: the Field of View (FOV) of the AFC, that needs to be able to contain the whole shape of Didymos (ECP and DCP) and Dimorphos (COP), and the need for bright images for the IP algorithm. The ECP consists of four square-shaped arcs while the DCP and the COP consist of several z-shaped arcs, all the trajectories with a total duration of 14 d.

The minimum and maximum distances with respect to the target are respectively: 20 km and 30 km for the ECP, 9 km and 23 km for the DCP and 4 km and 22 km for the COP [40].

5.2.2 Image Generation

Table 5.2: Didymos' system properties [28, 29]

Body	Didymos		Dimorphos	
Gravitational parameter $[km^3/s^2]$	$3.5 \cdot 10^{-8}$		$2 \cdot 10^{-10}$	
Extent along principal axes	Updated	Not updated	Updated	Not Updated
x-axis $[m]$	849 ± 5.6	832 ± 25	177 ± 1.2	208
y-axis $[m]$	851 ± 5.6	837 ± 25	174 ± 1.2	160
z-axis $[m]$	620 ± 5.6	786 ± 39	116 ± 1.2	133

The database of images used in this work to test and validate the developed CNN-based IP algorithm is generated with PANGU, a simulation tool developed by the STARDundee engineering company used widely across multiple ESA interplanetary missions to validate their optical navigation systems. With PANGU it is possible to model the shapes and surfaces of Didymos and Dimorphos and to render them, in order to provide a high-fidelity visualization of the mission scenario [102]. The shape models of Didymos and Dimorphos are provided by ESA (also available in GMV optical laboratory) and updated with the observations retrieved by the DART mission before the impact, with parameters summarized in Table 5.2. Given that the extents along the x and y axes are larger than the one along the z axis, the shapes of Didymos and Dimorphos are similar to two oblate ellipsoids. For Dimorphos, a scaled-down shape model of asteroid Itokawa, the target of the Hayabusa mission, is used. It is not known whether the impact with DART generated a crater on Dimorphos' surface, or whether said crater will be absorbed by the time the Hera spacecraft reaches the target [91]. As a reference, Table 5.2 shows also the characteristics of the shape models of Didymos and Dimorphos prior to DART's updates and obtained solely with ground observations.

PANGU shows the generated images on its viewer, set up with the properties of the AFC, reported on Table 5.3 [103, 104]. The viewer is a plane of the size of the image acquired by the camera, and the coordinates of each pixel are identified in the viewer's reference frame, which has the origin on the top left corner and the x- and y-axis referred to as i- and j- direction respectively, as shown in Fig. 5.4. The $z-$axis of the viewer's reference frame has the same direction of the camera's boresight. When the GNC system is in the asteroid imaging mode, the AFC has its boresight axis pointing towards Didymos or Dimorphos, and the spacecraft attitude is such that the position vector of the Sun is always lying on the xz plane of the viewer's reference frame. As a consequence, the binary asteroid system is shown in the PANGU viewer always illuminated from its right side [40].

Table 5.3: AFC properties [103, 104]

FOV	**Focal length**: f	**Aperture**	**Image size**	**Pixel size**: ν
5.5°	10.6 cm	2.5 cm	1024 × 1024 px	14 μm

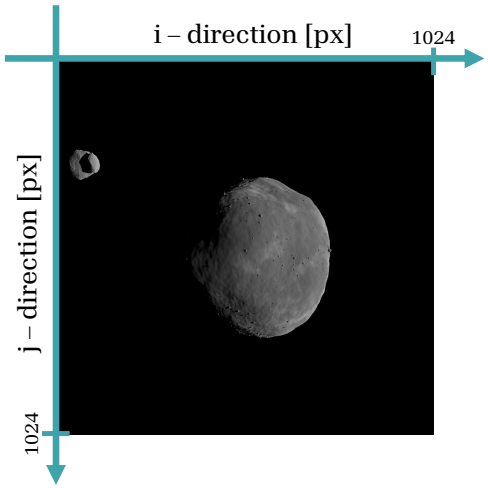

Figure 5.4: Example of image taken during ECP and shown in the PANGU viewer [142]

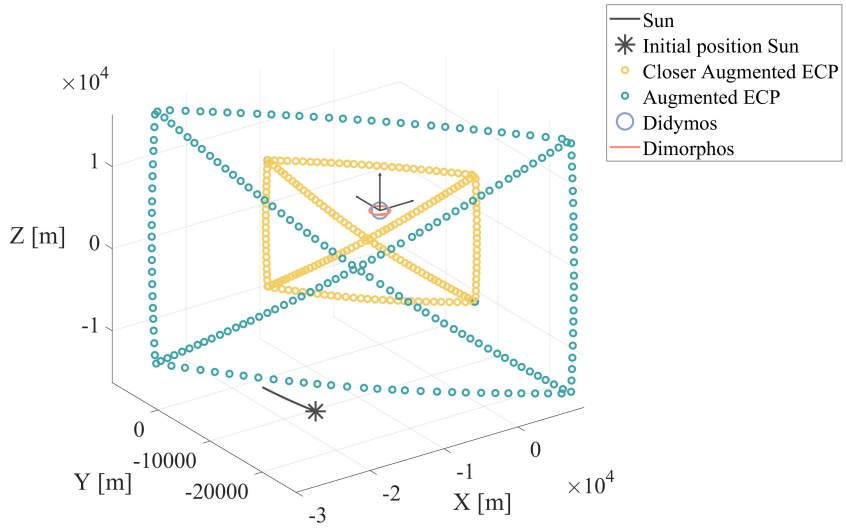

Figure 5.5: Augmented ECP trajectory [142]

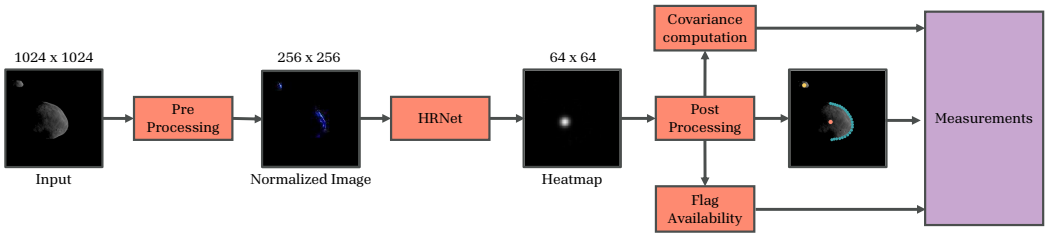

Figure 5.6: CNN-based IP algorithm [142]

5.2.3 Image Processing

In this section a summary of the operations that each image undergoes with the CNN-based IP algorithm is given, as represented in Fig. 5.6. We use PANGU to generate 40,000 images of the target with the updated shape taken during the ECP in order to calibrate the CNN-based IP algorithm's parameters to achieve the optimal results prior to the incremental validation test campaign. The trajectory is augmented by adding two fictitious diagonal arcs that connect the vertices of the square, as shown by the cyan circles in Fig. 5.5. The 40,000 images include a subset generated considering a closer augmented ECP trajectory, shown with the yellow circles of Fig. 5.5. A pointing error of a maximum absolute value of 10% of the AFC's FOV is considered for each

generated image to change the position of Didymos randomly on the PANGU viewer. No background noise is considered for the generation of these images. Training the algorithm with the $40,000$ images of the augmented ECP trajectory is only intended for the on-ground validation approach. It does not exclude the possibility of further fine-tuning or re-training of the algorithm prior to the application in the real mission.

Hereby are presented the operations performed on each image (for in-depth information on the pipeline of this algorithm please refer to [80, 142]):

1. *Pre-Processing*: The 1024×1024 px image acquired by the AFC is reduced in size (256×256 px) and its pixel intensities are normalized as required by the selected CNN architecture.

2. *HRNet*: The High-Resolution Network (HRNet) CNN architecture is used in this work, with the aim of regressing the location of specific keypoints on the image [107], as shown in Fig. 5.7: the COM of Didymos, the COM of Dimorphos (if visible) and 24 points on the right side of Didymos, i.e. its visible border, which are used to estimate the range with Didymos using the pinhole camera model [105]; the HRNet provides its solution in the form of heatmaps of size 64×64 px associated to the corresponding desired keypoint. Most of the CNN architectures which solve for the keypoint heatmap estimation problem consist in a main body structured with a high-to-low followed by low-to-high framework. This approach decreases the spatial resolution of the estimation, as key information of the pixels of the input image are distributed in less pixels. The HRNet tackles this issue by connecting high-to-low subnetworks in parallel, maintaining a high-resolution representation of the input image through the whole architecture [107].

3. *Post-Processing*: Each heatmap is analyzed in order to extract the x and y coordinates of its peak intensity, which represents the location of the regressed keypoint, as shown in Fig. 5.7. The coordinates of the keypoints in the 64×64 px heatmaps are then converted back to the original 1024×1024 px size image.

4. *Covariance computation*: The intensity and the shape of the cloud of points surrounding the heatmap's peak is examined to derive the regressed keypoint's

associated covariance matrix.

5. *Flag Availability*: The value of the peak intensity of the heatmap associated to the regression of the location of the COM of Dimorphos is analyzed to determine whether Dimorphos is visible or not in the images, as shown in Fig. 5.8.

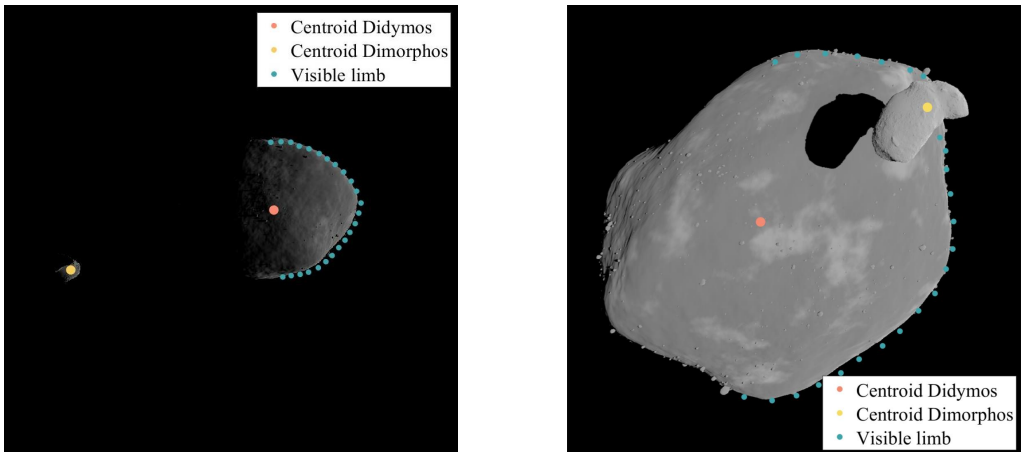

Figure 5.7: Two sample images generated with PANGU with the regressed keypoints [142]

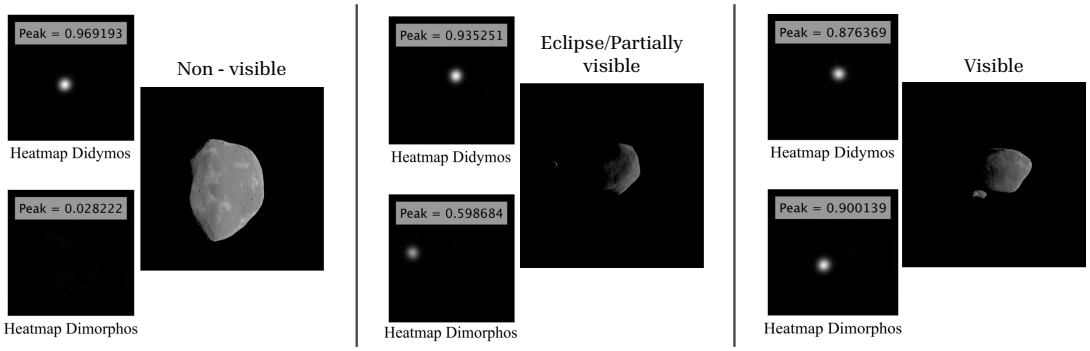

Figure 5.8: Heatmaps of the centroid of Didymos and Dimorphos associated with three sample images showing Dimorphos respectively non-visible, in eclipse and visible [142]

The HRNet is trained on Google Colab with the NVIDIA T4 GPU, and the trained model is imported on Matlab as an ONNX (Open Neural Network Exchange) format. The whole IP algorithm, with the aforementioned blocks has a total weight of 125 MB. Further details about this algorithm can be found in [80, 142].

5.2.4 Incremental validation

Table 5.4 summarizes the test campaign adopted for validating the developed CNN-based IP algorithm from MIL to HIL. Each test and its functionality is described in the following sections. With Open-Loop (OL) is intended that the Hera MCLS algorithm is used for navigation and the CNN-based IP algorithm is only run in parallel. With Closed-Loop (CL) the CNN-based IP algorithm replaces the MCLS for navigation. The updated and not updated shapes of Didymos and Dimorphos after DART's mission are shown in Table 5.2 and are both used and referred for simplicity as Shape 1 and Shape 2, respectively.

Although the algorithm is able to provide the estimation of the position of the centroids of Didymos and Dimorphos on the image, the range from Didymos and the associated covariances to these measurements, this incremental validation test campaign examines only the estimation of the position of the centroid of Didymos. This stems from the fact that the reference phases of the proximity operations undertaken in this work consider only this measurement for the visual navigation, which is the only output of the MCLS IP algorithm on board the Hera GNC system. The range measurements and the covariances of each measurement, if needed in the tests, are provided by other models and algorithms not analyzed in this work.

Table 5.4: Incremental validation test campaign

Name	**Loop**	**Trajectory**	**Shape**
MIL Test 1	Open	2^{nd} arc of ECP	1
MIL Test 2	Open	6^{th} arc of DCP	1
MIL Test 3	Closed	6^{th} arc of DCP	1
On-processor Test 1	Open	2^{nd} arc of ECP	1
On-processor Test 2	Open	6^{th} arc of DCP	1
HIL Test 1	Open	2^{nd} arc of COP	1
HIL Test 2	Open	2^{nd} arc of COP	2
HIL Test 3	Open	6^{th} arc of DCP	1
HIL Test 4	Open	6^{th} arc of DCP	2

5.2.4.1 MIL Test Setup

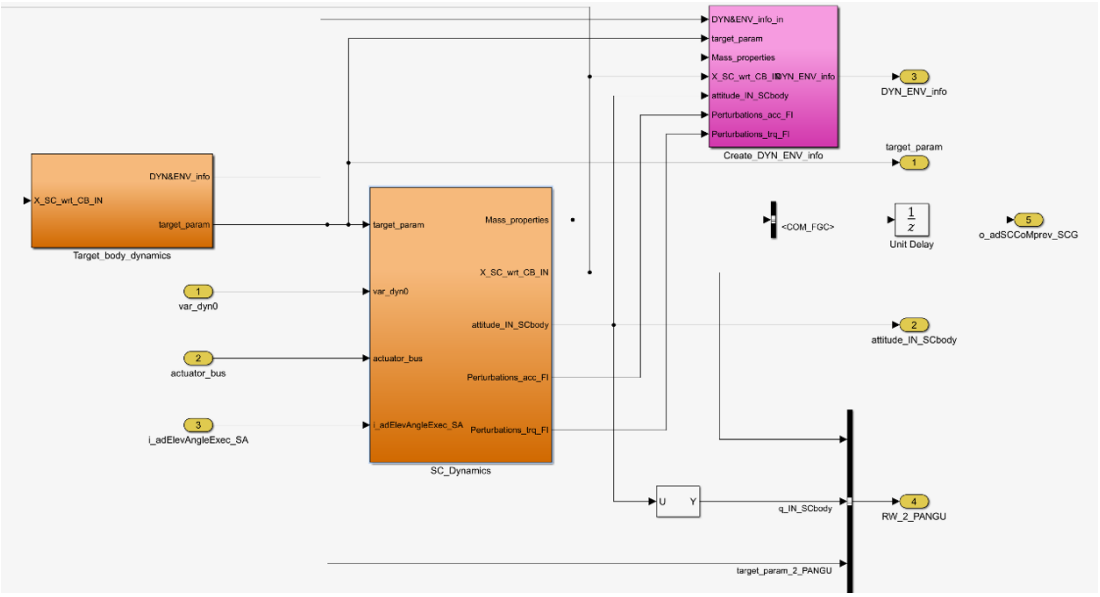

Figure 5.9: Hera DKE block

The MIL tests are run with the Functional Engineering Simulator (FES) developed by GMV on Simulink. The FES is a software environment that allows to test the GNC design/algorithms by closing the loop using models for the Dynamics, Kinematics, and Environment (DKE) effects. The DKE models are, thus, in charge of simulating the environment and physics laws affecting the spacecraft dynamics. Fig. 5.9 shows an example of the DKE layer in a MIL test architecture configuration. The list of the major blocks that can be identified are:

- *Target_body_dynamics*: contains the ephemeris of the celestial bodies involved in the simulations, the rotation matrix of the reference axes fixed to these bodies and an inertial reference, their radius, and, if needed, the offset between their COM and the center of gravity of the system.

- *SC_Dynamics*: Contains the Mass, Center of gravity and Inertia (MCI) properties of the spacecraft, and computes the forces and torques exerted on the spacecraft; finally, in this block the position and attitude of the spacecraft are propagated using the aforementioned computations.

The three major blocks of the *SC_Dynamics* layer are:

- *MCI_update*: contains the evolution of the MCI properties.
- *Forces_and_Moments*: contains the forces and torques exerted on the spacecraft by the central body gravity acceleration, the considered perturbations and those caused by the actions of the actuators.
- *Dynamics*: contains the translational and attitude dynamics equations which allows to propagate the relative state of the spacecraft.

The Attitude and Orbit Control System Units of Hera are the following: Gyro, Star Trackers, Sun Sensors and Reaction Wheels. Other GNC models include the thrusters, the AFC, represented by PANGU, and the Planet Altimeter. These models are part of the closed-loop configuration with the Hera GNC software, composed by the GNC Application software and the IP software used in the Hera mission baseline. The developed CNN-based IP algorithm is embedded to the FES and it is used to estimate the COM of Didymos given an image generated by the AFC model. The estimated COM is used together with the dynamics computed with the DKE block and the measurements obtained from the other sensors to provide the best estimate of the relative position and attitude of the spacecraft. Specifically, the developed CNN-based IP algorithm is embedded in the translational navigation filter of the FES of the GNC. During the ECP and the DCP, the purpose of the translational navigation of the Hera mission is to perform data fusion with the measurements of the position of the COM of Didymos (using the pinhole camera model [105]) and the Planet Altimeter, if available, in order to estimate the state vector of the spacecraft. This happens only during the ECP and the DCP as the distance to the binary system is above 9 km, which allows the primary body to not fill the entire camera's FOV. The measurements are taken every 10 min, except for communication windows of 8 hr to Earth, and in between the measurements the spacecraft's state is being propagated. The navigation filter is a hybrid between an Extended Kalman Filter (EKF) and an Unscented Kalman Filter (UKF): the propagation of the state of the spacecraft is done using the EKF approach and with the relative dynamics contained in the *Dynamics* block of the FES. When a

measurement is available, the innovation of the spacecraft's state is done with the UKF method. The covariance matrix is always propagated using the UKF approach [58].

In order to integrate the Matlab format of the CNN-based IP algorithm with the FES developed on Simulink, the ONNX format of the HRNet obtained as described before is adapted for code generation. From there, the Matlab/Simulink Coder is run, including the other blocks of the IP algorithm. The Coder settings involved no dynamic memory, no Open Multi Processing[3] (OpenMP) libraries and support for deep-learning code generation. A generic ARM-compatible device is selected as target hardware and C++ code is selected as output. The C++ code is then uploaded in the Simulink model of the FES as an S-function.

In this work we run three different MIL tests:

1. MIL Test 1: OL test with synthetic images generated during the 2^{nd} arc of the ECP with Shape 1 of Didymos and Dimorphos.

2. MIL Test 2: OL test with synthetic images generated during the 6^{th} arc of the DCP with Shape 1 of Didymos and Dimorphos.

3. MIL Test 3: CL test with synthetic images generated during the 6^{th} arc of the DCP with Shape 1 of Didymos and Dimorphos.

With the OL tests it is possible to analyze the accuracy of the estimations of the CNN-based IP algorithm with synthetic images generated with training-like conditions (MIL Test 1) and with unfamiliar conditions (MIL Test 2) of illumination and relative position of the target. While in MIL Test 1 and MIL Test 2 the Hera MCLS algorithm is the one used for navigation, with MIL Test 3 it is possible to evaluate the closed-loop behaviour of the GNC system when the provided centroid of Didymos is given by the developed CNN-based IP algorithm. No background noise is introduced in the images generated by the AFC model (embedded in PANGU model), as the behavior of the developed IP algorithm with respect to noises and distortions are analyzed with the HIL test. The MIL tests are run with Matlab on the NVIDIA GeForce RTX 2070 with Max Q-design GPU of the local machine.

[3] `https://www.openmp.org/wp-content/uploads/OpenMP-API-Specification-5-2.pdf`, last accessed: 25 September 2023

5.2.4.2 On-processor Test Setup

Additionally, the S-function of the CNN-based IP algorithm is run on a Zynq-7000 SoC processor, in order to evaluate the algorithm performances in terms of computational time and on-board memory requirements on a processor with the computational power similar to the one available on board the spacecraft. Once the C++ sources of the CNN-based IP algorithm are obtained, the zWrap toolchain[4] is employed to deploy the algorithm on a ZedBoard on which the Zynq 7000 SoC is located. The toolchain takes the source files as input and generates a boot image for the board, featuring a dual-core Asynchronous Multi-Processing (AMP) application in which the first ARM core is dedicated for socket-based communication to the host and the second core is entirely dedicated to the deployed CNN-based IP algorithm. A shared memory region, whose size and location is automatically inferred by the toolchain, is allocated to store the inputs and output variables. Apart from the application image, the toolchain also outputs a drop-in Matlab/Simulink function and a drop-in Simulink block to run the application with inputs provided from the host, in order to seamlessly convert existing MIL simulations into Processor-In-The-Loop (PIL) simulations. The communication from the host to the board happens through TCP/UDP. There is minimal overhead on the board side, as the only task for the application running on the first ARM core is to move the incoming packets to the shared memory region; this is possible because the input data are serialized (and deserialized) on the host side thanks to auto-generated interfaces during the image building process. The exact byte generation for the input and outputs is passed to the Zynq, so that no memory nor CPU time is needed to pass the data to the target function. The on-board application is connected to a Simulink model with the generated block, and a subset of 40 images generated with MIL Test 1 and MIL Test 2 are tested in OL. Therefore, the On-processor tests are:

1. On-processor Test 1: OL test with a subset of synthetic images generated during the 2^{nd} arc of the ECP with Shape 1 of Didymos and Dimorphos, run on the Zynq-7000 SoC processor.

[4] `https://github.com/gian-didom/zWrap`, last accessed: 25 September 2023

2. On-processor Test 2: OL test with a subset of synthetic images generated during the 6^{th} arc of the DCP with Shape 1 of Didymos and Dimorphos, run on the Zynq-7000 SoC processor.

With these two tests, we evaluate the execution time (that ideally should be around the 48 s required by the MCLS algorithm) and the memory requirements on a representative processor that emulates the capabilities of the one usually employed on spacecraft.

5.2.4.3 HIL Test Setup

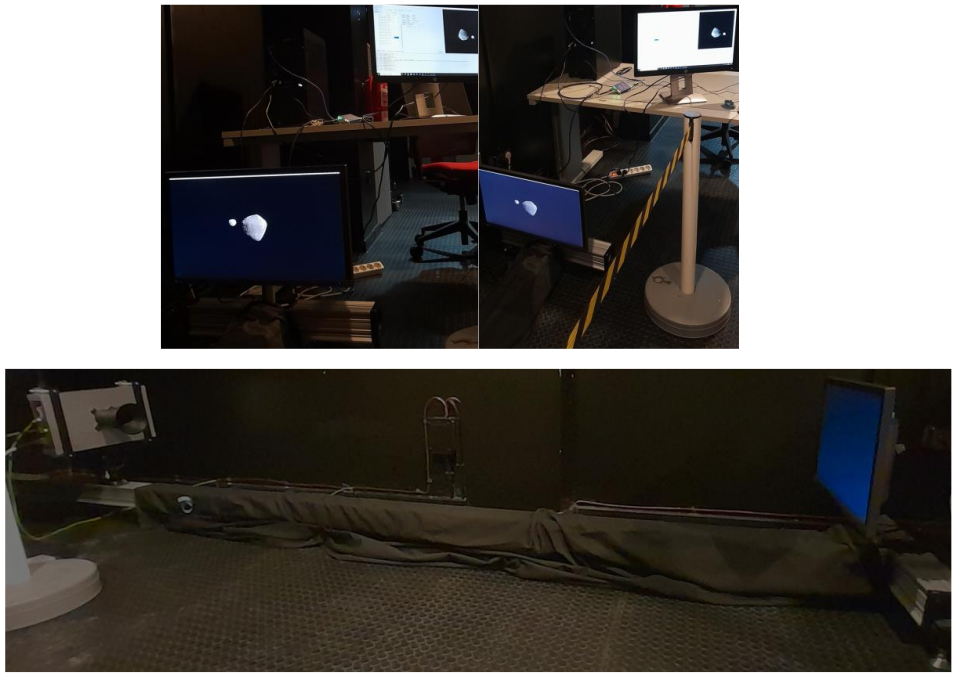

Figure 5.10: GMV Optical Laboratory in Hera setup (includes Hera AFC FUMO - courtesy of ESA)

The HIL tests are run in the GMV Optical Laboratory, used in past and on-going projects for validation of optical navigation solutions. It relies on confidence on the PANGU models of the target asteroid (without the need of the mock-up used in the robotic platform of GMV). Fig. 5.10 shows the current setup of the HIL test, featuring:

❖ the AFC FUMO, courtesy of ESA and developed by Jena Optronik GmbH [165].

- a monitor with 4k resolution where images of PANGU are projected; 2×2 px of the screen stimulates 1 detector px, in order to avoid aliasing and keep the smoothness of the image.

- a rail where the AFC FUMO and the monitor are mounted.

- the Hera Avionics Test Bench (ATB) PC, that runs the FES, projects the images on the high resolution screen, and controls the acquisition of images by the AFC FUMO.

This setup has its own specific mounting and inherent optical characteristics and it requires for each project/mission a dedicated calibration. Parameters such as point spread function, alignment (either physical or software corrections) and gamma need to be adjusted to be representative of what the camera "would see" in the real flight scenario. This means to correct for effects inherent to the optical setup and leaving the remaining effects such as camera electro-optical properties unaffected. The calibration was completed and with errors much smaller than required image processing errors performance. The photometrics are optimised to assume a good ground calibration and low in-flight degradation of this calibration/knowledge.

Fig. 5.11, Table 5.5, Fig. 5.12 and Fig. 5.13 show the results achieved for the calibration of the AFC FUMO setup, demonstrating the capacity of the GMV Optical Laboratory and in-house calibration procedures to offer good quality imaging setups without compromising the representativity (if required) of accurate imaging conditions in-flight:

- *Alignment and focus*: Fig. 5.11 and Table 5.5 show the achieved point spread function and alignment errors (only with physical correction). The Point Spread Function (PSF) illustrates the normalized luminosity captured by a portion of the camera sensor when a dot, approximately the size of a pixel sensor, is presented on the screen, enabling the analysis of both bloom effects and focus quality.

- *Radiometric correction*: The radiometric adjustments are balanced between flight configuration and laboratory conditions. The AFC FUMO is set to an integration

time of $\sim 50\ ms$, considering that in nominal flight conditions it can range from hundreds of μs to few ms. Gain and bias matrices (applied as a post-process to the acquired image) are used in conjunction with an alteration of the image displayed on the monitor using a gamma function in order to obtain a uniform brightness curve. Fig. 5.12 shows the column-wise average brightness obtained by the camera for the horizontal gradient that is shown.

❖ *Geometric distortion*: Fig. 5.13 shows the achieved distortion errors (to both correct screen distortions and emulated on-board image corrections). The plot on the left of Fig. 5.13 illustrates the normalized error between the true radial position of a displayed pixel and the position acquired by the camera sensor. The discontinued line signals the radius that corresponds with the corner of the sensor. The plot on the right of Fig. 5.13 displays the absolute error in pixel position, representing the disparity between the actual location of a displayed pixel and the position recorded by the camera sensor. The calculation of this error was performed across a grid of 31×31 positions. The warm-colored surface is associated to pre-correction error values while the cool-colored one represents said magnitude after performing the distortion correction.

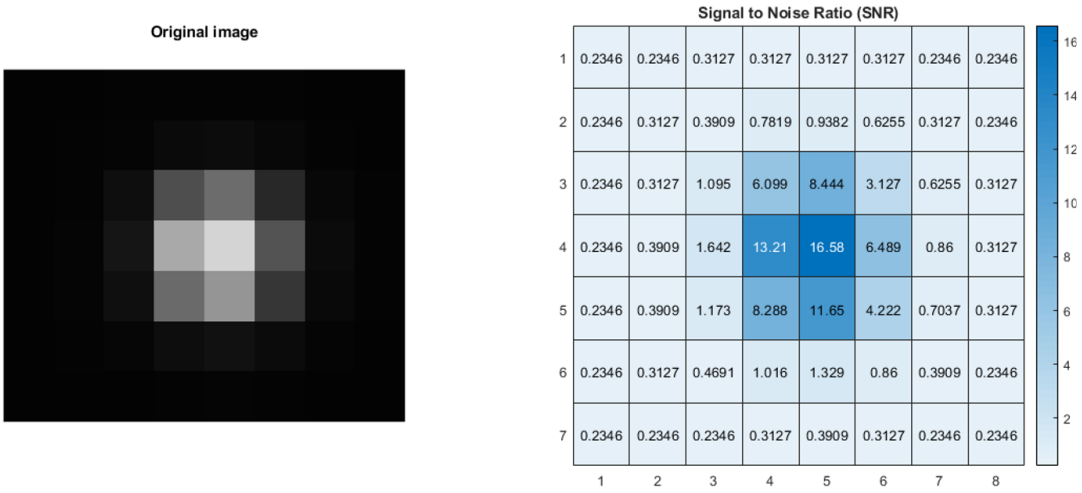

Figure 5.11: GMV Optical Laboratory: Achieved Point Spread Function in Hera HIL setup

Table 5.5: GMV Optical Laboratory: Achieved Alignment errors in Hera HIL setup

Parameter	**Misalignment detected**
Camera Yaw	$< 0.5°$
Camera Pitch	$< 0.5°$
Camera Roll	$< 0.1°$
Image center $i-$direction	$0.3\ px$
Image center $j-$direction	$-0.06\ px$

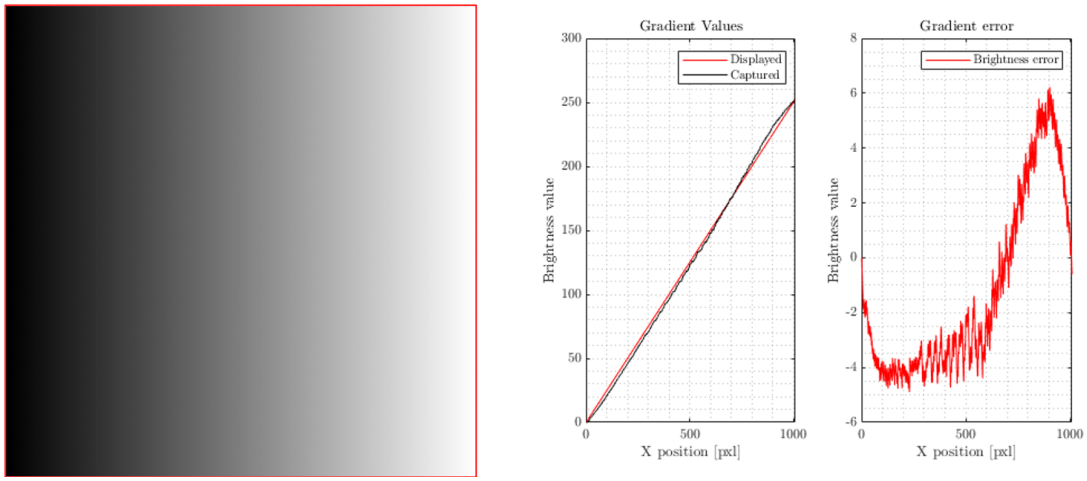

Figure 5.12: GMV Optical Laboratory: Gradient used (left) and achieved calibration errors (right)

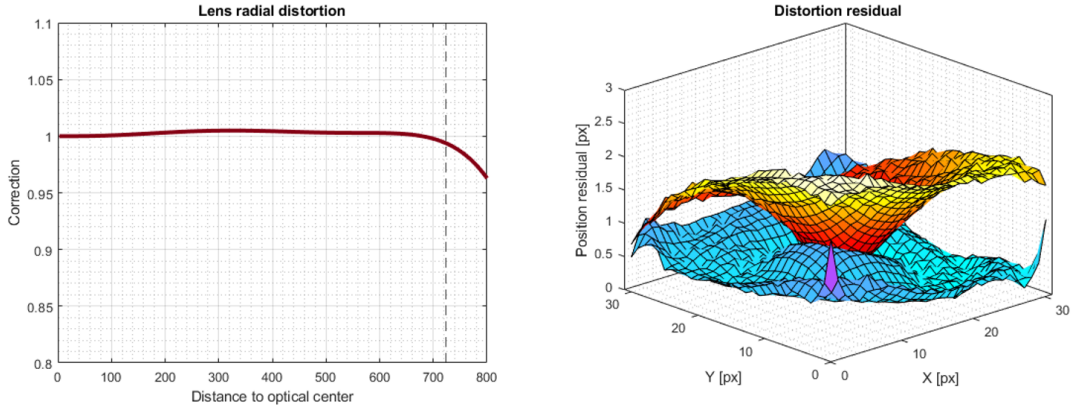

Figure 5.13: GMV Optical Laboratory: Achieved Distortion Errors in Hera HIL setup

Once the HIL setup is calibrated, the FES is run with the Hera ATB PC, and images generated with PANGU are projected on the high resolution screen. For each image,

the AFC FUMO acquires a photo which is used to test the CNN-based IP algorithm in OL. We run four different HIL tests:

1. HIL Test 1: OL test with acquired images during the 2^{nd} arc of the COP with Shape 1 of Didymos and Dimorphos.

2. HIL Test 2: OL test with acquired images during the 2^{nd} arc of the COP with Shape 2 of Didymos and Dimorphos.

3. HIL Test 3: OL test with acquired images during the 6^{th} arc of the DCP with Shape 1 of Didymos and Dimorphos.

4. HIL Test 4: OL test with acquired images during the 6^{th} arc of the DCP with Shape 2 of Didymos and Dimorphos.

HIL Tests 1 and 3 aim to test the robustness of the CNN-based IP algorithm to the camera electro-optical effects, while HIL Tests 2 and 4 introduce also the effect represented by an unfamiliar shape of the target that was never seen during training. Therefore, with HIL Tests 2 and 4 we are testing the CNN-based IP algorithm with the most realistic situation that will occur during the mission, i.e. the acquired images and the shape of the target are different from what were used to validate and optimize the algorithm on ground.

5.3 Results

In this section, the results of the incremental validation of the developed CNN-based IP algorithm applied to the Hera mission scenarios are presented. For the MIL OL Tests shown in Table 5.4 the accuracy on the estimation of the position of the centroid of Didymos (COM_{est}) on the images is assessed with the absolute error with respect to Ground Truth (GT) (COM_{GT}), defined as follows:

$$\epsilon_{COM} = |COM_{GT} - COM_{est}| \tag{5.1}$$

This metric is applied to both $i-$ and $j-$ directions of the PANGU viewer. These results are compared with the ones obtained in [80], where the same IP algorithm was applied to the shape models of Didymos and Dimorphos prior to DART's close encounter. For Didymos the average ϵ_{COM} obtained was 5.35 px on the $i-$direction and 4.41 px on the $j-$direction. These results were obtained by applying the developed IP algorithm over a set of 6052 images generated with PANGU during the ECP trajectory. Eq. Chapter 5Epsilon COM is also applied to HIL Test 2 and HIL Test 4 in order to quantify the absolute error made in estimating the centroid in the most realistic scenario where both the input image and the shape of the target are unfamiliar to the developed IP algorithm.

Additionally, with the MIL CL Test the closed-loop behaviour of the developed algorithm is tested. This is done by analyzing the performances in terms of position estimation of Hera with respect to Didymos in camera frame when the developed IP algorithm is implemented, using the following metrics:

$$\epsilon_{\boldsymbol{x}} = \boldsymbol{x}_{GT} - \boldsymbol{x}_{est} \tag{5.2}$$

where $\boldsymbol{x}_{GT}$ and $\boldsymbol{x}_{est}$ represent respectively the GT and the estimated position of Hera with respect to Didymos in camera frame.

For the HIL tests, an additional metric is introduced to capture the error introduced by the camera. Eq. 5.3 defines the absolute error between ϵ_{COM} applied to the images acquired by the camera (ϵ^c_{COM}) and applied to the corresponding image generated with PANGU (ϵ^p_{COM}). Eq. 5.3 is applied to the images showing Shape 1 of Didymos and Dimorphos (i.e. HIL Test 1 and Test 3), hence it is aimed to capture only the electro-optical effects introduced by the camera.

$$\epsilon_c = |\epsilon^c_{COM} - \epsilon^p_{COM}| \tag{5.3}$$

Eq. 5.3 is applied to both $i-$ and $j-$ directions of the PANGU viewer.

5.3.1 MIL Tests

The average computational time required for processing a single image from the IP block is 2.4828 s with a standard deviation of 0.21 s.

5.3.1.1 MIL Test 1

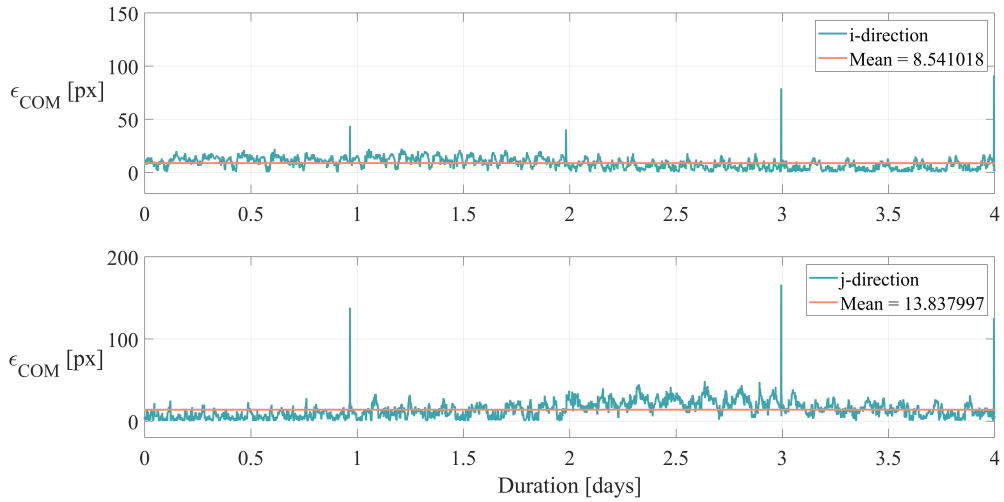

Figure 5.14: ϵ_{COM}: MIL Test 1

Fig. 5.14 illustrates the performance of the CNN-based IP algorithm in estimating the position of the Fig. 5.14 illustrates the performance of the CNN-based IP algorithm in estimating the position of the centroid of Didymos for MIL Test 1. It is possible to see that the absolute error oscillates around 8.54 px in the $i-$direction and around 13.83 px in the $j-$direction, with a standard deviation of $\sigma_i = 5.28$ px and 9.84 px, respectively. The 4 peaks of the error are obtained during the data transmission time, when the spacecraft is not pointing anymore to the target and, therefore, the images generated with PANGU do not present Didymos. The slight increase, with subsequent reduction, of the error in the $j-$direction from the second day of duration of the ECP arc is the result of a limited error made by the MCLS algorithm in the estimation of the position of COM_{GT} with Shape 1 of Didymos. Nevertheless, comparing with the results obtained in [80], the centroid estimation follows GT, therefore the developed algorithm is performing accurately with a dataset of images representing the target

with the same illumination and geometric conditions used for training.

5.3.1.2 MIL Test 2

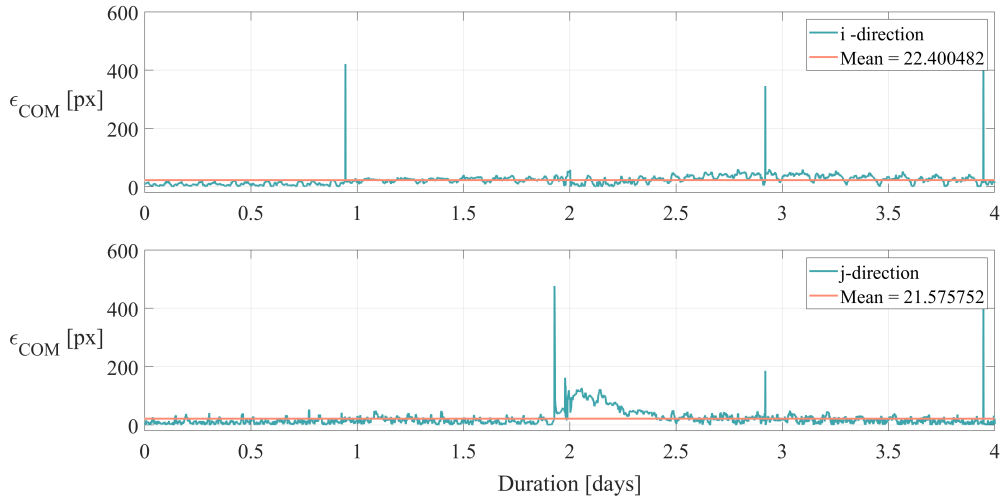

Figure 5.15: ϵ_{COM}: MIL Test 2

Fig. 5.15 illustrates the performance of the CNN-based IP algorithm in estimating the position of the centroid of Didymos for MIL Test 2. It is possible to see that the absolute error oscillates around 22.4 px in the $i-$direction and around 21.57 px in the $j-$direction, with a standard deviation of $\sigma_i = 16.43$ px and 24.93 px. The peaks of the error are obtained during the data transmission time, when the spacecraft is not pointing towards the target and, therefore, the images generated with PANGU do not present Didymos. The slight increase, with subsequent reduction, of the error in the $j-$direction from the second day of duration of the DCP arc is the result of a limited error made by the MCLS algorithm in the estimation of the position of COM_{GT} with Shape 1 of Didymos.

Nevertheless, the values of ε_{COM} are similar to the ones obtained in [80], therefore meeting the Hera mission requirements of pointing accuracy. In particular, it can be seen that the error in the $i-$ direction, the direction of the incoming illumination, is comparable to the one in the $j-$direction, which means that the developed IP algorithm is not affected by the illumination conditions, as it was already proven in [80]. The

error is higher compared to the one obtained for MIL Test 1 mainly because the range from the asteroid is lower and the projected image of Didymos in the camera is bigger. An additional reason could be the point of observation of the spacecraft relatively to the target which results in a different projection of the asteroid onto the images. Nevertheless, the spacecraft during the phases of the proximity operations considered in this work is orbiting the target asteroids observing it from any possible orientation, given the relative geometry of the hyperbolic arcs and the asteroid's rotation period. Therefore, the contribution to the error of the point of observation is less relevant.

5.3.1.3 MIL Test 3

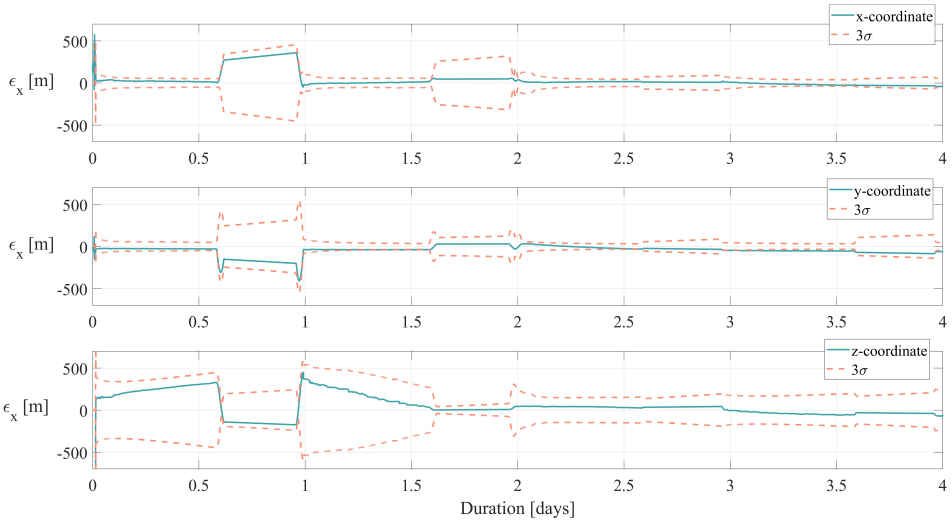

Figure 5.16: ϵ_x: MIL Test 3

Fig. 5.16 represents the error in the estimated position in camera frame for MIL Test 3, together with the associated covariance cone (3σ). It can be seen that the position of the spacecraft with respect to Didymos can still be estimated accurately in closed-loop when the developed IP algorithm is replaced in the loop, with an error of the order of 50 m in the camera plane ($x-$, $y-$ coordinates) and of 100 m in the boresight direction ($z-$coordinate). It is also shown that the position error follows accurately the covariance cone, which increases during the data transmission time interval, when the spacecraft is not pointing towards the target.

5.3.2 On-processor Tests

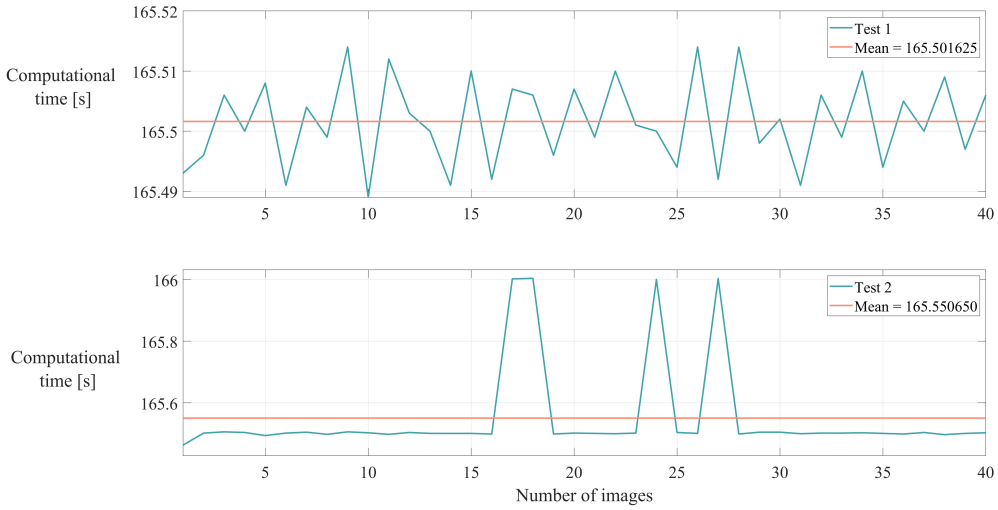

Figure 5.17: Execution time for On-processor Test 1 and 2

The On-processor tests show a longer execution time with respect to local machine; the Zynq is able to process a single image of a subset of 40 images generated with both On-processor Test 1 and On-processor Test 2, with an average computational time of 165 s, as shown in Fig. 5.17, higher than the 48 s required by the MCLS algorithm. The nature of the implementation, with no underlying operative system or dynamic memory allocation, and the type of algorithm resulted in a real-time implementation; indeed, the recorded computational time registers a standard deviation of just 0.15 s, less than 0.01%. Moreover, such variations take into account the communication overhead, as the time is measured on the host side before and after the communication.

The on-board memory requirements are organized as follows:

- 108.95 MB for the `.text` section, containing function symbols and constant data. This accounts for most part of the on-board memory requirements since it contains all the weights and biases of the network.
- the `.data` section accounted for 1.43 KB. This contains non-constant, initialized variables.

- ❖ the `.bss` section accounted for 155.24 MB and refers to the space occupied by uninitialized variables.

Overall, the total RAM required is about 264 MB. Therefore, the weights and biases of the network accounts for 41% of the total RAM required. It should be noted that no memory optimization is performed during this test. Moreover, a static analysis of the stack size requirements show that the maximum stack size for the net to run is about 200 KB. These figures offer large space for improvement, hence exploring solutions involving lower-precision arithmetic, dedicated hardware, and clever review of the static-declared variables can greatly improve the memory required by the application.

5.3.3 HIL Tests

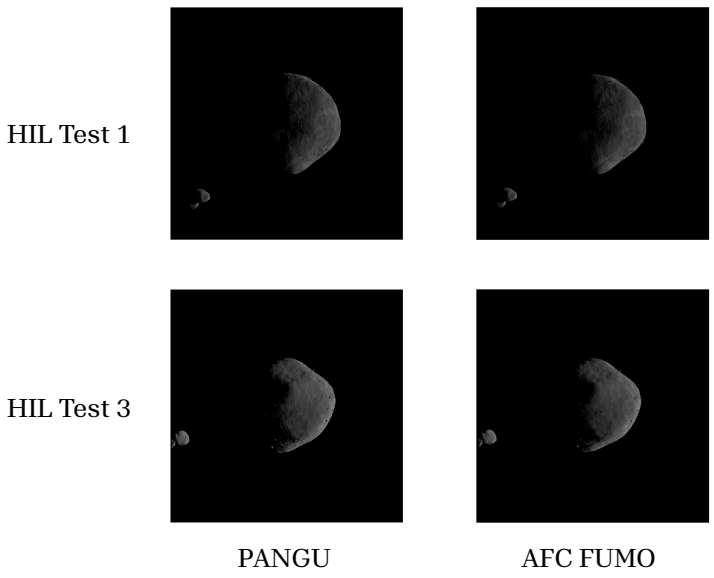

Figure 5.18: Example image captured with the AFC FUMO (right) and its corresponding PANGU image (left) for the HIL Test 1 (above) and HIL Test 3 (below)

Fig. 5.18 shows 2 images taken with the HIL setup employed in this work, with the corresponding PANGU image. It can be seen how the dedicated calibration minimizes the effects introduced by the camera.

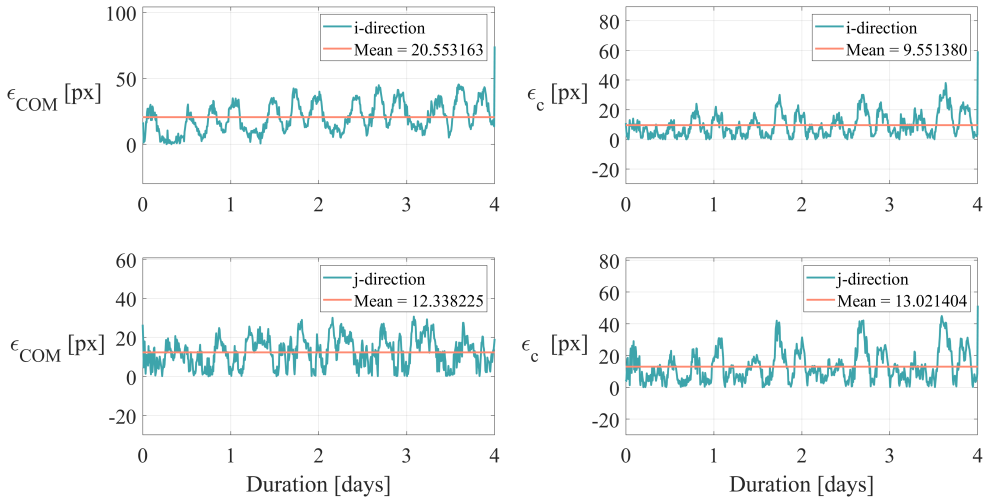

Figure 5.19: ϵ_{COM}: HIL Test 2 (left); ϵ_c: HIL Test 1 (right)

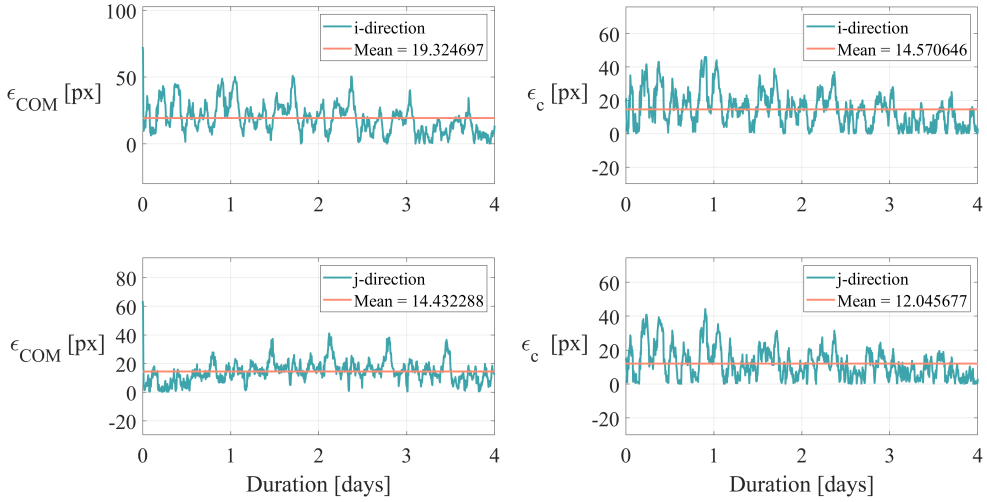

Figure 5.20: ϵ_{COM}: HIL Test 4 (left); ϵ_c: HIL Test 3 (right)

5.3.3.1 HIL Test 1 and HIL Test 2

Fig. 5.19 shows the value of ϵ_{COM} (left) obtained with HIL Test 2 and the value of ϵ_c (right) obtained with HIL Test 1, divided in $i-$ (above) and $j-$directions (below). It is possible to see that the absolute error of the centroid estimation with respect to GT oscillates around 20.55 px in the $i-$ direction and around 12.33 px in the $j-$direction, with $\sigma_i = 13.42\ px$ and $\sigma_j = 8.12\ px$, respectively. Therefore, even in the most realistic

scenario where both the shape of the target and the input images are different the CNN-based IP algorithm centroid estimation follows GT. The average bias introduced by the camera for HIL Test 1 is negligible, with a value of 9.55 px and 13.02 px, for the $i-$ and $j-$ directions, respectively.

5.3.3.2 HIL Test 3 and HIL Test 4

Fig. 5.20 shows the value of ϵ_{COM} (left) obtained with HIL Test 4 and the value of ϵ_c (right) obtained with HIL Test 3, divided in $i-$ (above) and $j-$directions (below). It is possible to see that the absolute error of the centroid estimation with respect to GT oscillates around 19.32 px in the $i-$ direction and around 14.43 px in the $j-$direction, with $\sigma_i = 11.77\ px$ and $\sigma_j = 9.67\ px$, respectively. The slight increase, with subsequent reduction, of the error in the $j-$direction from the second day of duration of the DCP arc seen on HIL Test 4, is the result of a limited error made by the MCLS algorithm in the estimation of the position of COM_{GT} with Shape 1 of Didymos. The same reason justifies the imperceptible decrease of the error in the i-direction. Nevertheless, the obtained values of the error show that even in the most realistic scenario where both the shape of the target and the input images are different from the training conditions the CNN-based IP algorithm centroid estimation follows GT. The average bias introduced by the camera for HIL Test 3 is negligible, with a value of 14.57 px and 12.04 px, for the $i-$ and $j-$ directions, respectively

5.4 Conclusion

This paper discusses the validation of a CNN-based IP algorithm addressing the problem of centroiding (Geometrical Center) applied to the autonomous visual based navigation around a binary asteroid system. The ECP, the DCP and the COP of the proximity operations of the Hera mission around the Didymos system are studied as case scenario. The test campaign consists of OL and CL MIL tests with the FES of the GNC developed by GMV, OL On-processor tests run on a Zynq 7000 SoC and OL HIL tests run at the GMV Optical laboratory with the AFC FUMO.

The OL MIL tests show that the developed algorithm is able to estimate accurately the position of the centroid of Didymos, showing its ability to perform well with a dataset of images representing the asteroid in familiar conditions seen during training (2^{nd} arc of the ECP) and to generalize its solution with a dataset of images representing the asteroid in unfamiliar orbital conditions (6^{th} arc of the DCP). In particular, the CL MIL Test shows that the developed IP algorithm can be implemented in the GNC system to estimate the position of the spacecraft. Future work is directed towards validating with MIL tests the developed IP algorithm considering all the arcs of the ECP and DCP.

The On-processor tests shows that the computational time required to process a single image is higher than the one baselined for the mission. Furthermore, the total RAM required to run the algorithm on board is high compared to the one available from a standard OBC processor. Future works foresee the implementation of the algorithm on other architectures (e.g. a LEON3 processor similar to the one used on the Hera spacecraft) and the evaluation of different implementations. For instance, working in single or fixed precision is expected to improve the computational performances with minimal impact on the accuracy and output of the network. Moreover, hardware-accelerated implementations exploiting Field Programmable Gate Array (FPGA) architectures are expected to decrease the computational time required for a single image processing by at least an order of magnitude, as both the IP pipeline and the HRNet structure are well-suited for parallelization.

The HIL tests show that the electro-optical effects introduced by the camera are minimal when estimating the centroid of Didymos. The CNN-based IP algorithm is robust to a different shape of the target with respect to the one used in training. Nevertheless, the results obtained depend on the dedicated calibration, which in this work aimed to minimize the difference between the acquired image and the PANGU image. During mission operations the images acquired with the camera will be different from the synthetic ones of PANGU: the different shape of the target, the presence of stars in the background and any other disturbance, the different illumination conditions and the high albedo that characterizes asteroids are all factors to take into account

when performing the calibration from ground. To optimize the centroiding estimation, a subset of images of the target acquired by the camera will be needed in order to fine-tune in-flight the developed IP algorithm prior to its utilization in the dedicated proximity operations.

In this work the challenges faced usually by a standard IP algorithm are analyzed through the DDVV strategy of GMV. Nevertheless, the behaviour of the developed CNN-based IP algorithm in other contingencies is essential to determine its generalization capability and the ability to bridge domain gaps. Future work will analyze the robustness of the algorithm in scenarios never seen during training such as: adverse illumination conditions, very different shape of the target, presence of noises and distortions and more in general using images generated with other tools.

Chapter 6

Pose estimation of Dimorphos using CNN-based Image Processing algorithm

To live is to suffer, to survive is to find some meaning in the suffering

Friedrich Niestzche

Kaluthantrige A., Feng, J.[‡] and Gil-Fernández, J.

In development

[‡]Associate professor, Department of Mechanical and Aerospace Engineering, University of Strathclyde

[¶]Guidance, Navigation and Control Engineer, ESA ESTEC

Paper content

This chapter discusses the development and application of an artificial intelligent-based image processing algorithm for estimating the six degrees of freedom (6-DoF) pose, position and attitude, of Dimorphos during the Close Observation Phase of ESA's Hera mission. This chapter does not address a specific research question; rather, it serves as a preliminary investigation aimed at addressing one of the significant challenges anticipated during the Hera mission's proximity operations.

Abstract

The Close Observation Phase (COP) is the proximity operation of the European Space Agency (ESA)'s Hera mission with the objective of obtaining high-resolution images of the target asteroid Didymos and its moon Dimorphos. The relative attitude of Dimorphos with respect to the spacecraft remains unsolved as standard feature tracking navigation techniques require closer distances to be able to extrapolate relevant feature from the target's surface. In this work we estimate the continuous six degree of freedom pose (position and attitude) of Dimorphos during the COP using a Convolutional Neural Networks (CNN)-based Image Processing (IP) algorithm, which is independent from the surface appearance. Instead, the algorithm relies on the lit limb of the target asteroid, and it consists of two stages. In the first stage, we use CNNs with the images captured by the spacecraft on-board camera to regress a set of keypoints segmenting Dimorphos from its background. In the second stage, we use Neural Networks (NN) to map these keypoints to the four quaternions representing the estimated relative rotation matrix of Dimorphos with respect to the spacecraft. The estimated keypoints are also used to estimate the position of the centroid of Dimorphos and its relative distance with respect to the spacecraft, which together provides the estimated relative position vector of the spacecraft.

6.1 Introduction

A joint space mission born with the collaboration between NASA and the European Space Agency (ESA) is underway with the aim of sending a group of spacecraft to the binary asteroid system known as (65803) Didymos. The objective of this cooperative effort can be summarized in three main goals:

- To explore the viability of a planetary defense strategy involving a kinetic impactor;
- To enhance our understanding of small celestial bodies within the solar system;
- To advance the technology required for future asteroid missions.

NASA launched the Double Asteroid Redirection Test (DART) mission in November 2021, and its primary task to execute a kinetic impact on the secondary body of the Didymos system, Dimorphos, was accomplished in September 2022. ESA's contribution, the Hera mission, is scheduled to reach the asteroid approximately five years after the impact. Hera's mission objectives include a detailed investigation of the effects caused by DART's kinetic impact and the execution of additional scientific observations. As a component of the Hera mission, two CubeSats will be deployed from the main spacecraft upon arrival. These CubeSats will orbit the Didymos system closely, enabling comprehensive scientific observations. Juventas, one of these CubeSats, is designed to land on the surface of Dimorphos. During Juventas' descent, on-board cameras will capture images of Dimorphos' surface, potentially including the impact site of DART [36, 37].

The two CubeSats will be released during the Close Observation Phase (COP) of the proximity operations of the Hera mission. The COP has the objective of obtaining high-resolution images of Dimorphos and fully characterizing the impact crater. The success of the landing phase require accurate knowledge of the relative attitude of Dimorphos, as well as a high-level of autonomy to operate safely at close distances [166]. Table 6.1 shows the properties of the binary asteroid system estimated with DART's observations prior to the impact [28, 29].

Table 6.1: Shapes of Didymos and Dimorphos prior to DART's impact [28, 29]

Parameter	**Didymos**	**Dimorphos**
Extent along principal axis x $[m]$	849 ± 5.6	177 ± 1.2
Extent along principal axis y $[m]$	851 ± 5.6	174 ± 1.2
Extent along principal axis z $[m]$	620 ± 5.6	116 ± 1.2

Autonomous optical navigation is designed for this phase based on line-of-sight and range measurements from both the primary body and Dimorphos in order to estimate the relative position of the spacecraft. Autonomy is essential due to potential com-

munication delays or limited coverage that makes impractical to rely solely on ground control station commands for navigating relative maneuvers. The navigation system includes the on-board Asteroid Framing Camera (AFC) taking images of the asteroid, an Image Processing (IP) algorithm that extracts information from these images, and a navigation filter that combines the visual data with the dynamical environment to estimate the relative state of the spacecraft with respect to the target [58]. The close distance between the primary and the spacecraft during the COP allows the implementation of feature tracking relative navigation to solve the primary's relative attitude. An IP algorithm extracts relevant features from the captured images of the target. Given the latter's shape, the features are then tracked and combined with a Kalman Filter to solve for the target's position and attitude. This approach was used in previous asteroid rendezvous missions as well, such as Rosetta or Hayabusa 2. In the former the features were used to reconstruct the shape and the attitude of the target with the aid of ground operators. In the latter the process was made entirely on board, using the features extracted in the first phases of the close proximity operations to reconstruct the target's shape prior to the attitude [118, 167–169].

Nevertheless, estimating the relative attitude of Dimorphos remains an unsolved problem as feature tracking algorithms require closer distances in order to be able to detect relevant features, due to Dimorphos' reduced size. Furthermore, studies on the attitude dynamics of Dimorphos consequently to the DART impact suggest that unstable tumbling is possible, which could potentially add further challenges for a feature tracking relative navigation algorithm [91].

In this work we develop a monocular pose estimation (position and attitude) algorithm for Dimorphos during the COP using a Convolutional Neural Networks (CNN)-based IP algorithm. Monocular pose estimation consists on leveraging 2D images taken by a camera on board the spacecraft to estimate the relative pose of a target. Estimation methods are divided into model-based, which makes use of a simplified wireframe 3D model of the target, and non-model based, which relies on the appearance or relevant features of the target. Given that a precise wireframe model of asteroids is difficult to attain prior to the close encounter of the spacecraft, our methodology is non-model

based [94, 170, 171].

The key of the developed algorithm is to leverage the lit limb of the target to estimate the rotation matrix representing the relative orientation of Dimorphos with respect to the spacecraft. By relying on the visible portion of the shape of the target, the developed algorithm is not constrained on the prior knowledge of the spinning state of the target [172]. Furthermore, relevant features such as craters or boulders can be detected only at reduced relative distances from the target, which is not the case for the whole COP trajectory. The choice of CNNs over standard IP algorithms is dictated by the robustness of the former over the adverse characteristics of the taken images, such as noise, distortions introduced during acquisition, the presence of stars or other undesired objects, the overall brightness and the irregular shape of Dimorphos. The challenges represented by these disturbances are addressed by the authors of this work in [80].

This paper is structured as follows. Section 6.2 describes in detail the developed algorithm. In Section 6.3 we show the obtained results during the COP trajectories and discuss the performances and applicability of the algorithm. Finally, Section 6.4 concludes this research and recommends future research directions.

6.2 Methodology

This section provides a detailed description of the monocular pose estimation algorithm developed in this work. With centroid or Center of Mass (COM) we refer to the geometrical center of the target body projected on the image. Fig. 6.1 shows the main steps of the pipeline of our methodology. The pipeline of our IP algorithm consists of three main modules: Regression, Mapping and Pinhole. The first module refers to the regression of the COM of Dimorphos and of a number of keypoints on its lit limb once an image is available at epoch t_{k+1}, and it is carried out by CNNs using the High-Resolution Network (HRNet) architecture. The second module refers to mapping the regressed keypoints to the rotation matrix describing the relative attitude of Dimorphos with respect to the spacecraft. The second module is carried out by a Neural Network

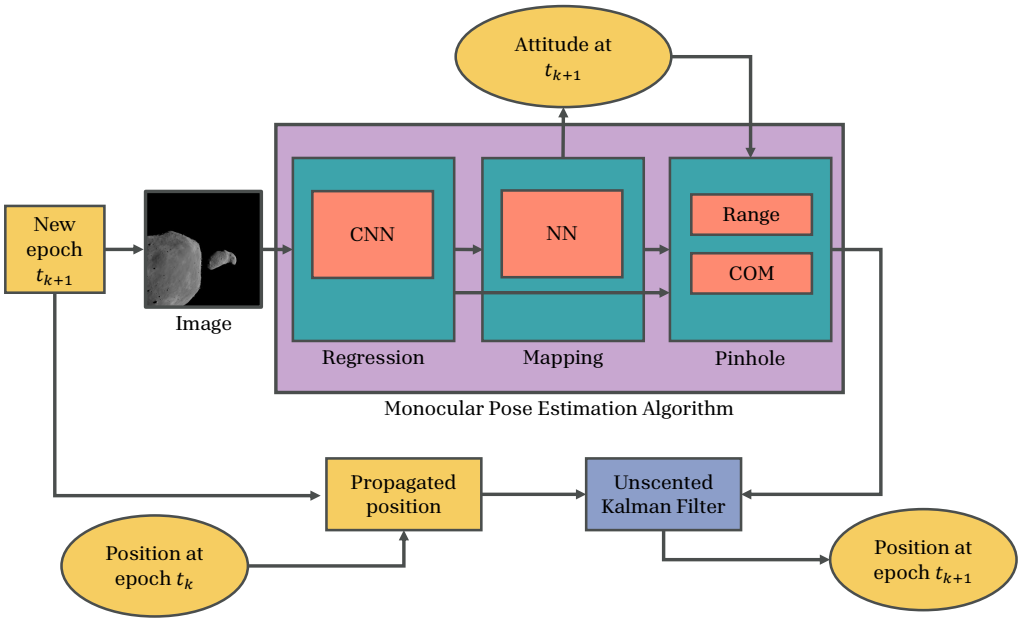

Figure 6.1: Pipeline of CNN-based IP algorithm for Dimorphos' pose estimation

(NN) developed in this work. In the third and final module the regressed keypoints are used to estimate the range of the spacecraft from the secondary using the pinhole camera model. The estimated range together with the estimated position of the COM are then combined with an Unscented Kalman Filter (UKF) together with the information derived from the dynamical environment to provide an estimate of the relative position of Dimorphos with respect to the spacecraft. The estimated relative attitude and position represent together the full estimated pose of Dimorphos at t_{k+1}.

The algorithm presented in this work builds upon [80], where the main objective was to build an IP algorithm estimating the position of the COMs of Didymos and Dimorphos, the range from Didymos and the Sun-phase angle, while having the camera pointing towards Didymos. The shape models used were the ones obtained via ground observations, before the updates provided by DART in September 2022. In contrast, in this research the camera points towards Dimorphos, the target of the developed pose estimation algorithm. Furthermore, the shape models are updated with DART's close encounter observations. Compared to [142] we use two reference trajectories for testing the algorithm (Section 6.2.1) and the same software to generate synthetic images of Didymos and Dimorphos (Section 6.2.2). The details of the developed algorithm are

presented in the next part of this section.

6.2.1 Reference trajectories

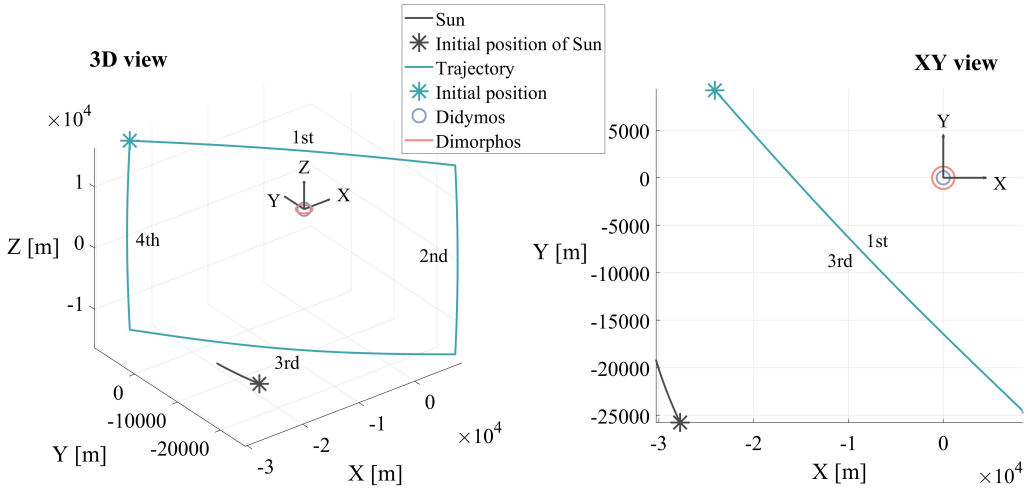

Figure 6.2: ECP trajectory [142]

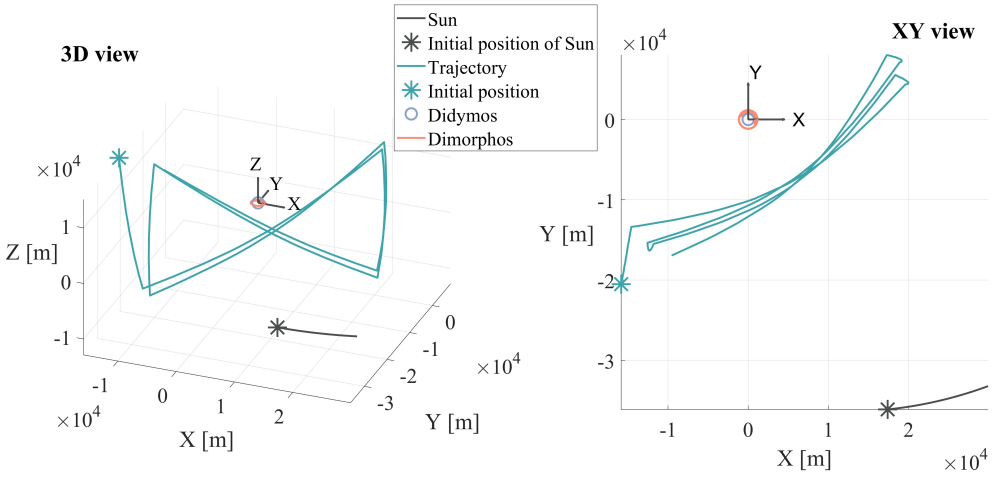

Figure 6.3: DCP trajectory [142]

The three reference trajectories used in this work are the Early Characterization Phase (ECP),the COP and the Detailed Characterization Phase (DCP) of the Hera mission. The ECP and the DCP are the first proximity operations, when the spacecraft

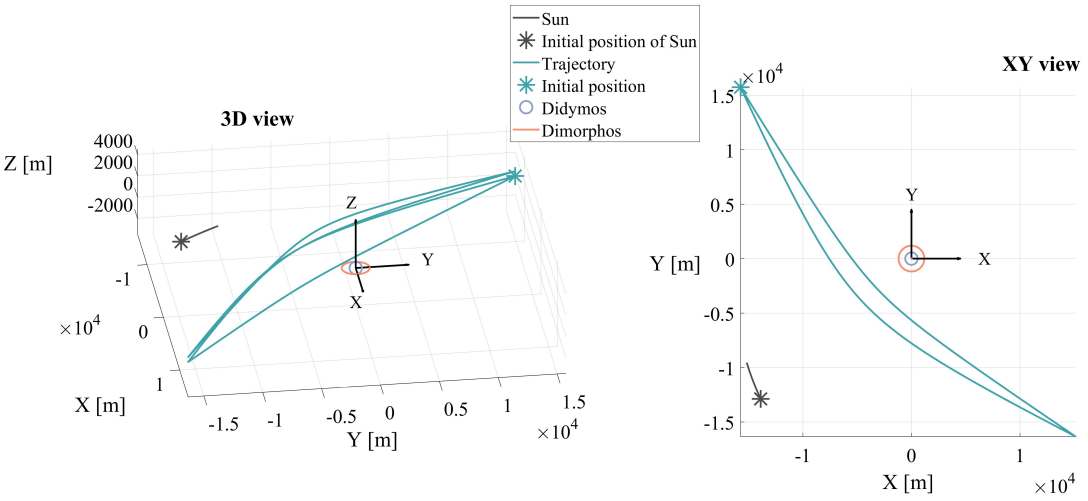

Figure 6.4: COP trajectory [173]

is conducting a physical and dynamical characterization of the target binary asteroid system [35]. Fig. 6.2, Fig. 6.3 and Fig. 6.4 illustrate respectively the ECP, the DCP and the COP trajectory in the Target Body Equatorial Inertial (TB) reference frame, which has the origin centered on the geometrical center of Didymos, the fundamental plane coplanar with the equatorial plane of Didymos and the X-axis of the Earth-centered Ecliptic Inertial reference frame. The ephemeris of the target are reported in Table 6.2 [20, 101, 142, 173].

In this work the orbit of Dimorphos around Didymos prior to the impact is used. DART's impact changed the orbital period of Dimorphos by an additional 33.25 *min* ± 15 *s*. This value is still evolving, which suggests that the impact generated debris whose gravitational attraction on Dimorphos act as a force against its along-track velocity [174]. Furthermore, prior to the impact, Dimorphos was tidally-locked to Didymos, i.e. its rotation period, along one of its principal axis of rotation, was equal to its orbital period, shown in Table 6.2. Nevertheless, studies shown that Dimorphos' spin state was excited by the impact, causing rotations along its non-principal axes. Dissipative effects generated by the tidal forces of Didymos may not be extremely efficient for Hera to find Dimorphos in a relaxed spin state [154]. For the sake of simplicity, we consider Dimorphos in its relaxed rotation prior to the impact.

Table 6.2: Selected orbital properties of Didymos system [20, 101]

Heliocentric orbit	
Semi-major axis $[au]$	$1.642665 \pm 2.7214e-9$
Eccentricity []	$0.383264 \pm 1.3374e-10$
Inclination $[°]$	$3.41415 \pm 1.6188e-8$
Longitude of ascending node $[°]$	$72.987867 \pm 2.1852e-7$
Orbital period $[yr]$	$2.105386 \pm 5.2320e-10$
Dimorphos' orbit around Didymos	
Semi-major axis $[m]$	1190 ± 30
Eccentricity []	0
Orbital period $[hr]$	11.93 ± 0.01
Rotational period $[hr]$	11.93 ± 0.01

The ECP, the DCP and the COP trajectories are provided by ESA. The trajectories are made by patching several hyperbolic arcs in order to be able to escape the gravitational attraction of Didymos for the safety of operations. The distance with the target and the position of the arcs with respect to the Sun take into account two main drivers: the Field of View of the AFC, that needs to be able to contain the whole shape of Didymos (ECP and DCP) and Dimorphos (COP), and the need for bright images (Sun phase angle $\gamma < 90°$) for the IP algorithm. The ECP consists of four square-shaped arcs while the DCP and the COP consist of several z-shaped arcs, all the trajectories with a total duration of 14 d. The minimum and maximum distances are respectively: 20 km and 30 km for the ECP, 9 km and 23 km for the DCP and 4 km and 22 km for the COP, shown in Fig. 6.5, Fig. 6.6 and Fig. 6.7 [40, 142] respectively.

6.2.2 Image generation

The database of images used in this work to develop the monocular pose estimation algorithm is generated with the software Planet and Asteroid Generation Utility (PANGU), a simulation tool developed by the STARDundee engineering company used widely across multiple ESA interplanetary missions to validate their optical navigation systems. With PANGU it is possible to model the shapes and surfaces of Didymos and

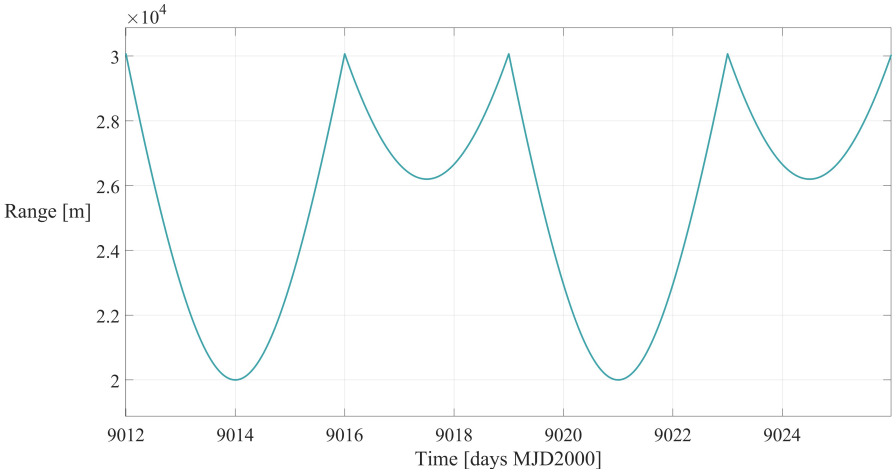

Figure 6.5: Range from Didymos during ECP trajectory [142]

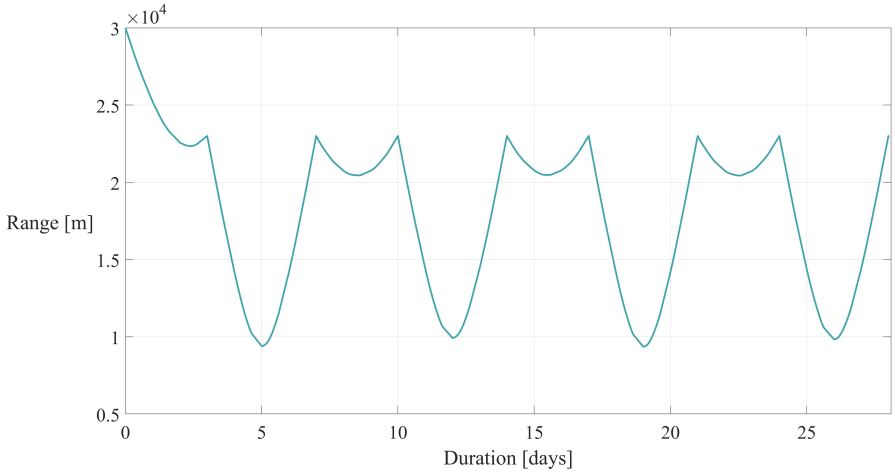

Figure 6.6: Range from Didymos during DCP trajectory [142]

Dimorphos and to render them, in order to provide a high-fidelity visualization of the mission scenario [102]. The shape models of Didymos and Dimorphos are provided by GMV Aerospace and Defence, in charge of the development of the software for the GNC of the Hera mission, and updated with the observations retrieved by the DART mission before the impact, shown in Table 6.1. Given that the extents along the x and y axes are larger than the one along the z axis, the shapes of Didymos and Dimorphos are similar to two oblate ellipsoids. For Dimorphos, a scaled-down shape model of asteroid Itokawa, the target of the Hayabus mission, is used. It is not known whether the impact with DART generated a crater on Dimorphos' surface, or whether said crater will be

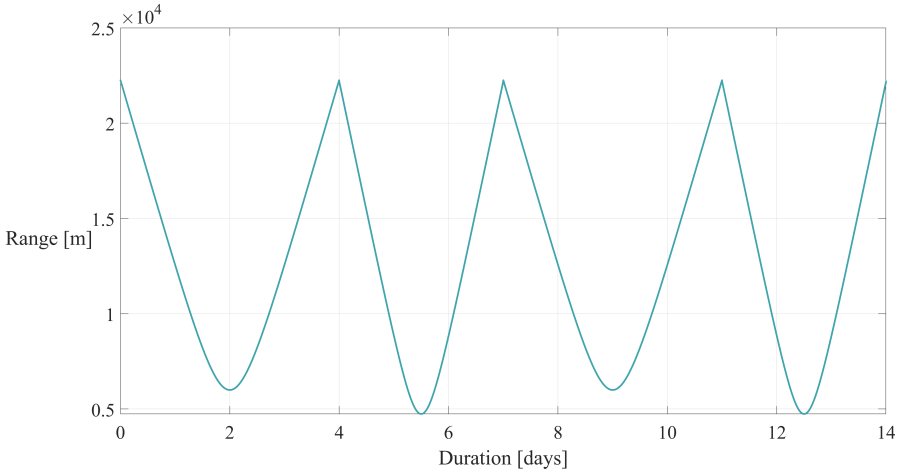

Figure 6.7: Range from Didymos during COP trajectory

absorbed by the time the Hera spacecraft reaches the target. Postimpact measurements revealed an elongated ellipsoidal shape, which is still into evolution due to the chaotic rotation/orbital motion of Dimorphos [174].

PANGU shows the generated images on its viewer, set up with the properties of the AFC, reported on Table 6.3 [103, 104]. The viewer is a plane of the size of the image captured by the camera, and the coordinates of each pixel are identified in the viewer's reference frame, which has the origin on the top left corner and the x- and y-axis referred to as i- and j-direction respectively, as shown in Fig. 6.8. When the GNC system is in the asteroid imaging mode, the AFC has its boresight axis pointing towards Didymos or Dimorphos, and the spacecraft attitude is such that the position vector of the Sun is always parallel and opposite to the $i-$direction. As a consequence, the binary asteroid system is shown in the PANGU viewer always illuminated from its right side.

Table 6.3: AFC properties [103, 104]

Field Of View (FOV)	**Focal length**: f	**Aperture**	**Image size**	**Pixel size**: ν
5.5°	10.6 cm	2.5 cm	1024×1024 px	14 μm

In this work, PANGU is used to generate:

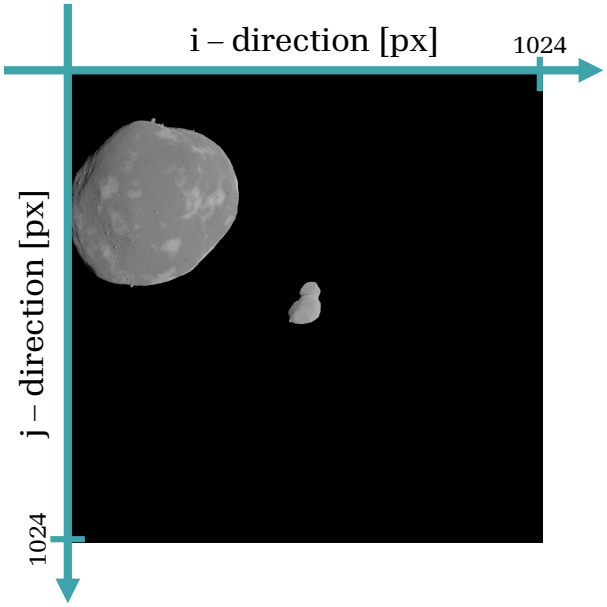

Figure 6.8: Example of image taken during ECP and shown in the PANGU viewer

- Dataset 1: $40,000$ images taken during the ECP. The trajectory is augmented by adding two fictitious diagonal arcs that connect the vertices of the square, as shown by the cyan circles in Fig. 6.9. A subset of Dataset 1 is generated considering a closer augmented ECP trajectory, shown with the yellow circles of Fig. 6.9. A pointing error of a maximum absolute value of 10% of the AFC FOV is considered for each generated image to change the position of Dimorphos randomly on the PANGU viewer.

- Dataset 2: $6,052$ images taken sampling the COP trajectory every 200 s with a pointing error per image generated as in Dataset 1.

- Dataset 3: 450 images taken sampling the DCP trajectory every 3600 s with a pointing error per image generated as in Dataset 1.

Dataset 1 is used as the training and validation database for the HRNet and the NN. The ECP trajectory is augmented in order to see the asteroid from different point

of views. The goal is to tune the monocular pose estimation algorithm leveraging the information collected with the ECP, the first phase of the proximity operations. Afterwards, the algorithm is tested using Dataset 2, generated during the COP, where this algorithm is necessary to achieve the objectives of this phase of the mission. Dataset 3, generated with the DCP trajectory, is used for testing the algorithm and analyze its generalization capability, even if the pose estimation of Dimorphos during this phase of the proximity operations is not required.

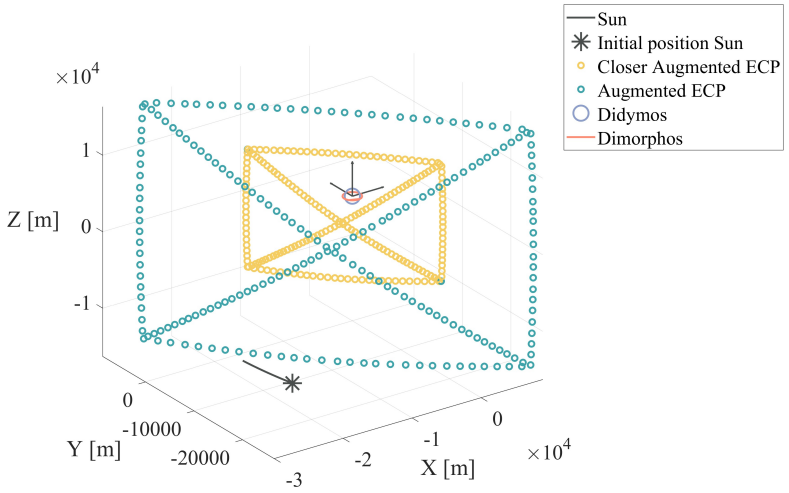

Figure 6.9: Augmented ECP trajectory [142]

6.2.3 CNN-based Monocular Pose Estimation algorithm

The key of the developed algorithm is the direct correlation between the lit limb of Dimorphos and its relative orientation with respect to the camera, given that the shape model of Dimorphos, represented by a scaled-down Itokawa, is an irregular oblate ellipsoid, and that the source of illumination is always on the right side of the images. Once the relative orientation is solved, we use the pinhole camera model to solve for the range and we combine it with the position of the COM to estimate the relative position of the spacecraft. Dataset 1 is split randomly in $38,000$ images for training and $2,000$ images for validation, while the $6,052$ images of Dataset 2 and the 450 images of Dataset 3 are used for testing. The four sets of images are pre-processed manually by discarding

the images where Dimorphos is not visible at all due to the presence of Didymos. The resulting sizes of the training, validation and testing datasets are respectively $33,530$ (83.13%), $1,790$ (4.44%), $5,016$ (12.43%).

6.2.3.1 Regression

The first step of the developed algorithm is the regression of the position of the COM and of a set of keypoints on the lit limb of Dimorphos. This is performed by the HRNet, a CNN architecture that has the ability to preserve the high resolution of the input image throughout the whole newtork, which leads to a keypoints regression with high accuracy and high spatial resolution [107]. In particular, the pose-hrnet-w32 architecture of the HRNet is used for this algorithm [122].

We selected 30 keypoints on the lit limb within an arc of angular aperture 2θ with $\theta = 130°$ being the angle formed with the $i-$direction of the PANGU viewer. The number of keypoints on the lit limb and the angular aperture θ selected in this work results from a trade-off between maximising the accuracy of the estimated pose of Dimorphos and the overall required computational power. Fig. 6.10 shows a sample image of Dataset 1 with the Ground Truth (GT) position of the COM and of the 30 keypoints on the lit limb. The GT position of the keypoints is obtained removing Didymos from the images, as it sometimes covers partially or totally Dimorphos, and it is calculated as explained in [142].

Table 6.4 shows the parameters describing the HRNet together with the computational performance.

6.2.3.2 Mapping

The second step of the developed algorithm consists in mapping the lit limb with the relative orientation of Dimorphos with respect to the spacecraft. Given an image of Dimorphos, the X and Y coordinates of the position of the i-th keypoint K_i on the image depends on three factors: the projected shape Ψ of Dimorphos on the image as seen by the spacecraft (i.e. its relative orientation), the Sun phase angle γ and the range from the spacecraft r. Indeed, when the range of the spacecraft from Dimorphos

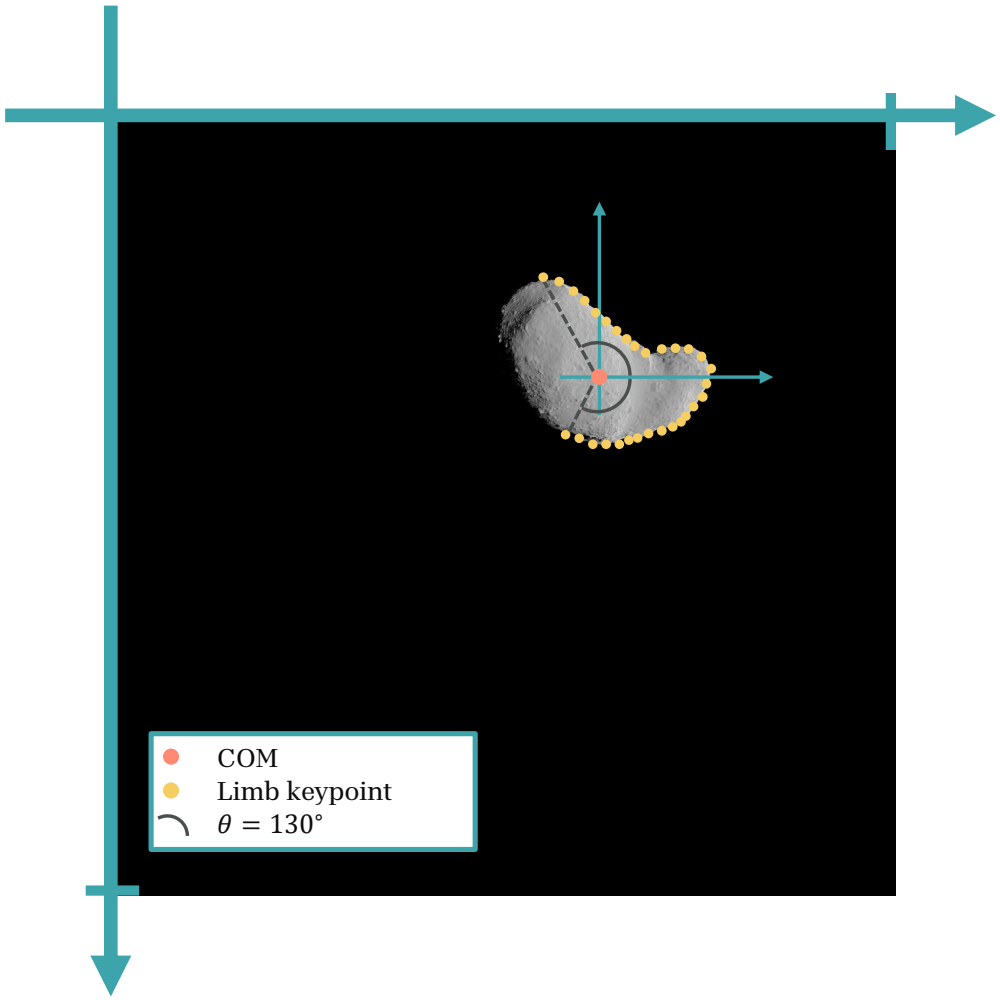

Figure 6.10: Example of GT keypoints on image of Dataset 1

decreases, the projection of Dimorphos on the image is bigger in size, and the keypoints on the lit limb are located further apart from each other. In order to eliminate the dependency of the keypoints' positions on the range, the coordinates X and Y of each i-th keypoint K_i on the lit limb is normalized using the coordinates X_{COM} and Y_{COM} of the position of the COM, as shown in Eq. 6.1. The end result is a set of 30 normalized

Table 6.4: Parameters of the HRNet [107]

Parameter	**Value**
Optimizer	Adam
Learning rate	0.001
Decaying rate	0.1
Batch size	32
Number of epochs	210
Processor	NVIDIA V100 Tensor Core GPU
Training time	$\sim 48\ hr$
Deploying time	$\sim 10\ s$
Number of parameters	$28,536,575$
Total weight	$109\ MB$

keypoints k_i with coordinates x_i and y_i, function of (Ψ, γ).

$$x_i = \frac{30(X_i - X_{COM})}{\sum_1^{30} |X_i - X_{COM}|}$$

$$y_i = \frac{30(Y_i - Y_{COM})}{\sum_1^{30} |Y_i - Y_{COM}|} \tag{6.1}$$

As explained in Section 6.2.1, the need for bright images during the proximity operations result in a Sun phase angle always lower than 90°. Moreover, the relative orientation of the spacecraft is such that the lit limb is always the right one. Therefore, the relative position of the keypoints on the image loses its dependency from the Sun phase angle γ, as lower values than 90° do not change the portion of illuminated border. Consequently, the set of 30 normalized keypoints k_i are solely functions of the projected shape Ψ of Dimorphos on the images, which depends on the relative orientation of Dimorphos with respect to the spacecraft.

Given the rotation matrix R_T^C from the TB reference frame to the camera reference frame and the rotation matrix R_T^B from the TB reference frame to the body fixed frame of Dimorphos, the relative rotation matrix R_C^B that represents the attitude of

Dimorphos with respect to the camera can be calculated with Eq. 6.2.

$$R_C^B = R_T^B \cdot inv(R_T^C) \tag{6.2}$$

The relative rotation matrix R_C^B is translated using Eq. 6.3 into the 4 quaternions [46].

$$\begin{aligned} q_0 &= \frac{1}{2}\sqrt{1 + C_{11} + C_{22} + C_{33}} \\ q_1 &= \frac{1}{4q_0}(C_{23} - C_{32}) \\ q_2 &= \frac{1}{4q_0}(C_{31} - C_{13}) \\ q_3 &= \frac{1}{4q_0}(C_{12} - C_{21}) \end{aligned} \tag{6.3}$$

The notation C_{ij} refers to the i-th and j-th element of the rotation matrix R_C^B. In this work, the short rotation around the Euler principal axis ($q_0 > 0$) is considered. Dataset 1 is used to calculate the GT values of the position of the normalized keypoints with Eq. 6.1 and of the 4 quaternions with Eq. 6.3, which are used to supervise the training of the NN developed in this work, therefore learning the relationship between the regressed lit limb of Dimorphos and its relative attitude.

The NN architecture consists of 7 fully connected layers with Rectified Linear Unit functions and a number of nodes per layer that decreases throughout the network. The input layer has a number of neurons equal to 60, which represents the x and y coordinates of the position of each of the 30 normalized keypoints. The output layer has 4 neurons which are normalized in order to get the estimation of the 4 quaternions. Table 6.5 shows the parameters describing the NN together with the computational performance. The NN architecture is built considering a compromise between the accuracy of the results obtained with a subset of images of Dataset 1 and the total weight of the model.

6.2.3.3 Pinhole

The last step of the developed algorithm consists in estimating the relative position of Dimorphos with respect to the spacecraft using the pinhole camera model. The latter

Table 6.5: Parameters of the NN developed in this work

Parameter	**Value**
Optimizer	Adam
Learning rate	0.001
Decaying rate	0.1
Batch size	32
Number of epochs	1000
Processor	NVIDIA GeForce RTX 2070 with Max-Q Design
Training time	$\sim 6\ hr$
Deploying time	$\sim 5\ s$
Number of parameters	$13,719,124$
Total weight	$40\ MB$

is a first-order approximation of the relationship between the 3D space and the 2D image obtained with the camera [106]. This model was used by the author in [142] to estimate the range with Didymos during the ECP and the DCP of the Hera mission, using the shape models of Didymos and Dimorphos prior to DART observations. The shape of Didymos was approximated to a sphere and with the pinhole camera model the range ρ was calculated by comparing the radius in pixel n_R of the asteroid to the corresponding value in meters R using Eq. 6.4:

$$n_R \cdot \nu = \frac{f \cdot R}{\rho} \tag{6.4}$$

where ν and f are respectively the pixel size and the focal length of the AFC camera, whose values are reported on Table 6.3. While this methodology works for a sphere that is always projected as a circle on a 2D image, in the case of an ellipsoidal shape such as the one of Dimorphos an additional step is required.

For each image, we calculate n_L, which represents the number of pixels from the regressed position of Dimorphos' COM to the keypoint P on its lit limb at $\theta = 0°$, as shown in Fig. 6.11. With the estimated R_C^B, hereafter referred to as R for simplicity,

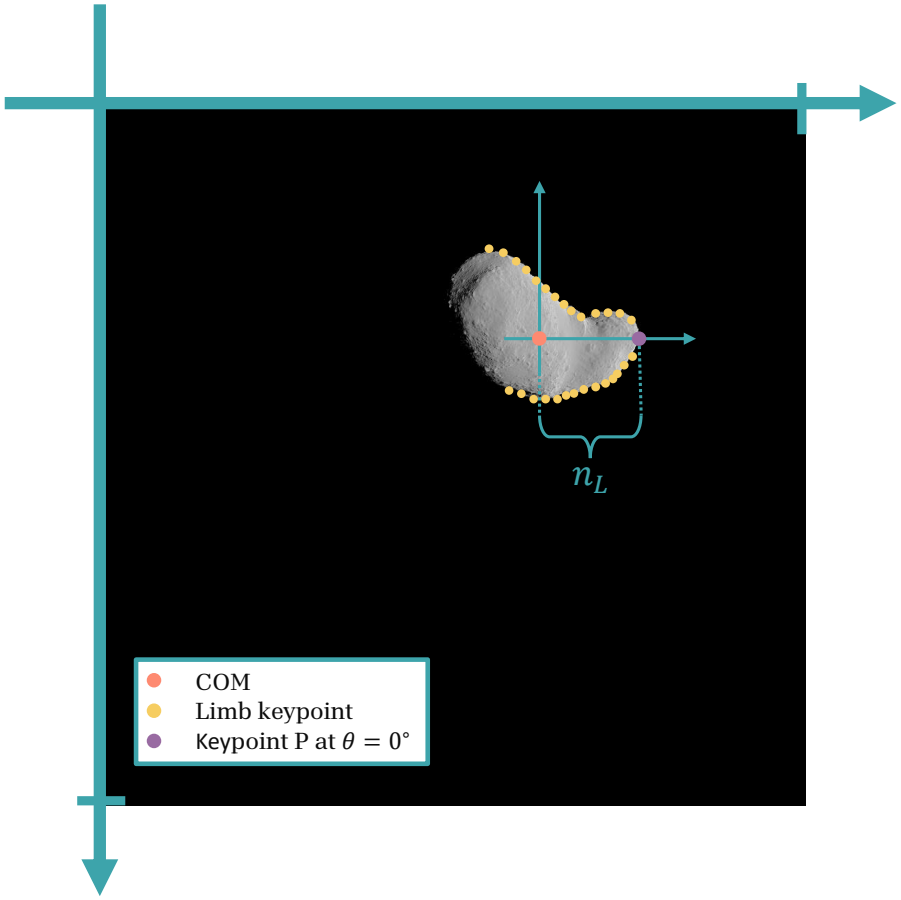

Figure 6.11: Characteristic length of Dimorphos

and the pinhole camera model, the corresponding value of n_L in meters is given by Eq. 6.5.

$$L = \sqrt{(a \cdot (R_{11})^2 + (b \cdot (R_{21}))^2 + (c \cdot (R_{31})^2} \tag{6.5}$$

where a, b and c represent the extent of Dimorphos along the principal axis x, y and z respectively, shown in Table 6.1, and R_{ij} represent the ij-th element of the matrix R. Comparing the lengths n_L and L, Eq. 6.4 can be solved for the range ρ as shown in Eq. 6.6.

$$\rho = \frac{f \cdot L}{n_L \cdot \nu} \tag{6.6}$$

6.2.4 Navigation filter

We use the UKF developed in [142] to couple the dynamics and the measurements obtained with the monocular pose estimation algorithm and to estimate the relative position of Dimorphos with respect to the spacecraft. The UKF uses non-linear functions to propagate the state of the spacecraft including its covariances with a technique called the Unscented Transformation [123]. The developed UKF in this work is a translational navigation filter as it is applied only for the relative position and not for the relative attitude which is given by the NN as shown in Section 6.2.3.2. The sole force considered in this work is the gravitational attraction of Didymos and Dimorphos, as in Eq. 6.7.

$$\boldsymbol{f} = -\frac{\mu_D \boldsymbol{r_{DH}}}{r_{DH}^3} - \frac{\mu_d \boldsymbol{r_{dH}}}{r_{dH}^3} \tag{6.7}$$

where $\boldsymbol{r_{DH}}$ and $\boldsymbol{r_{dH}}$ are the relative position vector of the spacecraft with respect to Didymos and with respect to Dimorphos respectively in the TB reference frame. By using the relative form of Eq. 6.7 we obtain Eq. 6.8 [46]:

$$\ddot{\boldsymbol{r_{DH}}} = -\frac{\mu_D \boldsymbol{r_{DH}}}{r_{DH}^3} + \mu_d \left(-\frac{\boldsymbol{r_{dH}}}{r_{dH}^3} - \frac{\boldsymbol{r_{Dd}}}{r_{Dd}^3} \right) \tag{6.8}$$

where $\boldsymbol{r_{Dd}}$ is the position vector of Dimorphos with respect to Didymos. Notably, the term we are estimating in Eq. 6.8 is $\boldsymbol{r_{dH}}$ that is the opposite of the relative position vector of Dimorphos with respect to the spacecraft $\boldsymbol{r_{Hd}}$. The dynamics equations does not include the maneuvers that connect each arc of the analyzed proximity operations trajectory, as the measurements are expected to capture this information.

The measurements obtained by the monocular pose estimation algorithm are the X and Y coordinates of the position of the COM of Dimorphos and the range from the spacecraft, which are related to the position vector $\boldsymbol{r_{dH}}$ with Eq. 6.9 and Eq. 6.10.

$$COM = K \begin{bmatrix} R_T^C & | & r_{DH} \end{bmatrix} \boldsymbol{r_{dH}} \tag{6.9}$$

$$\rho = ||\boldsymbol{r_{dH}}|| \tag{6.10}$$

where K is the calibration matrix that depends on the properties of the AFC (Ta-

ble 6.3). The rotation matrix R_T^C is assumed to be given by the attitude determination system of the spacecraft. The measurements are available every 200 s for Dataset 2 and every 3600 s for Dataset 3.

The complete settings of the UKF parameters are given in Table 6.6.

Table 6.6: Unscented Kalman Filter variables

Variable	**Symbol**	**Value**
Initial error in position	err_p	(2, 2, 2) $[km]$
Initial covariance matrix of the state	P	(1000^2 $[m^2]$, 1000^2 $[m^2]$, 1000^2 $[m^2]$)
Covariance matrix of the process	Q	(1000^2 $[m^2]$, 1000^2 $[m^2]$, 1000^2 $[m^2]$)
Covariance matrix of the measurements	R	(15^2 $[px^2]$, 10^2 $[px^2]$, 500^2 $[m^2]$)

6.3 Results

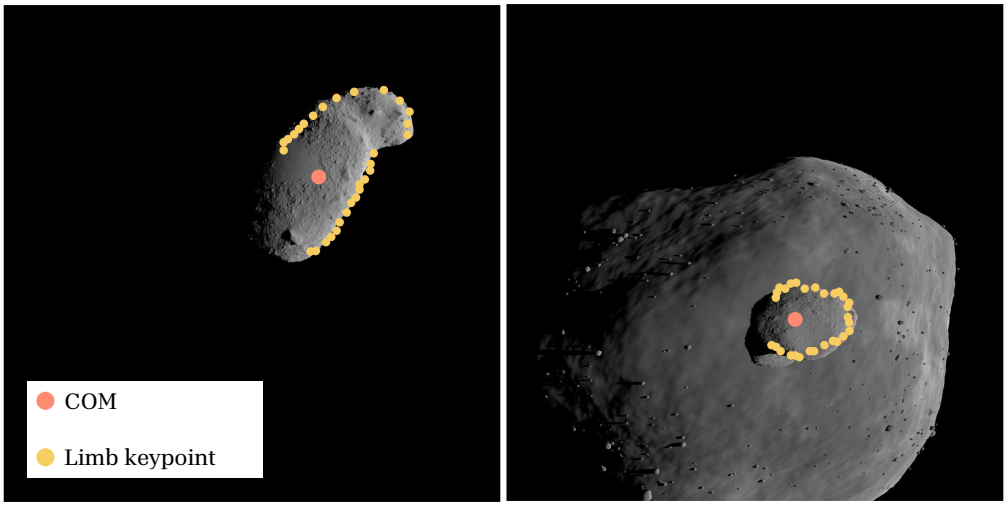

Figure 6.12: Example keypoints regression results

In this section, the results of the CNN-based IP algorithm for the relative pose estimation of Dimorphos during the DCP and the COP trajectories are presented.

The HRnet is able to estimate the position of the keypoints on each image of the testing dataset, as shown in the example of Fig. 6.12. Two separate error metrics for the relative position and attitude respectively are adopted in the evaluation of the accuracy of the proposed algorithm [145]. Firstly, the translational error between the estimated relative position X_{est} and X_{GT} is computed as in Eq. 6.11. $\boldsymbol{\epsilon_T}$ is a vector of components $[\epsilon_x, \epsilon_y, \epsilon_z]$.

$$\boldsymbol{\epsilon_T} = |X_{est} - X_{GT}| \tag{6.11}$$

Secondly, the attitude accuracy is measured in terms of the Euler axis-angle error between the estimated relative quaternion q_{est} and q_{GT} with Eq. 6.12:

$$q_e = (q_e^s \quad q_e^v) = q_{GT} \otimes q_{est}$$

$$\epsilon_R = 2 \cdot \arccos(|q_e^s|) \tag{6.12}$$

q^s and q^v refer respectively to the scalar and the vectorial component of the quaternion.

As reference values to validate the algorithm, 1 km and 10° are considered as maxima for the error in the estimated position (for each coordinate) and for the estimated attitude respectively. These values are obtained considering previous small body missions and standard landing procedure requirements [58].

The trained algorithm is deployed on Matlab with the local GPU NVIDIA GeForce RTX 2070 with Max Q-design. The average computational time required for the algorithm to process an image and output the results is 6.42 s.

6.3.1 COP pose estimation results

The estimated trajectory of the COP resulting from the navigation filter is shown in Fig. 6.13, and the errors ϵ_T and ϵ_R are shown in Fig. 6.14 and Fig. 6.15.

The initial error in the position estimate quickly decreases with the first measurement as shown in Fig. 6.14. The error oscillates around a mean value of 87.85 m, -710.31 m and -267.44 m for the $x-$, $y-$ and $z-$coordinates respectively, with peaks lower than 1 km for each axis. The effect of the spacecraft maneuvers can be barely

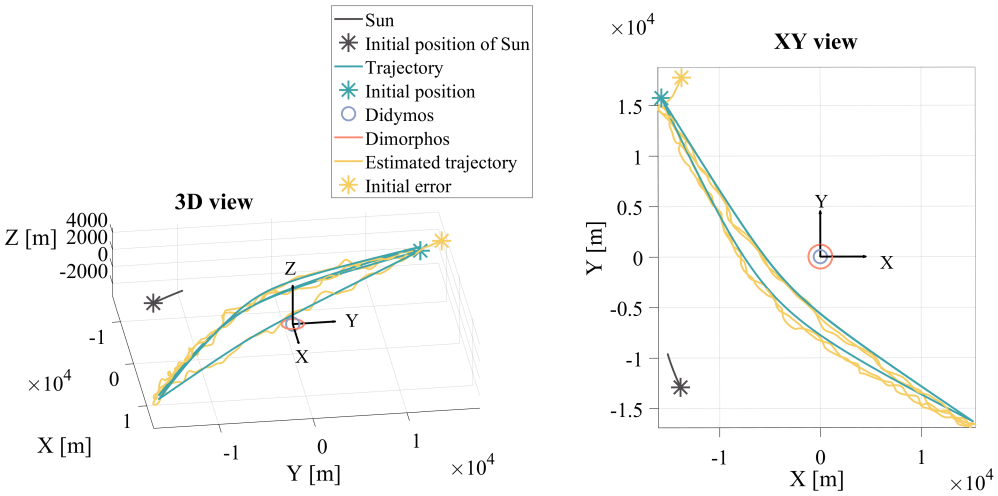

Figure 6.13: GT vs Estimated trajectory of the COP

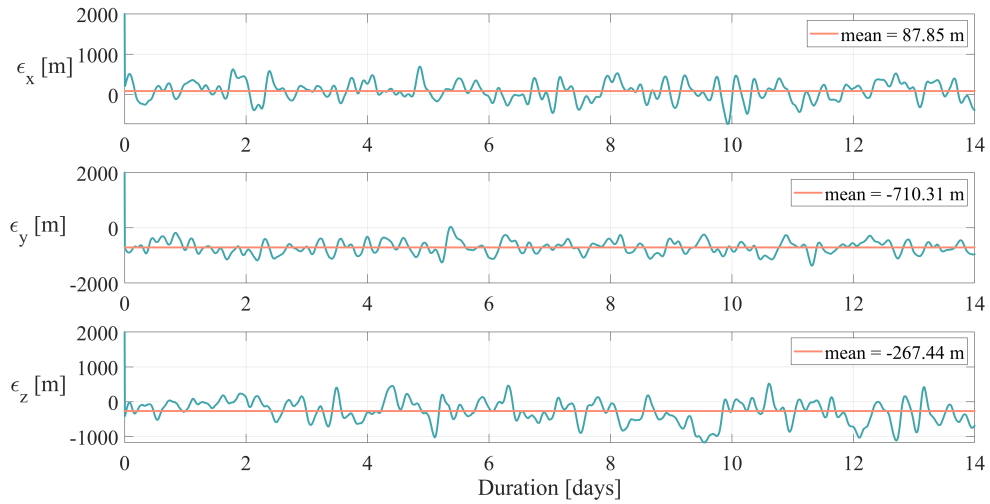

Figure 6.14: Error in position estimation of the COP

seen on the position error. This shows the capability of the filter to react to unmodelled accelerations like the maneuvers of the spacecraft and keep the navigation error low. Notably, the position estimation is not depending on the range of the spacecraft from Dimorphos, which can be seen by comparing Fig. 6.14 with Fig. 6.7. The promising performances of the algorithm during this trajectory can also be seen from Fig. 6.13, where the estimated and the true trajectories of the COP diverge limitedly.

Fig. 6.15 shows that the attitude estimation error oscillates around 3.55° with a

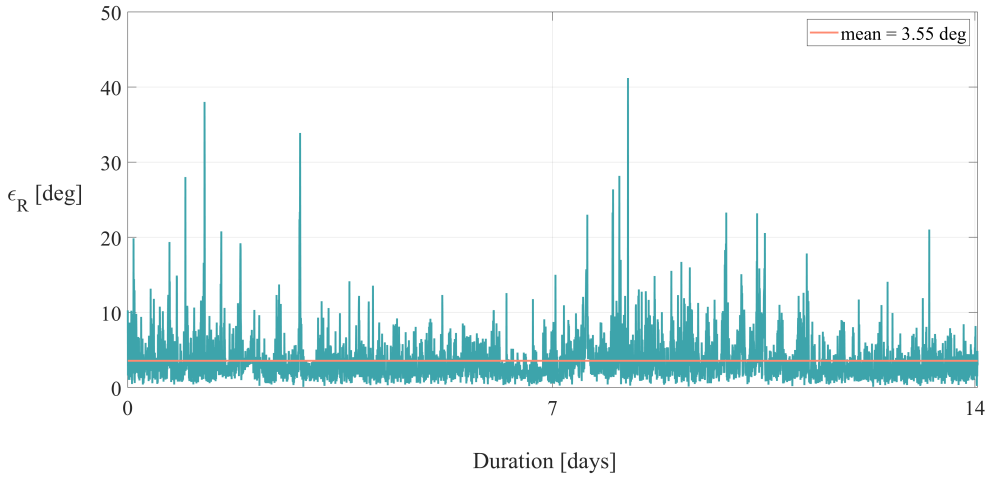

Figure 6.15: Error in attitude estimation of the COP

maximum value of around 40° obtained for one image of the testing dataset, which does not affect the range estimation since the position estimation error shown in Fig. 6.14 does not increase. The standard deviation on the $x-$, $y-$ and $z-$coordinate of the position estimation error and the attitude estimation error are respectively $\sigma_x = 132$ m, $\sigma_y = 211$ m, $\sigma_z = 148$ m, $\sigma_R = 1.2°$. Since both the means of the errors in the position and attitude estimation are lower than the maxima of 1 km and 10°, the CNN-based monocular pose estimation is validated for the COP trajectory.

6.3.2 DCP pose estimation results

The estimated trajectory of the DCP resulting from the navigation filter is shown in Fig. 6.16, and the errors ϵ_T and ϵ_R are shown in Fig. 6.17 and Fig. 6.18.

It can be seen that the CNN-based monocular pose estimation algorithm's performances are lower for this trajectory. In particular, although the initial error in the position estimate decreases with the first measurement, it stays high for the three position coordinates, oscillating around -1446.3 m, -2271.4 m and 2128.4 m respectively. Furthermore, for the $z-$coordinate the error increases around mid trajectory, reaching peaks of almost 4 km. Notably, the position estimation is not depending on the range of the spacecraft from Dimorphos, which can be seen by comparing Fig. 6.17 with

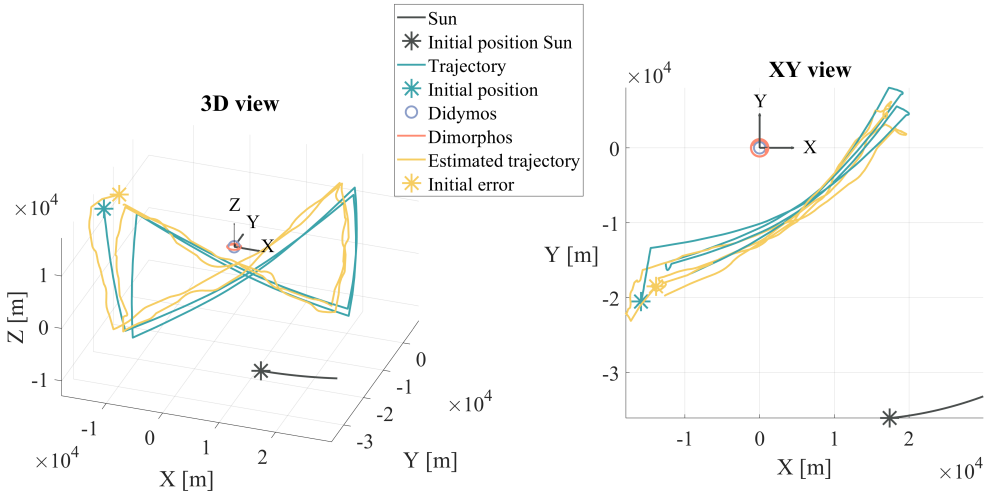

Figure 6.16: GT vs Estimated trajectory of the DCP

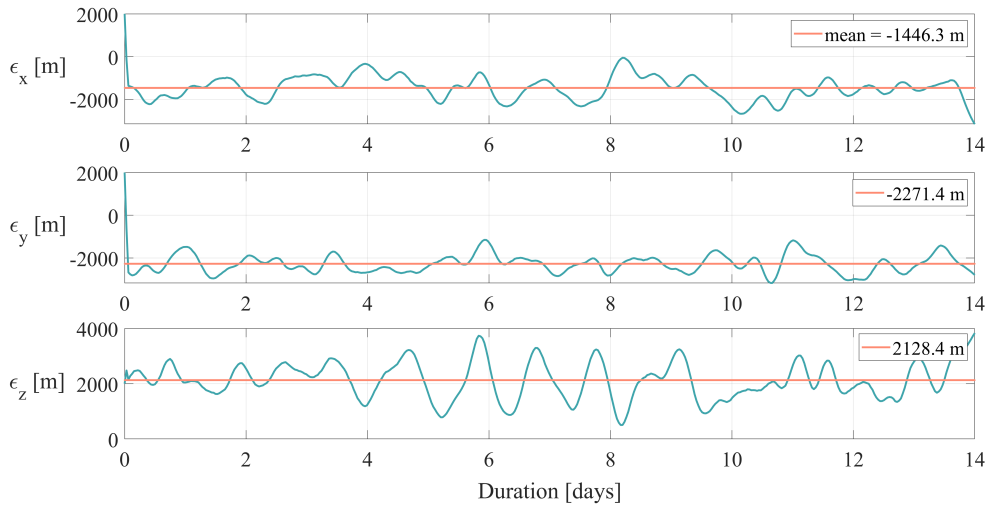

Figure 6.17: Error in position estimation of the DCP

Fig. 6.6. The worse performances of the algorithm for this trajectory can also be seen in Fig. 6.16 where the estimated trajectories have limited divergences from the true ones of the COP.

Fig. 6.18 shows that the attitude estimation error oscillates around 38.47° with peaks reaching almost 100°. This means that the algorithm failed to meet the accuracy requirement and it is not capable of estimating the relative attitude of Dimorphos during the DCP trajectory. The standard deviation on the $x-$, $y-$ and $z-$coordinates

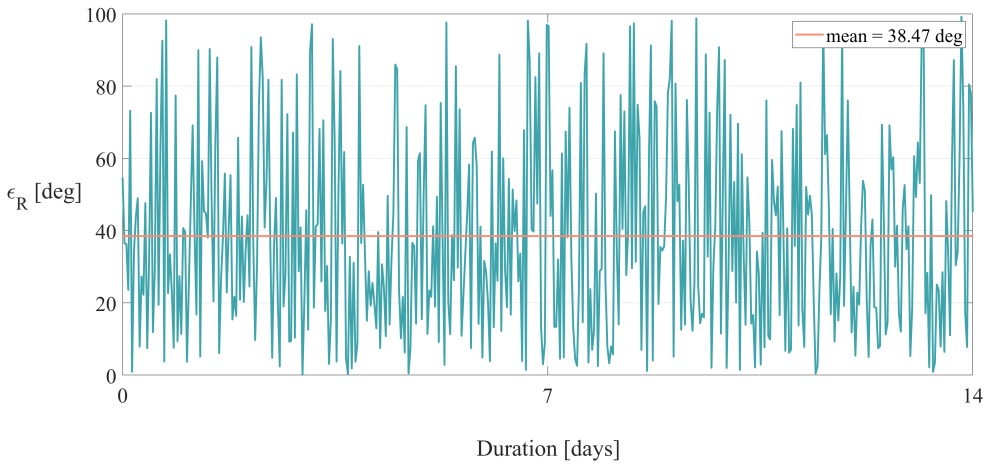

Figure 6.18: Error in attitude estimation of the DCP

position estimation error and the attitude estimation error are respectively $\sigma_x = 696$ m, $\sigma_y = 421$ m, $\sigma_z = 323$ m, $\sigma_R = 27.27°$. Since both the means of the errors in the position and attitude estimation are higher than the maxima of 1 km and 10°, the CNN-based monocular pose estimation algorithm is not validated for the DCP trajectory.

6.4 Conclusions

A CNN-based monocular pose estimation algorithm is presented in this work. The algorithm is an appearance-based method that estimates the continuous 6-dof pose of Didymos' moon Dimorphos relatively to the Hera spacecraft during the DCP and the COP of the proximity operations of the mission. The algorithm uses the HRNet CNN architecture and a NN architecture developed in this work to estimate the relative attitude of the target, the distance from the target and the position of the COM of the target from synthetic images generated with the rendering software PANGU. The shape model of Dimorphos obtained by DART prior to the impact is taken into account. The COM measurements and the range measurements are combined with an UKF to estimate the relative position of Dimorphos with respect to the spacecraft and complete the pose estimation. The algorithm is trained with images obtained with the first phase

of the proximity operation, i.e. the ECP.

The results show that the algorithm is able to meet the pose estimation accuracy requirements for the COP, both for the relative position ($< 1\ km$) and for the relative attitude ($10°$). In particular, the algorithm shows no dependency on the distance between the spacecraft and the target. Nevertheless, the results show limited performances for the pose estimation of Dimorphos during the DCP. Both the position and attitude estimations diverge considerably from GT values, making it impossible to use the algorithm during this phase of the proximity operations. Ultimately, the algorithm is highly depending on the projected shape of the target on the images; therefore, the CNN and NN architectures lacks generalization capabilities and requires a larger pool of data for training. This also means that when the Hera spacecraft will arrive to the Didymos system it will require to collect a high amount of images of the target asteroid for its fine-tuning in order to optimize its performances on pose estimation. It has to be noted that the spacecraft might find the target still in an tumbling state, which could potentially lead to a continuous variation of its principal moments of inertia, i.e. its shape.

Future work will go into the direction of increasing the robustness of the algorithm by considering during training not only different relative orbital geometry of the systems but also slightly different shapes of the target.

Chapter 7

Conclusion and Future Work

> We are more fulfilled when we are involved in something bigger than ourselves
>
> *John Glenn*

7.1 Discussion and Answers to the Research Questions

In the introduction of this thesis, an overall thesis statement was made and several RQs were formulated to support the statement and to drive the research presented. Each chapter of this thesis answered to the RQs and fulfilled the ROs as described in Section 1.3.2. This chapter reports the main high-level conclusions that answer the introduced RQs, which are repeated here for convenience.

7.1.1 RQ 1

To what extent can optical navigation strategies benefit from AI-based IP algorithms?

7.1.1.1 RQ 1a: What are the IP tasks that can be improved compared to standard approaches?

In Chapter 2, the HRNet-based IP algorithm used throughout the thesis was introduced, and applied to the ECP and the DCP proximity operations of the Hera mission around the binary asteroid system (65803) Didymos. Fig. 2.1 shows the pipeline of this algorithm. The latter inputs 1024×1024 px synthetic images generated with PANGU and emulating the on-board camera pictures, and solves for the regression of specific keypoints on the image, which are used to estimate variables that can improve the overall navigation strategy.

In particular, the algorithm has been able to solve for the centroiding of Didymos and Dimorphos, the range from the primary and the Sun phase angle. Given that standard approaches solve just for the centroiding of the primary body, the last three quantities represent results of additional IP tasks that can be performed by an AI-based IP algorithm.

Additionally, standard IP algorithms are affected by the adverse illumination conditions of the scenario, the irregular shape of the target and the disturbances caused by the presence of two bodies. The developed algorithm demonstrated to be independent from such quantities. In particular it has been able to solve for the centroiding of Dimorphos during partial and total eclipse, which is a unique contribution of this work. Finally, the algorithm has been able to generalize its solution for most of the DCP, showing robustness over different trajectories and, thus, different orbital geometries.

In conclusion, this research demonstrated the improved performance of AI-based IP algorithms compared to standard approaches, both in terms of IP tasks that can be performed, and in terms of robustness to IP typical challenges.

7.1.1.2 RQ 1b: What degree of performance can be achieved adopting a stand-alone AI-based optical navigation system for positioning?

In Chapter 3, the previously developed algorithm has been improved and combined with an UKF to analyze the navigation performance during the DCP of the Hera mission, as shown in Fig. 3.1. The algorithm uses the estimated centroid of Didymos, centroid of Dimorphos (if available), and range from the primary to estimate the relative position of the spacecraft with respect to Didymos. Furthermore, the algorithm uses an IP-based covariance method to analyze the reliability of the provided measurements.

The results showed that the stand-alone HRNet-based optical navigation system has been able to estimate the position of the spacecraft accurately, even if the dynamical model considered did not account for the maneuvers between each arc of the trajectory.

In conclusion, the algorithm performs well for navigation purposes and it could be implemented on board the spacecraft, taking into account that it would require an additional fine-tuning with a subset of images taken with the on-board camera to optimize its output according to the real mission scenario.

7.1.2 RQ 2

What are the challenges of validating AI-based IP algorithms for the implementation on a real asteroid rendezvous mission?

7.1.2.1 RQ 2a: What are the tests needed to bridge domain gaps and optimize the generalization capabilities of AI-based IP algorithms?

In Chapter 4, the HRNet-based IP algorithms built in the previous chapters has been stress-tested with a series of FTs aimed to analyze its generalization capability. The test campaign consisted in feeding the developed algorithm with images never seen during training, which emulate the potential contingencies typical to a standard mission scenario. Specifically, the images showed the binary asteroid system in conditions of adverse Sun phase angles, different noise levels, and different shape models of the target.

The results showed that the HRNet-based IP algorithm has been able to perform accurately in these adverse conditions, demonstrating a high-level of robustness and a

capability to bridge domain gaps.

Additionally, the HRNet-based IP algorithm has been able to perform well considering images generated with a different rendering software and different shape models of Didymos and Dimorphos compared to the ones used for training. This test showed that the developed algorithm is robust to the most probable contingency, i.e. images captured from the on-board camera different from the ones used for the ground validation and different shape of the target asteroid.

In conclusion, the AI-based IP algorithm has been able to generalize its solutions in different contingency scenarios affecting the proximity operations around the target.

7.1.2.2 RQ 2b: What are the constraints encountered during the incremental test campaign from the SW and HW point of view?

In Chapter 5, the HRNet-based IP algorithm has gone through the DDVV strategy adopted by GMV, in charge of the GNC SW of the Hera mission. The strategy consists of a test campaign aimed to analyze the performance of the developed algorithm when interfaced with the SW and HW solutions adopted for the mission. In particular, the test campaign consisted of OL and CL MIL tests run with the FES of the GNC system, OL On-processor tests run on a processor with computational power similar to the ones used on board spacecraft, and OL HIL tests using the FUMO of the AFC.

The OL and CL MIL tests showed that the developed algorithm performs well in the FES simulator of the GNC, interfacing well with the other SW models of the GNC sensors and actuators selected for this mission. Nevertheless, when implemented on OBC performance-like processor, the algorithm required a computational time higher than the one baselined for the mission, and a total RAM which is very high for a spacecraft. The HIL tests showed that the developed algorithm performs well even with images distorted by the electro-optical disturbances introduced by the AFC FUMO, demonstrating a high level of robustness even with HW-introduced uncertainties.

In conclusion, the AI-based IP algorithm does not present any constraint from the SW point of view, as it performs well both with the FES of the GNC system and with the disturbances introduced by the camera. Nevertheless, its implementation on an

OBC requires additional work to decrease the computational power required.

7.2 Limitations and Future Work

Provide explanation for model's behavior.

In Chapter 3, the HRNet outputs have been analyzed in order to calculate the associated covariance to the estimates of the position of the centroid of Didymos and Dimorphos. Specifically, the HRNet generates heatmaps associated to each of the estimated keypoint. The heatmap consists of a 64×64 px black image with a cloud of points whose intensity and shape represents the level of confidence of the HRNet in estimating the associated keypoint. By analyzing the heatmap, the developed algorithm is able to discriminate a reliable measurement from an unreliable one, according to weather said keypoint is visible or not in the image. This has been demonstrated also with the confusion matrix shown in Table 3.6, which shows the performance of the heatmap/based algorithm to recognize the presence/absence of Dimorphos in the images. Nevertheless, in Chapter 4, Table 4.9 shows the amount of images discarded by the analysis of the heatmaps generated by the HRNet. The results show that even if the centroid of Didymos is visible, the HRNet is not able to estimate its position. Future work will target the explainability of the model, essential to justify the decision-making process of the HRNet and to aptly tune the whole IP algorithm to optimize its estimations.

Tackle the challenges related to fine-tuning during simulative operational scenarios.

In Chapter 4, a limited amount of images never seen during training has been used to fine-tune the HRNet-based IP algorithm in order to mimic a potential operational scenario where it is required to adapt the algorithm to a new environment. Nevertheless, the results showed that the algorithm performed better before fine-tuning was applied. Moreover, adding more images to the fine-tuning dataset did not seem to provide any pattern in the results, which improved/reduced independently from the number of images used. Therefore, future research will go towards analyzing different datasets and

setting up a know-how on optimizing the fine-tuning dataset to affect the algorithm and improve its results in unseen mission scenarios.

Improve the applicability on OBCs.

In Chapter 5, tests on an OBC performance-like processor have been run to analyze the applicability of the HRNet-based IP algorithm on board a spacecraft. Nevertheless, the test showed that the deployment time per image does not meet the GNC system requirements. Furthermore, the total RAM required is too high to run the algorithm on board. On-going research is currently focused on reducing the computational complexity of the algorithm by implementing pruning and quantization techniques. The former consists in reducing the size of the model by zeroing weights and biases which are not affecting the outcomes of the model itself. The latter focuses on reducing the precision of the weights and biases, e.g. by working on fixed precision, reducing the number of bits required and/or going from floating points to integers. Future work foresees HW-accelerated implementations such as FPGAs that allow parallelization of computations to reduce the computational time required per single image.

Increase the generalization capability of the CNN-based monocular pose estimation algorithm.

In Chapter 6, the HRNet-based IP algorithm has been extended to solve for the pose estimation of Dimorphos during the DCP and the COP of the Hera mission. The results showed good performance during the COP, meeting the relative position and relative attitude requirements for the mission. In particular, the algorithms estimation showed no dependency on the range from the target asteroid. Nevertheless, when applied to the DCP, the performances were limited and not suitable for navigation. Future research will improve the generalization capability of the algorithm by considering a more completed training dataset involving images of the asteroid seen from different perspectives and with different shapes.

7.3 Unique contributions

Below is a list of the distinct contributions made to the research topic addressed in this thesis. Chapter 2:

- ❖ Estimation of the position of the centroid of the secondary body in images of a binary system;
- ❖ Estimation of the Sun phase angle (Sun-asteroid-spacecraft) using the regressed position of the subsolar point on the surface of the target body.

Chapter 3:

- ❖ Return of a flag that signals whether the secondary body of a binary system is visible or not (outside of the FOV or behind the projected image of the primary).

Chaper 5:

- ❖ Integration in a model-based environment of a GNC system and subsequent incremental validation test campaign of a single AI-based algorithm.

7.4 List of publications

Below is the list of publications, separated in peer-reviewed Journal Papers and Conference Papers, which are the result of the work carried in this 4-years Ph.D.

Journal

Published

- ❖ **Kaluthantrige, A.**, Feng, J. and Gil-Fernández, J., 2023. *CNN-based Image Processing algorithm for autonomous optical navigation of Hera mission to the binary asteroid Didymos.* Acta Astronautica, [online] 211(May), pp.60–75. Available at: https://doi.org/10.1016/j.actaastro.2023.05.029.
- ❖ **Kaluthantrige, A.**, Feng, J. and Gil-Fernández, J., 2024. *Convolutional Neural Network-based autonomous navigation of Hera mission around Didymos.* Journal of Guidance, Control, and Dynamics, [online]. Available at: https://doi.org/10.2514/1.G008054.

❖ **Kaluthantrige, A.**, Pugliatti, M., Feng, J., Topputo, F. and Gil-Fernández, J., 2025. *Robustness analysis of data-driven Image Processing algorithms applied to the Hera mission.* Journal of Spacecraft and Rockets, [online]. Available at: https://arc.aiaa.org/doi/10.2514/1.A36170.

In-Review

❖ **Kaluthantrige, A.**, Feng, J., Di Domenico, G. and Gil-Fernández, J., n.d. *Incremental validation test campaign of a CNN-based Image Processing algorithm for autonomous visual-based navigation applied to the Hera mission.* Journal of Advances in Space Research.

In development

❖ **Kaluthantrige, A.**, Feng, J. and Gil-Fernández, J., n.d. *Pose estimation of Dimorphos using CNN-based Image Processing algorithm.* Journal of Guidance, Control, and Dynamics.

Conference

❖ Di Domenico, G., **Kaluthantrige, A.**, Feng, J., Topputo, F. and Gil-Fernández, J., 2024. *Hardware-Accelerated Implementation of a Convolutional Neural Network-based Image Processing Algorithm for the ESA Hera Mission* In: International Astronautical Congress (IAC), Milan, Italy. Available at: https://iafastro.directory/iac/archive/browse/IAC-24/.

❖ **Kaluthantrige, A.**, Pugliatti, M., Feng, J., Gil-Fernández, J. and Topputo, F., 2024. *Robustness analysis of data driven image processing methods for autonomous navigation with application to the Hera mission* In: International Astronautical Congress (IAC), Milan, Italy. Available at: https://iafastro.directory/iac/archive/browse/IAC-24/.

❖ **Kaluthantrige, A.**, Feng, J. and Gil-Fernández, J., 2024. *Hardware-In-The-Loop Test of a CNN-based Image Processing algorithm for autonomous visual-based navigation applied to the Hera mission* In: International Astronautical

Congress (IAC), Milan, Italy. Available at: https://iafastro.directory/iac/archive/browse/IAC-24/.

- **Kaluthantrige, A.**, Feng, J., Gil-Fernández, J. and Di Domenico, G., 2023. *Validation of CNN-based Image Processing algorithm for the Hera mission with Model-in-the-loop and Open-loops tests on OnBoard Computer* In: International Astronautical Congress (IAC), Baku, Azerbaijan. Available at: https://iafastro.directory/iac/archive/browse/IAC-23/.

- **Kaluthantrige, A.**, Feng, J. and Gil-Fernández, J., 2023. *Pose estimation of chaotic motion of Didymos' Moon using CNN-based Image Processing algorithm* In: ESA GNC and ICATT Conference, Sopot, Poland. Available at: https://indico.esa.int/event/449/.

- **Kaluthantrige, A.**, Feng, J. and Gil-Fernández, J., 2023. *Pose estimation of Didymos' Moon using CNN-based Image Processing algorithm for Hera mission* In: 8th IAA Planetary Defense Conference (PDC), Vienna, Austria. Available at: https://iaaspace.org/event/8th-iaa-planetary-defense-conference-2023/.

- **Kaluthantrige, A.**, Feng, J. and Gil-Fernández, J., 2022. *Pseudorange measurement and Sun phase angle estimation using CNN-based Image Processing algorithm for Hera mission.* In: Advanced Maui Optical and Space Surveillance Technology Conference (AMOS), Maui, Hawaii, United States of America. Available at: https://amostech.com/downloads/amos-2022/.

- **Kaluthantrige, A.**, Fodde, I., Feng, J. and Gil-Fernández, J., 2022. *Autonomous navigation around DIdymos using CNN-based Image Processing.* In: AAS/AIAA Astrodynamics Specialist Conference, Charlotte, North Carolina, United States of America. Available at: https://www.space-flight.org/docs/2022_summer/2022_summer.html.

- **Kaluthantrige, A.**, Feng, J., Gil-Fernández, J. and Pellacani, A., 2022. *Centroiding regression using CNN-based Image Processing Algorithm with application*

to a binary asteroid system. In: World Congress on Computational Intelligence (WCCI), Padova, Italy. Available at: https://wcci2022.org/.

- **Kaluthantrige, A.**, Feng, J., Gil-Fernández, J. and Pellacani, A., 2022. *Centroiding technique using Machine Learning algorithm for space optical navigation.* In: 3rd IAA Conference on Space Situational Awareness (ICSSA), Madrid, Spain. Available at: https://iaaspace.org/event/3rd-iaa-conference-on-space-situational-awareness

Bibliography

[1] E. Asphaug, "Growth and evolution of asteroids," *Annual Review of Earth and Planetary Sciences*, vol. 37, pp. 413–448, 2009.

[2] W. F. Bottke, D. D. Durda, and et al., "The fossilized size distribution of the main asteroid belt," *Icarus*, vol. 175, no. 1, pp. 111–140, 2005.

[3] C. R. Chapman, "The hazard of near-Earth asteroid impacts on earth," *Earth and Planetary Science Letters*, vol. 222, no. 1, pp. 1–15, 2004.

[4] J. V. Morgan, T. J. Bralower, and et al., "The Chicxulub impact and its environmental consequences," *Nature Reviews Earth and Environment*, vol. 3, no. 5, pp. 338–354, 2022.

[5] N. V. Vasilyev, "The Tunguska Meteorite problem today," *Planetary and Space Science*, vol. 46, no. 2-3, pp. 129–150, 1998.

[6] S. J. Weidenschilling, "Formation of planetesimals and accretion of the terrestrial planets," *Space Science Reviews*, vol. 92, no. 1-2, pp. 295–310, 2000.

[7] M. Granvik, A. Morbidelli, and et al., "Debiased orbit and absolute-magnitude distributions for near-Earth objects," *Icarus*, vol. 312, pp. 181–207, 2018. [Online]. Available: https://doi.org/10.1016/j.icarus.2018.04.018

[8] O. Popova, P. Jenniskens, and et al., "Chelyabinsk meteoroid entry and airburst damage," *Proceedings of Meteoroids 2013 Conference*, pp. 119–124, 2013. [Online]. Available: https://www.researchgate.net/publication/260122967_Chelyabinsk_meteoroid_entry_and_airburst_damage

[9] L. Prockter, S. Murchie, and et al., "The NEAR shoemaker mission to asteroid 433 eros," *Acta Astronautica*, vol. 51, no. 1-9, pp. 491–500, 2002.

[10] B. G. Williams, "Technical challenges and results for navigation of NEAR Shoemaker," *Johns Hopkins APL Technical Digest (Applied Physics Laboratory)*, vol. 23, no. 1, pp. 34–45, 2002.

[11] J. Veverka, B. Farquhar, and et al., "The landing of the NEAR-Shoemaker spacecraft on asteroid 433 Eros," *Nature*, vol. 413, no. 6854, pp. 390–393, 2001.

[12] M. Yoshikawa, J. Kawaguchi, and et al., "Sample Return Missions," *Sample Return Missions*, no. 3, pp. 123–146, 2021.

[13] J. Kawaguchi, H. Kuninaka, and et al., "MUSES-C, Its launch and early orbit operations," *Acta Astronautica*, vol. 59, no. 8-11, pp. 669–678, 2006.

[14] C. T. Russell, F. Capaccioni, and et al., "Dawn mission to vesta and ceres," *Earth, Moon and Planets*, vol. 101, no. 1-2, pp. 65–91, 2007.

[15] M. C. De Sanctis, E. Ammannito, and et al., "Mineralogical characterization of some V-type asteroids, in support of the NASADawnmission," *Monthly Notices of the Royal Astronomical Society*, vol. 412, no. 4, pp. 2318–2332, 2011.

[16] Y. Tsuda, T. Saiki, and et al., "Hayabusa2 mission status: Landing, roving and cratering on asteroid Ryugu," *Acta Astronautica*, vol. 171, no. January, pp. 42–54, 2020. [Online]. Available: https://doi.org/10.1016/j.actaastro.2020.02.035

[17] K. Berry, B. Sutter, and et al., "OSIRIS-REx Touch-And-Go (TAG) Mission Design and Analysis 36 th ANNUAL AAS GUIDANCE AND CONTROL CONFERENCE AAS 13-095 OSIRIS-REX TOUCH-AND-GO (TAG) MISSION DESIGN AND ANALYSIS The Origins Spectral Interpretation Resource Identification Security Regolith Ex-plorer (OSIRIS-REx) mission is a NASA New Frontiers mission launching," 2013.

[18] E. Beshore, D. Lauretta, and et al., "The OSIRIS-REx asteroid sample return mission," *IEEE Aerospace Conference Proceedings*, vol. 2015-June, no. 520, pp. 1–14, 2015.

[19] A. F. Cheng, J. Atchison, and et al., "Asteroid Impact and Deflection Assessment mission," *Acta Astronautica*, vol. 115, pp. 262–269, 2015. [Online]. Available: http://dx.doi.org/10.1016/j.actaastro.2015.05.021

[20] S. P. Naidu, L. A. M. Benner, and et al., "Radar observations and a physical model of binary near-Earth asteroid 65803 Didymos , target of the DART mission," *Icarus*, vol. 348, no. September 2019, p. 113777, 2020.

[21] W. F. Bottke, D. Vokrouhlický, and et al., "The yarkovsky and yorp effects: Implications for asteroid dynamics," *Annual Review of Earth and Planetary Sciences*, vol. 34, no. Volume 34, 2006, pp. 157–191, 2006. [Online]. Available: https://www.annualreviews.org/content/journals/10.1146/annurev.earth.34.031405.125154

[22] G. Madeira, S. Charnoz, and et al., "Dynamical origin of Dimorphos from fast spinning Didymos," *Icarus*, vol. 394, no. January, p. 115428, 2023. [Online]. Available: https://doi.org/10.1016/j.icarus.2023.115428

[23] P. Pravec, P. Scheirich, and et al., "Binary asteroid population. 3. Secondary rotations and elongations," *Icarus*, vol. 267, no. December 2015, pp. 267–295, 2016.

[24] C. A. Thomas, S. P. Naidu, and et al., "Orbital period change of Dimorphos due to the DART kinetic impact," *Nature*, vol. 616, no. 7957, pp. 448–451, 2023.

[25] R. T. Daly, C. M. Ernst, and et al., "Successful kinetic impact into an asteroid for planetary defence," *Nature*, vol. 616, no. 7957, pp. 443–447, 2023.

[26] R. H. Cueva, J. W. McMahon, and et al., "The Secular Dynamical Evolution of Binary Asteroid System (65803) Didymos Post-DART," *Planetary Science Journal*, vol. 5, no. 2, 2024.

[27] P. Scheirich and P. Pravec, "Preimpact Mutual Orbit of the DART Target Binary Asteroid (65803) Didymos Derived from Observations of Mutual Events in 2003–2021," *Planetary Science Journal*, vol. 3, no. 7, p. 163, 2022. [Online]. Available: http://dx.doi.org/10.3847/PSJ/ac7233

[28] John Hopkins University Applied Physics Laboratory, "Design Reference Asteroid," Tech. Rep. 101955, 2022.

[29] ESA Headquarters, "HERA Didymos reference model," Tech. Rep. 5, 2021.

[30] Z. J. Fletcher, K. Ryan, and et al., "Didymos Reconnaissance and Asteroid Camera for OpNav (DRACO): design, fabrication, test, and operation," vol. 12180, p. 11, 2022.

[31] ESA, "Didymos and Dimorphos - NASA Science," 2022. [Online]. Available: https://science.nasa.gov/solar-system/asteroids/didymos/

[32] N. L. Chabot, A. S. Rivkin, and et al., "Achievement of the Planetary Defense Investigations of the Double Asteroid Redirection Test (DART) Mission," *Planetary Science Journal*, vol. 5, no. 2, 2024.

[33] Y. Zhang, P. Michel, and et al., "Creep stability of the DART/Hera mission target 65803 Didymos: II. The role of cohesion," *Icarus*, vol. 362, no. March 2021, p. 114433, 2021. [Online]. Available: https://doi.org/10.1016/j.icarus.2021.114433

[34] P. Michel, A. F. Cheng, and et al., "Asteroid Impact and Deflection Assessment (AIDA) mission: science investigaation of a binary system and mitigation test," in *European Planetary Science Congress 2015, held 27 September-2 October, 2015 in Nantes, France, Online at http://meetingorganizer. copernicus. org/EPSC2015, id. EPSC2015-123*, vol. 10, 2015, p. 123. [Online]. Available: http://meetingorganizer.copernicus.org/EPSC2015/EPSC2015-123.pdf

[35] P. Michel, M. Küppers, and et al., "The HERA mission: European component of the asteroid impact and deflection assessment (AIDA) mission to a binary asteroid," in *49th Lunar and Planetary Science Conference 2018*, 2018.

[36] ——, "The ESA Hera Mission: Detailed Characterization of the DART Impact Outcome and of the Binary Asteroid (65803) Didymos," *Planetary Science Journal*, vol. 3, no. 7, p. 160, 2022. [Online]. Available: http://dx.doi.org/10.3847/PSJ/ac6f52

[37] H. R. Goldberg, Ö. Karatekin, , and et al., "The Juventas CubeSat in Support of ESA's Hera Mission to the Asteroid Didymos, Proceedings of the Small Satellite Conference, SSC19-WKIV-05," 2019.

[38] F. Ferrari, V. Franzese, and et al., "Trajectory Options for Hera ' s Milani CubeSat Around (65803) Didymos," *The Journal of the Astronautical Sciences*, pp. 973–994, 2021.

[39] ESA, "Hera," 2023. [Online]. Available: https://www.esa.int/Space_Safety/Hera

[40] ESA ESTEC, "HERA : Proximity Operation Guidelines," Tech. Rep., 2020.

[41] Y. Kawabata and Y. Kawakatsu, "On-board orbit determination using sun sensor and optical navigation camera for deep-space missions*," *Trans. JSASS Aerospace Tech. Japan*, vol. 15, pp. 13–19, 2017.

[42] J. M. Rebordão, "Space optical navigation techniques: an overview," vol. 8785. SPIE, 11 2013, pp. 87 850J1–87 850J20.

[43] R. E. Kalman, "A new approach to linear filtering and prediction problems," *Journal of basic engineering*, pp. 34–45, 1960. [Online]. Available: http://asmedigitalcollection.asme.org/fluidsengineering/article-pdf/82/1/35/5518977/35_1.pdf

[44] D. C. Woffinden and D. K. Geller, "Relative angles-only navigation and pose estimation for autonomous orbital rendezvous," *Journal of Guidance, Control, and Dynamics*, vol. 30, no. 5, pp. 1455–1469, 2007. [Online]. Available: https://doi.org/10.2514/1.28216

[45] L. Zhang, S. Zhang, and et al., "Relative attitude and position estimation for a tumbling spacecraft," *Aerospace Science and Technology*, vol. 42, pp. 97–105, 2015.

[46] D. A. Vallado, *Fundamentals of Astrodynamics and Applications*, 2013.

[47] D. J. Scheeres, S. J. Ostro, and et al., "Orbits close to asteroid 4769 castalia," *ICARUS*, vol. 121, pp. 67–87, 1996.

[48] J. C. Melman, E. Mooij, and et al., "State propagation in an uncertain asteroid gravity field," *Acta Astronautica*, vol. 91, pp. 8–19, 2013.

[49] Y. Wang and S. Xu, "Equilibrium attitude and stability of a spacecraft on a stationary orbit around an asteroid," *Acta Astronautica*, vol. 84, pp. 99–108, 2013.

[50] I. Jean, A. Ng, and et al., "Impact of solar radiation pressure modeling on orbital dynamics in the vicinity of binary asteroids," *Acta Astronautica*, vol. 165, pp. 167–183, 12 2019.

[51] I. A. Nesnas, B. J. Hockman, and et al., "Autonomous Exploration of Small Bodies Toward Greater Autonomy for Deep Space Missions," *Frontiers in Robotics and AI*, vol. 8, no. November, pp. 1–26, 2021.

[52] B. D. Warner, *Lightcurve Photometry and Analysis*, 2006. [Online]. Available: http://link.springer.com/10.1007/978-3-319-32750-1

[53] P. Pravec, P. Scheirich, and et al., "Photometric survey of binary near-Earth asteroids," *Icarus*, vol. 181, no. 1, pp. 63–93, 2006.

[54] S. Bhaskaran, "Autonomous navigation for deep space missions," *SpaceOps 2012 Conference*, 2012.

[55] J. Gil-Fernandez and G. Ortega-Hernando, "Autonomous vision-based navigation for proximity operations around binary asteroids," *CEAS Space Journal*, vol. 10, no. 2, pp. 287–294, 2018. [Online]. Available: https://doi.org/10.1007/s12567-018-0197-5

[56] J. A. Christian, "Accurate planetary limb localization for image-based spacecraft navigation," *Journal of Spacecraft and Rockets*, vol. 54, no. 3, pp. 708–730, 2017.

[57] T. Teil, H. Schaub, and et al., "Centroid and apparent diameter optical navigation on mars orbit," *Journal of Spacecraft and Rockets*, vol. 58, no. 4, pp. 1107–1119, 2021.

[58] A. Pellacani, M. Graziano, and et al., "HERA vision based GNC and autonomy," *European Conference for AeroSpace Sciences*, pp. 1–14, 2019.

[59] J. A. Christian and S. B. Robinson, "Noniterative horizon-based optical navigation by cholesky factorization," *Journal of Guidance, Control, and Dynamics*, vol. 39, no. 12, pp. 2755–2763, 2016.

[60] W. Qian, Z. Wei, and et al., "Model-based line-of-sight detection of an irregular celestial body for autonomous optical navigation," *Chinese Control Conference, CCC*, vol. 2015-September, pp. 5527–5532, 2015.

[61] J. A. Christian, "Pole Estimation and Optical Navigation Using Circle of Latitude Projections," *Journal of Guidance, Control, and Dynamics*, vol. 47, no. 3, pp. 407–416, 2024.

[62] H. Morita, K. Shirakawa, and et al., "Hayabusa Descent Navigation based on Accurate Landmark Tracking Scheme," pp. 21–31, 2006.

[63] N. Mastrodemos, B. Rush, and et al., "Optical Navigation For The Dawn Mission At Vesta," *Advances in the Astronautical Sciences*, vol. 140, no. 2, pp. 1739–1754, 2011.

[64] D. A. Lorenz, R. Olds, and et al., "Lessons learned from OSIRIS-REx autonomous navigation using natural feature tracking," *IEEE Aerospace Conference Proceedings*, pp. 1–12, 2017.

[65] N. Ogawa, F. Terui, and et al., "Image-based autonomous navigation of Hayabusa2 using artificial landmarks: The design and brief in-flight results of

the first landing on asteroid Ryugu," *Astrodynamics*, vol. 4, no. 2, pp. 89–103, 2020.

[66] C. Janiesch, P. Zchech, and et al., "Machine learning and deep learning," *Electronic Markets*, no. 31, pp. 685–695, 2021.

[67] R. Gentleman and V. J. Carey, *Unsupervised Machine Learning*. New York, NY: Springer New York, 2008, pp. 137–157. [Online]. Available: https://doi.org/10.1007/978-0-387-77240-0_10

[68] I. Goodfellow, Y. Bengio, and A. Courville, *Deep Learning*. MIT Press, 2016, http://www.deeplearningbook.org.

[69] A. Krizhevsky, I. Sutskever, and et al., "Imagenet classification with deep convolutional neural networks," *Commun. ACM*, vol. 60, no. 6, p. 84–90, May 2017. [Online]. Available: https://doi.org/10.1145/3065386

[70] K. Simonyan and A. Zisserman, "Very deep convolutional networks for large-scale image recognition," 2015. [Online]. Available: https://arxiv.org/abs/1409.1556

[71] K. He, X. Zhang, and et al., "Deep residual learning for image recognition," 2015. [Online]. Available: https://arxiv.org/abs/1512.03385

[72] M. Tan and Q. V. Le, "Efficientnet: Rethinking model scaling for convolutional neural networks," 2020. [Online]. Available: https://arxiv.org/abs/1905.11946

[73] A. Dosovitskiy and L. B. et al., "An image is worth 16x16 words: Transformers for image recognition at scale," 2021. [Online]. Available: https://arxiv.org/abs/2010.11929

[74] A. Khan, A. Sohail, and et al., *A survey of the recent architectures of deep convolutional neural networks*. Springer Netherlands, 2020, vol. 53, no. 8. [Online]. Available: https://doi.org/10.1007/s10462-020-09825-6

[75] D. Izzo, M. Märtens, and et al., "A survey on artificial intelligence trends in spacecraft guidance dynamics and control," *Astrodynamics*, vol. 3, no. 4, pp. 287–299, 2019.

[76] A. Çayir, I. Yenidoğan, and et al., "Feature extraction based on deep learning for some traditional machine learning methods," in *2018 3rd International Conference on Computer Science and Engineering (UBMK)*, 2018, pp. 494–497.

[77] E. Ferrante, O. Oktay, and et al., "On the adaptability of unsupervised cnn-based deformable image registration to unseen image domains," in *Machine Learning in Medical Imaging*, Y. Shi, H.-I. Suk, and M. Liu, Eds. Cham: Springer International Publishing, 2018, pp. 294–302.

[78] R. Linares, R. Furfaro, and et al., "Space Objects Classification via Light-Curve Measurements Using Deep Convolutional Neural Networks," *Journal of the Astronautical Sciences*, vol. 67, no. 3, pp. 1063–1091, 2020.

[79] K. Mcnally, D. Ramirez, and et al., "Artificial Intelligence for Space Resident Objects," no. April, pp. 20–23, 2021.

[80] A. Kaluthantrige, J. Feng, and et al., "CNN-based Image Processing algorithm for autonomous optical navigation of Hera mission to the binary asteroid Didymos," *Acta Astronautica*, vol. 211, no. May, pp. 60–75, 2023.

[81] M. Pugliatti, V. Franzese, and et al., "Data-Driven Image Processing for Onboard Optical Navigation Around a Binary Asteroid," *Journal of Spacecraft and Rockets*, vol. 59, no. 3, pp. 943–959, 2022.

[82] A. Escalante Lopez, P. Ghiglino, and et al., "Applying Machine Learning Techniques for Optical Relative Navigation in Planetary Missions," *IEEE Transactions on Geoscience and Remote Sensing*, vol. 62, pp. 1–11, 2024.

[83] T. Teil, S. Bateman, and et al., "Autonomous On-Orbit Optical Navigation Techniques for Robust Pose-Estimation," pp. 1–17.

[84] B. Gaudet, R. Linares, and et al., "Deep reinforcement learning for six degree-of-freedom planetary landing," *Advances in Space Research*, vol. 65, no. 7, pp. 1723–1741, 2020. [Online]. Available: https://doi.org/10.1016/j.asr.2019.12.030

[85] P. Peñarroya, S. Centuori, and et al., "A LiDAR-less approach to autonomous hazard detection and avoidance systems based on semantic segmentation," *Celestial Mechanics and Dynamical Astronomy*, vol. 135, no. 3, pp. 1–26, 2023. [Online]. Available: https://doi.org/10.1007/s10569-023-10140-9

[86] L. F. Palafox, C. W. Hamilton, and et al., "Automated detection of geological landforms on Mars using Convolutional Neural Networks," *Computers and Geosciences*, vol. 101, no. October 2016, pp. 48–56, 2017. [Online]. Available: http://dx.doi.org/10.1016/j.cageo.2016.12.015

[87] M. Pugliatti, M. Maestrini, and et al., "on-Board Small-Body Semantic Segmentation Based on Morphological Features With U-Net," *AAS*, no. February, pp. 1–20, 2021. [Online]. Available: https://sbn.psi.edu/pds/shape-models/

[88] F. Latorre, D. Spiller, and et al., "FULLY-CONVOLUTIONAL NEURAL NETWORK," pp. 1–12.

[89] P. Mancini, M. Cannici, and et al., "Deep learning for asteroids autonomous terrain relative navigation," *Advances in Space Research*, vol. 71, no. 9, pp. 3748–3760, 2023. [Online]. Available: https://doi.org/10.1016/j.asr.2022.04.020

[90] O. Knuuttila, A. Kestila, and et al., "CNN-Based Local Features for Navigation Near an Asteroid," *IEEE Access*, vol. 12, no. October 2023, pp. 16 652–16 672, 2024.

[91] H. F. Agrusa, I. Gkolias, and et al., "The excited spin state of Dimorphos resulting from the DART impact," *Icarus*, vol. 370, 2021.

[92] K. Sun, B. Xiao, and et al., "Deep high-resolution representation learning for human pose estimation," in *Proceedings of the IEEE Computer Society Conference on Computer Vision and Pattern Recognition*, pp. 5686–5696, june, 2019.

[93] L. Pasqualetto Cassinis, R. Fonod, and et al., "Evaluation of tightly- and loosely-coupled approaches in CNN-based pose estimation systems for uncooperative

spacecraft," *Acta Astronautica*, vol. 182, no. June 2020, pp. 189–202, 2021. [Online]. Available: https://doi.org/10.1016/j.actaastro.2021.01.035

[94] B. Chen, J. Cao, and et al., "Satellite pose estimation with deep landmark regression and nonlinear pose refinement," *Proceedings - 2019 International Conference on Computer Vision Workshop, ICCVW 2019*, pp. 2816–2824, 2019.

[95] J. A. Christian and E. G. Lightsey, "Onboard image-processing algorithm for a spacecraft optical navigation sensor system," *Journal of Spacecraft and Rockets*, vol. 49, no. 2, pp. 337–352, 2012.

[96] J. A. Christian, "Optical navigation using planet's centroid and apparent diameter in image," *Journal of Guidance, Control, and Dynamics*, vol. 38, no. 2, pp. 192–204, 2015.

[97] E. Adams, D. Oshaughnessy, and et al., "Double Asteroid Redirection Test: The Earth Strikes Back," *IEEE Aerospace Conference Proceedings*, vol. 2019-March, pp. 1–11, 2019.

[98] E. Smith, S. Zhan, and et al., "Testing Early and Often: End-to-End Testing on the Double Asteroid Redirection Test (DART)," *IEEE Aerospace Conference Proceedings*, pp. 1–9, 2020.

[99] A. Mertan, D. J. Duff, and et al., "Single image depth estimation: An overview," *Digital Signal Processing: A Review Journal*, vol. 123, pp. 1–18, 2022.

[100] M. Pugliatti, V. Franzese, and et al., "Design of the on-board image processing of the milani mission," pp. 1–21, 2022.

[101] JPL, "JPL Small-Body Database Browser," 2021. [Online]. Available: https://ssd.jpl.nasa.gov/sbdb.cgi?sstr=Didymos

[102] M. Dunstan and I. Martin, "Planet and Asteroid Natural Scene Generation Utility User Manual," STAR-Dundee, Tech. Rep. 2, 2017.

[103] ESA, "Hera Mission Instruments," 2021. [Online]. Available: https://www.heramission.space/hera-instruments

[104] H. Sierks, H. U. Keller, and et al., *The Dawn framing camera*, 2011, vol. 163, no. 1-4.

[105] R. Hartley and A. Zisserman, *Camera Models*. Cambridge University Press, 2004, p. 153–177.

[106] P. Sturm, *Pan-Tilt-Zoom (PTZ) Camera*, 2021.

[107] K. Sun, B. Xiao, and et al., "Deep high-resolution representation learning for human pose estimation," *Proceedings of the IEEE Computer Society Conference on Computer Vision and Pattern Recognition*, vol. 2019-June, pp. 5686–5696, 2019.

[108] M. I. Ribeiro, "Kalman and Extended Kalman Filters : Concept , Derivation and Properties," *Institute for Systems and Robotics Lisboa Portugal*, no. February, p. 42, 2004. [Online]. Available: http://citeseerx.ist.psu.edu/viewdoc/download?doi=10.1.1.2.5088&rep=rep1&type=pdf

[109] K. H. Glassmeier, H. Boehnhardt, and et al., "The Rosetta mission: Flying towards the origin of the solar system," *Space Science Reviews*, vol. 128, no. 1-4, pp. 1–21, 2007.

[110] M. Yoshikawa, J. Kawaguchi, and et al., "Hayabusa sample return mission," in *Asteroids IV*. University of Arizona press, 2015, vol. 1, pp. 397–418.

[111] S.-i. Watanabe, Y. Tsuda, and et al., "Hayabusa2 Mission Overview," *Space Sci Rev*, pp. 3–16, 2017.

[112] D. S. Lauretta, S. S. Balram-Knutson, and et al., "OSIRIS-REx: Sample Return from Asteroid (101955) Bennu," *Space Science Reviews*, vol. 212, no. 1-2, pp. 925–984, 2017.

[113] F. Ferrari, S. D. Raducan, and et al., "Ejecta Formation, Early Collisional Processes, and Dynamical Evolution after the DART Impact on Dimorphos," *Planetary Science Journal*, vol. 3, no. 7, p. 177, 2022.

[114] N. G. Dias, P. Gordo, and et al., "Analysis on the Isostatic Bipod Mounts for the HERA Mission LIDAR," *Applied Sciences (Switzerland)*, vol. 12, no. 7, 2022.

[115] F. Cabral and V. Moreno Villa, "Mission Analysis Report," GMV, Tech. Rep., 2022.

[116] L. Pasqualetto Cassinis, A. Menicucci, and et al., "On-Ground Validation of a CNN-based Monocular Pose Estimation System for Uncooperative Spacecraft," *8th European Conference on Space Debris*, 2021.

[117] J. Lyzhoft and B. Wie, "New image processing algorithm for terminal guidance of multiple kinetic-energy impactors for disrupting hazardous asteroids," *Astrodynamics*, vol. 3, no. 1, pp. 45–59, 2019.

[118] R. Pardo de Santanaya and M. Lauer, "Optical measurements for rosetta navigation near the comet," in *International Symposium on Space Fligth Dynamics*, no. 1, 2015, pp. 1–19.

[119] T. Hashimoto, T. Kubota, and et al., "Vision-based guidance, navigation, and control of Hayabusa spacecraft - Lessons learned from real operation," in *IFAC Proceedings Volumes (IFAC-PapersOnline)*, vol. 18, no. PART 1. IFAC, 2010, pp. 259–264.

[120] T. Saiki, Y. Takei, and et al., "Overview of Hayabusa2 Asteroid Proximity Operation Planning and Preliminary Results," *Transactions of the Japan Society for Aeronautical and Space Sciences, Aerospace Technology Japan*, vol. 19, no. 1, pp. 52–60, 2021.

[121] B. Williams, P. Antreasian, and et al., "OSIRIS-REx Flight Dynamics and Navigation Design," *Space Science Reviews*, vol. 214, no. 4, 2018.

[122] K. Sun, Y. Zhao, and et al., "High-Resolution Representations for Labeling Pixels and Regions," 2019. [Online]. Available: http://arxiv.org/abs/1904.04514

[123] S. J. Julier and J. K. Uhlmann, "Unscented Filtering and Nonlinear Estimation," 2004, vol. 92, no. 3, pp. 401–402.

[124] G. Flandin, B. Polle, and et al., "Vision based navigation for autonomous space exploration," *2010 NASA/ESA Conference on Adaptive Hardware and Systems, AHS 2010*, pp. 9–16, 2010.

[125] M. Mokuno and I. Kawano, "In-orbit demonstration of an optical navigation system for autonomous rendezvous docking," *Journal of Spacecraft and Rockets*, vol. 48, no. 6, pp. 1046–1054, 2011.

[126] M. Sabatini, G. B. Palmerini, and et al., "A testbed for visual based navigation and control during space rendezvous operations," *Acta Astronautica*, vol. 117, pp. 184–196, 2015. [Online]. Available: http://dx.doi.org/10.1016/j.actaastro.2015.07.026

[127] A. Pellacani, P. Kicman, and et al., "Design and validation of a GNC system for missions to asteroids: the AIM scenario," *CEAS Space Journal*, vol. 10, no. 4, pp. 555–566, 2018. [Online]. Available: https://doi.org/10.1007/s12567-017-0189-x

[128] P. Kicman, J. Lisowski, and et al., "Vision-based navigation around small bodies," in *Astrodynamics Network AstroNet-II*, G. Gómez and J. J. Masdemont, Eds. Cham: Springer International Publishing, 2016, pp. 137–149.

[129] G. Napolano, C. Vela, and et al., "A multi-sensor optical relative navigation system for small satellite servicing," *Acta Astronautica*, vol. 207, no. February, pp. 167–192, 2023.

[130] R. Brochard, J. Lebreton, and et al., "Scientific image rendering for space scenes with the surrender software," 2018.

[131] M. Pugliatti, C. Buonagura, and et al., "Corto: The celestial object rendering tool at dart lab," *Sensors*, vol. 23, p. 9595, 2023. [Online]. Available: https://www.mdpi.com/1424-8220/23/23/9595

[132] M. Pajusalu, I. Iakubivskyi, and et al., "SISPO: Space Imaging Simulator for Proximity Operations," *PLoS ONE*, vol. 17, no. 3 March, pp. 1–22, 2022.

[133] H. Benninghoff, F. Rems, and et al., "Development and hardware-in-the-loop test of a guidance , navigation and control system for on-orbit servicing," *Acta Astronautica*, vol. 102, pp. 67–80, 2014.

[134] F. Pace, E. Paolini, and et al., in *Modern Spacecraft Guidance, Navigation, and Control*.

[135] F. Piccolo, M. Pugliatti, and et al., "Toward Verification and Validation of the Milani Image Processing Pipeline in the Hardware-in-the-Loop Testbench Tinyv3Rse," in *Proceedings of the 44th Annual American Astronautical Society Guidance, Navigation, and Control Conference, 2022*, 2024, pp. 1081–1101.

[136] C. Beierle, J. Sullivan, and et al., "Design and Utilization of the Stanford Vision-Based Navigation Testbed for Spacecraft Rendezvous," in *International Workshop on Spacecraft Formation Flying*, 2017, pp. 17–26.

[137] M. Samaan, S. Lockhart, and et al., "On-Ground Calibration and Optical Alignment for the Orion Optical Navigation Camera," in *John Junkins Dynamical Systems Symposium*, 2018.

[138] T. H. Park, J. Bosse, and et al., "Robotic Testbed for Rendezvous and Optical Navigation: Multi-Source Calibration and Machine Learning Use Cases," in *AAS*, 2021, pp. 1–20. [Online]. Available: http://arxiv.org/abs/2108.05529

[139] H. Krüger and S. Theil, "TRON - Hardware-in-the-loop test facility for lunar descent and landing optical navigation," in *IFAC Proceedings Volumes (IFAC-PapersOnline)*, vol. 18, no. PART 1, 2010, pp. 265–270.

[140] M. Wilde, B. Kaplinger, and et al., "ORION: A simulation environment for spacecraft formation flight, capture, and orbital robotics," in *IEEE Aerospace Conference Proceedings*, vol. 2016-June. IEEE, 2016, pp. 1–14.

[141] M. Zwick, I. Huertas, and et al., "ORGL - ESA's Test Facility for Approach and Contact Operations in Orbital and Planetary Environments," in *International Symposium on Artificial Intelligence, Robotics and Automation in Space*,

2018. [Online]. Available: https://robotics.estec.esa.int/i-SAIRAS/isairas2018/Papers/Session4b/2_ORGL_i-Sairas2018_paper-49-30-Zwick-Martin.pdf

[142] A. Kaluthantrige, J. Feng, and et al., "Convolutional-neural-network-based autonomous navigation of hera mission around didymos," *Journal of Guidance, Control, and Dynamics*, vol. 0, no. 0, pp. 1–14, 0. [Online]. Available: https://doi.org/10.2514/1.G008054

[143] Y. Zhang, J. Jiang, and et al., "Edge detection in planet image using an improved partial area effect algorithms," in *Optical Sensing and Imaging Technologies and Applications*, M. Guina, H. Gong, J. Lu, and D. Liu, Eds., vol. 10846, International Society for Optics and Photonics. SPIE, 2018, p. 108462B. [Online]. Available: https://doi.org/10.1117/12.2505412

[144] L. Federici, A. Scorsoglio, and et al., "Image-Based Meta-Reinforcement Learning for Autonomous Guidance of an Asteroid Impactor," *Journal of Guidance, Control, and Dynamics*, vol. 45, no. 11, pp. 2013–2028, 2022.

[145] S. Sharma and S. D'amico, "Pose estimation for non-cooperative spacecraft rendezvous using neural networks," *Advances in the Astronautical Sciences*, vol. 168, pp. 3527–3546, 2019.

[146] R. Furfaro and A. M. Law, "Relative optical navigation around small bodies via extreme learning machines," vol. 156, 2016, Conference paper, p. 1959 – 1978. [Online]. Available: https://www.scopus.com/inward/record.uri?eid=2-s2.0-85007336458&partnerID=40&md5=6d6b59569c4a731253d50d116504e99a

[147] A. Scorsoglio, A. D'Ambrosio, and et al., *Journal of Spacecraft and Rockets*, vol. 59, no. 1, pp. 153–165, 2022. [Online]. Available: https://doi.org/10.2514/1.A35072

[148] P. Arcaini, A. Bombarda, and et al., "Dealing with Robustness of Convolutional Neural Networks for Image Classification," in *2020 IEEE International Conference on Artificial Intelligence Testing (AITest)*, 2020, pp. 7–14.

[149] I. J. Goodfellow, J. Shlens, and et al., "Explaining and harnessing adversarial examples," in *3rd International Conference on Learning Representations, ICLR 2015 - Conference Track Proceedings*, 2015, pp. 1–11.

[150] S. Dodge and L. Karam, "Understanding how image quality affects deep neural networks," in *2016 8th International Conference on Quality of Multimedia Experience, QoMEX 2016*, 2016.

[151] S. Ghosh, R. Shet, and et al., "Robustness of Deep Convolutional Neural Networks for Image Degradations," in *ICASSP, IEEE International Conference on Acoustics, Speech and Signal Processing - Proceedings*, vol. 2018-April, 2018, pp. 2916–2920.

[152] A. Pellacani, M. Graziano, and et al., "Design , Development , Validation and Verification of GNC technologies," in *8th European Conference for Aeronautics and Space Sciences (EUCASS)*, 2019.

[153] F. Ferrari, V. Franzese, and et al., "Preliminary mission profile of Hera's Milani CubeSat," *Advances in Space Research*, vol. 67, no. 6, pp. 2010–2029, 2021. [Online]. Available: https://doi.org/10.1016/j.asr.2020.12.034

[154] P. Pravec, A. Meyer, and et al., "Rotational lightcurves of Dimorphos and constraints on its post-DART impact spin state," *Icarus*, vol. 418, no. May, p. 116138, 2024. [Online]. Available: https://doi.org/10.1016/j.icarus.2024.116138

[155] M. Pugliatti, "Data-driven image processing for enhanced vision-based applications around small bodies with machine learning," Ph.D. dissertation, Politecnico di Milano, 2023.

[156] A. Petit, E. Marchand, and et al., "Vision-based space autonomous rendezvous: A case study," *2011 IEEE/RSJ International Conference on Intelligent Robots and Systems*, pp. 619–624, 2011.

[157] J. Lebreton, R. Brochard, and et al., "Image simulation for space applications with the SurRender software," pp. 1–16, 2021. [Online]. Available: http://arxiv.org/abs/2106.11322

[158] C. R. Bierle, "High fidelity validation of vision-based sensors and algorithms for spacecborne navigation," Ph.D. dissertation, Standford University, 2019. [Online]. Available: http://purl.stanford.edu/cd052qp9205

[159] A. Escalante Lopez, P. Ghiglino, and et al., "Churinet - Applying Deep Learning for Minor Bodies Optical Navigation," *IEEE Transactions on Aerospace and Electronic Systems*, vol. 59, no. 4, pp. 3566–3578, 2023.

[160] S. D'Amico, M. Benn, and et al., "Pose estimation of an uncooperative spacecraft from actual space imagery," *International Journal of Space Science and Engineering*, vol. 2, no. 2, p. 171, 2014.

[161] V. Badrinarayanan, A. Kendall, and et al., "Segnet: A deep convolutional encoder-decoder architecture for image segmentation," *IEEE transactions on pattern analysis and machine intelligence*, vol. 39, no. 12, pp. 2481–2495, 2017. [Online]. Available: https://arxiv.org/pdf/1511.00561.pdf

[162] A. Carbone, D. Spiller, and et al., "Hardware-in-the-loop simulations of future autonomous space systems aided by artificial intelligence," in *The Use of Artificial Intelligence for Space Applications*, C. Ieracitano, N. Mammone, M. Di Clemente, M. Mahmud, R. Furfaro, and F. C. Morabito, Eds. Cham: Springer Nature Switzerland, 2023, pp. 83–99.

[163] S. Silvestrini and M. Lavagna, "Processor-In-the-Loop Validation of AI-aided Algorithms for On-Board Autonomous Operations," in *16th International Conference on Space Operations*, no. May, 2021, pp. 1–10.

[164] R. Rodrigues, A. Murilo, and et al., "Hardware in the Loop Simulation for Model Predictive Control Applied to Satellite Attitude Control," *IEEE Access*, vol. 7, pp. 157 401–157 416, 2019.

[165] J. O. GmbH, "ASTROhead Cam," 2022. [Online]. Available: https://jena-optronik.de/products/cameras-and-camera-systems/astrohead-cam.html?file=tl_files/pdf/Data%20Sheet%20ASTROhead%20Cam.pdf

[166] I. Fodde, J. Feng, and et al., "Robust Trajectory Design for Ballistic Landings on Dimorphos." *AIAA Science and Technology Forum and Exposition, AIAA SciTech Forum 2022*, 2022.

[167] T. Kubota, T. Hashimoto, and et al., "Guidance and navigation of hayabusa spacecraft for asteroid exploration and sample return mission," *2006 SICE-ICASE International Joint Conference*, pp. 2793–2796, 2006.

[168] R. Pardo de Santanaya and M. Lauer, "Optical measurements for rosetta navigation near the comet," in *International Symposium on Space Fligth Dynamics*, no. 1, 2015, pp. 1–19.

[169] S. Bhaskaran, S. Nandi, and et al., "Small body landings using autonomous onboard optical navigation," *Journal of the Astronautical Sciences*, vol. 58, no. 3 PART 1, pp. 409–427, 2011.

[170] R. Opromolla, G. Fasano, and et al., "A review of cooperative and uncooperative spacecraft pose determination techniques for close-proximity operations," *Progress in Aerospace Sciences*, vol. 93, no. July, pp. 53–72, 2017.

[171] L. Pasqualetto Cassinis, R. Fonod, and et al., "Review of the robustness and applicability of monocular pose estimation systems for relative navigation with an uncooperative spacecraft," *Progress in Aerospace Sciences*, vol. 110, no. June, p. 100548, 2019. [Online]. Available: https://doi.org/10.1016/j.paerosci.2019.05.008

[172] R. Volpe, M. Sabatini, and et al., "Testing and Validation of an Image-Based, Pose and Shape Reconstruction Algorithm for Didymos Mission," *Aerotecnica Missili Spazio*, vol. 99, no. 1, pp. 17–32, 2020. [Online]. Available: https://doi.org/10.1007/s42496-020-00034-6

[173] A. Kaluthantrige, J. Feng, and et al., "Incremental validation test campaign of a CNN-based Image Processing algorithm for autonomous visual-based navigation applied to the Hera mission," *Acta Astronautica*, no. (unpublished), pp. 2–6, 2024.

[174] S. P. Naidu, S. R. Chesley, and et al., "Orbital and Physical Characterization of Asteroid Dimorphos Following the DART Impact," *Planetary Science Journal*, vol. 5, no. 3, p. 74, 2024. [Online]. Available: http://dx.doi.org/10.3847/PSJ/ad26e7